Etude spectroscopique de galaxies hôtes de quasars lumineux

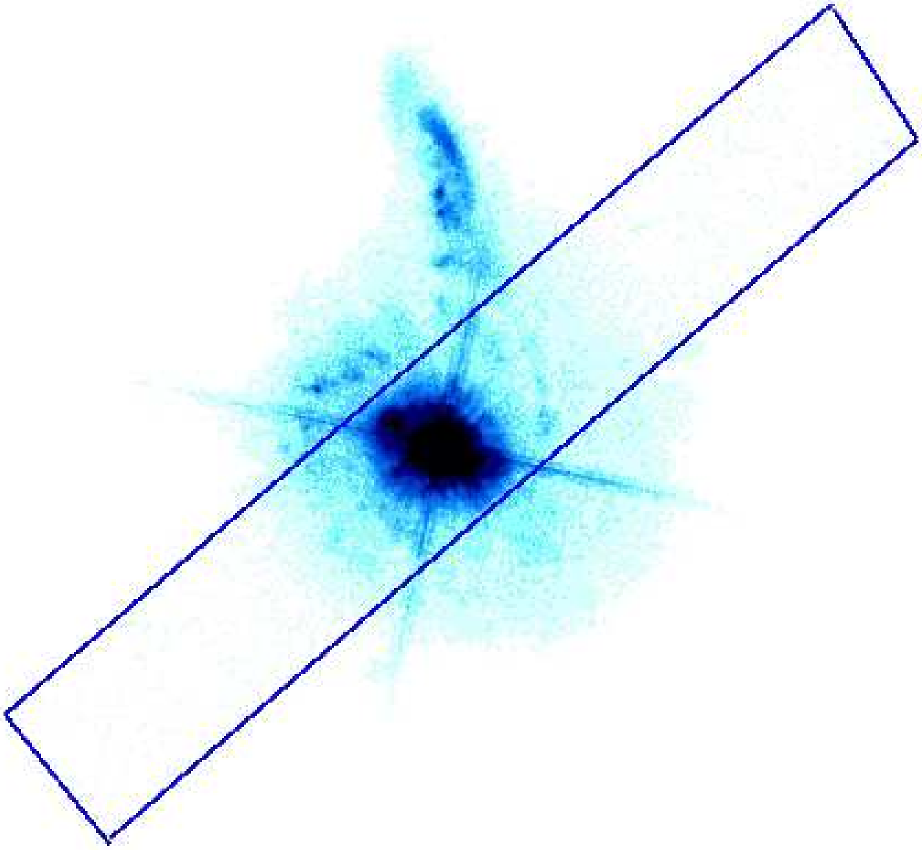

Dissertation présentée en vue de l'obtention du grade de docteur en sciences par

Géraldine Letawe

Département d'Astrophysique,
Géophysique et Océanographie
Faculté des Sciences

Université de Liège
Mars 2006

Remerciements

Je tiens à remercier vivement Pierre d'avoir partagé son impressionnante créativité et son savoir-faire tant au niveau technique de traitement d'images et de spectres qu'au niveau de l'interprétation des résultats. Merci à Frédéric pour les quelques instructifs séjours à l'étranger, pour les nombreuses explications, les conseils et relectures. Merci à Sandrine, toujours présente et efficace au moindre problème de programmation ou de gestion du système informatique.

Je remercie également nos collaborateurs à distance, d'Allemagne et de Suisse pour leurs contributions respectives au travail réalisé. Merci principalement à Pascale pour son regard à la fois critique et constructif et pour l'"écolage" qu'elle m'a offert au sujet de l'analyse des contenus stellaires et gazeux des galaxies, ainsi qu'à Knud, toujours prêt à tout quantifier, mesurer, et évaluer précisément pour s'assurer de la fiabilité de nos résultats.

Merci aux membres du groupe ATI, à Martine, et aux autres chercheurs du 1er étage pour les sympathiques moments partagés, et particulièrement aux *ptits nouveaux* Virginie et Yannick qui y assurent l'ambiance tout en renforçant l'équipe *quasar* du groupe.

Merci à tous mes amis, et aux membres de ma famille, qui m'ont soutenue et encouragée (moralement et organisationnellement pour certains) durant ces quelques années. Un gros bisou à Claire et Héloïse, mes deux petites filles que j'ai essayé de ne pas trop bousculer avec ce travail, ainsi qu'au numéro 3 à venir, qui me rappellent régulièrement le sens des priorités dans la vie... Merci bien sûr à Francois pour un petit peu tout, et principalement dans ce cadre pour sa confiance totale et manifeste en mes capacités à mener à bien l'entreprise. Et une pensée particulière à mon petit papa, qui sera certainement très fier de lire ce petit mot et de partager bientôt son titre de docteur...

Résumé

Nous avons obtenu et analysé des spectres optiques 2D d'un échantillon non biaisé de 20 quasars lumineux à bas redshift (z<0.35) et de leurs galaxies hôtes. Grâce à la méthode de déconvolution MCS, nous avons pu, dans la quasi totalité des objets observés, séparer efficacement les spectres du quasar et de la galaxie qui l'abrite.

Nous avons développé une technique d'analyse de courbes de rotation et participé à l'amélioration des algorithmes de déconvolution existants dans le cadre de la méthode MCS, ainsi qu'à la construction de quelques variantes adaptées à nos besoins spécifiques.

Ce travail a permis de mettre en évidence quelques systèmes spéciaux, analysés dans le détail, comme les cas de HE 0450-2958 dont la galaxie hôte est indétectable en optique, ou HE 1434-1600, une elliptique contenant du gaz fortement ionisé par le quasar à grande distance du centre galactique.

Nous avons également pu dégager quelques caractéristiques intéressantes de notre échantillon de galaxies hôtes :

- Des galaxies aussi bien elliptiques que spirales abritent des quasars lumineux. Elles contiennent pour la plupart une grande quantité de gaz ionisé (par le rayonnement du quasar, par des étoiles ou marginalement par des chocs). Malgré le manque d'information morphologique pour une partie de l'échantillon, nous pouvons conclure que la moitié de ces galaxies présentent des caractéristiques spectrales typiques de très jeunes spirales.

- Nous recensons deux principales origines de l'activité des trous noirs centraux. D'une part, les interactions ou fusions de galaxies, à petite ou grande échelle, capables d'amener de la matière à proximité du trou noir et donc de l'alimenter. Nous présentons des diagnostics spectraux de l'accroissement de la quantité de matière près du centre, du taux d'accrétion ainsi que de la puissance du quasar dans les galaxies en interaction. D'autre part, comme une fraction importante des galaxies de cet échantillon ne présentant pas de traces d'interaction révèlent néanmoins un contenu stellaire et gazeux typique de jeunes galaxies spirales, nous suggérons que des événements locaux (non résolus par nos observations), comme par exemple des vents galactiques créés par des supernovae, pourraient également amener du carburant au quasar dans de tels environnements riches en gaz.

Abstract

We have obtained and analyzed 2D optical spectra for an unbiased sample of 20 luminous quasars and their host galaxies at low redshift ($z < 0.35$). Thanks to the MCS deconvolution method, we have been able, in almost all cases, to efficiently separate the quasar and host spectra.

We have developed a method to analyze and model the radial velocity curves. Within the framework of the MCS deconvolution method, we have adapted several algorithms to the specificity of our spectral and imaging data.

This work has allowed the discovery of peculiar systems, which have been analyzed in more detail, such as HE 0450-2958, a bright quasar whose galaxy is not detectable in the optical, or HE 1434-1600, an elliptical host with gas highly ionized by the quasar far away from the nucleus.

We have also been able to identify several interesting characteristics of our quasar hosts sample:

- Luminous quasars are found in both elliptical and spiral hosts. These galaxies generally contain a large amount of gas (ionized by stars, by the AGN or marginally by shocks). Despite the lack of morphological classification for a part of the sample, we can conclude that at least half of the galaxies show spectral characteristics typical of young spirals.

- We find two major causes of central black hole ignition: First, interactions and minor or major merging processes appear able to bring material close to the center and feed the black hole. We present spectral evidences for the enhancement of accretion rate, amount of central ionized gas and power of the quasar in interacting hosts. On the other hand, as an important fraction of the galaxies showing no trace of interaction harbour stellar and gaseous contents typical of very young spiral systems, we suggest that local events (unresolved by our observations), such as maybe galactic winds driven by central supernovae, might also bring fuel to the quasar in such gas-rich environments.

Table des matières

Chapitre 1

Introduction

Dans cette introduction je présenterai le projet global de recherche dans lequel s'insère cette thèse. Je donnerai quelques notions de bases sur ce que l'on connaît actuellement des quasars et de leurs galaxies hôtes, avant de m'attarder sur les techniques de traitement de données et d'analyse employées et développées durant ce travail.

1.1 Le projet

La mise au point de la méthode de déconvolution d'images MCS en 1998 [75] et son application à la déconvolution de spectres en 2000 [25] ont permis d'ouvrir de nouveaux champs d'exploration en astronomie (voir la fin de ce chapitre pour plus de détails). Outre la capacité à améliorer la résolution des observations, la technique est particulièrement bien adaptée pour la séparation entre sources ponctuelles et diffuses. C'est donc tout naturellement que cette méthode a été utilisée pour l'étude des mirages gravitationnels ainsi que celle des quasars et de leurs hôtes, chacune mettant en jeu une ou plusieurs sources ponctuelles (les quasars) et une source plus étendue (la galaxie lentille ou la galaxie hôte).

Le projet présenté ici concerne le second domaine. Afin d'appliquer la déconvolution de spectres à l'analyse de galaxies hôtes de quasars, un échantillon de quasars proches ($z < 0.35$) et lumineux ($M_B < -23$) a été sélectionné dans le "Hamburg-Eso Survey", et observé en spectroscopie à deux dimensions (information spatiale le long de la fente en plus de spectrale) au VLT, avec FORS1 en mode MOS (Multi Object spectrograph). Le travail de cette thèse a donc consisté à réduire, déconvoluer et analyser l'ensemble des 20 quasars qui composent l'échantillon.

Parallèlement à cette étude, nous avons obtenu des observations pour certains objets en spectroscopie "3D", ou "intégrale de champ" (IFS), à savoir une information spectrale pour chaque zone du champ observé. Ces données commencent à être réduites et analysées, principalement par nos collaborateurs en Suisse et en Allemagne. Nous avons également obtenu quelques images à haute résolution avec le téléscope spatial Hubble (HST) qui permettront, entre autres, une meilleure compréhension des spectres 3D. Comme une partie de ces images concerne les mêmes quasars que notre échantillon de spectroscopie de fente, leur analyse a permis de confirmer et/ou clarifier certains résultats obtenus via les spectres (voir par exemple le chapitre 4).

1.2 Les quasars et leurs galaxies hôtes

1.2.1 Les noyaux actifs de galaxies

Les noyaux actifs de galaxies[1](“AGN” d'après leur abréviation anglaise) sont parmi les objets les plus spectaculaires dans l'Univers. Ils présentent des luminosités impressionnantes (jusqu'à dix mille fois la luminosité typique d'une galaxie) dans de très petits volumes. Cette radiation apparaît dans de très larges bandes de fréquence, et aussi bien les raies d'émission que le continu émis sont remarquables. Il est généralement admis que ces AGN sont des trous noirs supermassifs situés au centre des galaxies et qui accrètent la matière environnante. La matière accélérée vers le trou noir dégage une énergie et une luminosité qui dépassent de loin celles émises par tout autre processus de fusion ou d'explosion. C'est cette luminosité qui permet d'ailleurs l'observation de tels objets jusqu'à des redshifts très élevés (le plus lointain découvert jusqu'ici est à $z = 6.28$), en donnant ainsi une belle opportunité aux scientifiques de sonder et de mieux comprendre l'évolution de l'Univers depuis ses débuts.

On recense toute une faune d'AGN, se distinguant les uns des autres par des spécificités spectrales ou par l'historique de leur découverte. Voici un aperçu général des principales familles de noyaux actifs, pour lesquelles je garderai en général par la suite le nom anglais :

Seyferts Ce sont des galaxies spirales, a priori normales, au sein desquelles on détecte un noyau très lumineux. Ce noyau émet un continu intense ainsi que des raies d'émission larges (permises) et des raies étroites (permises et interdites). Cette classe d'AGN est elle-même divisée en sous-classes, les *Seyferts 1* présentant continu + raies larges + raies étroites tandis que les *Seyferts 2* ne montrent pas de raies larges et ont un continu plus faible. Les *Narrow Line Seyferts 1, NLS1,* quant à elles présentent des raies larges à peine plus larges que leurs raies étroites, mais des rapports de raies typiques des Seyferts 1.

Quasars ou QSOs Ce sont les objets pour lesquels la luminosité du noyau actif dépasse celle de la galaxie qui l'abrite. Ils ont au départ été détectés comme source ponctuelle (*QSO, Quasi Stellar Object*) en optique ou via leur émission radio (*QUAsi Stellar Astronomical Radio Source*). Ils présentent un continu intense depuis les rayons X jusqu'à l'infrarouge, ainsi que des raies larges et étroites en optique et UV. En fonction de l'intensité de leur rayonnement radio, on les classifie comme des quasars *Radio Loud* (“radio puissants”) ou *Radio Quiet* (“radio faibles”). On les sépare également en *type 1* (la grande majorité) ou

---

[1] Cette introduction se base principalement sur les ouvrages de Peterson 1997 [98], Krolik 1999 [66], et Weedman 1986 [116].

type 2 (une petite minorité observée à ce jour) selon la présence ou non des raies larges dans leur spectre.

Radio Galaxies Les émissions en radio des AGNs présentent généralement deux types de structure : un noyau compact et/ou des lobes étendus. Si l'émission est dominée par la partie compacte, on parle de *FR-I Radio Galaxies*, pour lesquelles l'emission radio est d'intensité décroissante plus on s'éloigne de l'AGN, se prolongeant pour la plupart en deux jets irréguliers. Les *FR-II Radio Galaxies*, globalement plus lumineuses que les FR-I, sont en général dominées en luminosité par les deux lobes très étendus placés symétriquement autour du noyau, dans lesquels l'intensité radio augmente en s'éloignant du centre en terminant par des zones de chocs. Dans cette sous-classe des FR-II, on distingue également les *Broad Line Radio Galaxies* (BLRG) ou *Narrow Line Radio Galaxies* (NLRG) en fonction de la présence ou non de raies larges. Les BLRG rejoignent la classe des Radio Loud Quasars, l'appelation RLQ étant préférée pour les objets dont la luminosité du continu domine les émissions étendues du domaine radio.

Blazars Cette famille regroupe les *BL Lac* et les *OVV, Optically Violent Variables*, toutes deux caractérisées par de l'émission radio et une forte variabilité de la luminosité intense de leur continu. Les OVV ont de faibles raies d'émission tandis que les BL Lac n'en présentent pas du tout.

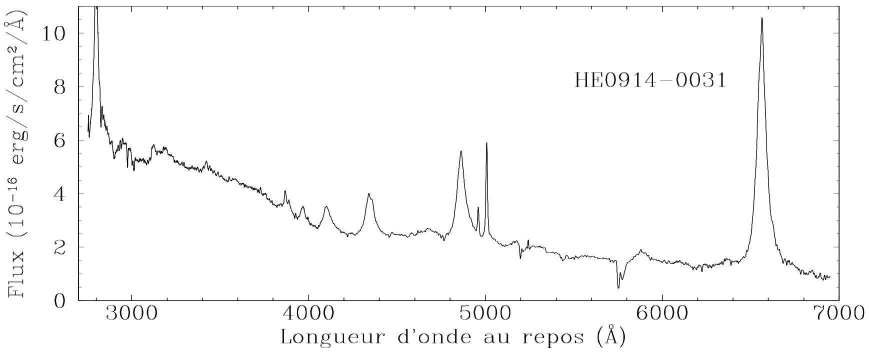

FIG. 1.1 – Spectre de quasar typique dans le domaine optique. Le continu est plus intense aux courtes longueurs d'ondes (=bleu), on y observe d'importantes raies d'émission, larges (principalement ici les raies de Balmer de l'hydrogène) ou étroites (les raies dites "interdites").

Le schéma habituel d'unification des AGN permet, sur base de la structure supposée des noyaux actifs, d'expliquer comment ces différentes familles pourraient n'être le reflet que d'un seul et même phénomène. Voici, succintement, une description qualitative des différents composants d'un noyau actif, du centre vers l'extérieur (Fig. 1.2).

1. le trou noir supermassif (entre un million et un milliard de masses solaires) qui, bien sûr, n'est pas observable directement.
2. la zone d'accrétion, où est produit un rayonnement non thermique intense : la matière accélérée tombant dans le trou noir transforme son énergie cinétique en radiation. Les gaz perdent ainsi jusqu'à 30% de leur énergie en tombant dans le trou noir. C'est ce rayonnement qui fournit la partie continue du spectre et qui va exciter les couches suivantes. Les zones d'accrétion sont probablement sous la forme d'un disque.
3. la BLR, ("broad line region"), zone d'où sont émises les raies les plus larges du quasar (les raies dites "permises", de largeur à mi-hauteur (FWHM) entre 2000 et 20000 $\mathrm{km\,s^{-1}}$). La vitesse de dispersion des particules y est élevée, le milieu est dense, principalement composé d'hydrogène, qui par ionisation-recombinaison émet des photons. Cette région serait entourée d'un tore de poussière.
4. la NLR, ("narrow line region"), zone d'où proviennent les raies les plus étroites du quasar (FWHM $\sim 500\,\mathrm{km\,s^{-1}}$). Le milieu y est suffisamment ténu que pour voir apparaître les transitions dites "interdites" : il y a suffisamment peu de collisions pour que les atomes excités reviennent à leur état initial par simple désexcitation. Ces raies sont toujours référenciées entre crochets (comme par exemple [OII]). Les particules y ont une dispersion de vitesse plus faible, d'où une largeur moindre des raies.
5. les deux jets radio (pas toujours présents), dont l'émission provient de rayonnement synchrotron. Les particules chargées du disque d'accrétion en rotation rapide créent un champ magnétique perpendiculaire au plan du disque. Les particules relativistes (essentiellement des électrons) sont accélérées par la forte pression de radiation, et collimatées le long des lignes du champ magnétique. En spiralant autour de ces lignes de champ, les électrons émettent dans le domaine radio, c'est le rayonnement synchrotron.

Selon le schéma d'unification, on peut interpréter les différentes familles d'AGN en fonction de l'angle sous lequel ce noyau est observé (voir Figs. 1.2 et 1.3).

- Si la ligne de visée de l'observateur passe par le tore de poussière, les raies larges de la BLR seront cachées, donnant lieu aux Seyfert 2 ou quasars de type 2 en fonction de la luminosité totale du noyau et NLRG si l'émission radio est importante. Une partie du continu reste quand même visible car sa lumière est diffusée par des électrons libres se trouvant en dehors de la zone obscurcie par la poussière, et par ce fait polarisée. En observant le noyau en lumière polarisée, on peut distinguer également les raies larges de la BLR.
- Si la ligne de visée ne traverse pas le tore de poussière, les raies larges seront présentes, ce qui pour les noyaux les plus lumineux donnera les quasars de type 1, et pour les moins lumineux les Seyferts 1 (on place conventionellement la limite entre Seyfert et Quasar à $\mathrm{M}_B = -23$), ou les BLRG si l'émission radio est importante.
- Les blazars quant à eux seraient observés perpendiculairement au disque, soit directement dans le jet radio, le continu masquant complètement les éventuelles raies d'émission.

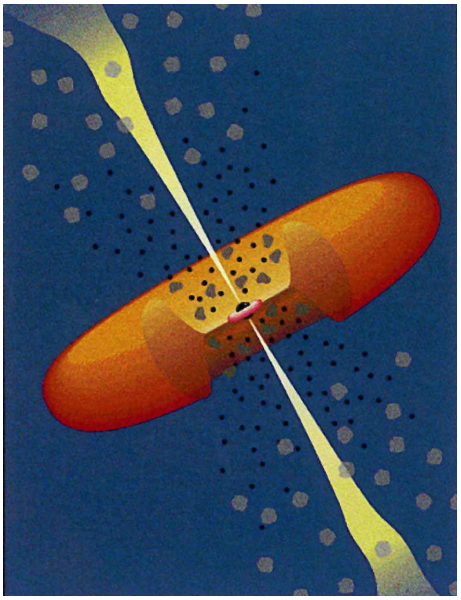

Fig. 1.2 – Représentation schématique traditionnelle des différents composants du quasar. Au centre le trou noir, entouré directement par le disque d'accrétion. En orange le tore de poussière qui entoure la zone d'accrétion. Les petits nuages gris irréguliers au centre schématisent la BLR et les plus gros la NLR. Les deux jets jaunes représentent l'émission radio.

La présence ou non d'émission radio ainsi que son intensité sont probablement liées à la vitesse de rotation du noyau central (qui conditionne l'intensité du champ électromagnétique) et au taux d'accrétion de matière dans le trou noir. Il faut en effet que l'alimentation en particules soit suffisante et que les effets électromagnétiques soient assez puissants pour engendrer et collimater des jets relativistes.

Les schémas d'unification semblent relativement acceptés pour les Seyferts et quasi tous les noyaux actifs en radio (voir pour illustration la Fig. 1.3), mais il reste néanmoins un certain nombre de points d'interrogation et d'incompatibilités observationnelles avec cette interprétation basée uniquement sur des effets d'orientation.

Il n'est par exemple pas encore prouvé que tous les quasars possèdent un tore de poussière : on observe peu de quasars de type 2, ce qui, si on suppose les orientations des quasars réparties uniformément, laisse supposer que le tore de poussière des quasars serait soit très fin, soit inexistant car balayé par le rayonnement intense du centre. Mais les quasars de type-2 sont par définition plus difficiles à repérer vu qu'ils sont obscurcis. Leur non-détection pourrait simplement n'être qu'un effet de sélection. Les recherches actuelles dans le domaine submillimétrique ou les rayons X durs, insensibles à l'obscurcissement par la poussière, commencent à produire de plus en plus de ces sources. L'existence d'un nombre important de quasars obscurcis semble d'ailleurs indispensable à l'explication du rayonnement de fond en rayons X durs.

Toutes les Seyferts 2 ne présentent pas de lumière polarisée en leur centre, et on n'ob-

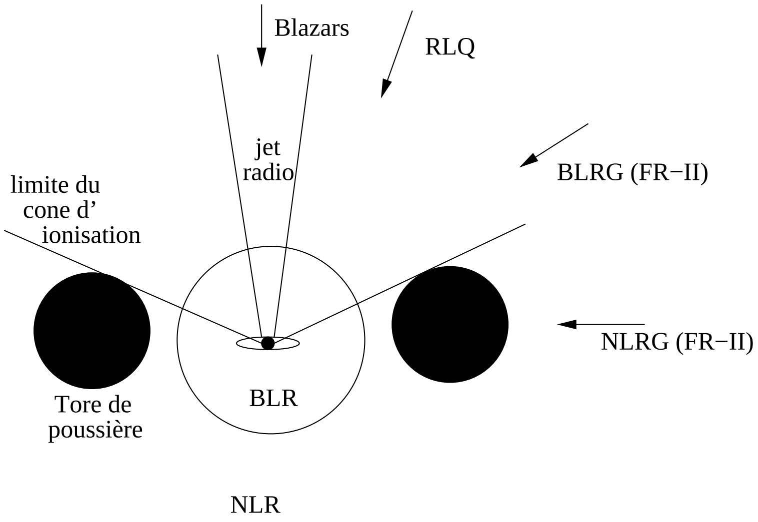

FIG. 1.3 – Les différents types d'AGN qui émettent en radio repris sur ce schéma peuvent être interprétés comme un même phénomène central vu sous différents angles. Au centre le trou noir et le disque d'accrétion, entourés des nuages de la BLR.

serve aucune Seyfert 2 fortement polarisée. Ce qui suggère que toutes les Seyferts 2 ne seraient pas des Seyferts 1 vues au travers d'un tore de poussière mais que d'autres différences intrinsèques existent.

Les NLS1 ne rentrent pas très bien dans un schéma basé sur les effets d'orientation. On les interprète comme de jeunes Seyferts 1 dont la masse du trou noir central est encore faible, mais qui accrètent la matière à des taux très élevés. Les observations dans le domaine des rayons X semblent confirmer cette hypothèse.

Enfin, les radio galaxies de type FR-I, elles non plus, ne s'ajustent pas dans ces représentations. On suppose, dans ce cas, que différents mécanismes physiques sont à l'oeuvre au niveau radio pour ce type de source. S'ils se plaçaient, au niveau angle de visée, entre les blazars et les RLQ de la Fig. 1.3, on s'attendrait à observer des raies larges dans leurs spectres, or ce n'est pas le cas. On l'explique soit par une épaisseur beaucoup plus importante du disque de poussière, réduisant l'ouverture du cône d'ionisation (les FR-I seraient alors de type blazar ou NLRG) soit par l'absence de BLR proprement dite quand le type d'émission FR-I apparaît.

Le fait même que tous les AGN observés ne puissent entrer dans le schéma d'unification laisse non seulement planer un doute sur sa validité, mais nous suggère aussi que les mécanismes à l'oeuvre dans les noyaux de galaxies sont très complexes et encore relativement peu connus, faisant manifestement intervenir plus qu'un simple effet d'orientation.

Citons deux exemples de théories alternatives à l'unification par effet d'orientation, proposant un scénario évolutif, un même objet passant d'un type d'AGN à l'autre au cours de sa vie. Page et al. (2004 [96]) et Fabian (1999 [33]), soutenus par des observations de

Mainieri et al. (2004 [78]), expliquent les quasars de type 2 comme une étape préliminaire aux quasars de type 1. La relation de proportionnalité établie ces dernières années entre la masse du trou noir central et celle du bulbe de la galaxie (Marconi & Hunt 2003 [81]) laisse penser que leurs croissances sont liées. Tous deux se formeraient dans une même sphère de gaz froid poussiéreux (nourrissant *et* la formation d'étoiles du bulbe *et* l'accrétion dans le trou noir) qui serait globalement opaque au rayonnement du disque d'accrétion. Ceci jusqu'au moment où l'AGN devient suffisamment puissant pour balayer ce nuage froid, laissant apparaître un quasar non obscurci qui rayonnera jusqu'à l'épuisement du disque d'accrétion, à moins qu'une collision galactique ne vienne fournir un apport supplémentaire de carburant frais. Reste à expliquer comment la BLR n'est pas balayée également et d'où viennent les NL lors de la phase obscurcie (si ce n'est d'une intense formation d'étoiles dans la galaxie hôte).

De leur côté, Lipari et al. (2006 [70]) distinguent les AGN jeunes par leurs larges raies d'absorption, du FeII important dans le domaine optique, des raies de la BL relativement peu larges, une NLR faible et compacte et une émission radio compacte également. Les AGN plus vieux n'auraient plus de FeII, des raies plus larges dans la BLR, une NLR étendue et brillante et des lobes radios étendus. Cette distinction, basée sur la présence de starbursts massifs, supernovae et vents galactiques dans les systèmes jeunes (IR-mergers), permet d'expliquer des caractéristiques d'émissions qui n'entrent pas dans le scénario habituel. L'orientation jouerait un second rôle dans la différentiation des Seyferts 1/2 ou BLRG/NLRG.

1.2.2 Les galaxies hôtes de quasars

Venons-en à présent aux galaxies qui abritent les AGN. Les Seyferts et Radio Galaxies sont les mieux connues, vu que ces objets étaient détectés en tant que galaxies avant l'identification de leur noyau actif. Pour la plupart, les Seyferts sont des galaxies spirales et les radio galaxies des elliptiques. On avait d'ailleurs, dans un premier temps, généralisé les spirales comme abritant des AGN sans émission radio et les elliptiques des AGN à émission radio forte (et ce, quasars compris).

L'étude des galaxies hôtes des quasars, par contre, est rendue difficile par l'énorme contamination lumineuse du noyau actif, qui est plus lumineux à lui seul que toute la galaxie. La plupart des études des galaxies hôtes de quasars menées jusqu'ici se sont axées principalement sur l'imagerie de ces objets, avec comme principale conclusion que les quasars les plus lumineux sont abrités par des galaxies plus lumineuses également. L'arrivée du téléscope spatial Hubble (HST) a permis d'améliorer la résolution des images des quasars et de leurs hôtes, permettant d'observer directement ces galaxies particulières. La variété des hôtes, des spirales aux massives elliptiques, avec ou sans trace d'interaction, est illustrée par la Fig. 1.4, issue d'une des premières études des galaxies hôtes de quasars avec le HST, par Bahcall et al. en 1997 ([2]).

Des observations et études plus récentes (Dunlop et al 2003 [30] ou Floyd et al. 2004 [36]) tendent à montrer que la luminosité du quasar est liée à la morphologie de la galaxie : tous les quasars plus brillants qu'une magnitude limite seraient abrités par des galaxies

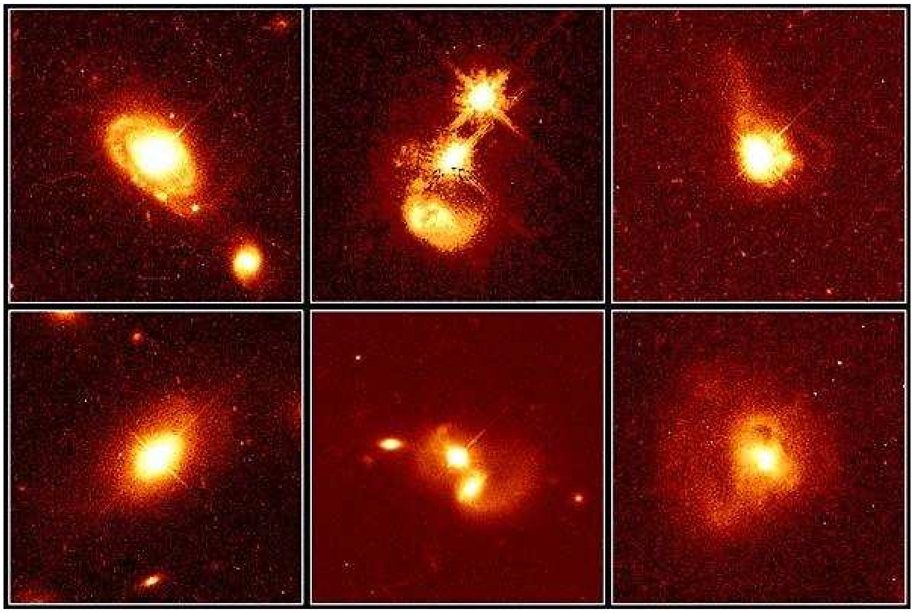

Fig. 1.4 – Premier chantillon de quasars obtenus au HST au milieu des années 90 par Bahcall et al. [2], reflétant la variété des galaxies hôtes.

elliptiques et ce, indépendamment de leur émission radio (voir Fig. 1.5).

La relation quasar-hôte

L'observation d'une corrélation entre la masse du trou noir et la masse du bulbe de la galaxie, et ce aussi bien dans les galaxies inactives (Marconi & Hunt 2003 [81]) qu'actives (McLure & Dunlop 2002 [86]), favorise les théories d'évolution conjointe du trou noir et de la galaxie, comme déja évoqué dans la section précédente. Cette constatation est renforcée par le fait que la population de quasars, qui varie à l'échelle de temps cosmologique, montre un pic important aux alentours des redshifts $z \sim 2-3$, qui coïncide avec l'époque principale de formation des galaxies.

La galaxie est le réservoir de matière première pour alimenter le trou noir central. Pour pouvoir amener la matière dans le disque d'accrétion, deux mécanismes sont proposés : soit des vents stellaires venant d'étoiles massives de l'entourage direct du noyau où une intense formation d'étoiles est supposée avoir lieu, soit (version plus à la mode) l'interaction ou la fusion avec des galaxies voisines, créant perturbations et forces de marées capables d'apporter la matière du milieu interstellaire vers le centre. Ces deux mécanismes sont liés, les perturbations créées par les collisions donnant également lieu à des intenses formations d'étoiles dans les zones centrales. Dans le cas de galaxies spirales, la présences de barres favoriserait également l'afflux de matière vers le trou noir (Crenshaw et al. 2003 [26]).

Des études ont également été menées pour mettre en évidence les différences fondamentales entre galaxies actives et inactives équivalentes par ailleurs. Il en ressort, entre autres, (1) que la proportion de galaxies en interaction ne semble pas plus élevée dans les galaxies

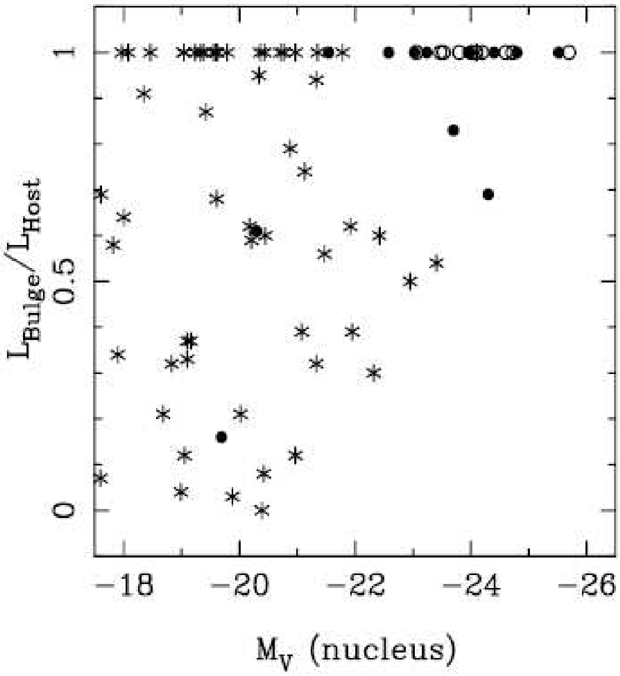

FIG. 1.5 – Graphique tiré de l'article de Dunlop et al. 2003 [30], illustrant le rapport de la luminosité du bulbe sur la luminosité totale de la galaxie en fonction de la magnitude du noyau actif. Un rapport de 1 correspond donc aux galaxies elliptiques, qui sont constituées uniquement d'un bulbe. Les cercles resprésentent les galaxies de leur échantillon, plein pour les RQQ et vide pour les RLQ, les astérisques proviennent d'études antérieures.

actives (Dunlop et al. 2003 [30]), (2) que les galaxies elliptiques actives sont plus bleues et plus lumineuses en moyenne que leurs équivalents sans AGN, reflétant des formations récentes d'étoiles (Jahnke et al. 2004 [51], Vanden Berk et al. 2005 [113]), ou encore (3) que les galaxies hôtes de quasars lumineux contiennent de grandes quantités de gaz moléculaire et donc ne peuvent être considérées comme des elliptiques "normales" (Scoville et al. 2003, [103]).

1.3 Méthodes d'analyse

1.3.1 Déconvolution d'images

La résolution des images astronomiques est limitée par le pouvoir de séparation des instruments employés, ainsi que par les turbulences de l'atmosphère terrestre lorsque les observations sont réalisées depuis le sol. Dans beaucoup de cas, on peut néanmoins améliorer la résolution des images obtenues par un traitement numérique adéquat.

La distribution de lumière observée peut être exprimée mathématiquement comme la convolution de la distribution originale par le profil instrumental total (typiquement l'image d'une source ponctuelle par l'instrument d'observation employé), comprenant également l'étalement de la source dû aux perturbations atmosphériques (seeing). La fonction de convolution est appelée PSF ("point spread function") de l'image, ou profil de réponse instrumentale. On peut écrire de manière générale

$$d(\vec{x}) = t(\vec{x}) * f(\vec{x}) + n(\vec{x})$$

où $f(\vec{x})$ et $d(\vec{x})$ sont les distributions originale et observée de lumière, $t(\vec{x})$ est la PSF totale, et $n(\vec{x})$ le bruit affectant les données (illustration Figure 1.6).

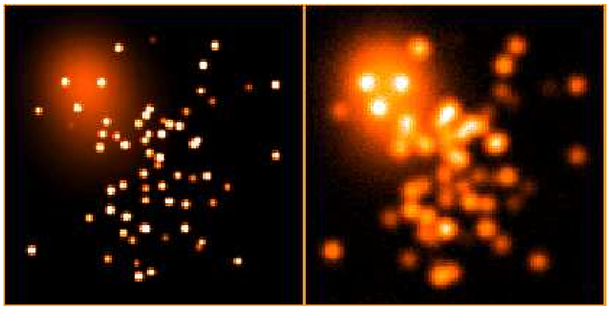

FIG. 1.6 – A gauche une distribution originale de lumière f, à droite l'image observée, d, après dégradation par les perturbations atmosphériques (seeing), le profil instrumental et le bruit de fond.

Les données observées sont bien sûr échantillonnées sur le réseau de pixels du détecteur (CCD), et l'objectif du traitement numérique des données est de reconstruire $f(\vec{x})$, en supposant connues $d(\vec{x})$ et $t(\vec{x})$.

Il existe plusieurs méthodes pour approcher au mieux la fonction $f(\vec{x})$. Nous ne parlerons que de celle employée dans ce travail, proposée par Magain, Courbin & Sohy en 1998 ([75]) et baptisée MCS par la suite.

La méthode MCS de déconvolution d'images se base sur le principe que des données échantillonnées ne peuvent être déconvoluées complètement sans violer le théorème de l'échantillonnage. Il est impossible de reconstruire les détails de l'image dont la taille est inférieure au pas de l'échantillonnage de cette même image. On ne tente donc pas avec cette méthode de reconstruire la fonction $f(\vec{x})$ avec une résolution infinie, mais bien avec une résolution accrue. L'image d'une source ponctuelle sera donc, après déconvolution, une certaine fonction $r(\vec{x})$ d'étendue compatible avec l'échantillonnage utilisé (gaussienne à 2D dans la plupart des utilisations). La déconvolution ne se fait pas via la fonction de PSF totale $t(\vec{x})$, mais via une fonction plus étroite $s(\vec{x})$ telle que $t(\vec{x}) = s(\vec{x}) * r(\vec{x})$.

Puisqu'on connaît exactement la forme que doit avoir toute source ponctuelle dans la distribution de lumière $f(\vec{x})$, on peut décomposer celle-ci en deux parties :

$$f(\vec{x}) = h(\vec{x}) + \sum_{k=1}^{K} a_k r(\vec{x} - \vec{c_k})$$

où K est le nombre de sources ponctuelles dans l'image, a_k et $\vec{c_k}$ leurs intensités et positions respectives. $h(\vec{x})$ est la composante étendue de la solution, qui reprend donc tous les objets non ponctuels de l'image. La méthode revient alors à ajuster au mieux $s(\vec{x}) * f(\vec{x})$ aux observations $d(\vec{x})$. Il est à noter que cette méthode est particulièrement bien adaptée aux quasars et à leurs galaxies hôtes, les premiers étant modélisés par les sources ponctuelles et les secondes par le fond numérique $h(\vec{x})$.
On peut également contraindre ce fond numérique $h(\vec{x})$ en se basant sur la connaissance a priori de sa résolution : on ne peut y trouver de détails plus fins que la résolution fixée $r(\vec{x})$. La solution $f(\vec{x})$ à rechercher doit donc minimiser la fonction S suivante (ici dans le cas discret, pour une image carrée de $N \times N$ pixels) :

$$S = \sum_{i=1}^{N} \frac{1}{\sigma_i^2} \Big[\sum_{j=1}^{N} s_{ij} \Big(h_j + \sum_{k=1}^{K} a_k r(\vec{x_j} - \vec{c_k}) \Big) - d_i \Big]^2 + \lambda \sum_{i=1}^{N} \Big[h_i - \sum_{j=1}^{N} r_{ij} h_j \Big]^2$$

les paramètres à ajuster étant les a_k, $\vec{c_k}$ pour chaque source ponctuelle et l'image de fond h. Le paramètre de Lagrange λ permet d'ajuster la valeur du χ^2 pour que le modèle soit statistiquement en accord avec les données.

Construction de la PSF Un travail important lors de la déconvolution d'images est la construction de la fonction de PSF $s(\vec{x})$. Elle est rendue possible par l'acquisition de l'image d'une étoile $t(\vec{x})$, source ponctuelle, dans les mêmes conditions d'observation que l'image à déconvoluer $d(\vec{x})$ et de préférence proche de cet objet dans le champ. On se base pour cela sur la relation $t(\vec{x}) = s(\vec{x}) * r(\vec{x})$, où r est de forme et largeur fixées, en général une gaussienne de largeur à mi-hauteur minimale de 2 pixels pour respecter le théorème de l'échantillonnage. La fonction s se construit en deux temps : premièrement on ajuste un modèle analytique à la forme globale de l'image de l'étoile, habituellement une fonction de Moffat $m(\vec{x}) = a(1 + b(\vec{x} - \vec{c}))^{-\beta}$, où $\vec{c}$ est le centre de l'étoile, a détermine son intensité, b sa largeur et β la forme de ses ailes. L'ajustement de ces paramètres se fait au moyen d'une minimisation du χ^2 suivant :

$$\chi_M^2 = \sum \frac{1}{\sigma^2} \left[m(\vec{x}) * r(\vec{x}) - t(\vec{x}) \right]^2 \tag{1.1}$$

où la somme porte sur tous les pixels de l'image. La fonction de Moffat $m(\vec{x})$ obtenue est donc celle qui, convoluée par la résolution choisie r, se rapproche le plus de l'étoile observée

t.
Bien entendu, une fonction analytique n'est pas suffisante pour représenter précisément l'étoile observée t. C'est pourquoi un deuxième ajustement est indispensable, pour modéliser les détails plus fins de l'image des résidus $K(\vec{x}) = t(\vec{x}) - [m(\vec{x}) * r(\vec{x})]$ de la première minimisation par l'image $F(\vec{x})$, numérique et plus analytique cette fois. Cette deuxième partie de construction de PSF se ramène à une dernière minimisation, celle de la fonction S :

$$S = \sum \frac{1}{\sigma^2} \left[F(\vec{x}) * r(\vec{x}) - K(\vec{x})\right]^2 + \lambda \sum \left[F(\vec{x}) - r(\vec{x}) * F(\vec{x})\right]^2 \tag{1.2}$$

Le paramètre de Lagrange λ permet de faire correspondre au mieux les résidus K au modèle numérique convolué $F * r$, au sens des moindres carrés, le deuxième terme de l'équation 1.2 assurant qu'on n'introduit pas dans la PSF de détail plus fin que la résolution choisie. La PSF finale s sera la somme de la fonction analytique m et de l'image numérique modélisée F.

La technique de déconvolution d'images connaît actuellement plusieurs variantes et raffinements, permettant entre autres de traiter plusieurs images des mêmes objets simultanément pour un même fond $h(\vec{x})$ et des a_k et $\vec{c_k}$ variables. Durant ce travail, nous avons participé au développement de quelques-unes de ces variantes :

Modèle analytique

Afin de déterminer la morphologie de la galaxie hôte sur base de l'image, nous avons introduit dans la déconvolution des images un modèle analytique de galaxie. La solution $f(\vec{x})$ est donc représentée par la fonction suivante :

$$f(\vec{x}) = h(\vec{x}) + I(\vec{x}) + \sum_{k=1}^{K} a_k r(\vec{x} - \vec{c_k}) \tag{1.3}$$

où $I(\vec{x})$ est le modèle analytique pour une galaxie, que l'on peut choisir comme un profil exponentiel (pour une galaxie spirale) ou de Vaucouleurs (pour une elliptique) en fonction de l'exposant α choisi (1/2 ou 1/8, respectivement) :

$$I(\vec{x}) = I(x, y) = I_0\, e^{-(Ax^2+By^2+Cxy)^\alpha}$$

Les paramètres A, B et C peuvent être reliés à l'orientation du grand axe de la galaxie et de son inclinaison sur la ligne de visée, par simple changement de repère. Ces données sont utiles dans la modélisation des courbes de rotation.

Employée sur les images d'acquisition de notre échantillon de quasars obtenues au VLT, la méthode a permis de déterminer approximativement l'orientation et l'inclinaison dans la plupart des cas. Cependant, la faible résolution de ces observations n'a pas permis de contraindre efficacement la morphologie de la galaxie. Par contre, la méthode s'avère très utile dans la déconvolution d'images du HST, dont la résolution spatiale est bien meilleure, où le profil "de Vaucouleurs" permet de modéliser le bulbe de la galaxie, laissant dans le fond numérique $h(\vec{x})$ d'éventuels bras spiraux ou irrégularités (Fig. 1.7).

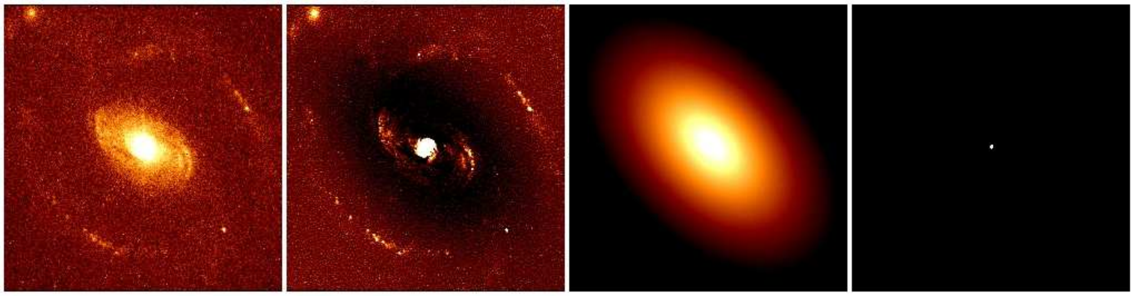

FIG. 1.7 – Illustration de déconvolution avec modèle analytique. De gauche à droite : l'image observée par le HST, ici d'une Seyfert, le fond numérique $h(\vec{x})$ qui contient les bras spiraux, le modèle analytique $I(\vec{x})$, la source ponctuelle à résolution fixée $r(\vec{x})$. La somme de ces trois dernières images est le résultat $f(\vec{x})$ de la déconvolution de la première (cfr Eq. 1.3).

Images du HST

Les images obtenues par l'ACS (Advanced Camera for Surveys) sur le HST offrent la meilleure résolution spatiale disponible en astronomie à ce jour. Ce type d'observation est très instructif dans le cadre de l'étude des galaxies hôtes de quasars, dont les détails, vus du sol, sont souvent masqués par l'étalement de la source ponctuelle intense qu'est le quasar. Hors de l'atmosphère, la PSF n'est plus perturbée par le seeing, mais malheureusement le trajet optique particulier des rayons lumineux dans l'instrument rend cette PSF très complexe (voir Fig. 1.8). Elle nécessite donc une construction minutieuse par une version raffinée de la méthode MCS décrite plus haut, dont les grandes lignes sont présentées ici.

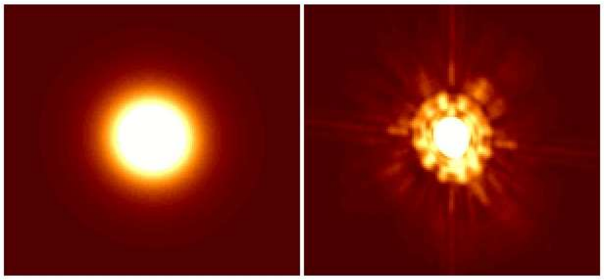

FIG. 1.8 – Comparaison de profils typiques de PSF : à gauche, une fonction de Moffat, pour une observation du sol, principalement dominée par l'étalement dû au seeing atmosphérique. A droite, le modèle de PSF de l'ACS au HST fourni par le logiciel TinyTim, dominé par la complexité de la trajectoire des rayons lumineux dans le système optique du HST.

1. Employer une fonction de Moffat comme profil de base pour la construction de la PSF n'est plus du tout judicieux, étant donné la structure détaillée que montre toute

observation de source ponctuelle via l'ACS (Fig. 1.8). Un logiciel, TinyTim[2], livré par les concepteurs de l'instrument, nous fournit une première estimation de la PSF (nous l'appellerons TinyTim par la suite). Ce logiciel modélise la trajectoire des rayons lumineux au travers de l'instrument en fonction de leur longueur d'onde et position d'origine, en tenant compte du filtre choisi pour l'observation, du type spectral de la source à représenter et de sa position finale sur le détecteur. Les astronomes se contentent d'ailleurs en général de cette PSF ajustée en centrage et intensité pour soustraire les sources ponctuelles de leurs observations.

2. De la même manière que la fonction de Moffat *convoluée par la fonction* $r(\vec{x})$ devait s'approcher au mieux de l'image de l'étoile observée du sol (Eq. 1.1), ce n'est pas la TinyTim elle-même qui va servir de base à la construction de la PSF de l'ACS, mais l'image que nous appellerons *TinyDec* qui, convoluée par une gaussienne de résolution déterminée $r(\vec{x})$, s'approche au mieux de la TinyTim fournie par le logiciel ($TinyTim = TinyDec * r$). Pour ce faire, nous appliquons un algorithme de minimisation semblable à la partie numérique de construction standard de PSF décrite à l'équation 1.2, avec comme image de résidus à modéliser $K(\vec{x}) = TinyTim(\vec{x}) - TinyTim(\vec{x}) * r(\vec{x})$.
3. Cette image TinyDec va donc jouer le rôle habituellement tenu dans l'algorithme classique de MCS par la partie analytique m. C'est ici qu'intervient enfin l'image d'une étoile $t(\vec{x})$ prise par le même instrument, au même endoit sur le détecteur que l'objet astronomique à traiter. Comme il y a énormément de détails fins à modéliser, dont la résolution augmente progressivement en s'approchant du centre, nous procédons à l'ajustement de la partie numérique F à ajouter à la *TinyDec* par étapes. Nous commençons par traiter l'image dans son ensemble, appliquant un terme de lissage fort (paramètre λ élevé dans l'équation 1.2), pour ne modéliser que les résidus à basse résolution mais souvent d'intensité importante. On réitère plusieurs fois l'opération, sur une zone de rayon de plus en plus petit, en diminuant progressivement le lissage et donc en modélisant des détails de la PSF de plus en plus fins. Voici à quoi ressemble ce processus itératif :

$$K_1(\vec{x}) = t(\vec{x}) - TinyDec(\vec{x}) * r(\vec{x})$$

Les résidus K_1 sont modélisés numériquement par l'image F_1 via l'équation 1.2, pour un rayon large et un lissage fort. Ensuite on calcule de nouveaux résidus

$$K_2(\vec{x}) = t(\vec{x}) - (F_1 + TinyDec)(\vec{x}) * r(\vec{x})$$

Ces nouveaux résidus K_2 sont à leur tour modélisés numériquement par l'image F_2, sur un plus petit rayon mais en diminuant le lissage, et ainsi de suite :

$$K_i(\vec{x}) = t(\vec{x}) - (F_1 + ... + F_{i-1} + TinyDec)(\vec{x}) * r(\vec{x})$$

où les K_i sont modélisés numériquement par l'image F_i, avec des rayons de plus en plus petits et des lissages de moins en moins fort.

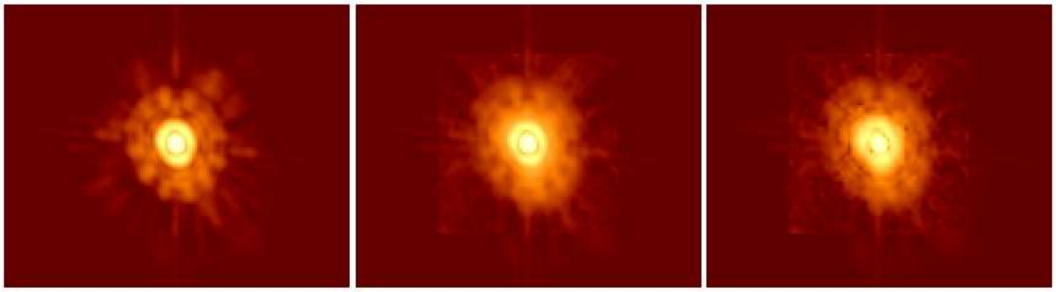

FIG. 1.9 – Différents stades de construction de la PSF pour l'ACS. Des détails de plus en plus fins sont ajoutés à chaque itération, sur une zone de plus en plus réduite spatialement. A gauche la *TinyDec* initiale, au milieu $TinyDec + F_1$, à droite le résultat obtenu après une dizaine d'itérations (voir texte).

Cette méthode employée telle quelle a déja donné de bons résultats (voir au Chapitre 4), mais elle ne cesse d'être raffinée au fur et à mesure de son utilisation, en y incluant par exemple les effets de "jitter", de légères vibrations du téléscope durant les observations, ou encore en modélisant dans la construction de la PSF les distorsions spatiales du champ, qui varient en fonction de la position de l'image sur le détecteur. Ce travail fait partie d'une autre thèse de doctorat débutée en 2005, celle de Yannick Letawe.

1.3.2 Déconvolution de spectres

Tout comme pour l'étude des images de galaxies hôtes de quasars, l'analyse des spectres de ces galaxies nécessite une séparation efficace entre le spectre du quasar et celui de la galaxie qui l'abrite. La méthode MCS adaptée aux spectres, proposée par Courbin, Magain, Sohy & Kirkove en 2000 ([25]), remplit ces objectifs. Nous présentons ici la méthode de base, ainsi que quelques raffinements apportés aux algorithmes au fur et à mesure de leur exploitation dans le cadre de ce travail.

La méthode de déconvolution de spectres se base, comme pour celle des images, sur le respect du théorème de l'échantillonnage : On ne peut trouver dans l'image déconvoluée de composantes de Fourier de fréquences supérieures à la moitié de la fréquence d'échantillonnage. L'objectif est d'améliorer la résolution des observations sans vouloir pour autant une résolution infinie, ce qui amène toujours des artefacts de déconvolution. Le spectre déconvolué d'un objet ponctuel à une longueur d'onde donnée ne sera pas un pic, mais une fonction $r(\vec{x})$ avec une largeur et une forme fixées par l'utilisateur.
Le spectre observé $t_j(\vec{x})$ d'une source ponctuelle (étoile de PSF) à une longueur d'onde donnée j sert de référence pour construire la fonction $s_j(\vec{x})$ qui permet, par convolution, de passer de la résolution finale choisie $r(\vec{x})$ aux données observées.

$$t_j(\vec{x}) = s_j(\vec{x}) * r(\vec{x}) \tag{1.4}$$

---

[2] réalisé par John Krist, http ://www.stsci.edu/software/tinytim/tinytim.html

La connaissance a priori de la forme $r(\vec{x})$ du spectre d'une source ponctuelle déconvoluée permet de décomposer les observations en une somme de sources ponctuelles plus un fond diffus $h(\vec{x})$ qui reprend toutes les sources plus étendues. La différence fondamentale avec le traitement des images est qu'ici, chaque ligne du spectre (donc chaque longueur d'onde) est modélisée séparément. La fonction $f_j(x)$ ci-dessous est une fonction à une dimension, et il en faut autant que d'éléments de résolution spectrale (de lignes j) pour modéliser un spectre complet à deux dimensions. On aura donc, pour un spectre qui contient K sources ponctuelles :

$$f_j(x) = h_j(x) + \sum_{k=1}^{K} a_{k,j} r(x - c_{k,j})$$

Les $a_{k,j}$ et $c_{k,j}$ représentent respectivement l'intensité et la position de la k$^{\text{ème}}$ source dans la ligne j. La largeur de la fonction r, choisie gaussienne, est la même sur tout le spectre. Travailler ligne par ligne permet de tenir compte de la variation de seeing en fonction de la longueur d'onde. La déconvolution d'un spectre à deux dimensions $d(\vec{x})$ se fait par l'ajustement des paramètres $a_{k,j}$, $c_{k,j}$ et des différentes fonctions numériques à une dimension $h_j(x)$, via la minimisation du χ^2 suivant :

$$\chi^2 = \sum_{j=1}^{M} \sum_{i=1}^{N} \frac{1}{\sigma_{i,j}^2} \left[s_j(x) * \left(h_j(x) + \sum_{k=1}^{K} a_{k,j} r(x - c_{k,j}) \right) - d_j(x) \right]_i^2 \tag{1.5}$$

Les indices i parcourent les N pixels de la direction spatiale du spectre, et les indices j les M composantes spectrales.

Des contraintes supplémentaires sont imposées au résultat de la déconvolution. Sur le fond h d'abord : Comme en imagerie, il n'y aurait pas de sens à trouver dans les spectres des détails à une résolution plus fine que celle des sources ponctuelles. Un lissage lui est donc imposé par la minimisation de la fonction L_1 :

$$L_1 = \sum_{j=1}^{M} \sum_{i=1}^{N} \left[h_j(x) - r(x) * h_j(x) \right]_i^2$$

Enfin, même si les positions des sources ponctuelles $c_{k,j}$ peuvent varier le long du spectre, par exemple à cause de variations de la réfraction atmosphérique avec la longueur d'onde, nous savons a priori que cette variation sera relativement lente. Nous pouvons donc imposer une corrélation entre les positions successives d'une même source le long du spectre, et ce en minimisant la fonction L_2 :

$$L_2 = \sum_{k=1}^{K} \sum_{j=B+1}^{M-B} \left[c_{k,j} - \frac{1}{G} \sum_{j'=-B}^{B} g_{j'} c_{k,j+j'} \right]^2 \tag{1.6}$$

La fonction g est une gaussienne, dont on peut adapter la largeur à mi-hauteur pour varier la portée de la corrélation. La somme entre crochets se calcule sur un bloc de $2B+1$ pixels

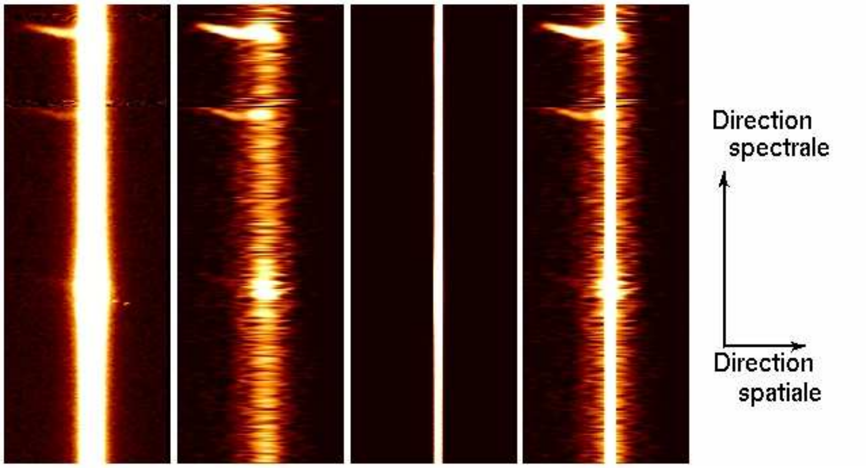

FIG. 1.10 – Morceau de spectre 2D d'un quasar et sa déconvolution. Chaque ligne correspond à une longueur d'onde différente (indice j dans l'Eq. 1.5), chaque colonne à une position différente le long de la fente (i dans l'Eq. 1.5). De gauche à droite : spectre observé $d(x)$, fond numérique h(x), source ponctuelle $r(x)$ et résultat de la déconvolution $f(x)$, somme des deux précédents qui, reconvolué par $s(x)$, est en accord avec le spectre observé $d(x)$.

centrés en j (B fixé par l'utilisateur), et est normalisée via le terme G qui assure un flux unitaire pour les g_j employés. On n'impose pas de corrélation aux pixels des B premières et dernières lignes du spectre, vu que pour eux la zone de corrélation dépasse l'extension spectrale des données.

La déconvolution spatiale de spectre se fait donc par minimisation de la fonction S ci-dessous, où les paramètres de Lagrange λ et μ permettent d'assurer que, au sens des moindres carrés, le résultat soit statistiquement compatible avec les données, ainsi que de contrôler les poids relatifs qu'on donne à chacune des contraintes.

$$S = \chi^2 + \lambda L_1 + \mu L_2 \tag{1.7}$$

Construction de la fonction $s(\vec{x})$.

La qualité de la déconvolution des spectres est, comme dans le cas des images, étroitement liée à la qualité de la PSF $s(\vec{x})$ construite sur base du spectre d'une ou plusieurs étoiles du champ observée(s) simultanément à l'objet étudié. Nous avons besoin, pour chaque élément de résolution spectrale, de la fonction $s_j(x)$ qui permet par convolution de passer d'une source ponctuelle modèle $r(x)$ à l'observation $t_j(x)$ de l'étoile (voir Eq. 1.4). La fonction s est décomposée en une partie analytique, une fonction de Moffat $M_j(x)$ (voir Eq. 1.8) qui constitue une première approximation, plus une image numérique qui permet une représentation plus précise de $s_j(x)$.

$$M_j(x) = a_j \left[1 + b_j(x - c_j)\right]^{-\beta_j} \tag{1.8}$$

Dans cette équation, a_j est l'intensité du profil, c_j son centre dans la direction spatiale, β_j caractérise les ailes du profil et b_j sa largeur. Une première étape dans la construction de s consiste à ajuster au profil observé $t(\vec{x})$ les différents paramètres du profil analytique convolué, en minimisant le χ^2 suivant :

$$\chi^2_M = \sum_{j=1}^{M} \sum_{i=1}^{N} \frac{1}{\sigma^2_{i,j}} \left[M_j(x) * r(x) - t_j(x)\right]^2_i$$

Pour exploiter au maximum les connaissances a priori de la forme du spectre de la PSF, on peut imposer des corrélations entre les paramètres de la fonction de Moffat à des longueurs d'onde voisines. On ne s'attend en effet pas à des variations importantes de profil d'une ligne à l'autre du spectre. La construction de la partie analytique de la PSF se ramène alors à une autre minimisation, celle de la fonction S_m :

$$S_m = \chi^2_M + \mu_1 L_1 + \mu_2 L_2 + \mu_3 L_3,$$

les fonctions L_i étant données par

$$\begin{aligned}
L_1 &= \sum_{j=B+1}^{M-B} \left[c_j - \frac{1}{G} \sum_{j'=-B}^{B} g_{j'} c_{j+j'}\right]^2 \\
L_2 &= \sum_{j=B+1}^{M-B} \left[b_j - \frac{1}{G} \sum_{j'=-B}^{B} g_{j'} b_{j+j'}\right]^2 \\
L_3 &= \sum_{j=B+1}^{M-B} \left[\beta_j - \frac{1}{G} \sum_{j'=-B}^{B} g_{j'} \beta_{j+j'}\right]^2
\end{aligned}$$

Les conventions de notation sont identiques à celles de l'Eq. 1.6. Les paramètres de Lagrange μ_i permettent de donner plus ou moins de poids à l'une ou l'autre des corrélations.

La PSF $s_j(x)$ ne correspond jamais exactement à une fonction de Moffat. Les résidus K_j de la modélisation analytique sont donc à leur tour modélisés par une image numérique $F_j(x)$ à convoluer, à laquelle on impose bien sûr une résolution limitée à celle de $r(x)$. La partie numérique de la PSF à traiter, K, est donnée par

$$K_j(x) = t_j(x) - [M_j(x) * r(x)]$$

Cette deuxième partie de construction de PSF se ramène à une dernière minimisation, celle de la fonction S_f :

$$S_f = \sum_{j=1}^{M} \sum_{i=1}^{N} \frac{1}{\sigma^2_{i,j}} \left[F_j(x) * r(x) - K_j(x)\right]^2_i + \lambda \sum_{j=1}^{M} \sum_{i=1}^{N} \left[F_j(x) - r(x) * F_j(x)\right]^2_i \tag{1.9}$$

Le paramètre de Lagrange λ permet à nouveau de faire correspondre au mieux les résidus K au modèle numérique convolué $F * r$, au sens des moindres carrés. Il est ajusté de manière à obtenir un résultat statistiquement correct, c'est-à-dire une valeur du χ^2 approximativement égale au nombre de degrés de liberté.

Chaque PSF finale s_j est donc la somme de la fonction analytique M_j et du résidu numérique modélisé F_j. La PSF $s(\vec{x})$ à deux dimensions permet donc, dans son emploi pour la déconvolution des spectres, de corriger les données des variations de seeing et de réfraction atmosphérique pour les différentes longueurs d'onde, en donnant aux résultats une résolution fixée et accrue qui respecte le théorème de l'échantillonnage.

Un raffinement des résultats peut être obtenu en suréchantillonnant la PSF s dans la direction spatiale. C'est possible quand on se base sur les spectres de plusieurs étoiles pour la construction de s : les étoiles n'étant pas toutes exactement centrées au même point, l'information spatiale nécessaire à la construction de s sur un réseau d'échantillonnage plus fin est disponible. Cela permet de suréchantillonner également les spectres déconvolués. Dans la pratique on se limite à la division du pas d'échantillonnage initial par un facteur 2.

Différentes adaptations des algorithmes ont été développées durant la thèse, en voici les principales :

Corrélation sur les résidus

Dans l'algorithme de construction de la PSF $s(\vec{x})$, une contrainte supplémentaire peut être apportée à la construction du fond numérique des résidus $F(\vec{x})$. En effet, on ne s'attend pas à ce que les différences entre le spectre observé $t(\vec{x})$ et la fonction de Moffat convoluée varient de manière spectaculaire d'une longueur d'onde à l'autre. Une corrélation est donc introduite entre les pixels d'une même colonne i du fond $F(\vec{x})$. La fonction à minimiser (voir Eq. 1.9) devient donc, pour un spectre initial comprenant M éléments de résolution spectrale ($=M$ lignes) et N pixels dans la direction spatiale ($= N$ colonnes) :

$$S_{f'} = S_f + \mu_f \sum_{i=1}^{N} \sum_{j=B+1}^{M-B} \left[f_{i,j} - \frac{1}{G} \sum_{j'=-B}^{B} g_{j'} f_{i,j+j'} \right]^2$$

Comme pour la construction de la Moffat, le paramètre B fixe la taille $(2B+1)$ de la zone où la corrélation est imposée. La somme entre crochets est centrée en j. La fonction $g_{j'}$ est une gaussienne centrée au pixel j', dont la largeur (à choisir par l'utilisateur) permet de caractériser l'étendue de la corrélation. Il est à noter que le lissage imposé dans l'Eq. 1.9 est dans la direction spatiale, alors que la corrélation présentée ici concerne la direction spectrale.

Contrôle du lissage du fond

Lors de la déconvolution de spectres, on sépare les sources ponctuelles des sources étendues grâce à notre connaissance a priori sur la forme du spectre d'une source ponctuelle. Nous n'en avons pas sur la forme des sources étendues. Un désavantage de la méthode est qu'elle ne permet pas de contrôler le lissage qu'on impose à l'image de fond $h(\vec{x})$. Le lissage est influencé par le paramètre de Lagrange λ de l'Eq. 1.7, mais son impact n'est pas aisément quantifiable et dépend du rapport signal sur bruit ; il peut donc de plus varier d'une longueur d'onde à l'autre. Une manière de garder un contrôle sur le lissage du fond est d'imposer qu'il soit lui-même le résultat d'une convolution par une fonction de largeur connue :

$$h_j(x) = R(x) * f_j(x)$$

La largeur de la fonction R, que l'on a choisie gaussienne, est constante pour toutes les longueurs d'onde, ce qui assure la même résolution pour le fond diffus sur tout le spectre. L'ajustement des paramètres se fait par la minimisation de la fonction S', où L_2 représente la corrélation sur les centres des sources décrite à l'Eq. 1.6.

$$S' = \sum_{j=1}^{M} \sum_{i=1}^{N} \frac{1}{\sigma_{i,j}^2} \left[s_j(x) * \left((R(x) * f_j(x)) + \sum_{k=1}^{K} a_{k,j} r(x - c_{k,j}) \right) - d_j(x) \right]_i^2 + L_2$$

Les paramètres à ajuster sont toujours les $a_{k,j}$ et $c_{k,j}$, et cette fois les différents $f_j(x)$. Une fonction $R(x)$ plus large que la résolution de départ (donc que t_j, par exemple) ne donnera pas lieu à proprement parler à une déconvolution du fond, mais permettra cependant de bien séparer les sources ponctuelles du fond diffus. Une fonction R plus étroite que la résolution fixée r ne garantira pas l'absence d'éléments "trop résolus" en vertu du théorème d'échantillonnage, puisqu'il n'y a plus d'autre contrainte sur le lissage des h_j (fonction L_1 de l'Eq. 1.7). Le choix de la largeur de R doit donc être testé et adapté, pour permettre la meilleure séparation possible des composantes tout en améliorant si possible la résolution des données.

Décalage fixe entre plusieurs sources

Bien que cette adaptation ne serve pas directement à l'analyse des galaxies hôtes de quasars, nous avons pris part à des collaborations qui justifiaient l'introduction et l'emploi de cette variante de l'algorithme de déconvolution de spectres.

Dans le cas typique des mirages gravitationnels, on observe plusieurs images du même objet (un quasar), superposées à la galaxie lentille (celle qui a permis la déflexion de la lumière provenant du quasar source). L'objectif de la déconvolution est souvent, dans ce cas, d'obtenir un spectre de la galaxie lentille avec un minimum de contamination par les différents spectres-images intenses du quasar. Dans des cas tels que ceux-là, nous disposons souvent d'une information complémentaire dont nous pouvons tirer parti dans la déconvolution : la distance entre les images du quasar est indépendante de la longueur d'onde. Cette information permet de diminuer le nombre de paramètres à ajuster : au lieu d'avoir $K \times M$ positions des sources à ajuster (avec K le nombre de sources ponctuelles et M le nombre de lignes du spectre), il n'y en aura plus que $M + K - 1$: On choisit une des sources comme référence pour les positions, et les autres positions s'obtiennent en ajoutant un décalage δ_k pour chacune des sources ponctuelles. Ce qui revient à ajuster les paramètres $a_{k,j}$, c_j, δ_k et $h_j(x)$ dans la minimisation du χ^2 :

$$\chi^2 = \sum_{j=1}^{M} \sum_{i=1}^{N} \frac{1}{\sigma_{i,j}^2} \left[s_j(x) * \left(h_j(x) + \sum_{k=1}^{K} a_{k,j} r\left(x - (c_j + \delta_k)\right) \right) - d_j(x) \right]_i^2$$

Le décalage δ_1 de la source de référence est bien sûr égal à zéro.
On peut combiner cette modification avec le contrôle du lissage du fond. Si, d'autre part, on dispose d'images très précises des mirages étudiés, les paramètres δ_k peuvent être fixés dès le départ. Pour des résultats faisant appel à cette variante de la méthode, voir par exemple Burud & al. (2002 [16]).

1.3.3 Courbes de rotation

L'analyse dynamique des galaxies consiste généralement en l'étude des courbes de rotation, qu'on peut extraire de leurs raies d'émission. En effet, indépendamment de son mouvement propre, la rotation de la galaxie entraîne un décalage en longueur d'onde de la raie (effet Doppler), la partie en approche relative étant décalée vers le bleu (*blueshift*) et la partie qui s'éloigne vers le rouge (*redshift*). Le décalage en longueur d'onde peut être relié à la vitesse radiale par la relation suivante :

$$v_{\mathrm{rad}} = c\,\frac{\Delta\lambda}{\lambda}$$

où c est la vitesse de la lumière, λ la longueur d'onde de la raie au centre de la galaxie et $\Delta\lambda$ le décalage en longueur d'onde de la raie par rapport à λ. Ces décalages ne sont pas constants le long de la galaxie. On peut donc en tirer une distribution de vitesse en fonction du rayon de la galaxie. Cette information est importante dans le sens où elle permet d'obtenir des contraintes sur la masse de la galaxie entière ou même de ses différents composants.

Dans le cas des galaxies hôtes de quasars, plusieurs étapes sont nécessaires à l'obtention d'une courbe de rotation analysable. Premièrement, l'extraction des raies de la galaxie qui, la plupart du temps, sont superposées aux raies beaucoup plus intenses du quasar. Ensuite, la détermination des vitesses de rotation à partir des raies extraites, et enfin leur interprétation par un modèle de répartition de masse. En effet, les objets étudiés étant lointains, le diamètre apparent de la galaxie est du même ordre de grandeur que la largeur de la fente employée pour obtenir le spectre. La galaxie est généralement inclinée par rapport à la ligne de visée, l'orientation de la fente ne correspond pas au grand axe de la galaxie et, enfin, la réponse instrumentale et les perturbations atmosphériques brouillent l'image obtenue. Nous avons mis au point un algorithme permettant d'obtenir une courbe de rotation en fonction du rayon, débarrassée de ces perturbations, que nous pouvons représenter par un modèle de répartition de masse typique de galaxie. Nous reprenons ici le détail de cette méthode, également synthétisée dans l'article repris au chapitre 2.

Extraction des raies

Comme expliqué dans la section précédente, la déconvolution de spectres se base sur les caractéristiques *spatiales* des spectres de sources ponctuelles pour pouvoir les séparer des fonds diffus tels que les galaxies. Pour atteindre cet objectif, un certain lissage spatial est appliqué à la partie diffuse. Ce traitement ne pose pas de problème pour l'analyse du spectre global de la galaxie, mais bien pour celle du décalage Doppler des raies d'émissions qui s'en trouvent souvent étalées spatialement, entraînant une perte d'information sur les vitesses de rotation qu'on peut en tirer. Afin d'éviter ce lissage spatial, nous nous basons ici sur les caractéristiques *spectrales* des raies d'émission des galaxies pour pouvoir les séparer du reste du spectre. De fait, les raies d'émissions de la galaxie sont toujours plus étroites que les raies du quasar. Nous décomposons donc chaque colonne du spectre en une somme de gaussiennes, correspondant aux différentes raies d'émission de la galaxie, plus un fond numérique lissé, qui englobe aussi bien le spectre du quasar que le continu de la galaxie.

Cette décomposition peut se résumer par l'ensemble des fonctions $Y_x(j)$, modélisation de la colonne x du spectre (spectre de la partie de la galaxie occupant la position x le long de la fente) qui couvre les différentes longueurs d'ondes j.

$$Y_x(j) = f_x(j) + \sum_{l}^{L} a_l r_l(j, c_x, \Delta_l, b_l) \tag{1.10}$$

f_x représente la composante lisse du spectre, et la somme porte sur les différentes raies présentes dans la galaxie.
Les raies d'émission de la galaxie sont modélisées dans la direction spectrale par des gaussiennes r_l (voir Eq. 1.11). Chaque raie l de la colonne x est caractérisée par une largeur b_l et un centre $c_x + \Delta_l$. On peut en effet bénéficier du fait que l'on connaît les décalages en longueur d'onde entre les différentes raies d'émission en fixant les écarts entre les raies par la constante Δ_l : Elle correspond au décalage en longueur d'onde "redshifté" de la raie l par rapport à une des raies qu'on choisit comme référence (et donc pour laquelle $\Delta_l = 0$). a_l est l'intensité de la raie l.

$$r_l(j, c_x, \Delta_l, b_l) = e^{-b_l(j-(c_x+\Delta_l))^2} \tag{1.11}$$

Les paramètres à ajuster sont donc, pour chaque raie et chaque colonne où cette raie est présente a_l et b_l, et pour chacune des colonnes où il existe au moins une raie un paramètre c_x.
Le caractère lissé dans la direction spectrale de la composante f_x est assuré par la minimisation de la fonction H. On minimise l'écart entre le fond et ce même fond convolué dans la direction spectrale par une gaussienne R de largeur fixée, c'est à dire débarrassé des détails de résolution plus fine que R.

$$H = \sum_{x}^{N} \sum_{j}^{M} \Big(f_x(j) - \big(R(j) * f_x(j)\big)_x \Big)^2$$

La décomposition du spectre se fait donc par la minimisation de la fonction S décrite ci-dessous, chaque colonne (position spatiale x) étant traitée séparément des autres.

$$S = \sum_{x}^{N} \sum_{j}^{M} \frac{1}{\sigma_{xj}^2} \big(Y_x(j) - g(x,j)\big)^2 + \lambda H$$

Les $g(x, j)$ représentent les données initiales et σ_{xj}^2 la variance pour le point d'observation (x, j). Le multiplicateur de Lagrange λ permet de donner plus ou moins de poids au lissage du fond dans la minimisation et d'assurer une convergence statistiquement correcte.

Pour limiter les perturbations dues aux raies intenses du quasar, nous normalisons le spectre initial, ligne par ligne, à une intensité de 1 (ce qui n'affecte pas ou peu les positions et intensités relatives le long d'une raie d'émission, puisque les raies du quasar sont beaucoup plus larges que celles de la galaxie). Cela permet d'améliorer la séparation entre les différentes composantes du spectre. Le spectre du quasar s'en trouve lissé, et donc plus facile à modéliser par la fonction f.

Un exemple d'une telle décomposition est donné dans la Fig. 2.4, pour les raies H_α et $[\mathrm{N}_{\mathrm{II}}]$ de HE1503+0228, objet étudié en détail dans l'article du chapitre 2 (Courbin et al. 2002 [24]).

Modélisation et ajustement de la courbe de rotation

Revenons dans le détail aux effets perturbateurs à corriger pour obtenir une courbe de rotation dépendant uniquement du rayon de la galaxie.

- La largeur de la fente employée pour obtenir le spectre est comparable à la dimension angulaire de la galaxie. Les observations le long de la fente ne représentent donc pas les décalages en longueur d'onde d'un point précis de la galaxie, mais plutôt une moyenne sur toute une partie de la galaxie.
- Les différentes parties de la galaxie contribuant à cette moyenne n'ont pas le même poids, car l'intensité des raies n'est pas constante le long du rayon de la galaxie. Il faudra donc pondérer la moyenne de manière adaptée.
- La galaxie n'est en général pas vue de face ni de côté, son plan est incliné d'un angle i par rapport à la ligne de visée. Les vitesses observées doivent être corrigées d'un facteur $\sin i$ afin de représenter les vitesses de rotation réelles.
- La fente du spectrographe n'est en général pas alignée avec le grand axe de la galaxie, puisque nous n'avions pas de connaissance a priori sur celle-ci au moment de l'observation. Les variations de vitesse ou d'intensité, observées le long de la fente, ne peuvent donc être directement assimilées à des variation le long du rayon de la galaxie.
- Chaque point de l'observation ne correspond pas à un seul point de la galaxie, mais est contaminé par les zones voisines dans la galaxie. En effet les contributions lumineuses des différentes parties de la galaxie sont brouillées et étalées par l'atmosphère et la réponse instrumentale, aussi bien dans la direction spectrale que spatiale (effet de seeing).

La méthode que nous avons développée prend en compte ces différents facteurs.

Modèle de galaxie : Nous avons adopté un modèle simple pour la répartition de masse dans la galaxie hôte, comprenant un disque fin, un halo sphérique de matière sombre et une masse centrale. La vitesse à une distance r du centre de la galaxie est modélisée par :

$$V_{\mathrm{mod}}(r) = \sqrt{-(F_{\mathrm{disk}} + F_{\mathrm{dark}} + F_{\mathrm{cm}})}$$

Les forces radiales sont dérivées de différents potentiels proposés dans Binney & Tremaine (1987 [7]).

1. Pour le disque : potentiel de Kuzmin

$$F_{\mathrm{disk}}(r, z) = -\frac{r^2 G M_{\mathrm{disk}}}{(r^2 + (a + |z|)^2)^{\frac{3}{2}}} \tag{1.12}$$

   où on prend $z = 0$, négligeant l'épaisseur du disque. M_{disk} est la masse totale du disque et a lui donne une échelle de longueur.

2. La matière sombre est supposée à symétrie sphérique par rapport au centre de la galaxie. Avec une densité de matière

$$\rho(r) = \frac{\rho_0}{1 + (\frac{r}{r_0})^2}$$

   on obtient une force radiale donnée par

$$F_{\mathrm{dark}}(r) = -\frac{4\pi G \rho_0 r_0^3}{r}(\frac{r}{r_0} - \arctan\frac{r}{r_0})$$

   où r_0 donne un rayon caractéristique à la distribution de masse dans le halo et ρ_0 sa densité centrale.

3. La force radiale exercée par la masse centrale est simplement

$$F_{\mathrm{cm}}(r) = -\frac{G M_{\mathrm{cm}}}{r}$$

Nous obtenons donc un modèle analytique de la vitesse de rotation de la galaxie en fonction du rayon, basé sur cinq paramètres à ajuster : M_{cm}, ρ_0, r_0, M_{disk} et a. C'est un modèle relativement simplifié par rapport à la réalité, mais la résolution des observations ne permet de toutes façons pas d'observer des détails plus fins. Nous avons testé l'ajout d'un bulbe à la modélisation de la répartition de masse, mais cela n'améliore pas les ajustements effectués (le bulbe s'étend uniquement sur quelques pixels centraux). Pour les mêmes raisons, la masse centrale est également assez mal contrainte. En guise d'illustration, un exemple des contributions des différentes composantes de masse à une courbe de rotation typique est montrée Fig. 1.11.

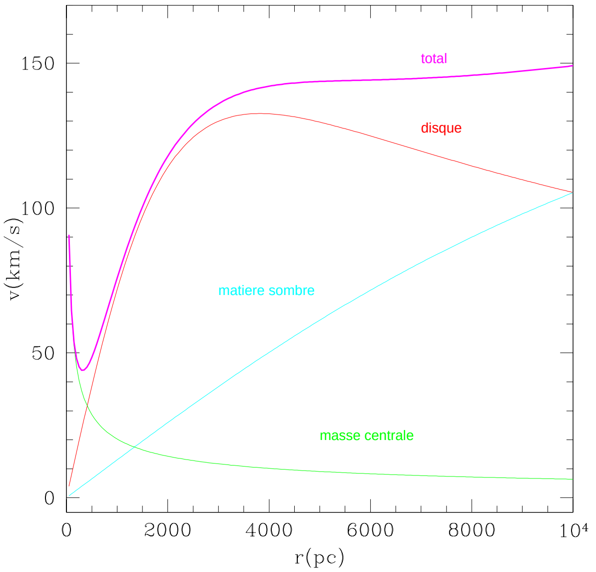

FIG. 1.11 – Illustration des contributions à la vitesse radiale des différentes composantes du modèle de répartition de masse employé. De bas en haut, on rencontre successivement la courbe de vitesse créée par la masse centrale, le halo de matière sombre, le disque et enfin la courbe de vitesse résultante. Les valeurs des paramètres utilisés dans cet exemple sont : $a = 2700$ pc, $M_{\rm disk} = 3\ 10^{10}$ $\mathrm{M}_\odot$, $\rho_0 = 0.01$ $\mathrm{M}_\odot/\mathrm{pc}^3$, $r_0 = 10^4$ pc et $M_{\rm cm} = 10^8$ $\mathrm{M}_\odot$.

Correction de la courbe de rotation : Le principe de la méthode est d'appliquer les différentes perturbations effectives au modèle analytique et de minimiser l'écart entre ce modèle corrigé et nos données (les raies extraites), et cela en adaptant les 5 paramètres du modèle $V_{\rm mod}$.

La fonction à minimiser est le χ^2 suivant :

$$\chi^2 = \sum_{j=1}^{N} \frac{1}{\sigma_j^2} \left[(s * V_{\rm moy})_j \ \sin i - d_j \right]^2$$

- N est le nombre de pixels j le long de la fente pour lesquels on a extrait une vitesse observée d_j par la méthode décrite à la section précédente.
- Les erreurs de mesure σ_j sont estimées via la comparaison des mesures d_j dans les raies d'émission se retrouvant sur plusieurs spectres, quand cela est possible.
- $V_{\rm moy}(j)$ représente la moyenne du modèle de vitesse au point j le long de la fente (voir plus loin pour la définition de la zone sur laquelle la moyenne porte).
- s est la PSF à une dimension obtenue via les spectres d'étoiles, c'est en fait une moyenne des PSFs à une dimension employées pour la déconvolution des spectres dans cet intervalle de longueurs d'onde. Convoluer $V_{\rm moy}$ par s permet de tenir compte du brouillage du signal dans la direction spatiale.

Enfin, puisque la normale au plan de la galaxie est incliné d'un angle i par rapport à la ligne de visée, multiplier le modèle convolué par $\sin i$ permet de ne garder que la composante de la vitesse dans la direction de la ligne de visée, c'est à dire celle qui amène un effet Doppler et donc un décalage spectral observable.

La Fig. 2.5 à gauche illustre les effets dont il faut tenir compte dans la correction des courbes de rotation. La galaxie est supposée plane et circulaire (pointillés). Vue avec une inclinaison i, nous l'observons elliptique (traits interrompus). L'orientation de la fente ne correspond en général pas avec le grand axe de la galaxie, et la fente couvre une partie non négligeable de la galaxie, d'où la nécessité de moyenner le modèle sur une partie de la galaxie..

Domaine d'intégration pour la moyenne : La largeur de la fente relativement à la galaxie (voir Fig. 2.5) impose de moyenner le modèle de vitesse sur une portion non négligeable de galaxie. Une moyenne est indispensable puisque le décalage effectivement mesuré de la raie reflète la superposition des raies décalées provenant des différents endroits de la galaxie au travers de la fente (les blueshifts compensant en partie les redshifts, et donc aplatissant la courbe de rotation réelle).

La droite sur laquelle la moyenne doit se faire correspondrait, dans le cas le plus simple, (galaxie vue de face et donc fente forcément orientée selon le grand axe) à la largeur de la fente (voir Fig.2.5, à droite, ligne barre-pointée). Les galaxies dont on observe une courbe de rotation ont forcément une inclinaison non nulle. Comme le modèle de vitesse est exprimé en fonction du rayon réel de la galaxie (c'est-à-dire dans le plan de la galaxie) et pas du rayon projeté sur le plan du ciel, nous devons faire correspondre à la largeur de la fente une droite d'intégration dans le plan de la galaxie, donc allongée et inclinée (ligne pointillée de la Fig. 2.5, à droite). Ainsi la moyenne se fait sur les parties de la galaxie qui contribuent réellement au flux en P, les limites physiques de l'intégrale étant les bords f_e et f_i de la fente, elle aussi considérée dans le plan de la galaxie.

L'équation de la droite le long de laquelle on effectue l'intégrale pour un point P de la fente s'obtient par considérations géométriques. L'angle ϕ représente l'orientation de la fente par rapport au grand axe de la galaxie (axe x sur la Fig. 1.12) et i l'inclinaison. Les coordonnées de deux points de cette droite suffisent à déterminer son équation : a, l'intersection de la droite d'intégration et de l'axe x, et b la position de P dans le plan de la galaxie, qu'on observerait de face (voir Fig. 1.12).
Dans le référentiel constitué des grand et petit axes de la galaxie (x et y sur le schéma), et en nommant x_P la distance de P à l'origine du référentiel, les coordonnées du point a sont $(\frac{x_P}{\cos\phi}, 0)$ et celles de $b = (x_P \cos\phi, -\frac{x_P \sin\phi}{\cos i})$, la coordonnée en y du point P subissant une dilatation de $1/\cos i$ du fait de l'inclinaison de la galaxie. Ce qui nous donne l'Eq. 1.13 pour la droite d'intégration.

$$y = \frac{\cot\phi}{\cos i}\,(x - \frac{x_{\mathrm{P}}}{\cos\phi}) \tag{1.13}$$

Les intersections de cette droite avec les bords D_1 et D_2 de la fente de largeur f, eux-mêmes inclinés, nous donnent les bornes $X_{\mathrm{f_i}}$ et $X_{\mathrm{f_e}}$ de l'intégrale (Eqs. 1.14).

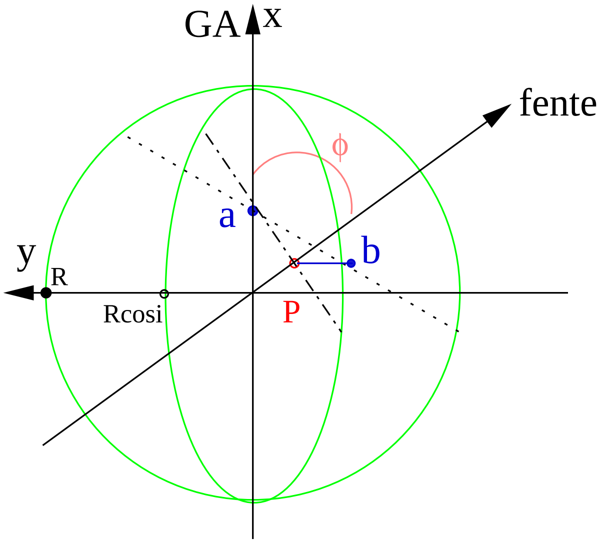

FIG. 1.12 – Illustration du calcul de l'équation de la droite d'intégration via les points a et b (voir texte). La moyenne des vitesses au point P se fait le long de la ligne pointillée, qui correspond à la perpendiculaire à l'axe de la fente (ligne barre-pointée), mais dans le plan de la galaxie.

$$\begin{aligned} D_1 &\equiv y = -\tfrac{\tan\phi}{\cos i}\left(x - \tfrac{f}{2\sin\phi}\right) &\Longrightarrow X_{\mathrm{f_i}} = x_P\cos\phi + \frac{f}{2}\sin\phi \\ D_2 &\equiv y = -\tfrac{\tan\phi}{\cos i}\left(x + \tfrac{f}{2\sin\phi}\right) &\Longrightarrow X_{\mathrm{f_e}} = x_P\cos\phi - \frac{f}{2}\sin\phi \end{aligned} \tag{1.14}$$

Calcul de la moyenne L'expression analytique de la moyenne des vitesses pour un point P le long de la fente est reprise dans l'Eq. 1.15.

$$V_{\mathrm{moy}}(P) = \frac{1}{I_{\mathrm{tot}}}\int_{X_{\mathrm{f_i}}}^{X_{\mathrm{f_e}}} I_{\mathrm{mod}}[r(x)]\cdot V_{\mathrm{mod}}[r(x)]\cdot\frac{x}{r(x)}\cdot dx \tag{1.15}$$

L'intégrale se calcule sur les abscisses x, le long du grand axe. Les bornes de l'intégrale sont illustrées à la Fig. 1.13. Comme le modèle de vitesse est dépendant du rayon et pas de x, il nous faut une relation entre r et x, qui nous est donnée par la relation $x^2+y^2=r^2$ appliquée à l'Eq. 1.13. La distance r d'un point de la droite d'intégration au centre de la galaxie en fonction de l'abscisse x du point considéré est donc :

$$r(x) = \sqrt{x^2 + \frac{\cot^2\phi}{\cos^2 i}\left(x - \frac{x_P}{\cos\phi}\right)^2}$$

La seule composante intéressante de la vitesse donnée par le modèle est celle qui donnera lieu à une vitesse radiale, c'est-à-dire la composante dans la direction de la ligne de visée.

La vitesse de rotation en un point, selon le modèle, est perpendiculaire au vecteur qui relie le centre de la galaxie à ce point. Comme le montre la Fig. 1.13, il ne faut garder que la composante dans la direction du petit axe, puisque l'inclinaison de la galaxie se fait par une rotation de i autour du grand axe. La composante de la vitesse de rotation à garder est donc :

$$V = V_{\mathrm{mod}} \cdot \cos\alpha = V_{\mathrm{mod}} \cdot \frac{x}{r(x)}$$

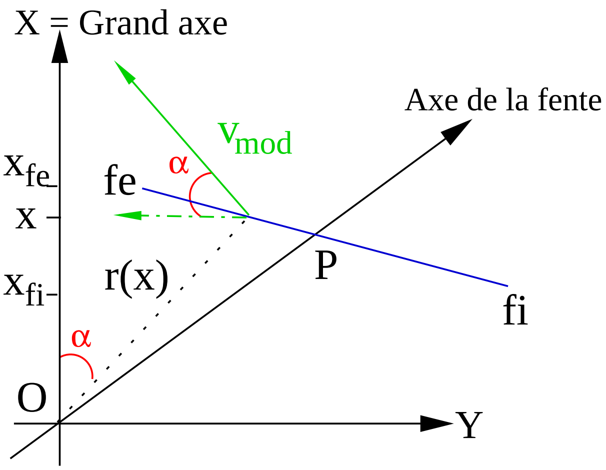

FIG. 1.13 – Seule la composante de V_{mod} dans la direction du petit axe donnera lieu à un décalage observable de longueur d'onde pour une galaxie inclinée.

Enfin, nous avons pris comme hypothèse que l'intensité des raies dépend uniquement de la distance r au centre de la galaxie. Il est possible, comme expliqué dans la section suivante, de construire un profil d'intensité en fonction du rayon de la galaxie, en se basant sur les intensités des raies extraites le long de la fente. Nous donnons ainsi un poids $I_{\mathrm{mod}}[r(x)]$ à chaque élément de vitesse $V_{\mathrm{mod}}[r(x)]$ apparaissant dans l'intégrale, poids proportionnel à l'intensité lumineuse émise à une distance $r(x)$ du centre de la galaxie. Le terme I_{tot} assure la normalisation de la pondération et représente le flux total des zones intervenant dans l'intégrale.

Modélisation et ajustement de l'intensité de la raie dans la galaxie Le calcul de la vitesse moyenne de la section précédente se fait via la pondération de la vitesse en chaque point $r(x)$ de la ligne d'intégration par l'intensité de la galaxie à une distance $r(x)$ de son centre. Il faut donc disposer d'un modèle de distribution d'intensité $I_{\mathrm{mod}}(r)$, qu'on suppose également à symétrie circulaire dans le plan de la galaxie. Cette hypothèse peut être remise en cause dans le cas de galaxies en interaction, ce qui implique généralement une asymétrie dans les raies d'émission. Mais, dans ce cas, les courbes de vitesses radiales ne peuvent de toute façon être interprétées fiablement comme étant uniquement dépendantes de l'attraction gravitationnelle de la matière galactique.

Les seules données dont on peut disposer sur l'intensité des raies sont celles qu'on extrait des spectres initiaux réduits (paramètres a_l de l'Eq. 1.10). Ce sont donc des intensités mesurées le long de la fente du spectrographe. De manière analogue au traitement des vitesses, on adapte les paramètres d'un modèle de distribution d'intensité en fonction du rayon (gaussienne, Moffat,...), pour que cette distribution théorique, une fois corrigée des effets de projection, orientation, seeing,... colle au mieux aux intensités observées.

Les corrections à apporter sont moins nombreuses que celles traitées dans le cas des vitesses : Les intensités sont scalaires et non vectorielles, il n'y a donc pas de composante selon la ligne de visée à prendre en compte. On couvre le même domaine d'intégration, il n'y a pas de pondération supplémentaire à considérer.

Dans l'hypothèse de symétrie circulaire dans le plan de la galaxie, plusieurs distributions théoriques de lumière le long des raies peuvent être envisagées :

- Moffat : $I_{\text{mod}}(r) = I_0\,(1 + b_0 r^2)^{-\beta}$
- Gaussienne : $I_{\text{mod}}(r) = I_0\, e^{-b_0 r^2}$
- Exponentielle décroissante : $I_{\text{mod}}(r) = I_0\, e^{-\frac{r}{r_0}}$
- ...

L'ajustement des paramètres du modèle d'intensité choisi se fait par la minimisation du χ^2 suivant :

$$\chi^2 = \sum_{j=1}^{N} \frac{1}{\sigma_j^2} \Big[(s * I_{\text{sum}})_j \, \sin i - a_j \Big]^2$$

Les a_j sont les intensités d'une des raies extraites. Les autres paramètres sont les mêmes que pour le modèle de vitesse. On tient compte ici de l'inclinaison de la galaxie et de l'effet de seeing dans la direction spatiale (longueur de la fente).

Les contributions provenant des différentes zones de la galaxie ne sont pas à moyenner mais cette fois à sommer, puisqu'il s'agit d'intensités qui se renforcent et plus de décalages qui se compensent partiellement. Cette somme est donnée par l'intégrale suivante, qui couvre le même domaine que la moyenne des vitesses :

$$I_{\text{sum}} = \int_{X_{f_i}}^{X_{f_e}} s_2 * I_{\text{mod}}\big[r(x)\big] \; dx$$

On tient ici également compte du brouillage dans la direction de la largeur de la fente : la fonction s_2 est la PSF dans la direction de la ligne d'intégration, soit selon la largeur de fente vue dans le plan de la galaxie. En effet, puisqu'on applique la convolution par s_2 au modèle I_{mod} exprimé en fonction du rayon, il faut que la PSF appartienne au même plan (celui de la galaxie). Elle est ainsi construite sur base de s, la PSF dans la direction spatiale des observations, c'est-à-dire selon la longueur de la fente. On suppose que le seeing est le même dans les deux directions (le long de la fente et perpendiculairement à la fente) et que ces composantes sont séparables, pour pouvoir simplement "dilater" s en s_2.

Si on considère s_2 de forme gaussienne, nous avons besoin pour la caractériser de sa largeur à mi-hauteur. La construction de la PSF s_2 se fait par calcul du rapport entre les longueurs de fente avant et après inclinaison de la galaxie. La largeur de la PSF est proportionnelle à la longueur de la fente, et la fente apparaîtrait plus longue si la galaxie était vue de face, comme le montre la Fig. 1.14.

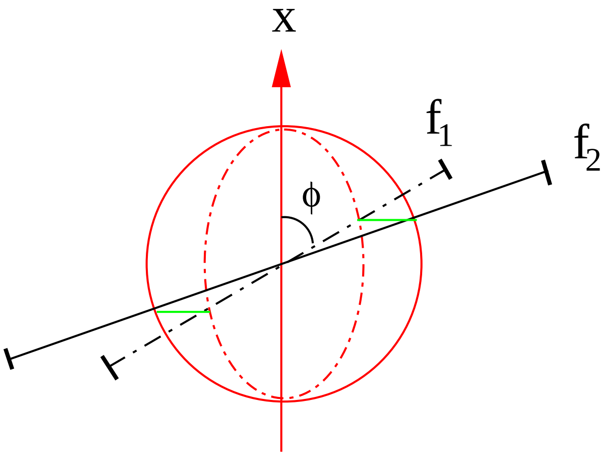

FIG. 1.14 – La longueur de la fente réelle (f_1, trait discontinu) est allongée quand on la considère sur une galaxie non inclinée (f_2, trait plein).

Quel que soit le point (x, y) du plan incliné d'un angle i, il correspond à un point de coordonnées $(x, \frac{y}{\cos i})$ sur la galaxie vue de face. On peut appliquer cette transformation aux coordonnées de l'extrémité de la fente de longueur f :

$$(f\cos\phi, f\sin\phi) \longrightarrow (f\cos\phi, f\frac{\sin\phi}{\cos i})$$

Ce qui nous permet de calculer le rapport R entre les longueurs de fente sans et avec inclinaison (f_2/f_1) :

$$\begin{aligned} \mathrm{R} = \frac{f_2}{f_1} &= \frac{\sqrt{f^2\cos^2\phi + \frac{f^2\sin^2\phi}{\cos^2 i}}}{f} \\ &= \cos\phi\sqrt{1 + \frac{\tan^2\phi}{\cos^2 i}} \end{aligned}$$

Ce résultat nous permet d'obtenir ω_2, la largeur à mi-hauteur de la PSF s_2, par rapport à ω, largeur à mi-hauteur de la PSF s, qui peut être mesurée.

$$\omega_2 = \mathrm{R}\ \omega = \omega\cos\phi\sqrt{1 + \frac{\tan^2\phi}{\cos^2 i}}$$

L'échantillonnage de la PSF s_2 est bien sûr à adapter en fonction du pas employé sur la droite d'intégration.

Tous les éléments de la modélisation du profil d'intensité sont ainsi connus et permettent l'élaboration du profil $I_{\mathrm{mod}}(r)$.

Ajustement de la forme de la galaxie

La correction des courbes de rotation est fortement dépendante des angles i et ϕ, respectivement inclinaison de la galaxie et orientation de la fente par rapport à son grand axe. L'algorithme de déconvolution d'image avec modèle analytique nous permet d'estimer ces paramètres d'orientation. Il va de soi que ce travail n'a de sens que si la galaxie est spirale, donc suit un profil exponentiel, dont les paramètres sont ajustés par la déconvolution. Dans le repère d'observation de la galaxie (x' et y') (Fig. 1.15), on a donc

$$G'(x', y') = I_0 \, e^{-(Ax'^2+By'^2+Cx'y')^{1/2}}$$

Exprimée maintenant dans des axes qui suivent la symétrie elliptique du disque incliné, l'équation devient

$$G(x, y) = I_0 \, e^{-(\frac{x^2}{a^2}+\frac{y^2}{b^2})^{1/2}}$$

La matrice de changement de repère nous permet facilement de relier les coefficients A, B et C aux paramètres qui nous intéressent, à savoir a, b et θ.

$$\begin{aligned} a^2 &= \frac{2\cos 2\theta}{(A+B)\cos 2\theta + A - B} \\ b^2 &= \frac{2\cos 2\theta}{(A+B)\cos 2\theta + B - A} \\ \theta &= \frac{1}{2}\arctan\frac{C}{B-A} \end{aligned}$$

Le rapport entre petit et grand axe nous donne l'ellipticité, de laquelle on peut déduire l'inclinaison i de la galaxie : $\frac{b}{a} = \cos i$. L'angle θ, l'orientation de l'ellipse par rapport à l'orientation de l'image observée, permet de déduire directement l'orientation relative entre la fente du spectrographe et le grand axe de la galaxie ϕ.

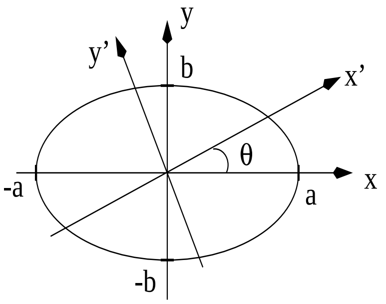

FIG. 1.15 – Les axes de l'ellipse, x et y, ne correspondent pas aux axes réels x' et y' de l'image observée. Il nous faut donc déterminer à la fois a et b pour en tirer l'inclinaison de la galaxie, et θ pour l'orientation de la fente.

Nous reprenons dans cet ouvrage, par ordre chronologique, les différents articles publiés (ou à soumettre prochainement) au cours du travail de recherche de la thèse, avec leur texte original en anglais. Pour chacun, une mise en contexte (en français), quelques compléments éventuels, ainsi qu'un résumé des principaux résultats sont repris en tête de chapitre.

Chapitre 2

HE1503+0228, comme exemple test de la méthode

L'étude de l'échantillon de 20 quasars et de leurs galaxies hôtes a démarré avec un objet "simple" : HE 1503+0228. Il a été choisi pour ses belles émissions dans la galaxie, et dans les raies et dans le continu, déjà visibles avant la déconvolution (c'est en effet un quasar à la limite de séparation quasar/Seyfert, donc avec un noyau pas trop brillant, facile à séparer de la source diffuse que constitue la galaxie.

L'occasion, donc, de se familiariser avec les nouvelles techniques de réduction et de déconvolution, puis d'exploiter au maximum les potentialités de l'analyse spectrale. Outre la déconvolution proprement dite et une première approche de l'analyse de populations stellaires, l'étude de HE 1503+0228 a été l'occasion de mettre au point une technique de modélisation de la répartition de la masse dans la galaxie sur base des courbes de vitesses radiales extraites des spectres à deux dimensions. Cette méthode, détaillée dans l'introduction et synthétisée dans l'article consacré au quasar, tient compte aussi bien des effets géométriques de projection, que du seeing, de la taille de la fente et de la variation d'intensité de la raie le long de la fente du spectrographe.

Tous les résultats de l'analyse de l'hôte de HE 1503+0228 ont pointé vers une galaxie spirale typique, comparable à une spirale sans noyau actif :

- la courbe de vitesse radiale est parfaitement représentée par un modèle de galaxie spirale (disque + halo de matière sombre + masse centrale)
- l'analyse du contenu gazeux de la galaxie nous montre que l'excitation du gaz est principalement assuré par les étoiles
- les différents indicateurs de population stellaires, via les raies d'absorption dans la galaxie, reflètent également des étoiles typiques de galaxie spirale.

L'article qui suit présente le détail de ces analyses.

On-axis spatially resolved spectroscopy of low redshift quasar host galaxies: HE 1503+0228, at $z = 0.135$

F. Courbin [1,2], G. Letawe [1], P. Magain [1], L. Wisotzki [3],
P. Jablonka [4], K. Jahnke [5], B. Kuhlbrodt [5], D. Alloin [6],
G. Meylan [7], D. Minniti [2], I. Burud [7]

1. Institut d'Astrophysique et de Géophysique, Université de Liège, Allée du 6 Août, 17, Sart Tilman (Bat. B5C), Liège 1, Belgium
2. Universidad Católica de Chile, Departamento de Astronomia y Astrofisica, Casilla 306, Santiago 22, Chile
3. Institut für Physik, Universität Potsdam, Am Neuen Palais 10, 14469 Potsdam, Germany
4. GEPI, Observatoire de Paris, Place Jules Janssen, F-92915 Meudon Cedex, France
5. Hamburger Sternwarte, Universität Hamburg, Gojenbergsweg 112, D-21029 Hamburg, Germany
6. European Southern Observatory, Casilla 19, Santiago, Chile
7. Space Telescope Science institute, 3700 San Martin Drive, Baltimore, MD 21218 USA

Published in Astronomy and Astrophysics, 2002, v.394, pp 863-872.

Abstract : We present the first result of a comprehensive spectroscopic study of quasar host galaxies. On-axis, spatially resolved spectra of low redshift quasars have been obtained with FORS1, mounted on the 8.2m ESO Very Large Telescope, Antu. The spectra are *spatially deconvolved* using a spectroscopic version of the "MCS deconvolution algorithm". The algorithm decomposes two dimensional spectra into the individual spectra of the central point-like nucleus and of its host galaxy. Applied to HE 1503+0228 at $z = 0.135$ (M_B=−23.0), it provides us with the spectrum of the host galaxy between 3600Å and 8500Å (rest-frame), at a mean resolving power of 700. The data allow us to measure several of the important Lick indices. The stellar populations and gas ionization state of the host galaxy of HE 1503+0228 are very similar to the ones measured for normal non-AGN galaxies. Dynamical information is also available for the gas and stellar components of the galaxy. Using deconvolution and a deprojection algorithm, velocity curves are derived for emission lines, from the center up to 4" away from the nucleus of the galaxy. Fitting a simple three-components mass model (point mass, spherical halo of dark matter, disk) to the position-velocity diagram, we infer a mass of M(r<1kpc) = $(2.0 \pm 0.3)10^{10}$ $M_{\odot}$ within the central kiloparsec of the galaxy, and a mass integrated over 10 kpc of M(r<10kpc) = $(1.9 \pm 0.3)10^{11}$ $M_{\odot}$, with an additional 10% error due to the uncertainty on the inclination of the galaxy. This, in combination with the analysis of the stellar populations indicates that the host galaxy of HE 1503+0228 is a normal spiral galaxy.

Keywords Galaxies: dynamics, stellar populations – quasars: individual: HE 1503+0228 – techniques: deconvolution

Based on observations made with ANTU/UT1 at ESO-Paranal observatory in Chile (program 65.P-0361(A)), and with the ESO 3.5m NTT, at La Silla observatory (program 62.P-0643(B)).

2.1 Introduction

Luminous quasars are now known to be generally located at the cores of large galaxies. With the recent discovery that supermassive black holes appear to reside in most if not all galaxies with substantial bulges (e.g., Magorrian et al. 1998 [77]), it is now quite likely that quasar-like activity is an extremely common but transient phenomenon, linking the growth of now extinct black holes to the violent processes during phases of active accretion (cf. McLeod et al. 1999 [85]). However, very little of the physical processes operating during such episodes of nuclear activity is actually understood: neither do we know the actual conditions for fueling (or refueling) massive black holes, nor the time-scales involved. A particularly interesting problem is the importance of the feedback from a high-luminosity Active Galactic Nucleus (AGN) onto its host galaxy, in the form of huge quantities of ionizing radiation as well as possible mechanical outflows (jets).

Quasar host galaxies have been studied almost exclusively by imaging (e.g., Bahcall et al. 1997 [2], Stockton et al. 1998 [108], Márquez et al. 2001 [82]). Recent Hubble Space Telescope optical studies have established that high-luminosity quasars generally reside in big ellipticals, irrespective of radio properties (McLeod & Rieke 1995 [84], Disney et al. 1995 [29], Hughes et al. 2000 [45]). There also seems to be a trend that more luminous QSOs are hosted by more massive galaxies (McLure et al. 1999 [87], McLeod & Rieke 1995 [84]).

A more detailed understanding of the physical conditions in host galaxies can only be obtained from spectroscopic observations. Available evidence in this field is extremely scarce, and although extensive quasar host spectroscopy was conducted already in the early 1980s (e.g., Boroson et al. 1985, [10]), they have never really been followed up with improved instrumentation and analysis techniques, except for a few isolated objects (among them 3C 48 being the probably best-studied case in this field – e.g., Chatzichristou et al. 1999 [21], Canalizo & Stockton 2000 [17]). Particularly important is the fact that nearly all these observations up to now were designed as "off-nuclear" spectroscopy, avoiding the

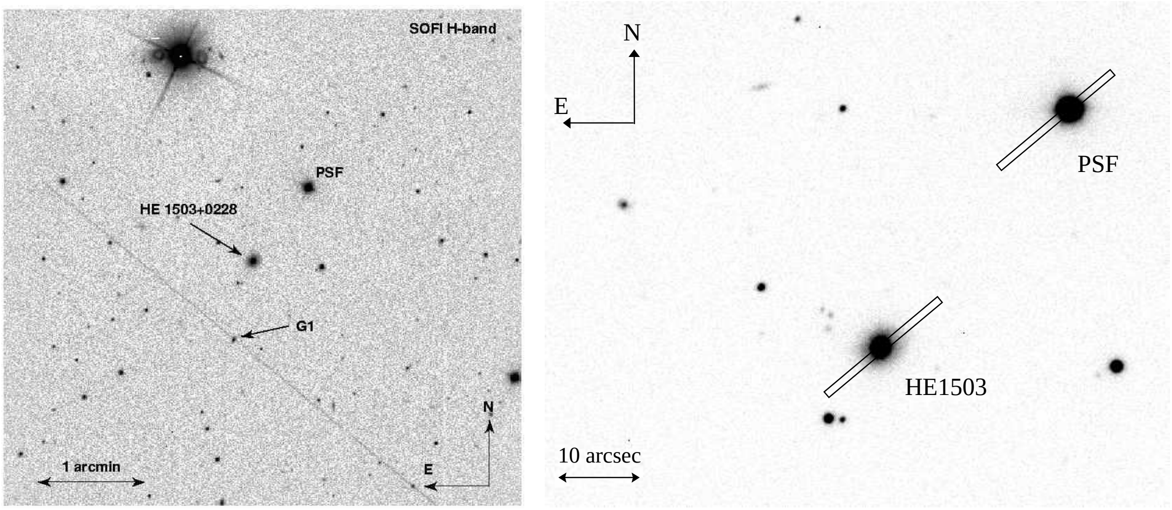

Figure 2.1: *Left:* field of view of 5' × 5 ' around HE 1503+0228. The exposure (H-band) is 480 sec long. It has been obtained with SOFI on the ESO 3.5m NTT. The seeing is 0.8" sampled with a 0.29" pixel. *Right:* part of the VLT/FORS1 pointing image. The seeing is 0.62" on this 30sec R-band exposure. The 1" slits used to obtain the spectra of the target and of the PSF star are indicated.

strong contamination from the AGN itself, but yielding only information on the host for distances of $> 5 - 10\,\mathrm{kpc}$ from the nucleus.

With the aim of studying the stellar and gas content of quasar host galaxies, as well as their dynamics, we have initiated a spectroscopic campaign with the ESO-VLT to observe a sample of luminous radio-quiet quasars at low redshift. The sample is based on the Hamburg/ESO Survey (HES; Wisotzki et al. 2000 [119]), a wide-angle ($\sim 7500\,\mathrm{deg}^2$) search for optically bright ($B < 17.5$) quasars in the southern sky. This survey is particularly suited to provide samples for host galaxy studies, mainly because of two reasons: (1) because of its bright limiting magnitude, the survey yields low-redshift quasars in large numbers, (2) the selection does not encompass morphological criteria, i.e., there is no limitation to point sources as in most other optical quasar surveys. This fact and the wide range of selection criteria employed in the HES (cf. Wisotzki et al. 2000 [119]) ensure that quasars are selected irrespective of morphological properties of their host galaxies (see also Köhler et al. 1997 [64]). Our objects all have $M_B < -23$ and $z < 0.33$.

The present paper is aimed at exposing the techniques used to obtain high quality spectra of quasar hosts, decontaminated from the contamination by the quasar, and to show their application to one object, taken as a test case: HE 1503+0228, at $z = 0.135$.

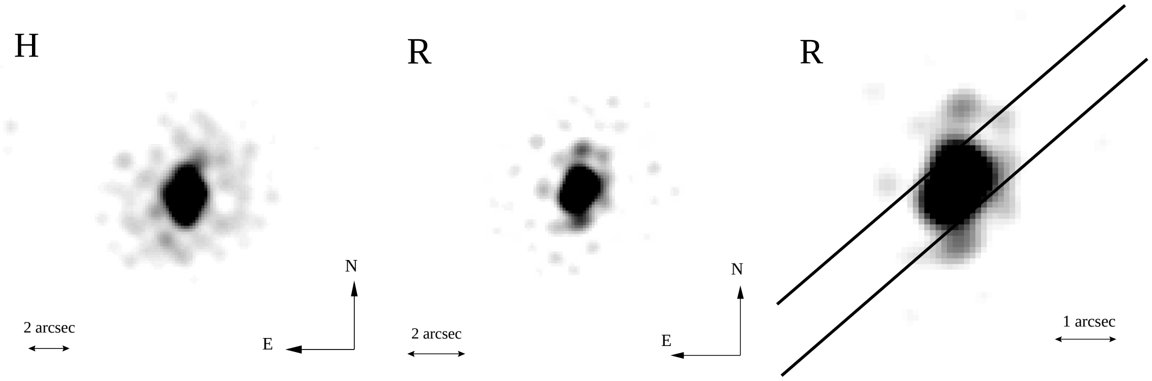

Figure 2.2: *Left and middle:* deconvolved NTT and VLT images, where the quasar has been removed from the data. *Right:* zoom on the host galaxy and position of the slitlet used to obtain the spectroscopic data.

2.2 Observations – data reduction

2.2.1 Imaging

We have obtained H-band images of HE 1503+0228, at La Silla observatory (ESO, Chile) on the night of 1999 February 24^{th}. SOFI was used, the near-IR imager of the 3.5m ESO New Technology Telescope (NTT). The pixel size was 0.29" and numerous dithered images of the field were taken in order to produce a combined sky subtracted frame with a total exposure time of 480 sec and a final mean seeing of 0.8". The image is displayed on the left panel of Fig. 2.1. It shows the environment of the quasar on a 5' × 5' field, with no obvious companion.

Additional data were obtained with the first of the four 8.2m telescopes (UT1) at Paranal observatory. A shallow 30s R-band image was taken, in order to design the spectroscopic mask. The seeing was 0.62", sampled with a pixel scale of 0.2".

Both the near-IR and optical images were deconvolved using the MCS deconvolution algorithm (Magain et al. 1998 [75]). While one single optical image of HE 1503+0228 was obtained, many dithered IR images were available in the H-band. Eight stacks of images were produced with the data and simultaneously deconvolved as explained in Courbin et al. (1998). This procedure allows for better decomposition of the data into a sum of point source and "background" channels, hence a better extraction of the image of the host, uncontaminated by the AGN's light. The deconvolved data are shown in Fig. 2.2, where the quasar has been subtracted.

The photometry of the host of HE 1503+0228 has been performed on the deconvolved images, in a 10" diameter aperture. The magnitudes we infer in that way are $R = 16.78 \pm 0.20$ and $H = 14.57 \pm 0.20$.

Determining the shape of the galaxy is of importance as the inclination of the disk component in the mass model (see next sections) depends on the observed galaxy shape, hence affecting the mass determination of the galaxy. We make the assumption that the

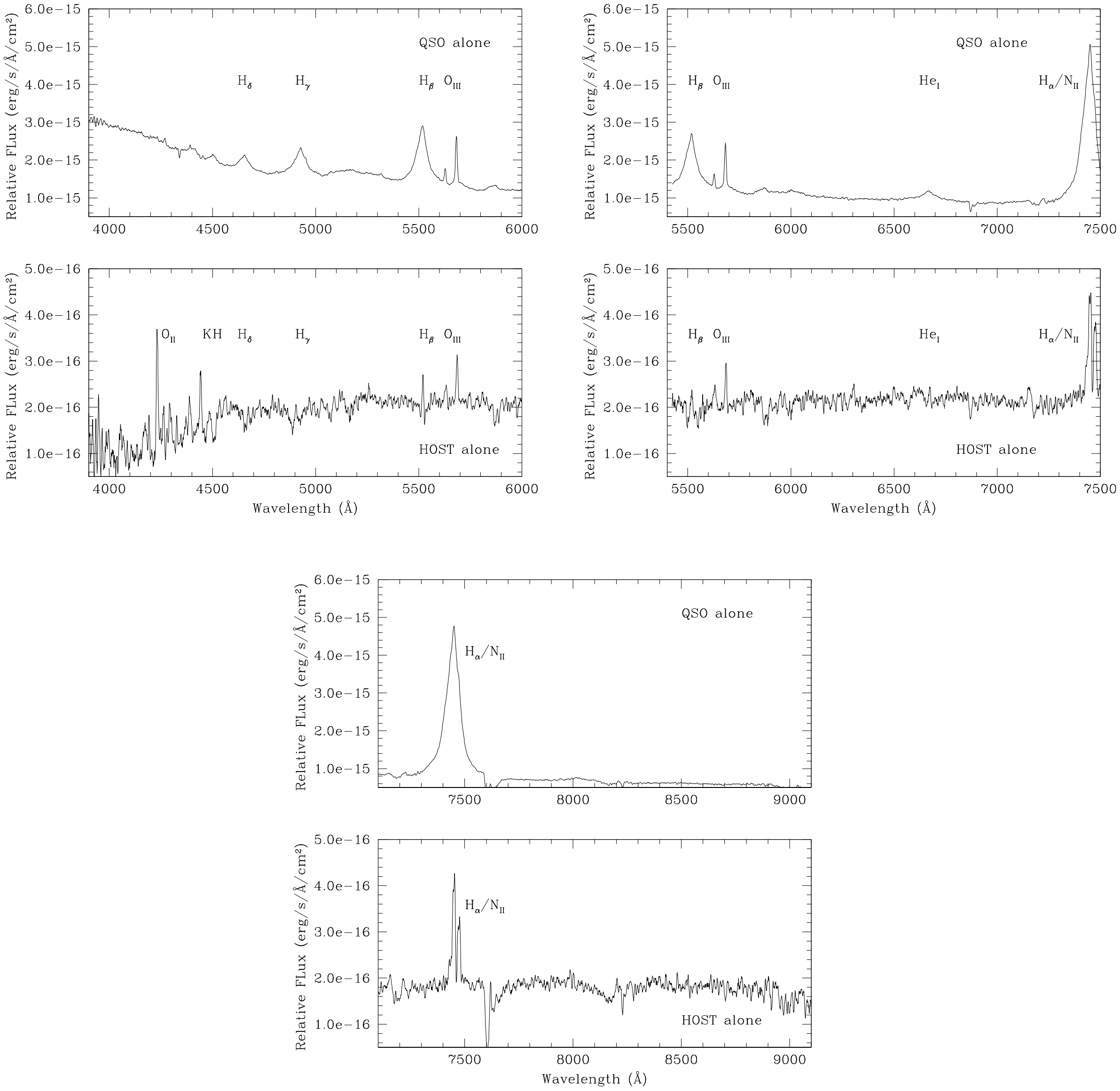

Figure 2.3: One dimensional deconvolved spectrum of HE 1503+0228 and its host galaxy. Each panel corresponds to one FORS1 grism and displays the individual flux calibrated spectrum of the quasar and its host alone. Note that the host spectrum shows no trace of the AGN broad emission lines, that are seen narrow in the host galaxy. Note also the very good agreement in the deconvolution of the 3 grisms in the overlapping regions.

galaxy has an intrinsic circular geometry, to turn the fitted ellipticities into an inclination angle. Given the relatively low signal-to-noise of our images we chose to determine the shape of the host by fitting analytical profiles to the data (Kuhlbrodt et al. in preparation). Our model is composed of a nucleus, a disk, and a spheroid, convolved with the observed PSF before any fitting is performed. In the case of HE 1503+0228 the spheroid is used to model a bar-like feature in the center of the galaxy, that may affect the fit of the disk component if it were not taken properly into account.

The analysis yields the Position Angle (PA=$38^\circ \pm 3^\circ$) of the host, its inclination ($i = 32^\circ \pm 2^\circ$), and the angle ($\phi = 12 \pm 3^\circ$) between the slit and the major axis of the galaxy. These values are in fact very close to the values found just by measuring the outmost isophotes in the VLT images.

2.2.2 Spectroscopy

The spectroscopic data were taken on the night of 2000, April 11^{th} with FORS1 mounted on Antu, the first of the four 8.2m VLT Unit Telescopes at Paranal observatory (ESO, Chile). Three grisms were used (G600B, G600R, G600I) to cover the whole optical spectral range 4000-9500Å with a mean spectral resolution of about 700. The seeing during the observations was good, about 0.6". Each grism was exposed 1200 sec, under photometric conditions and dark time, which yields a mean S/N of about 150-200 per pixel (quasar+host). The large pixel size of the detector was used, 0.2".

We show in the right panel of Fig. 2.1 and in Fig. 2.2 the orientation of the slitlets relative to the quasar host and to the PSF star. In Fig. 2.2, the images have been deconvolved and the quasar has been removed from the data. The FORS mask consists of 19 slitlets with fixed length and width (19" x 1"). One slit was centered on HE 1503+0228, one slit was centered on a bright PSF star and the rest of the slits were used either to observe fainter PSF or galaxies. Galaxy G1 is indicated in Fig. 2.1. It is at $z \sim 0.3$ and is unrelated to the quasar.

At the adopted spectral resolution, the area accessible on the CCD without loosing spectral information at the edges of the array is restricted to a strip of sky about 40" wide. As we have to observe simultaneously the quasar and at least one PSF star, the PA of the mask is therefore imposed to us by the instrumental design, i.e., the 40" strip of sky has to include both the quasar and the PSF star(s). This means that the slitlet centered on the quasar is not necessarily oriented along one of the axes of symmetry of our targets. It also means that we do not observe at parallactic angle. This is however not a major problem as FORS1 has an efficient atmospheric refraction corrector and the data remain unaffected by slit losses.

A two-dimensional wavelength calibration was applied in order to correct for slit curvature, followed by a two-dimensional sky subtraction. The spectrum of HE 1503+0228 and of the PSF star were reduced exactly in the same way, and they were rebinned to a common pixel size of 1Å in the spectral direction. They were also rebinned to a common starting wavelength, which ensures that to each spectral resolution element of the quasar, corresponds the same spectral resolution element in the PSF.

2.3 Extraction of the host's spectrum

Most current spectroscopic studies of quasar host galaxies are designed as off-axis observations, with the slit of the spectrograph placed one to several times the size of the seeing disk away from the center of the AGN (e.g., Hughes et al. 2000 [45]).

While such an observational strategy is minimizing contamination by the quasar, it has severe drawbacks. First, one can only study the outer parts of the galaxy. This is limiting the study to particular regions of the hosts. It also requires very long exposure times on large telescopes to detect the extremely faint wings of the hosts. Second, all velocity information is lost, as is the spatial information in general, along the galaxy's axes of symmetry. Finally, the method is still restricted to the most extended objects and does not allow a full decontamination of the quasar's light.

Instead, our observations are taken on-axis, placing the slit of the spectrograph on the quasar's center of light. This avoids all drawbacks of the off-axis observations, but requires clean post-processing techniques in order to remove accurately the spectrum of the AGN. For this purpose we use the spectroscopic version of the MCS deconvolution algorithm (Magain et al. 1998 [75], Courbin et al. 2000 [25]). Using the *spatial* information contained in the spectrum of PSF stars located close to the object of interest, the algorithm sharpens the data in the spatial direction, sub-samples them in order to achieve smaller pixel size, and decomposes them into two channels containing (i) the spectrum of the AGN and (ii) the two-dimensional spectrum of the host galaxy.

In the deconvolved spectrum, the new sub-sampled pixel size is 0.1" and 1Å in the spectral direction. In Fig. 2.3 are displayed the one dimensional flux calibrated spectra, integrated along the spatial direction on the deconvolved data. Interestingly, the three FORS1 grisms have significant regions of overlap that are in perfect agreement with one another. In addition, at the redshift of HE 1503+0228, most emission lines are present in two grisms. This allowed us to construct a combined 2-D flux calibrated spectrum. All measurements presented in this paper, except for velocity curves, are done on the final combined spectrum.

2.4 Dynamics of the host galaxy

2.4.1 Redshift

From the different emission lines of the quasar and of the galaxy, we can extract a sharp value for the redshift of HE 1503+0228, by simple Gaussian fitting. The lines of the host galaxy in the deconvolved spectrum have to be measured with particular care: in the center of the host, the lines are double, due to the velocity field of the galaxy and to the deconvolution method. This is mainly due to the extreme contrast between the narrow emission lines of the host, and the broad lines of the quasar: some of the flux in the sharpest parts of the host's emission lines is taken in the point-source component (the quasar) of the deconvolved spectrum, i.e., the central parts of the lines are dimmed. We

Table 2.1: Redshift of HE 1503+0228, as infered from the emission lines of the host galaxy alone, and from the quasar alone. The redshifts are the same for the quasar and for its host.

Line	Redshift (host only)	Redshift (quasar only)
OII (3727Å)	0.1353	0.1352
Hβ (4861Å)	0.1357	0.1352
OIII (4959Å)	0.1362	0.1349
OIII (5007Å)	0.1356	0.1348
OI (6300Å)	0.1355	0.1352
NII (6548Å)	0.1352	–
Hα (6563Å)	0.1353	0.1352
NII (6583Å)	0.1354	–
SII (6716Å)	0.1356	0.1343
Mean	<0.1355>	<0.1350>
Mean error	(±0.0003)	(±0.0003)

have therefore taken the mean wavelength between the two sides of emission lines, when measuring the host's redshift. The results for each line are given in table 2.1. The details of the individual emission lines is accessible via a method described in Section 2.4.2, which does not alter the center of the lines.

2.4.2 Velocity curves: extraction method

In the spectroscopic version of the MCS algorithm (Courbin et al. 2000 [25]), the difference in spatial properties between the AGN (point source) and the host galaxy (extended component) is used to separate the spectra of these two sources. A smoothing in the spatial direction is applied for this purpose to the extended component. While such a decomposition method is well suited to most spectral regions of the host, it is not optimal for deriving velocity curves: spatial smoothing (which is not precisely known as it varies with the local S/N) may modify the spectral position of the lines at a given spatial position, by averaging spatial components of different radial velocities.

We have devised another method which is better suited for extracting radial velocity curves of the host galaxy. Instead of using the difference in *spatial* properties to extract the spectra, we take advantage of the different *spectral* properties of the AGN and host to determine the radial velocity as a function of distance.

The fact that the spectral lines of the host are much narrower than any feature in the AGN spectrum is used to determine the spectral position and intensities of the host spectral lines as a function of spatial position. More specifically, at each spatial coordinate we fit the sum of a Gaussian profile of variable width representing the host emission line, plus a smooth numerical curve accounting for the AGN spectrum plus the continuum of the host.

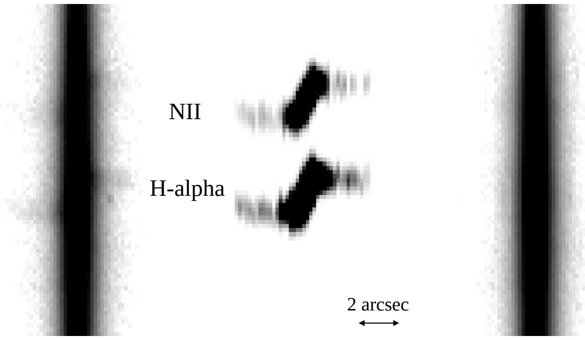

Figure 2.4: Example of emission lines extraction. Here are the Hα and [NII] emission lines in I-band grism. The left part shows a zoom on initial reduced spectrum. The middle one shows the emission lines alone whereas the right part shows the quasar and galactic continuum.

In doing this fit, we also take advantage of the constant shift in wavelength between two given emission lines: several emission lines are fitted simultaneously under the constraint that they are separated by a fixed gap in wavelength. Thus, when we refer to the Hα velocity curve, we in fact use the Hα and [NII] emission lines simultaneously. Similarly, the Hβ curve is obtained from the Hβ and the [OIII] (5007Å) lines, simultaneously . An example of such an extraction is displayed on Fig. 2.4.

In converting the wavelength shifts into velocity curves, we take several effects into account:

(1) The orientation of the slit does not coincide with the major axis of the galaxy. This is due to observational constraints, i.e. the fact that we had to obtain the spectrum of a PSF star simultaneously with the quasar and host (see Section 2.2).

(2) The slit width is comparable to the angular size of the galaxy. The observed wavelength shifts are thus averages of velocity components coming from many parts of the galaxy.

(3) The galaxy is not seen edge-on, but with an inclination angle i. Radial velocities have thus to be divided by $\sin i$ to be transformed into rotation velocities.

(4) The radial velocity curves are smeared by convolution with the seeing profile, both in spatial and spectral directions.

The procedure we use assumes a simple analytical mass model for the host galaxy, which includes a thin disk, a spherical dark matter halo, and a central point mass. The velocity at a distance r away from the galaxy's center is then given by:

$$V_{\mathrm{mod}}(r) = \sqrt{-r(F_{\mathrm{disk}} + F_{\mathrm{dark}} + F_{\mathrm{CM}})} \tag{2.1}$$

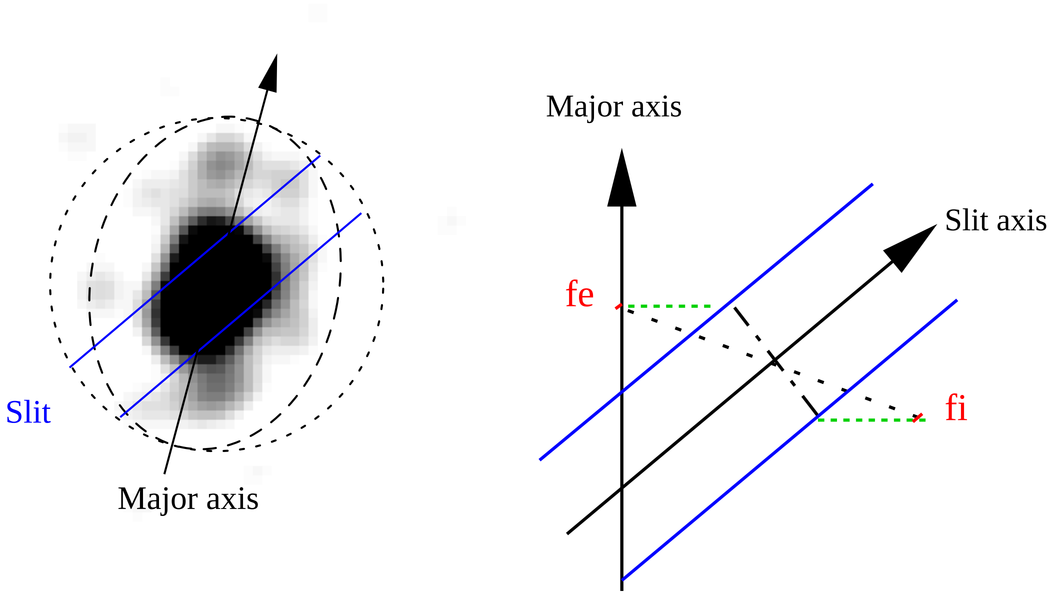

Figure 2.5: Schematic illustration of geometrical effects considered for deriving the velocity curves. *Left* : the original face-on galaxy is assumed to be circular (dotted line). Seen with an inclination i, it appears elliptical (dashed line). In addition, the slit is not aligned with the major axis of the inclined galaxy. *Right* : The mean velocity at one position along the slit, which would be integrated along a line perpendicular to the slit (dashed-dotted line) if the galaxy was seen face-on, has now to be integrated along a line which is inclined (and lengthened) with respect to the slit (dotted line; see text).

The radial forces in equation (2.1) are computed using a Kuzmin potential for the disk:

$$F_{\mathrm{disk}}(r,z) = -\frac{r^2 G M_{\mathrm{disk}}}{(r^2+(a+|z|)^2)^{\frac{3}{2}}} \tag{2.2}$$

where we assume $z = 0$, hence neglecting the thickness of the disk. M_{disk} is the total mass of the disk and a measures its scale length.

Dark matter is assumed to be spherically symmetrical about the galaxy's center. The force it creates at the distance r away from the center, given a radially dependent density distribution is:

$$F_{\mathrm{dark}}(r) = -\frac{4\pi G \rho_0 r_0^3}{r}\left(\frac{r}{r_0} - \arctan\frac{r}{r_0}\right) \tag{2.3}$$

where r_0 is the scale length for the mass distribution within the dark matter halo and ρ_0 its central density (Binney & Tremaine 1987, [7]).

The force from the central mass M_{cm} is simply

$$F_{\mathrm{CM}}(r) = -\frac{G M_{\mathrm{cm}}}{r} \tag{2.4}$$

The five parameters $M_{\rm disk}$, a, ρ_0, r_0 and $M_{\rm cm}$ are determined by a least squares fit to the data, i.e., to the measured velocity shifts at each spatial pixel along the slit. We therefore minimize the following χ^2:

$$\chi^2 = \sum_{j=1}^{N} \frac{1}{\sigma_j^2} \left\{ (s * V_{\rm mean})_j \;\sin i - d_j \right\}^2 \tag{2.5}$$

where N is the total number of pixels along the slit, and where $d_j \pm \sigma_j$ is the measured radial velocity shift at pixel j along the slit. $V_{\rm mean}$ is a one dimensional vector that contains the mean (see next paragraph for the signification of "mean") velocity predicted by our mass model at pixel j along the slit. Due to the seeing, this velocity is affected by blurring in the spatial direction, hence the need for the convolution by the 1 dimensional PSF s obtained from the spectrum of stars. As the galaxy has an inclination i, we multiply the result of the convolution by $sin\ i$ before comparing with the observed velocity d_j. The error σ_j on the radial velocity measurements is estimated by comparing the measured d_j for the same emission lines in different grisms. This was possible for the Hα, [NII], Hβ and [OIII] emission lines.

All the calculations in Eq. 2.5 assume that the galaxy is seen face-on, the inclination being taken into account by the $\sin i$ term. Due to the non-zero angle ϕ between the slit and the major axis of the galaxy, the velocity in Eq. 2.5 is a weighted mean $V_{\rm mean}$ of several velocity components across the slit.

For each pixel j along the slit, lets say at point P (see Fig. 2.6), one can compute a mean velocity as follows:

$$V_{\rm mean}(P) = \frac{1}{I_{\rm tot}} \int_{X_{\rm f_i}}^{X_{\rm f_e}} I[r(x)] \cdot V_{\rm mod}[r(x)] \cdot \frac{x}{r(x)} \cdot dx \tag{2.6}$$

$V_{\rm mean}(P)$ is the average of all the velocity components located along the dash-dotted line in Fig. 2.5. If the galaxy was seen face-on (as we would like it to be in Eq. 2.5), this line would be rotated and lengthened, and mapped onto the dotted line of Fig. 2.5. The integral in Eq. 2.6 runs along this dotted line. Its equation (Eq. 2.7) is easily obtained from geometrical considerations, given the inclination i of the galaxy with respect to the plane of the sky and given the orientation ϕ of the slit relative to the major axis of the galaxy:

$$y = \frac{\cos\phi}{\cos i}\ (x - \frac{x_{\rm P}}{\cos\phi}). \tag{2.7}$$

$x_{\rm P}$ is the coordinate of the point P on the major axis X (Fig. 2.6) of the galaxy.

The integration in Eq. 2.6 is then performed as follow: for each position x along the major axis of the galaxy, we calculate the distance $r(x)$ from the galaxy's center O to the point of the integration line that is considered. This distance is used to weight each velocity component $V_{\rm mod}[r(x)]$ of the velocity model, according to the light distribution of the galaxy in the emission line. We have estimated the light distribution $I(r)$ of the galaxy,

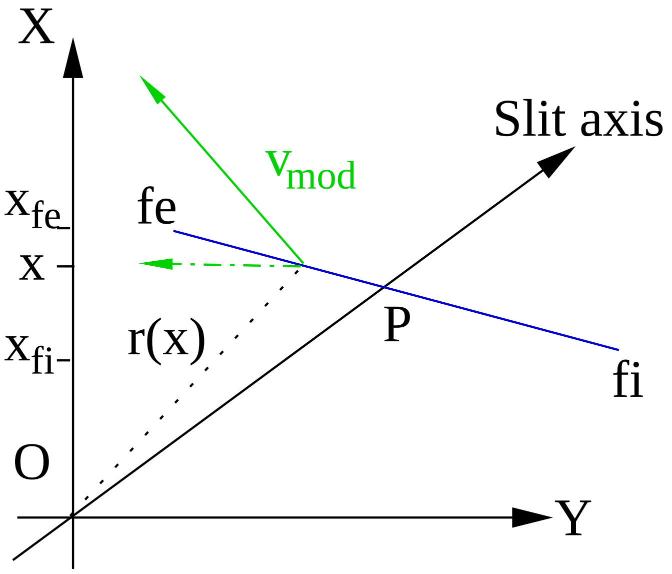

Figure 2.6: Description of the integration domain for the computation of $V_{\rm mean}(P)$. The major axis of the galaxy is along X. f_e and f_i are the limits of the integral also shown in Fig. 2.5. Only the component of the model velocity $V_{\rm mod}$ along the Y axis contributes to the integral when the galaxy is seen inclined.

assuming it is intrinsically symmetrical about the center of the galaxy. We model it by fitting a Moffat profile to the 1-dimensional intensity profile along the emission line, and applying deprojection (note that the fit of the emission line is one-dimensional, but since $I(r)$ is known analytically, one can compute weights in 2 dimensions when calculating the integral in Eq. 2.6). When doing the fit, the Moffat profile is convolved with the PSF. Correct normalisation is assured by $I_{\rm tot}$: the total flux of the regions contributing to the measured emission at position P along the slit.

The term $\frac{x}{r(x)}$ in Eq. 2.6 is the projection of the rotation velocity on the minor axis of the galaxy, which will give rise to a radial velocity once inclination is taken into account. The component of the velocity along the X-axis does not contribute to the mean velocity calculation, once inclination has been taken into account.

The intersections between the integration line and the slit edges, f_i and f_e, give us the limits of the integration, as shown in Figs. 2.5 and 2.6).

An example of a inclination/seeing-corrected velocity curve is given in Fig. 2.7 for the Hα/N[II] lines. In our calculations of the linear scales and distances we have used H_0=65 km.s^{-1}Mpc^{-1}, $\Lambda = 0$, and $\Omega_M = 0.3$, leading to a scale of 1" = 2.5 kpc.

2.4.3 Velocity curves: results

We give in Table 2.2 the best fit for the 5 parameters of our mass model. The mean velocity curve, as extracted from the Hα and Hβ lines is displayed in Fig. 2.8. This mean corresponds to four independent curves obtained for the Hα and the Hβ lines, both seen

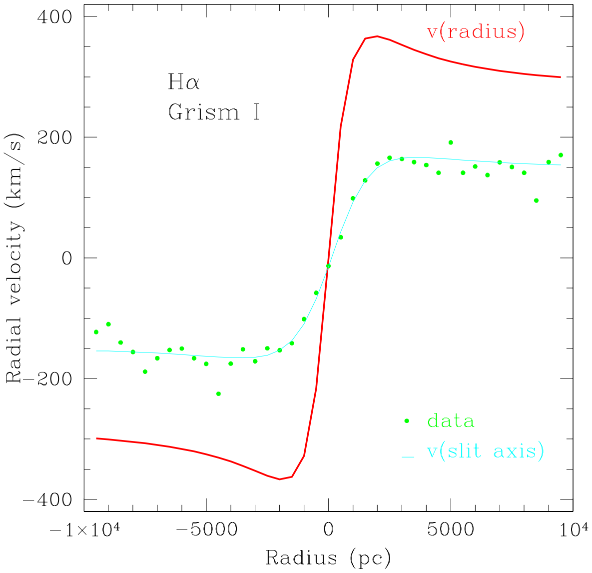

Figure 2.7: Inclination/seeing corrected velocity curves for the Hα and [NII] emission line (I-grism only): the dots show the velocity measurements. The solid line superposed is the fit of our three components model after taking into account misalignment between the slit and the major axis of the galaxy (see text). This solid line shows the variation of V_{mean} *along the slit*. It is then corrected for inclination and seeing, following Eq. 2.5, to give the true velocity as a function of distance to the center of the galaxy.

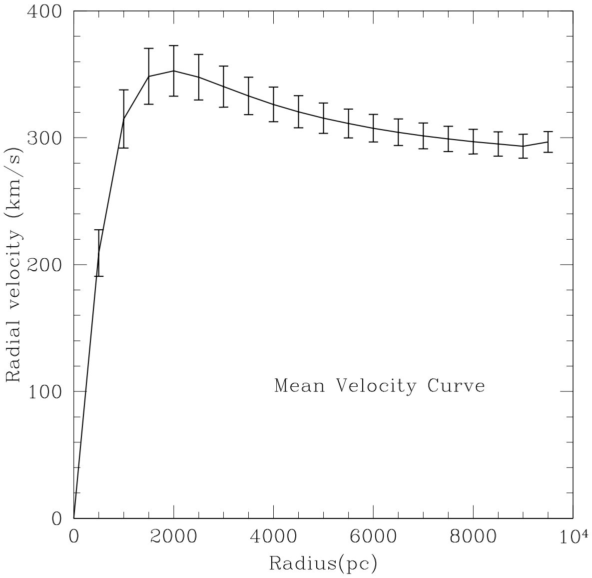

Figure 2.8: Mean velocity curve between four models fitted on the Hα line (2 grisms) and on the Hβ line (2 grisms). The error bars are derived from the dispersion between the four curves. The result is corrected for seeing and slit effects, as well as for inclination.

Table 2.2: Mass model parameters for our velocity curves in each individual grism and for each emission line. a and r_0 are in parsec, ρ_0 in $M_\odot/pc^3$ and $M_{\rm disk}$ and $M_{\rm cm}$ in $M_\odot$.

Line	Grism	a	$M_{\rm disk}$	ρ_0	r_0	$M_{\rm cm}$
Hα	R	1088	$7.9\ 10^{10}$	0.30	2033	$6.1\ 10^{7}$
Hα	I	1163	$8.6\ 10^{10}$	0.31	2074	$4.8\ 10^{7}$
Hβ	B	908	$4.8\ 10^{10}$	0.56	1753	$3.5\ 10^{6}$
Hβ	R	1428	$5.9\ 10^{10}$	0.23	2196	$2.5\ 10^{5}$

Table 2.3: Weighted means of the masses obtained in Table 2.2 where the weights are computed from the residuals of each individual fit. $M_{\rm tot}$ is the sum of $M_{\rm disk}$ and $M_{\rm dark}$. Units are solar masses.

Masses	$r < 1$ kpc	$r < 3$ kpc	$r < 10$ kpc
$M_{\rm disk}$	$1.9\pm0.3\ 10^{10}$	$5.1\pm0.7\ 10^{10}$	$7.0\pm0.9\ 10^{10}$
$M_{\rm dark}$	$1.1\pm0.3\ 10^{9}$	$1.6\pm0.3\ 10^{10}$	$1.2\pm0.1\ 10^{11}$
$M_{\rm tot}$	$2.0\pm0.3\ 10^{10}$	$6.7\pm1.0\ 10^{10}$	$1.9\pm0.2\ 10^{11}$

in two different grisms.

Table 2.3 gives our mass estimates which are weighted means of the four fits presented in Table 2.2, the weights being a function of the residuals after modeling of the data obtained in each individual grism. These weights are the same as the ones applied to compute the mean velocity curve of Fig. 2.8.

We investigate in Table 2.4 the effect of the error on the inclination of the galaxy and on its PA. Uncertainties on inclination and orientation of the major axis lead to error bars on masses, which are summarized in Table 2.4.

These results should be interpreted with care, as there is a strong correlation between the model parameters and since the adopted model is simpler than reality. However, while the details of the mass distribution within the galaxy remain inaccurate, we can still determine the total mass of dark matter and as well the disk mass enclosed in a given radius.

Given the results in Tables 2.2, 2.3 and 2.4, we infer a mass estimate of $M(r < 1$ kpc$) = (2.0 \pm 0.3)10^{10}\ M_\odot$. The corresponding mass, integrated over 10 kpc is $M(r < 10$ kpc$) = (1.9 \pm 0.3)10^{11}\ M_\odot$. Table 2.4 shows that an additional error of 10% should be added, due in part to the uncertainty on the PA of the major axis of the host, but mainly to the uncertainty on its inclination.

Table 2.4: Effect of the error on the inclination (32 ± 2°) and PA (38 ± 3°) of the host galaxy. Results are given for weighted means of 4 velocity curves, as in Table 2.3, varying the inclination and the PA within their error bars.

Masses ($M_\odot$)	$r < 1$ kpc	$r < 3$ kpc	$r < 10$ kpc
Inclination			
$M_{\rm disk}$	$1.9^{-0.2}_{+0.2}\ 10^{10}$	$5.1^{-0.6}_{+0.6}\ 10^{10}$	$7.0^{-0.8}_{+0.8}\ 10^{10}$
$M_{\rm dark}$	$1.1^{-0.02}_{+0.2}\ 10^{9}$	$1.6^{-0.1}_{+0.2}\ 10^{10}$	$1.2^{-0.1}_{+0.1}\ 10^{11}$
$M_{\rm tot}$	$2.0^{-0.2}_{+0.2}\ 10^{10}$	$6.7^{-0.7}_{+0.8}\ 10^{10}$	$1.9^{-0.2}_{+0.2}\ 10^{11}$
Major axis			
$M_{\rm disk}$	$1.9^{+0.02}_{-0.03}\ 10^{10}$	$5.1^{+0.1}_{-0.2}\ 10^{10}$	$7.0^{+0.2}_{-0.2}\ 10^{10}$
$M_{\rm dark}$	$1.1^{+0.1}_{+0.04}\ 10^{9}$	$1.6^{+0.1}_{-0.01}\ 10^{10}$	$1.2^{+0.01}_{-0.05}\ 10^{11}$
$M_{\rm tot}$	$2.0^{+0.03}_{-0.03}\ 10^{10}$	$6.7^{+0.2}_{-0.2}\ 10^{10}$	$1.9^{+0.03}_{-0.07}\ 10^{11}$

2.5 Stellar and Gas Content

One of the primary goals of our study is to infer the characteristics of the stellar population of quasar host galaxies: does the stellar population of HE 1503+0228 match that of a normal galaxy ? Where does it lie in the Hubble sequence ?

Let us first note that $H = 14.57$ mag corresponds, with the same cosmological parameters used earlier, to an absolute magnitude of $M_H = -24.5$ mag. This, in addition to the profile fitting described in the previous sections, indicates a normal early type local spiral galaxy (Bothun et al. 1985 [11]; Arimoto & Jablonka 1991 [1]). While the photometric data alone already allow to point out a plausible morphological type for the host of HE 1503+0228, spectroscopy is the key to the determination of its stellar content. A few considerations have to be made before looking at the spectral features in any detail.

First, galactic extinction has to be taken into account. The extinction towards HE 1503+0228 is $A_B = 0.217$ corresponding to E(B-V)=0.05 (Schlegel et al. 1998 [102]). Our spectrum of HE 1503+0228 has been corrected accordingly.

Second, although no velocity standard stars were taken during the observations, the resolution in the R-grism (4.9Å; 3.6Å at rest-frame) is good enough to make use of the stellar library of Jacoby et al. (1984) (FWHM =3.5 Å). This gives a velocity dispersion of $\sim$ 170 km/s, which we only take as an indicative upper limit value.

Third, we observed HE 1503+0228 with three different grisms, each having a different dispersion. The three spectra were combined in order to cover the wide wavelength range 3670Å to 9165Å (3150Å to 8073Å once corrected from the redshift z=0.1355, or v=37837.4 km/s). In doing this, we have degraded the observations to the resolution of the less resolving grism, i.e., 5.7 Å (or $\sim$ 5 Å at rest-frame).

Finally, due to the low signal-to-noise ratio of the spectrum in its bluer part, we consider

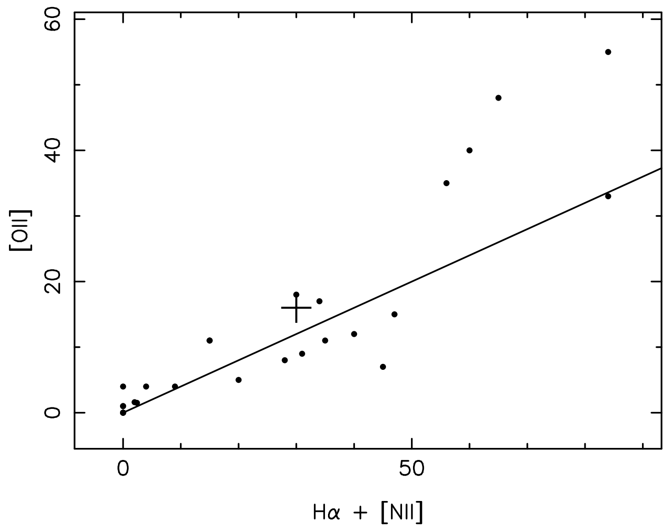

Figure 2.9: The relation between the equivalent widths of Hα+[NII] and [OII]. The black dots show the *normal* spiral galaxies of Kennicutt's sample. The plain line correspond to [OII] = 0.4 Hα+[NII], mean relation of the galaxies dominated by photoionization. The cross indicates the position of HE 1503+0228.

only features from 4000 Å on (3523Å at rest-frame).

We have only considered the integrated spectrum of HE 1503+0228. In fact, the signal-to-noise of the measurements on each individual spatial resolution element of the 2D data varies between 3 and 6, and therefore does not give much hope in tracing any radial variation in the stellar population, unless deeper data are obtained.

In the following, we measure well known indicators for the underlying stellar populations, for the host of HE 1503+0228, and we compare them with the values obtained for two control samples: the one of Trager et al. (1998 [112]) for the elliptical galaxies, and the one of Kennicutt (1992 [57, 58]) for the spiral galaxies.

2.5.1 Emission lines

One of our concern was to verify that the deconvolution procedure had indeed left out any non thermal excitation process.

We have measured the equivalent widths (EW) of the most prominent emission lines seen in the spectrum of HE 1503+0228, i.e., [OII], [OIII](4959Å), [OIII](5007Å) and Hα+[NII] (see Table 2.5).

Kennicutt (1992 [58]) provided measurement of the Oxygen lines [OII] (3727Å), [OIII] (5007Å) and Hα+[NII]. He noted that among galaxies with normal star formation rates (EW(Hα+[NII]) $\leq$ 40Å), the [OIII] lines are rarely detected at all (EW $\leq$ 0.5Å). For HE 1503+0228, while EW(Hα+[NII]) $\sim$ 30Å, we detect [OIII], with an equivalent width of $\sim$ 4Å. This is the only and discreet sign of an excitation process in or surrounding

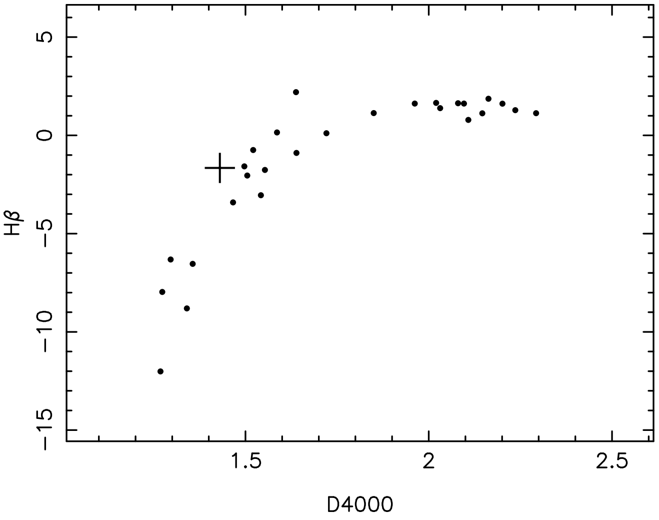

Figure 2.10: The relation between the 4000Å break and the equivalent width of Hβ for normal spiral galaxies (Kennicutt 1992 [57, 58]) (dots) and HE 1503+0228 (cross).

Table 2.5: Lick indices for the spectral features in the host galaxy of HE 1503+0228.

Name	D4000	G4300	Ca4455	Mg_2	Fe5270	Fe5335	[OIII]	Hα+ [NII]
Value	1.48	3.41	2.03	0.157	1.89	1.12	4.2	30.
Error	0.04	0.16	0.12	0.002	0.08	0.11	0.3	2.

HE 1503+0228 which is not directly related to star formation and, hence, which might be triggered by the central AGN radiation field. Kennicutt (1992 [58]) also reported that galaxies dominated by stellar photoionization follow a mean relation EW([OII]) $\sim$ 0.4 EW(Hα+[NII])(with an rms of 50%). HE 1503+0228 falls nearly exactly on this relation, as shown in Fig. 2.9. Kennicutt's galaxies are represented by plain dots, the mean relationship between Hα+[NII] and [OII] is the solid line. The position of HE 1503+0228 in this plane is indicated by a cross.

HE 1503+0228 exhibits a weak [OIII] (5007Å) line. We have left out from the Kennicutt sample the objects which displays strong [OIII] (5007Å) lines, when analysing in the next section the absorption line features. This ensures that we compare HE 1503+0228 with objects of similar properties.

To further investigate this matter, we have measured the line intensity ratios, [OIII]/ Hβ (0.05), [OIII]/ Hβ (0.54), [NII]/ Hα (-0.20). Due to the deconvolution procedure, the ratios between Oxygen and Balmer lines are upper limits. Indeed, the Balmer lines are probably underestimated. When placed in the diagnostic diagrams of Sodré and Stasińska (1999 [105]), the host galaxy of HE 1503+0228 falls perfectly on the sequence drawn by the normal spiral galaxies.

To summarize, our analysis of the emission lines suggests that HE 1503+0228 is a

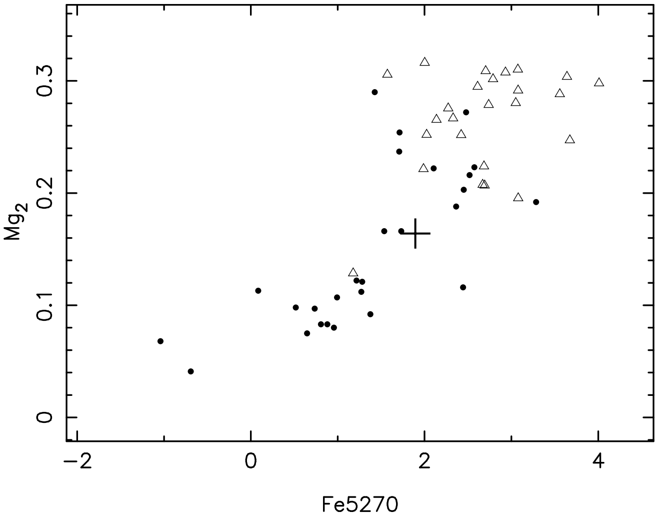

Figure 2.11: The relation between the Fe5270 and Mg_2 index for the normal spirals of Kennicutt et al. (1992 [58]) (dots) and the ellipticals of Trager et al. (1998 [112]) (open triangles). As in Fig. 2.9 and 2.10, the cross indicates the position of HE 1503+0228.

perfectly normal spiral galaxy, where the gas emission is dominated by ionization by stars rather than by the central AGN.

2.5.2 Absorption lines

Our spectra have sufficient signal-to-noise to measure the Lick indices for several stellar absorption features. As the spectral resolution of the Lick system is lower than the resolution of our data, we have convolved the spectrum of HE 1503+0228 with the appropriate Gaussian kernel, in order to match a 200 km s^{-1} rest-frame resolution.

For a full compatibility between the measurements done for HE 1503+0228 and for the galaxy control sample (see previous section), we have re-measured the Lick indices on Kennicutt's galaxies in exactly the same way as for HE 1503+0228.

A difficulty when looking at the stellar population in HE 1503+0228 is to avoid contamination due to the gas emission. This emission can either "fill-in" absorption lines –the Balmer lines is a well known example, but Mgb can be affected as well (Goudfrooij & Emsellem 1996 [39])– or contaminate the continuum side bands used for the measurements of the equivalent widths. We have identified four absorption lines that are strong enough and free of this contamination by emission lines. They correspond to the Lick indices G4300, Ca4455, Ca4668, Fe5270 and Fe5335. With only a tiny change in the definition of the continuum window used for the Mg_2 index, we could avoid contamination by the [OIII] (4959Å) emission line for this index. The small change we impose on the continuum side bands produces a change of at most ±0.04mag (or 20%) in the measurement of the Mg_2

index. In addition to the indices for the absorption lines, we also measure the important calcium break at 4000Å, which gives the D4000 index (Bruzual 1983 [14]).

Table 2.5 summarizes the results of our measurements. The available signal-to-noise ratio (per Å) for performing the measurements varies between $\sim$ 10 (blue part) and $\sim$25 (red part).

The continuum shape of HE 1503+0228 is rather flat, indicative of on-going star formation. Similarly to the result of Fig. 2.9, Fig. 2.10 puts HE 1503+0228 among normal spiral galaxies. The latter figure compares the index D4000, which measures the 4000Å break, with the equivalent width of Hβ which is indicative of the presence of star formation. HE 1503+0228 nicely falls on the sharp relation traced by normal spirals.

As for the chemical abundances, we chose to present in Fig. 2.11 the Mg_2 and Fe5270 indices. They trace the α and iron peak-elements, respectively. Here again, HE 1503+0228 is located exactly on the Hubble sequence, at the location of spiral galaxies, rather than ellipticals. Furthermore, the values of the absorption line equivalent widths strongly suggests the stellar population of an early type spiral galaxy.

2.6 Conclusions

We have undertaken a VLT program aimed at unveiling the spectroscopic properties of quasar host galaxies for a sample of radio quiet, bright quasars at low redshift. Our long term scientific goal is double: (1) to compare the stellar populations of quasar hosts with those of other ("normal") galaxies, and (2) to study their dynamics, as close as possible to the central AGN.

The present paper considers HE 1503+0228 as a test case. An important part of our work is dedicated to the correction of geometrical effects and removal of the atmospheric blurring. This is crucial in the central parts of the galaxy, with sizes comparable to the seeing disk.

We find that the stellar population of the host galaxy of HE 1503+0228 compares well with that of the normal non-AGN spiral galaxies of Kennicutt (1992 [57, 58]) and Trager et al. (1998 [112]). They show no trace of enhanced star formation. The interstellar medium does not show significant ionization by the central AGN. Its mass M(r $<$ 10 kpc) $= (1.9 \pm 0.3)10^{11}$ $M_\odot$ also compares very well with that of other spiral galaxies. To summarize, the host galaxy of HE 1503+0228 is a normal spiral galaxy.

Acknowledgements The authors would like to thank Sandrine Sohy for help with some of the intensive programing involved in this work. Géraldine Letawe is a teaching assistant supported by the University of Liège, (Belgium) and is partially funded by the Pôle d'Attraction Interuniversitaire, P4/05 (SSTC, Belgium). Frédéric Courbin acknowledges financial support through Marie Curie grant MCFI-2001-0242. Chilean grant FONDECYT/3990024 and additional support from the European Southern Observatory are also gratefully acknowledged. Dante Minniti is supported in part by Fondap Center for Astrophysics.

Chapitre 3

Spectroscopie du quasar HE 1434-1600 : un hôte elliptique avec un milieu interstellaire fortement ionisé

L'objet étudié dans ce deuxième article est, dans l'échantillon, celui qui comporte les raies d'émission les plus étendues spatialement (jusqu'à 4 secondes d'arc). Leur symétrie, ainsi que l'important contenu gazeux de la galaxie, nous ont d'abord fait penser à une spirale. Or, il s'est rapidement avéré que l'hôte est en fait une galaxie elliptique, mais avec quelques caractéristiques particulières justifiant la publication de ces résultats.

- La distribution en intensité des raies d'émission est inattendue, avec des maxima non centrés sur la galaxie mais écartées de 2" de part et d'autre du centre. Les courbes de vitesse radiale sont très pentues au centre puis relativement plates, nécessitant une grande concentration de masse au centre. Aucun paramètre réaliste n'a permis d'ajuster un modèle aux courbes de vitesse radiale, nous forçant à exclure l'hypothèse de gaz en rotation.
- Ce quasar a un compagnon proche, dont le redshift a pu être déterminé par des observations spectroscopiques supplémentaires acquises en 2002. Il fait également partie d'un petit amas (5 galaxies proches ont été recensées)
- Le milieu interstellaire est, dans certaines parties de la galaxie éloignées du centre, fortement ionisé par le quasar lui même, avec peut-être une contribution de jets radios favorisant l'ionisation par le quasar.

L'interprétation est la suivante : le milieu interstellaire a été balayé par l'interaction avec la galaxie voisine, laissant la possibilité au rayonnement du quasar de se propager jusqu'à de grandes distances dans la galaxie.

Les images obtenues récemment (en 2005) par le HST confirment que l'hôte de HE 1434-1600 est bien elliptique, et nous apprennent que les zones d'émission intense correspondent à des filaments de gaz hautement ionisé. Cependant, ces filaments sont probablement les résidus d'une précédente interaction, la galaxie voisine n'ayant pas l'air d'avoir encore été perturbée par une collision majeure.

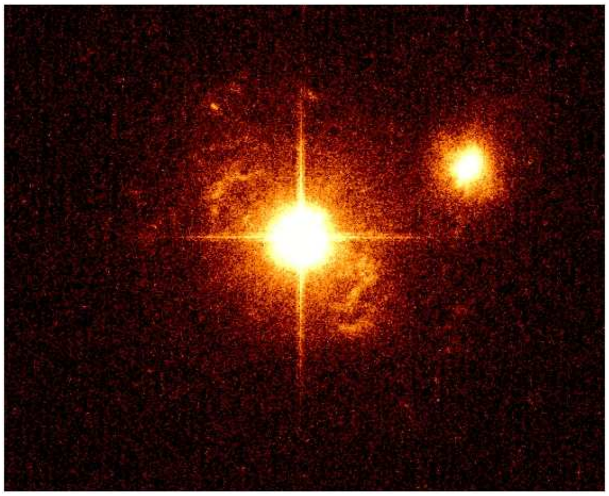

Fig. 3.1 – Image de HE 1434-1600 obtenue en 2005 via le HST/ACS, avant déconvolution. On repère des filaments de gaz ionisés de part et d'autre du quasar, exactement dans l'axe de la fente d'observation employée pour les spectres VLT FORS2, ainsi que la galaxie voisine en haut à droite de l'image qui semble relativement peu perturbée par une interaction.

On-axis spectroscopy of the $z = 0.144$ radio-loud quasar HE 1434−1600: an elliptical host with a highly ionized ISM

G. Letawe[1], F. Courbin[1], P. Magain[1], M. Hilker[2], P. Jablonka[3], K. Jahnke[4], L. Wisotzki[4,5]

1. Institut d'Astrophysique et de Géophysique, Université de Liège, Allée du 6 Août, 17, Bat. B5C, Liège 1, Belgium
2. Sternwarte der Universität Bonn, Auf dem Hügel 71, 53121 Bonn, Germany
3. GEPI, Observatoire de Paris, Place Jules Janssen, F-92915 Meudon Cedex, France
4. Astrophysikalisches Institut Potsdam, An der Sternwarte 16, 14482, Potsdam, Germany
5. Institut für Physik, Universität Potsdam, Am Neuen Palais 10, 14469 Potsdam, Germany

Published in Astronomy and Astrophysics, 2004, v.424, pp 455-464.

Abstract : VLT on-axis optical spectroscopy of the $z = 0.144$ radio-loud quasar HE 1434−1600 is presented. The spatially resolved spectra of the host galaxy are deconvolved and separated from those of the central quasar in order to study the dynamics of the stars and gas as well as the physical conditions of the ISM. We find that the host of HE 1434−1600 is an elliptical galaxy that resides in a group of at least 5 member galaxies, and that most likely experienced a recent collision with its nearest companion. Compared with other quasar host galaxies, HE 1434−1600 has a highly ionized ISM. The ionization state corresponds to that of typical Seyferts, but the ionized regions are not distributed in a homogeneous way around the QSO, and are located preferentially several kiloparsecs away from it. While the stellar absorption lines do not show any significant velocity field, the gas emission lines do. The observed gas velocity field is hard to reconcile with dynamical models involving rotating disk, modified Hubble laws or power laws, that all require extreme central masses ($M > 10^9$ M$_\odot$) to provide only poor fit to the data. Power law models, which best fit the data, provide a total mass of $M(<10\ \mathrm{kpc}) = 9.2\,10^{10}$ M$_\odot$. We conclude that the recent interaction between HE 1434−1600 and its closest companion has strongly affected the gas velocity and ionization state, from the center of the galaxy to its most external parts.

Keywords Galaxies: dynamics, interaction, black holes – quasars: individual: HE 1434-1600, quasar host galaxies – techniques: image processing, deconvolution

Based on observations made with the ESO Very Large Telescope ANTU/UT1 at ESO-Paranal observatory, Chile (program 65.P-0361(A)).

3.1 Introduction

Spectroscopy of quasar host galaxies, either with a long slit or through the use of integral field spectrographs now available on large telescopes, is able to provide unique clues to the stellar content, the physics of the interstellar medium (ISM) and the dynamics of these complex objects. Since their otherwise luminous active galactic nucleus (AGN) is extinguished by the central molecular torus, the radio galaxies can be rather easily studied, even in spectroscopy (e.g., Vernet et al. 2001 [115]). This is also true for Seyfert galaxies where the brightness of the central AGN is much lower than in genuine quasars. On the contrary, obtaining high quality spectra of the host of bright quasars remains a much more challenging task because of the high luminosity contrast between the central AGN and the host.

We have carried out a systematic spectroscopic campaign of the host galaxies of a sample of bright quasars, using the European Very Large Telescope (VLT), at the Paranal observatory, Chile. The quasar sample is selected from the Hamburg-ESO Survey (HES; Wisotzki et al. 2000 [119]). It includes 20 intrinsically bright quasars with $M_B < -23$ and $z < 0.33$. No prior morphological selection criteria have been applied to the sample. The full sample, for which optical and near-IR imaging is also available (Jahnke 2002 [50]; Jahnke et al. 2003 [52] 2004 [51]) will be fully described and analyzed in Letawe et al., in prep., while the deconvolution techniques used to decompose the data into two independent spectra of the unresolved central quasar and of the extended host galaxy are presented in Magain et al. (1998 [75]) and Courbin et al. (2000 [25]). A first application of these techniques to the quasar HE 1503+0228 is presented in Courbin et al. (2002 [24]). It shows that the host of this quasar is a normal spiral galaxy with $M(r < 10 \text{ kpc}) = (1.9 \pm 0.3) \times 10^{11}$ $\mathrm{M}_\odot$ and with stellar populations typical of a normal spiral galaxy.

Some of the objects in our sample display peculiar features. HE 1434−1600, with $z = 0.144$ and absolute B magnitude of -24.3, is a rather special case, which appeared to deserve further investigations. The peculiar velocity field, prominent emission lines and rich environment, led us to obtain more data for this radio-loud quasar than for the rest of the sample. The present paper describes the observations of what appears to be an elliptical galaxy that is probably experiencing a collision, and that shows a particularly strongly ionized Inter Stellar Medium (ISM).

In this paper, the conversion of angular scales into linear distances is done using $H_0 = 65$ km s^{-1} Mpc^{-1}, $\Omega_m = 0.3$ and $\Omega_\Lambda = 0.7$ leading to a scale of 2.73 kpc per arcsecond at $z = 0.144$.

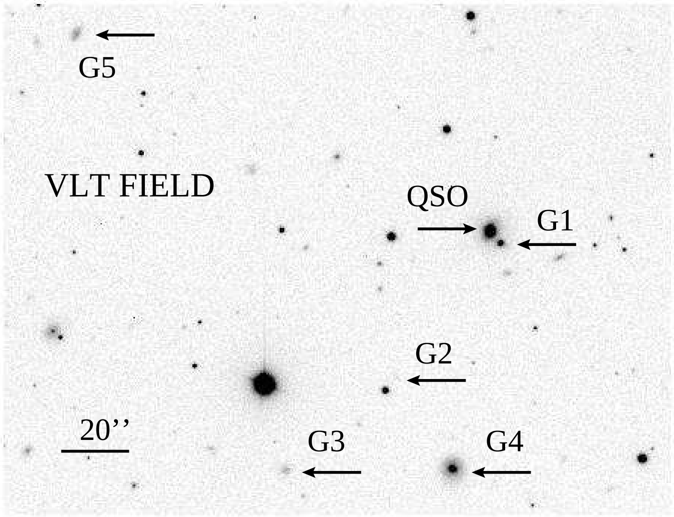

Figure 3.2: Part of the FORS1 field of view around HE 1434−1600. Five galaxies with measured redshifts are indicated by horizontal arrows. They all have redshifts very similar to that of the quasar, $z \sim 0.144$ (see Section 3.5). North is up and East is left, as all other figures in this paper.

3.2 Imaging

3.2.1 Optical – near-IR

Optical, near-IR and radio images of HE 1434−1600 were available, in addition to the spectroscopic data. Two VLT R-band images were taken prior to each spectroscopic observation in order to construct the slitlet mask. These images were obtained on the nights of April 11, 2000 (30 sec exposure, seeing 0",7) with FORS1 and on the night of May 13, 2002 (15 sec, seeing 1",1) with FORS2. Fig. 1 shows part of the FORS1 field of view. Additional images were obtained in the V-band at the 1.54m Danish telescope at La Silla observatory and in the infrared J-band with the ESO 3.5m New Technology Telescope (NTT) equipped with the instrument SOFI. The V- and J-band data are the same as used by Jahnke (2004 [51]). The technical details of the observations are given in Table 3.1.

Table 3.1: Details of the imaging observations. The first column gives the telescope and instrument used, column 4 gives the pixel size in arcseconds, while the last column gives the integration time in seconds.

Instr.	Band	Date	scale	t
VLT-FORS2	R	13-05-2002	0.252	15s
VLT-FORS1	R	11-04-2000	0.200	30s
NTT-SOFI	J	24-02-1999	0.290	300s
1.54m-DFOSC	V	14-04-1997	0.390	600s

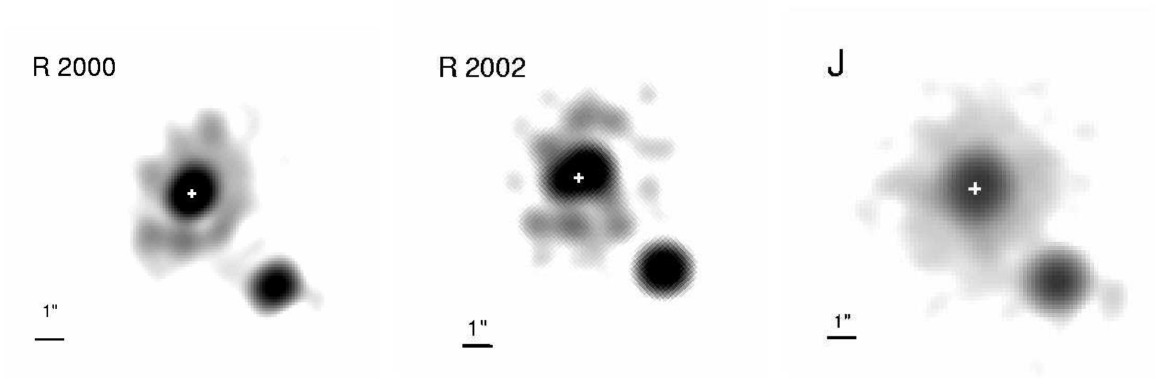

Figure 3.3: Deconvolved images of the host galaxy alone, with the quasar removed. The position of the quasar is indicated by the cross. The intensity scale is different in each image, as well as the angular resolutions. While the J-band image appears smooth, both R images show structure about 2" away from the center of the host galaxy.

All images, except the low S/N V-band image, were deconvolved using the MCS algorithm (Magain, Courbin & Sohy 1998 [75]), to separate the quasar from its host galaxy and to reveal possible substructures that may help to explain the spectroscopic observations. The deconvolved host images all show extended and rather uniform emission (Fig. 3.3), with a significant bulge contribution. There are, however, some deviations from the smooth profile, 2–5" away from the nucleus. These small-scale substructures match well the ones seen in [OIII] in the spectroscopic observations (see Section 3.3).

A close companion, labeled G1 on Fig. 3.2, can be seen next to HE 1434−1600, located 4" from the center, or 11 kpc. Its redshift (see Section 3.5) is the same as that of HE 1434−1600. A $r^{-1/4}$ law fits well its 1D intensity profile, while an exponential disk does not. Moreover, its shape is that of an elliptical galaxy.

Photometry of the quasar host has been performed by Jahnke et al. (2004 [51]) in a multicolour study of QSO hosts. After masking of the close companion they were able to model the host of HE 1434−1600 with a pure spheroid light distribution. The measured magnitudes of the host are $V = 17.0$, $R = 16.4$, $J = 15.1$, and $K = 13.7$. They corrected for galactic extinction using the maps by Schlegel et al. (1998 [102]) and applied a K-correction term that was computed from a measured broad-band SED (spectral energy distribution). For that purpose, template SEDs were fitted to six photometric points in the optical and NIR and the template was used to derive a K-correction term (see Jahnke et al. 2004 [51] for details). Including these corrections the colours of the host are $V - R = 0.43$, $V - J = 1.66$ and $V - K = 2.75$, i.e. significantly bluer colours than expected for an inactive galaxy of this luminosity (Fukugita et al. 1995 [38], Fioc & Rocca-Volmerange 1999 [35]). Modeling of the stellar populations points to either an overall young dominant stellar population of 1–2 Gyr, or may also be indicative of continuous star formation, plus a small fraction (1 % in mass) of a recent (e.g., 100 Myr) star burst population.

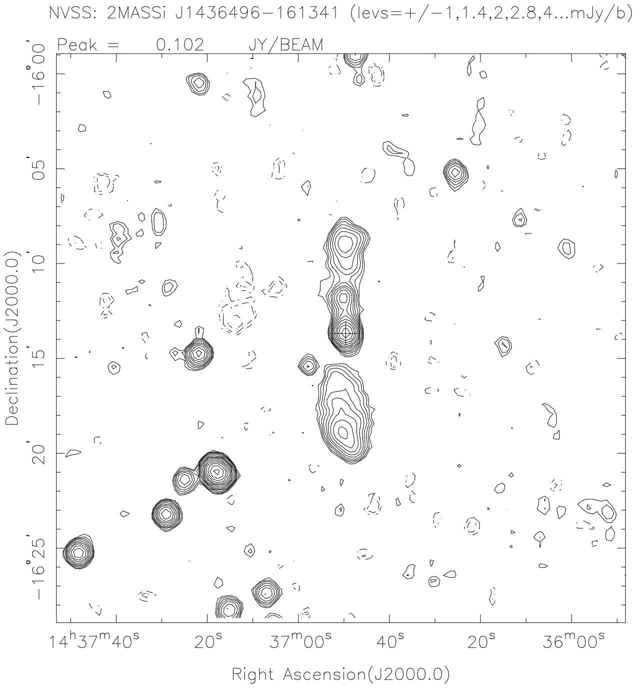

Figure 3.4: NVSS image centered on the position of HE 1434−1600. The field of view is 30'×30', and the beam size in this 1.4 GHz map is 45". The central "hot spot" corresponds to HE 1434−1600. Two lobes also extend over 5–6' to the north and south of the quasar.

3.2.2 Radio map

A radio map of HE 1434−1600 has also been retrieved from the NRAO VLA Sky Survey (Condon et al. 1998 [22]), through the online NASA Extragalactic Database (NED). It shows large lobes extending up to 6' or 980 kpc, North and South of the quasar (Fig. 3.4). With an integrated radio flux of 7.14 mJy at 1.4 GHz and a magnitude $B = 15.62$ (quasar plus host), we estimate a radio loudness $R = F_{5\,\mathrm{GHz}}/F_{4400} \sim 10$, a value which places HE 1434−1600 at the limit between radio-loud and radio-quiet quasars (Kellermann 1989 [56]). Such a radio structure has generally been found to be associated with extended optical emission lines for example in radio galaxies (e.g., Fosbury et al. 1984, [37]), Seyferts (Morganti et al. 1998 [92]) or in Radio Loud Quasars (RLQ) (Boroson et al. 1984 [9], 1985 [10]; Stockton & MacKenty 1987 [109]). We investigate in Section 3.4 the possibility that HE 1434−1600 is a radio loud quasar (although almost radio quiet) with jet induced ionization of the ISM.

3.3 Spectroscopy: observations and data reduction

Our first spectroscopic observations were obtained during the night of April 11, 2000, with the FOcal Reducer/low dispersion Spectrograph 1 (FORS1) mounted on the 8.2m VLT/UT1 ANTU, at ESO-Paranal. Since the aim of the project is to spatially deconvolve

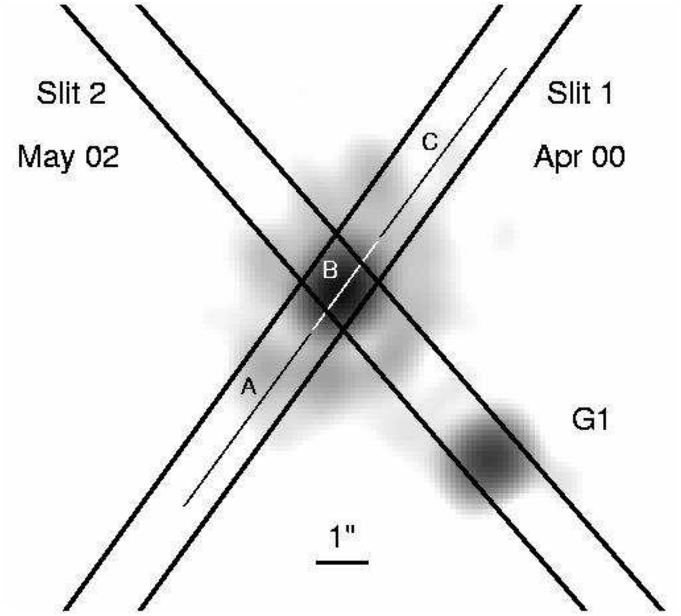

Figure 3.5: Slit orientations represented in overlay on the deconvolved R-band image of the host, after removal of the quasar. The companion galaxy G1 is also visible on this image. Slit 1 corresponds to the data taken in April 2000, and slit 2 corresponds to the May 2002 data. In each case the slit width is 1". A, B and C are the three regions we used to extract the spectra (see Section 3.3). The total size of this image is about the size of the central hot-spot in the radio map of Fig. 3.4.

the spectra, the Multi-Object-Spectroscopy (MOS) mode was chosen in order to allow the simultaneous observation of the quasar and of neighbouring stars used to determine the Point Spread Function (PSF). The same approach was used in Courbin et al. (2002 [24]) to study the host of HE 1503+0228, at $z = 0.135$. Since 19 slitlets are available, we were also able to observe several galaxies in the vicinity of the quasar.

Three grisms were used (G600B, G600R, G600I), with a resolving power $R \sim 700$. The exposure time for each grism was 1200 seconds and the full spectrum covers the wavelength range between 3250 Å and 8000 Å in the rest frame. All basic reduction steps were made with the IRAF package, leading to flatfielded, flux calibrated and rebinned spectra with 0",2 per pixel in the spatial direction and 1 Å per pixel in the spectral direction. Since there is a significant slit curvature in some of the slitlets, a 2D wavelength calibration was performed, as well as a 2D sky subtraction. The seeing varied between 0",5 and 0",6. The slit orientation (PA) was 35° clockwise from north. We refer to these data as *slit 1* all along the text and in Fig. 3.5.

Additional data were obtained with FORS2 at VLT/UT4 YEPUN, on the night of May 13, 2002, with the slit oriented to include both the quasar host and the companion galaxy G1. The PA of this slit is −41° (*slit 2* in Fig. 3.5). As for the FORS1 observations, the MOS configuration was chosen in order to observe several PSF stars. Only one grism was used,

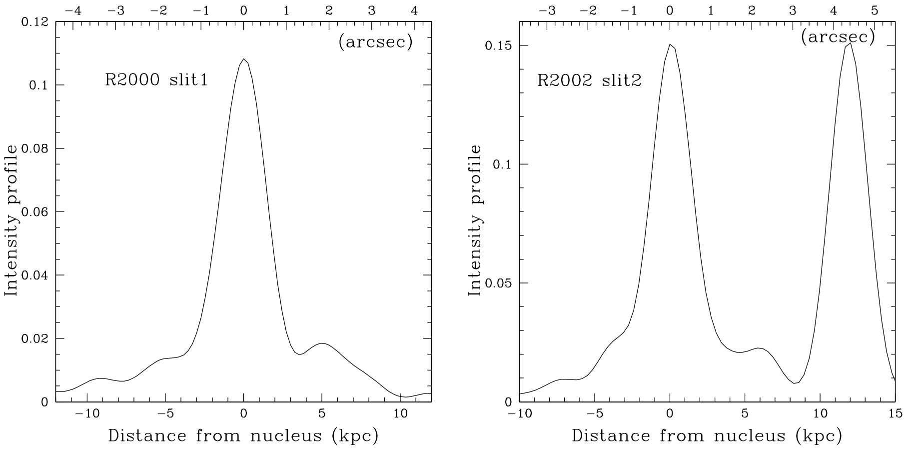

Figure 3.6: Extracted intensity profiles along *slit1* and *slit 2* of the host galaxy, as defined in Fig. 3.5. Each profile is obtained by spatially integrating the deconvolved R-band image across the 2 slits, after removal of the quasar. Obvious structures with a typical size of 1 kpc do appear 2" away from the quasar.

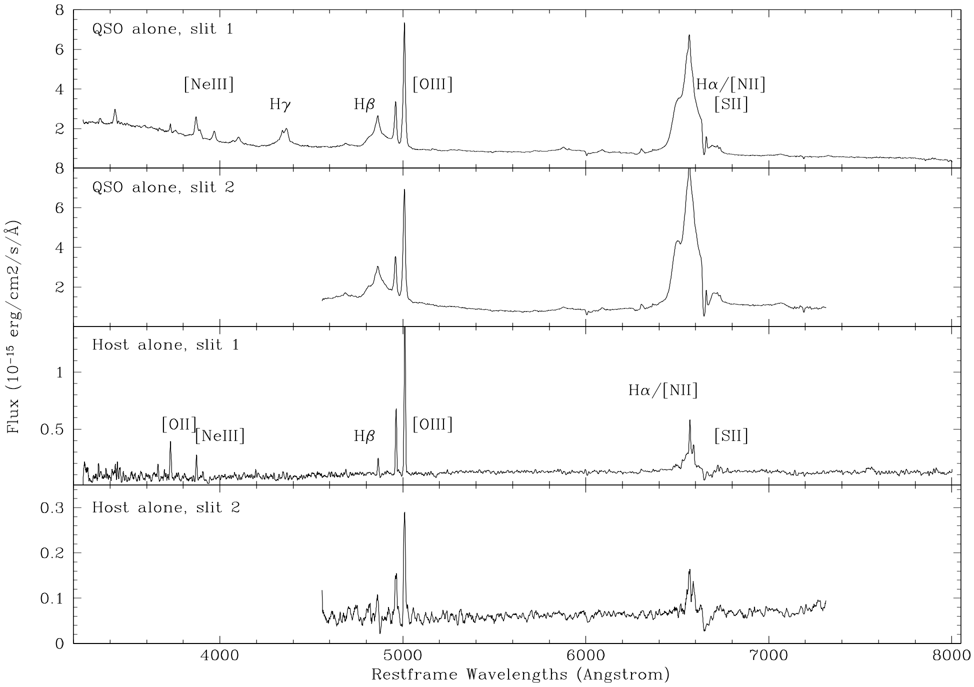

Figure 3.7: 1D spectra of the quasar and the host galaxy after deconvolution. The spectrum of the host is integrated over 6". All spectra are displayed in the rest frame, for the two slit orientations. The quasar spectra are shown in the two upper panels, while the spectra of the host galaxy alone, are shown in the two lower ones. Note the different flux scales.

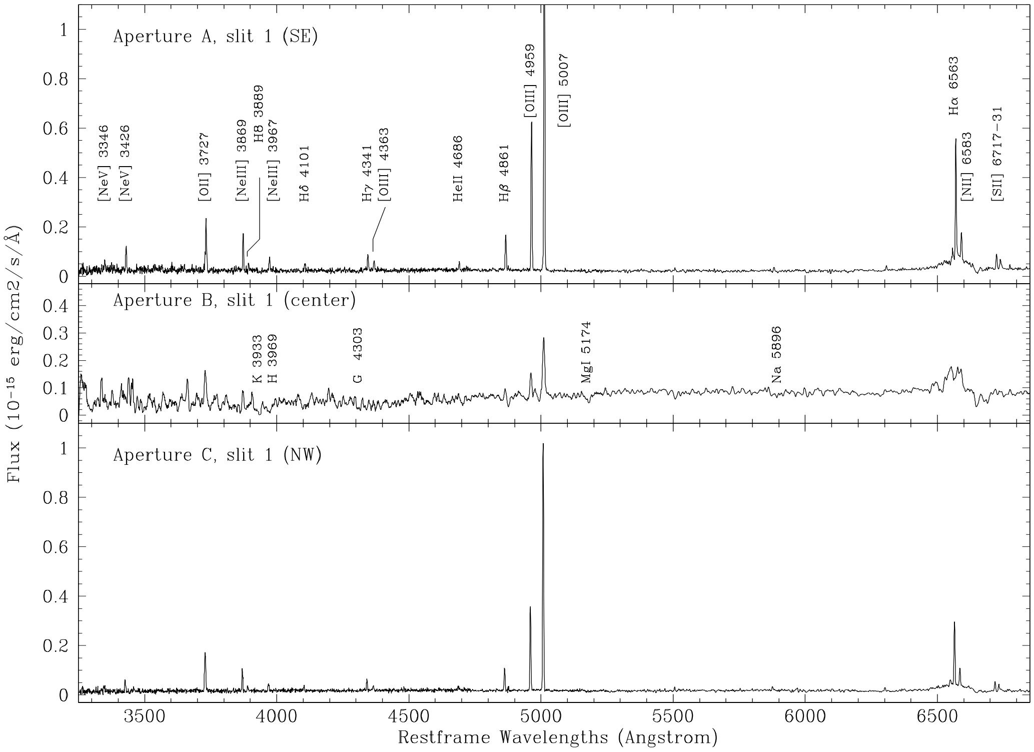

Figure 3.8: Deconvolved spectra of host galaxy, for the three regions A, B, C, defined in Fig. 3.5. The size of the central aperture (B) is 2", while apertures A and C, that correspond to the external parts of the galaxy, are 4" wide.

G600RI, covering the spectral range 4560–7310Å in the rest frame. A single exposure of 1500 seconds was taken. The reduction was carried out in the same way as for the FORS1 observations. However, in this case, the pixel scale is 1.5Å in the spectral direction and 0.252" in the spatial direction. The resolving power is the same as for FORS1, $R \sim 700$.

Figure 3.6 displays the intensity profiles of the (deconvolved) host galaxy of HE 1434-1600 in broad band, along the two slit positions, showing structures with a typical size of a few kpc. These structures are real and play in important role in the interpretation of the spectra, as they are prominent in the emission lines of the host.

The spectroscopic version of the MCS deconvolution algorithm was used to process the 2D spectra, in the same way as for HE 1503+0228 (Courbin et al. 2002 [24]), leading to the decompositions displayed in Figs. 3.7 and 3.8. While the quasar spectra are very similar in both slits, the host shows much stronger and more spatially extended emission lines in *slit 1* than in *slit 2*.

3.4 The ISM of the host

The ISM of the host of HE 1434−1600 is particularly highly ionized. The spectra extracted in Fig. 3.8, e.g., along *slit 1* not only show prominent [OIII] emission lines, but also HeII, [NeIII] and [NeV] emissions. The ionization potentials of these species are respectively 54.6, 40.96 and 97.26 eV, i.e. 1.5 to 3 times higher than the already high ionization potential of [OIII] (35 eV). Line ratios measured at different locations along the slit can be used to understand the physical processes at work in the host of HE 1434−1600. We have measured them for all significant emission lines, relative to Hβ, as is summarized in Table 3.2.

Baldwin et al. (1981 [4]), and Veilleux and Osterbrock (1987 [114]), have introduced the so-called *diagnostic diagrams* in order to distinguish between several plausible ionization processes. Comparing the logarithms of several line ratios, in particular those involving highly ionized species versus less ionized ones, they have been able to separate HII regions from other objects powered by non-thermal processes.

The relevant intensity ratios for the host of HE 1434−1600 are summarized in Table 3.3 and compared to the published sample of AGNs and HII regions of Veilleux & Osterbrock (1987 [114]) in Fig. 3.9. No extinction correction has been applied, as the intensity ratios are for lines at similar wavelengths. Reasonable reddening corrections would only lead to negligible changes.

The most striking result is that, while the measurements for *slit 2* show intermediate ionization levels, all three ratios for the extractions along *slit 1* fall well into the AGN zone, even for regions situated as far as 6 kpc from the central quasar. This empirical comparison of the ionization level of the ISM in the host of HE 1434−1600 with the sample of Veilleux & Osterbrock (1987 [114]) suggests that at least a significant part of the ionization comes from non-thermal processes. In addition, the significant differences between *slit 1* and *slit 2*, as well as between the external apertures (A and C) and internal apertures (B) extractions of the spectra, along *slit 1*, show that the ionization degree is not constant throughout the galaxy. The ionization, if produced by the central QSO, might not be isotropic because

Table 3.2: Line intensities relative to Hβ, in apertures A, B and C of *slit 1*, and integrated in a 6" aperture in *slit 2*, that avoids the companion galaxy G1.

Line	λ()	A	B	C	Slit 2
NeV	(3346)	0.26	–	0.15	–
NeV	(3426)	0.64	–	0.57	–
OII	(3727)	1.46	3.42	2.06	–
NeIII	(3869)	0.94	1.47	0.86	–
H8	(3889)	0.12	–	0.21	–
NeIII	(3967)	0.44	–	0.34	–
Hδ	(4101)	0.27	–	0.17	–
Hγ	(4341)	0.46	–	0.34	–
OIII	(4363)	0.32	–	0.29	–
HeII	(4686)	0.21	–	0.22	–
Hβ	(4861)	1.00	1.00	1.00	1.00
OIII	(4959)	4.08	2.18	3.43	2.44
OIII	(5007)	12.14	6.72	10.12	4.40
Hα	(6563)	4.10	8.95	3.88	3.38
NII	(6583)	1.52	6.32	1.53	1.29
SII	(6717)	0.44	0.53	0.41	0.34
SII	(6731)	0.37	0.34	0.37	0.36

Table 3.3: Intensity ratios in apertures A, B and C of *slit 1* and for *slit 2* (s2).

Ratio	A	B	C	s2
log ([OIII]λ5007)/(Hβ λ4861)	1.1	0.8	1.0	0.4
log ([OII]λ3727)/([OIII]λ5007)	-0.9	-0.3	-0.7	–
log ([NII]λ6583)/(Hα λ6563)	-0.4	-0.2	-0.4	-0.4

of shadowing effects on UV radiation from the nucleus. However, it is more likely that density variations in the gas clouds give rise to different ionization degrees, as suggested by Stockton et al. (2002 [110]).

The strongest narrow line emissions we detect in the host of HE 1434−1600 are located far away from the nucleus, at about 5–6 kpc along the direction of *slit 1*. The spectrum obtained through *slit 2* does not show such strong emission lines far away from the nucleus. Making the analogy with Seyfert galaxies that display radio jets may be relevant. In some of these galaxies, ionized gas is detected as far as several kiloparsecs away from the center. Evans et al. (1999 [32]), Wilson et al. (1994 [118]), Fosbury et al. (1984 [37]), Tadhunter & Tsvetanov (1989 [111]) argue that the high level of ionization is due both to the UV radiation from the nucleus and to shock induced ionization by the radio jet. A more recent example of shock induced ionization is presented in Morganti et al. (2003 [91]), who observed the Seyfert galaxy IC 5063. Thanks to the high spatial resolution of their radio observation, the authors identify a radio jet, exactly overimposed on ionization "hot spot"

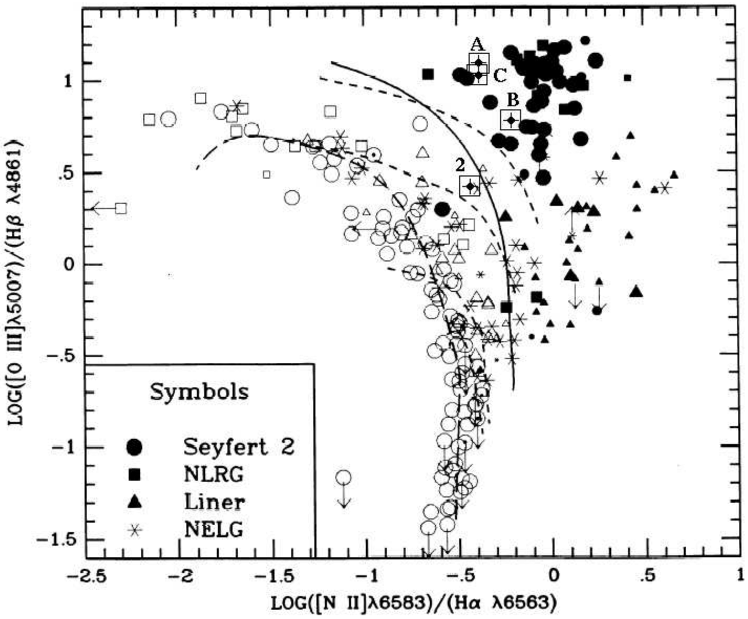

Figure 3.9: Diagnostic diagram from Veilleux & Osterbrock (1987 [114]), where the measurements for different regions of the host of HE 1434−1600 have been overplotted. Four points are available, for apertures A, B, C of *slit 1* and for *slit 2*. They are represented as crosses with associated 1σ error box. Open symbols, following Veilleux & Osterbrock, represent typical HII regions. Black symbols are active galaxies. All measurements of Veilleux & Osterbrock include the nucleus and the host of the objects.

seen in the optical spectrum of the galaxy, e.g., in [OIII].

In our case, the low resolution radio map of Fig. 3.4 shows radio jets oriented N-S, i.e. nearly exactly in between *slit 1* and *slit 2*. If the emission is induced by a shock, and if the shock is along the direction of the radio jet, one would thus expect similar contributions in both slits, in sharp contrast with the observations. VLA or VLBI observations of HE 1434−1600 would help to clarify which influence, if any, the radio jet has on this high ionization.

Extended Emission Line Regions (EELR) are also found in RLQ (Boroson et al. 1985 [10]), that have strong [OIII](5007Å) and other highly ionized emissions, no FeII in their central part (i.e., the quasar spectrum), extended radio lobes, and steep radio spectra. HE 1434−1600 displays these characteristics, except for the last feature for which we lack information. EELR are often spatially unrelated with interstellar emissions, but scales involved for the EELR are systematically larger (around 70–80 kpc) than ours ($<$ 10 kpc). In the studies of Stockton et al. (2002 [110]) and Wilman et al. (2000 [117]), assumption is made that direct radiation from the central AGN is the source of ionization, while the source of gas is thought to be recent interaction or merger. This scenario explains why EELR are not found in all RLQ. The link between radio jets and EELR however remains unclear. EELR where at least two different ionization levels coexist can be explained by density

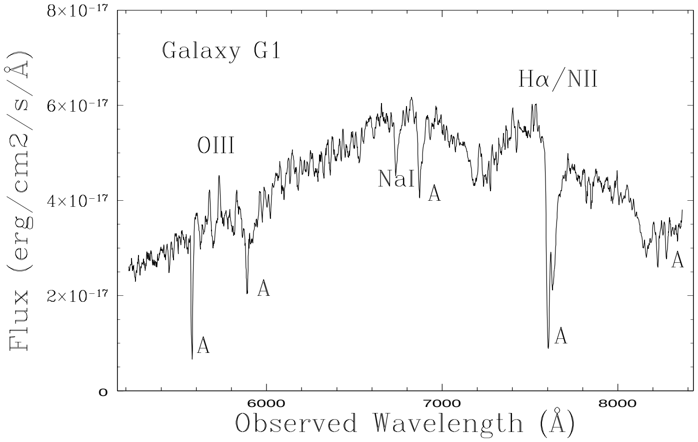

Figure 3.10: Integrated spectrum of companion galaxy G1 (see Fig. 3.5). One strong absorption feature is detected: the sodium NaI(5896Å) line. All other absorptions are tellurics (labeled "A" on the figure). The emission lines visible here are extended emissions of the host of HE 1434−1600, that are contaminating the spectrum of G1.

variations (Stockton et al. 2002 [110]). This seems to be the case for HE 1434−1600. Whether or not a shock induced ionization exists, direct ionization by the high energy radiation from the AGN, typical in EELR, even in regions as far as 6 kpc from the nucleus, is sufficient to explain the spectral features of the present object.

3.5 Redshift and environment

3.5.1 HE 1434−1600

Measuring the redshift of HE 1434−1600 on all available emission lines leads to slightly different estimates when using the central quasar or its host galaxy. We measure $z = 0.1448 \pm 0.0001$ for the host only, and $z = 0.1443 \pm 0.0001$ for the quasar only ($\Delta v = 150$ km s^{-1}), or a mean redshift of $z = 0.1445 \pm 0.0003$. The measurement done on the host's spectrum is for the center of the galaxy, hence not affected by rotation, if any. However, if the velocity field observed for the gas (see next section) is due to gas inflow/outflow due to merger activity, this value might be biased.

3.5.2 Environment

Redshifts were also determined for 5 other objects in the vicinity of HE 1434−1600, indicated in Fig. 3.2. One of them is galaxy G1, located 4" away from HE 1434−1600 and present only in *slit 2*. The redshift measurement is based on the identification of the sodium absorption line NaI(5896Å). The apparent emission lines visible on this spectrum are only due to contamination by the extended host galaxy of HE 1434−1600. The spectrum of G1

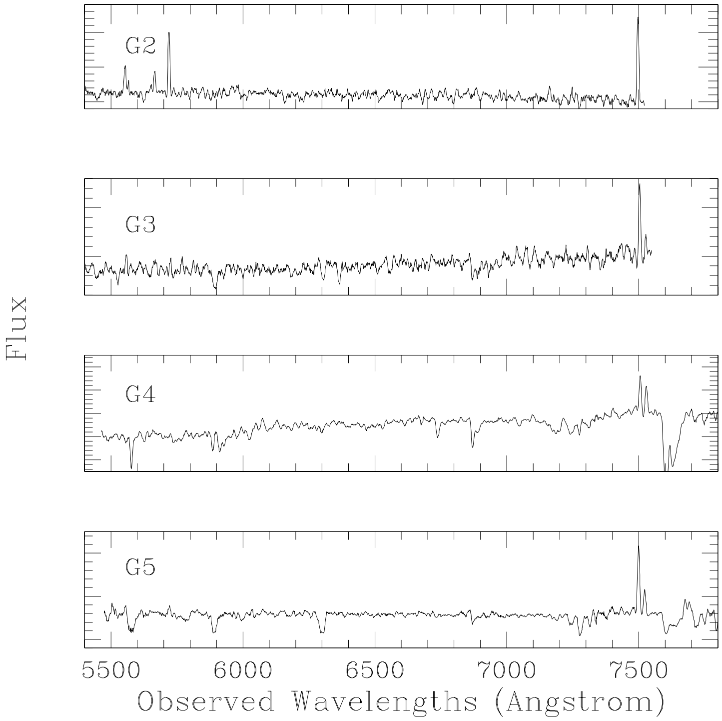

Figure 3.11: Flux calibrated spectra of 4 neighbours of HE 1434−1600. All show clear Hα and [NII] emissions. G2 and G3 show the [OIII] and Hβ emission lines as well.

Table 3.4: Redshifts of the brightest galaxies in the field of view of HE 1434−1600. Each galaxy is indicated in Fig. 3.2. The coordinates and velocities are relative to the HE 1434−1600.

Galaxy	x(")	y (")	Redshift	Velocity (km s^{-1})
HE 1434−1600	+0.0	+0.0	0.1443	0
G1(companion)	+2.6	−3.0	0.1428	−450
G2	−25.0	−38.4	0.1426	−526
G3	−54.0	−63.4	0.1436	−210
G4	−9.2	−63.0	0.1437	−180
G5	−110.0	+52.0	0.1429	−420

is presented in Fig. 3.10. Measuring the redshift directly from NaI and other weaker Fe lines or by cross-correlating the spectrum with that of a template spectrum of an elliptical galaxy yields $z = 0.1428 \pm 0.0003$.

The redshifts of four other galaxies, picked-up randomly because they were in the unvignetted area of the CCD chip (Fig. 3.11), were also measured, mainly based on the Hα emission line (Table 3.4). Galaxy G4 even shows rotation, with a prospected rotation velocity of $\mathrm{v_{rot}} \sim 80$ km s^{-1}, measured 1",4 from the center of the galaxy, in the flat part of the rotation curve. G1, the closest companion to HE 1434−1600, is the only galaxy out of the 5 known companions that does not show emission lines.

With at least 6 objects at almost the same redshift, HE 1434−1600 is part of a small group of galaxies whose velocity dispersion is $\sigma_v = 197$ km s^{-1}, with a 95 percent confidence interval of 123 km s^{-1} $\leq \sigma_v \leq$ 480 km s^{-1}. Considering the group as an isothermal sphere with a mean radius of r = 100" (Binney and Tremaine 1987 [7]), its mass is, $M_{\mathrm{group}} \sim 4 \cdot 10^{12}$ M$_{\odot}$. This places it among the loosest groups of galaxies, e.g., when compared with the groups found in the Las Campanas Redshift Survey (Heinämäki et al. 2003 [43]), who find group masses in the range $M = 10^{12}$–10^{15} M$_{\odot}$.

3.6 Dynamics of the host galaxy

Because our observational strategy is to take the spectra "on-axis" rather than a few arcseconds away from the AGN center, the dynamical information about the host galaxy is not lost. The signal-to-noise ratio of the data is sufficient to perform quantitative measurement of the stellar and gas velocity fields.

3.6.1 Stellar dynamics

The Calcium CaII absorption doublet is detected in the spectrum obtained in April 2000. It is outside the accessible wavelength range in the observations taken in May 2002. Because of the low signal-to-noise in these lines, we can not perform a full extraction of the stellar velocity field. We can however get significant hints about the stellar rotation/motion, by dividing the galaxy into two parts along the spatial direction, and by cross-correlating them. Two spatial extractions were done along *slit 1*. The light of the quasar host was integrated in two "boxes" lying between 0",8 and 2",8 away from the center of the galaxy. Their cross-correlation, displayed in Fig. 3.12 shows a sharp peak centered at $v = 2 \pm 10$ km s^{-1}. Similar results are found on the *slit 2* spectrum. We can therefore conclude that stars do not display a global rotation in the host of HE 1434−1600.

3.6.2 Gas dynamics

Contrary to the absorption lines, an obvious velocity field is seen in the emission lines of the host galaxy. An example of emission lines is shown in Fig. 3.14, where the continuum of the host galaxy has been removed. The gas seen through the two slit orientations behaves

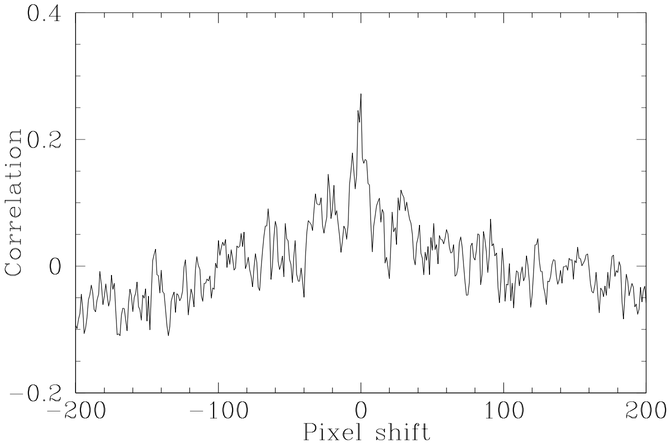

Figure 3.12: Correlation function of the two extracted regions of the host's spectrum (see text) along *slit 1*. Only the spectral regions with no emission lines are considered, i.e., from 5246 Å to 5706 Å, in the rest frame. The centroid of the correlation peak is located at 0.03 ± 0.1 pixels, which translates into $v = 2 \pm 10$ km s^{-1}, hence confirming that the stars in the host are not affected by any circular motion.

differently. While *slit 1* reveals the gas motion, the emission lines seen along *slit 2* remain perfectly straight.

The spatial profiles in the lines in Fig. 3.14 show, as said previously, that the gas is not distributed uniformly in the galaxy. In particular, the [OIII] emission line is composed of two bright spots located 2",2 and 2",4 away from the nucleus, and that correspond perfectly to the two bright spots already seen in the spatial profiles of Fig. 3.6. They are not deconvolution artifacts. In fact, they are detectable in the original data without subtracting the quasar (Fig. 3.13).

The velocity curves have been determined from several emission lines, extracted from reduced spectra to avoid artifacts deconvolution could bring, specially near the nucleus. The extraction method is described in Courbin et al. (2002 [24]). These curves are displayed in Fig. 3.15. While there is no velocity field along *slit 2*, the curve for *slit 1* is very sharp in the central kiloparsec, and almost flat in the outer parts of the galaxy. This is hard to reconcile with models involving pure rotation, but we nevertheless attempted to follow the same approach as in Courbin et al. (2002 [24]), for the spiral host of HE 1503+0228.

A mass model is assumed for the galaxy, including a rotating disk, a central point mass and a dark matter halo. This mass model is then used to predict the velocity of the galaxy at a given point of the slit, taking into account the inclination of the disk and convolution by the seeing profile, using the known spectrum of the PSF. Many different initial conditions were used when fitting the model, with no successful solution. In fact, we found no way to model simultaneously the sharp central velocity trough, that requires a very large central mass, and the flat external parts, that require large amounts of dark matter, while keeping the various parameters at reasonable values.

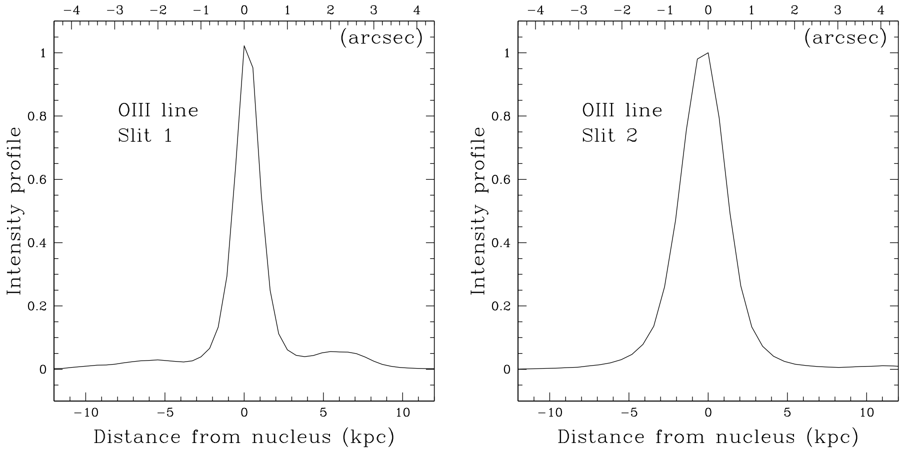

Figure 3.13: Spatial profile of the [OIII] emission line for *slit 1* and *slit 2* prior to any host/nucleus decomposition. The dip in intensity profile through *slit 1*, 3" away from the quasar, and the two "hot spots" of Fig. 3.14 are already visible in this raw undeconvolved intensity profile.

We have thus considered other mass distributions, such as a modified Hubble profile, power-law density profile or isochrone potential (Binney & Tremaine 1987 [7]), all encountering the same difficulty. In the best fits, central masses of the order of $M \sim 10^{10}$ $M_\odot$ are always found. For comparison, the central mass found for HE 1503+0228 was $M \sim 5 \cdot 10^7$ $M_\odot$, three orders of magnitude smaller. Other groups have estimated the central masses in galaxies, most of the time for isolated ellipticals like in the SAURON survey (e.g., NGC 3377, Copin et al. 2003 [23]), more massive ellipticals (M87, Macchetto et al. 1997 [74], Cen A, Marconi et al. 2001 [80]), or Seyfert galaxies (NGC 4041, Marconi et al. 2003 [79]; Mrk 110, Kollatschny 2003 [65]). The masses they find, either using the black hole central velocity dispersion relation, or direct dynamical modeling, is always in the range $M = 10^7$–10^8 $M_\odot$, with some supermassive black holes reaching up to 10^9 $M_\odot$, e.g., in the Seyfert NGC 5252 (Macchetto 2003 [73]). The central mass in HE 1434−1600, assuming gas rotation, is still an order of magnitude above the most massive black holes found in other galaxies.

The central mass can be estimated independently using the known correlation between $R_{\rm BLR}$, the radius of the Broad Line Region (BLR), and the monochromatic AGN continuum luminosity at 5100 Å (Kaspi et al. 2000 [54]). This luminosity-based $R_{\rm BLR}$ is combined with a measurement of the BLR velocity extracted from the Full Width at Half Maximum of the Hβ emission line. Assuming that the motion in the BLR in AGN is virialized, one can use the simple Keplerian relation

$$M_{\rm BH} = R_{\rm BLR}\, v_{\rm BLR}^2\, G^{-1}, \tag{3.1}$$

to estimate the mass of the central black hole. In the case of HE 1434−1600 we find $M_{\rm BH} \sim 3.6\ 10^8$ $M_\odot$. Again, this is two orders of magnitude lower than obtained with our galaxy mass models.

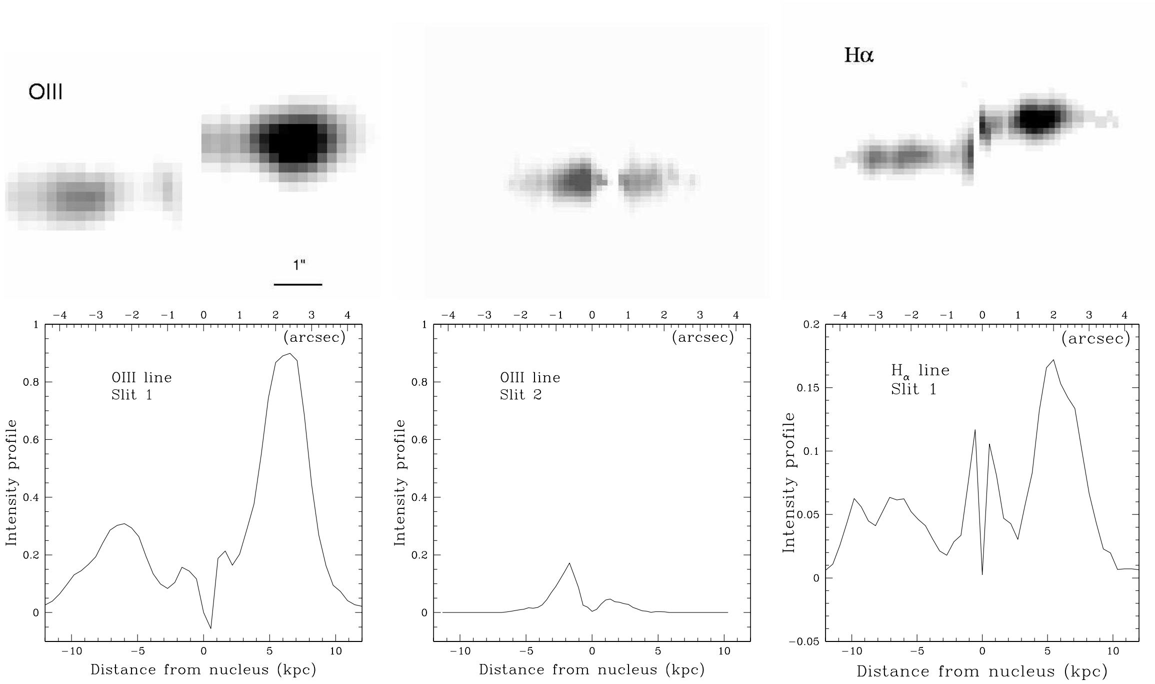

Figure 3.14: *Top:* zoom on the [OIII] (5007Å) emission line in *slit 1* (left), in *slit 2* (middle). The Hα emission lines is displayed on the right panel. The spatial direction is horizontal and the wavelength direction vertical. Both the quasar spectrum and the continuum of the host galaxy have been subtracted. The sharp structures in the very center (central kpc) of the galaxy corresponds to oversubtraction of the quasar. The gas motion is striking in *slit 1*, while the stars are not showing any motion in this same slit position. No gas velocity field is detected for *slit 2*. *Bottom:* Corresponding intensity profiles.

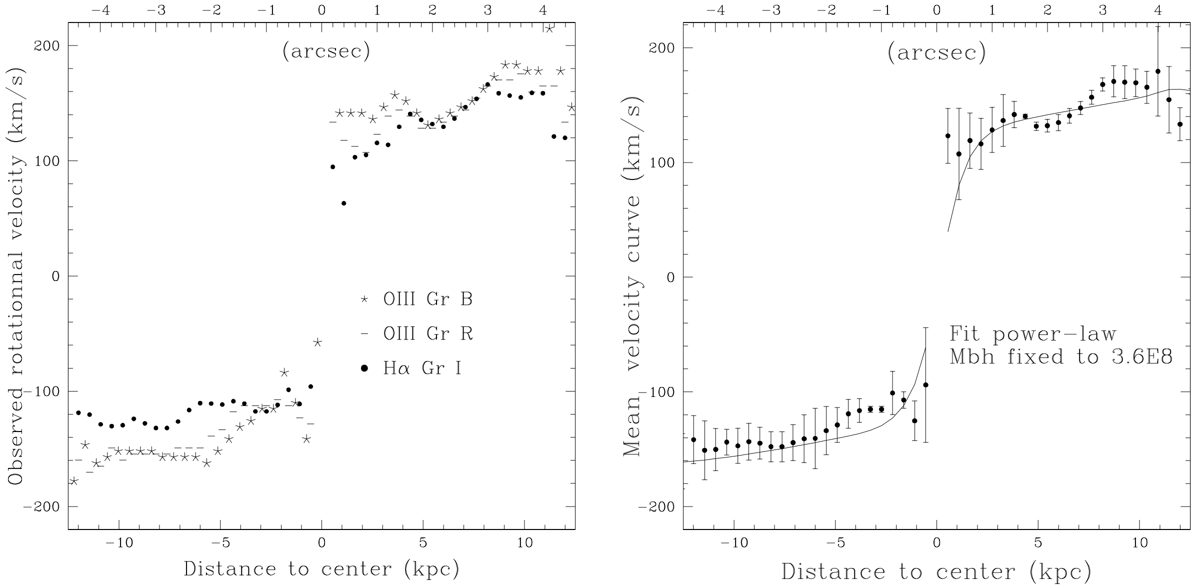

Figure 3.15: *Left:* velocity curves obtained for the [OIII] doublet and for the Hα emission line. *Right:* mean velocity curve. The data points are the mean of the two [OIII] measurement and of the Hα measurement. The error bars correspond to the dispersion between the three curves of the left panel. Our best fit model is overplotted. With a central mass fixed to 3.6 10^8 $M_\odot$, the χ^2 of the fit is acceptable only for model with mass components unrealistically concentrated near the nucleus (see text).

We have tried to fit the velocity curves with models including a central mass fixed at the above value, i.e. $M_{\rm BH} = 3.6\,10^8$ $\mathrm{M}_\odot$. We can obtain rather reasonable fits (see Fig. 3.15), but at the expense of completely unrealistic parameters (e.g., a disk with a huge mass density confined to a few parsecs). Indeed, the lower $M_{\rm BH}$ is always compensated by other mass components which become concentrated near the nucleus. Nevertheless, all models lead to a total mass of $\sim 9.2\,10^{10}$ $\mathrm{M}_\odot$, within a radius of 10 kpc.

3.7 Discussion – Conclusions

In the framework of a comprehensive spectroscopic study of quasar host galaxies, we have obtained VLT optical observations of the $z = 0.144$ quasar HE 1434−1600, that retained our attention and triggered follow-up observations. Two slit orientations were used (see Fig. 3.5) and the data were spatially deconvolved, resulting in spectra of the host galaxy decontaminated from the light of the central quasar.

We found that the host galaxy of HE 1434−1600 is a rather peculiar object. We observed that :

1. Optical and near-IR imaging of HE 1434−1600 reveals an elliptical morphology, with colors bluer than inactive elliptical galaxies, indicating a contribution of a young stellar population.

2. The galaxy harbours a bright quasar, whose radio loudness index places it at the limit between radio quiet and radio loud. Extended lobes are seen in the radio up to 5' away from the quasar.

3. The ISM of the host is heterogeneous and highly ionized by the central AGN. Ionization triggered by the radio jet cannot be excluded.

4. While the gas emission lines observed through *slit 1* all show a clear velocity field, the stellar absorption lines do not display any sign of rotation, in accordance with the observed elliptical morphology.

5. Neither the stars nor the gas are affected by a velocity field in the *slit 2* observations, almost perpendicular to *slit 1*.

6. No mass model involving rotation of a gas disk fit the gas velocity of *slit 1* properly unless invoking extremely high central masses for the galaxy, an order of magnitude above that of the most massive black holes known ($> 10^9$ $\mathrm{M}_\odot$).

7. HE 1434−1600 is part of a small group with $\sigma_v \sim 197$ km s^{-1} or $\mathrm{M}_{\rm group} \sim 4 \cdot 10^{12}$ $\mathrm{M}_\odot$.

8. The closest companion G1, of HE 1434−1600 is located 4" away from it, with a velocity difference of 450 km s^{-1}. No trace of gas emission is detected.

To explain the main characteristics of the host galaxy of HE 1434−1600 and environment, we propose the following interpretation.

The motion of the gas, as deduced from the emission lines, cannot be interpreted as Keplerian motion in any reasonable mass model. It must be affected by some interaction with an intervening object. At least two possibilities arise: (1) the dynamics of the gas is modified by interaction with matter and/or radiation from the AGN or (2) it has been affected by a recent collision with the neighbouring galaxy G1. As the central AGN of HE 1434−1600 does not appear very different from other quasars in the sample, which display relatively mundane host galaxies in which the ISM does not show obvious signs of disturbance by the central AGN (e.g., HE 1503+0228, Courbin et al. 2002 [24]), we consider the second explanation as most likely.

We propose that the ISM of both galaxies (host and G1) has been swept out during a recent close interaction and has had insufficient time to relax. Using the velocity dispersion in the group as an estimate of the relative velocity of the two interacting galaxies, we estimate that it would have taken $\sim 3 \times 10^7$ years for the two galaxies to reach their present projected separation. This is much smaller than the typical relaxation time of a merger ($\sim 10^9$ years, Wright 1990 [121], Barnes 1989 [5]).

Now, we need to explain why, although quasars of similar luminosities (e.g., HE 1503 +0228) seem unable to ionize the interstellar gas outside the central AGN region, the central engine of HE 1434−1600 is able to strongly excite and ionize the ISM as far as 5 to 6 kiloparsec. If the collision with galaxy G1 has been strong enough to remove the gas out of the host galaxy, even in the most central regions, nothing is left to absorb the ionizing radiation of the quasar which is then able to propagate freely to large distances, until it hits the gas clouds moving far away from the center and strongly ionizes them.

In our opinion, a recent collision with galaxy G1 is thus the key factor allowing one to explain both the peculiar motion of the gas and its high degree of ionization by the central quasar, even very far away from the source of radiation.

Acknowledgements The authors would like to thank Françoise Combes and Raffaela Morganti for useful discussions and suggestions. The NASA Extragalactic Database (NED) has been used for this research. Géraldine Letawe is a teaching assistant supported by the University of Liège, (Belgium). Frédéric Courbin acknowledges financial support from the European Commission through Marie Curie grant MCFI-2001-0242. The Pôle d'Attraction Interuniversitaire, P5/36 (PPS Science Policy, Belgium) is also thanked.

Chapitre 4

Découverte d'un quasar brillant sans galaxie massive apparente

L'article suivant illustre la belle complémentarité entre la spectroscopie de fente qu'on peut réaliser du sol et l'imagerie à haute résolution qu'il est possible d'obtenir avec le téléscope spatial Hubble (HST). Il met en lumière un objet particulièrement intéressant puisque relativement difficile à comprendre.

Le spectre déconvolué de HE 0450-2958 est difficile à interpréter seul. A première vue, on pourrait en dire que le quasar semble situé en dehors de sa galaxie, baignant uniquement dans un nuage de gaz.

Parallèlement à l'analyse des spectres des quasars et de leurs galaxies, nous avons, fin 2004, commencé à traiter les premières images obtenues avec le HST. Il a fallu adapter le programme de déconvolution aux PSF particulières de l'ACS, instrument employé pour nos observations spatiales. Le choix de HE 0450-2958 s'est rapidement imposé comme exemple test, vu l'énigme que posaient ses spectres.

Les résultats ont été surprenants : pas de trace de galaxie hôte, à part une tâche légèrement décentrée par rapport au quasar, que les spectres nous ont permis d'interpréter comme du gaz fortement ionisé par le noyau actif (appelé “blob” dans l'article), et une galaxie voisine manifestement perturbée par une interaction récente. Nous avons fait des simulations pour pouvoir fixer une limite supérieure en magnitude à la galaxie hôte invisible, qui s'avère être au moins 6 fois trop faible par rapport à ce qu'on attend pour une galaxie qui abrite un tel quasar.

Suite à la parution de cet article dans la revue *Nature* en septembre 2005, plusieurs groupes de chercheurs ont proposé des interprétations à ce phénomène.

- Comme ce système est un émetteur infrarouge intense, découvert par le satellite IRAS (dont la résolution ne permet pas de localiser avec précision la zone d'émission et donc d'attribuer l'émission IR au quasar ou à la galaxie voisine), il contient beaucoup de poussière. Au moment de l'article, nous avions localisé cette poussière dans la galaxie voisine au vu de son décrément de Balmer très important. Il serait cependant possible que la poussière obscurcisse complètement la galaxie hôte elle-même de manière inhomogène, laissant uniquement filtrer la lumière issue de la zone “quasar+blob”.

- Si on suppose qu’il n’y a vraiment pas de galaxie qui abrite le quasar, on peut faire l’hypothèse que ce trou noir actif ait été éjecté lors d’une collision à trois corps ou par “recul” lors de l’émission d’ondes gravitationnelles, par exemple dans la galaxie voisine (Haehnelt et al. 2006 [42], Hoffman et al. 2006 [44]). Ce serait la première observation de ce phénomène attendu par la théorie et les modèles numériques de simulations de collision. Il reste un petit débat quant à la possibilité que le nuage de gaz collé au quasar puisse avoir été éjecté avec lui (sa “Narrow Line Region”) ou soit juste un nuage de gaz *in situ* qui se trouve être illuminé par le quasar. Des observations en rayons X pourraient confirmer ou infirmer la présence d’un ou deux autres trous noirs supermassifs dans la galaxie voisine.
- Merritt et al. (2006 [88]) pensent que HE 0450-2958 est une “Narrow Line Seyfert 1” et que nous avons surestimé la masse du trou noir. Ils s’attendent à ce que sa galaxie hôte soit une spirale relativement faible, justifiant pleinement sa non détection par nos observations sans qu’elle ait rien de particulier. L’aspect “Narrow Line Seyfert 1” est abordé dans le chapitre 5 : ce quasar est loin d’être une Seyfert au vu de sa luminosité, peu d’études des “Narrow Line Quasars” existent et rien ne permet encore d’affirmer que ce type de noyau actif n’apparaît que dans des galaxies spirales ou faibles.
- Une interprétation tout-à-fait différente du système HE 0450-2958, autrement appelée IRAS 04505-2958 est donnée par Lipari et al. (2005 [71]). Ce que nous avons appelé la galaxie compagnonne du quasar est interprété ici comme une importante quantité de matière éjectée du système (un “outflow”). Cet objet rentre dans un ensemble de galaxies actives présentant les mêmes caractéristiques (emission intense en infrarouge, raies nucléaires du FeII, BAL (larges raies d’absorption) et vents galactiques/outflows). Dans leur échantillon, IRAS 04505-2958 est celui qui présente des éjections les plus éloignées du quasar. La classification en BAL se base uniquement sur la présence d’une absorption de largeur moyenne dans la raie CIV du carbone. Il n’est pas fait mention dans cet article de la nature de la galaxie hôte, mis à part la présence de l’éjection massive de matière. De plus la présence d’étoiles de différents âges dans la galaxie, comme observé par Canalizo & Stockton (2001, [18]), est difficilement conciliable avec l’éjection de matière du quasar.

Nous avons quelques observations en attente qui, nous l’espérons, permettront de pouvoir choisir entre l’un ou l’autre de ces scénarios dans les prochains mois :

- avec le VLT et VISIR dans l’infrarouge moyen pour l’obscuration de la galaxie par de la poussière
- avec le VLT et ISAAC dans l’infrarouge proche pour chercher des traces d’étoiles plus vieilles
- avec des spectres FORS au VLT dans le visible, posés plus profondément pour faire ressortir des traces éventuelles de continuum faible
- avec NICMOS sur le HST dans l’infrarouge proche pour détecter à meilleure résolution une galaxie normale ou qui aurait partiellement été obscurcie par de la poussière

dans le visible (demande d'observation soumise en janvier 2006)
- avec Chandra en rayons X pour chercher la trace d'autres trous noirs au niveau de la galaxie voisine, pour confirmer ou infirmer le scénario d'éjection (demande d'observation soumise en mars 2006).

Discovery of a bright quasar without a massive host galaxy

P. Magain[1], G. Letawe[1], F. Courbin[2], P. Jablonka [2,3,4],
K. Jahnke[5], G. Meylan[2], L. Wisotzki[5]

1. Institut d'Astrophysique et de Géophysique, Université de Liège, Allée du 6 Août, 17, Bat. B5C, Liège 1, Belgium
2. Laboratoire d'Astrophysique, Ecole Polytechnique Fédérale de Lausanne (EPFL), Observatoire, CH-1290 Sauverny, Switzerland
3. Observatoire de l'Université de Genève, CH-1290 Sauverny, Switzerland
4. On leave from GEPI, Observatoire de Paris, Place Jules Janssen, F-92915 Meudon Cedex, France
5. Astrophysikalisches Institut Potsdam, An der Sternwarte 16, 14482, Potsdam, Germany

Published in Nature, 2005, v.437, Issue 7057, pp. 381-384.

Quasars are thought to be powered by the infall of matter onto a supermassive black hole at the centre of massive galaxies (Richstone et al. 1998 [99], Dunlop et al. 2003 [30]. As the optical luminosity of quasars exceeds that of their host galaxy, disentangling the two components can be difficult. This led in the 1990's to the controversial claim of the discovery of 'naked' quasars (Bahcall et al. 1994 [3], Boyce et al. 1999 [13], Disney et al. 1995 [29], Hutchings 1995 [46], Bahcall et al. 1997 [2]). Since then, the connection between quasars and galaxies has been well established (McLure et al. 1999 [87]). Here we report on the observation of a quasar lying at the edge of a gas cloud, whose size is comparable to that of a small galaxy, but whose spectrum shows no evidence for stars. The gas cloud is excited by the quasar itself. If a host galaxy is present, it is at least six times fainter than would normally be expected (McLure et al. 1999 [87], Floyd et al. 2004 [36]) for such a bright quasar. The quasar is interacting dynamically with a neighbouring galaxy - which matter might be feeding the black hole.

4.1 Observations and analyses

HE0450-2958 is a bright quasar (M_V = -25.8) at a redshift of z = 0.285, associated with powerful infrared (IR) emission (de Grijp et al. 1987 [27], Low et al. 1988 [72]). Early imaging revealed a quasar-galaxy pair with signs of violent dynamical interaction (Boyce et al. 1996 [12]), and a starburst in the galaxy. A collision between the two systems about 10^8 years ago probably triggered both the starburst and the quasar activity (Canalizo & Stockton 2001 [18]).

We use the MCS deconvolution technique (Magain et al. 1998 [75], Courbin et al. 2000 [25] and 2002 [24], Letawe et al. 2004 [69]) on our new HST images, in order to explore the vicinity of the quasar (Fig 4.1). These images confirm the strongly irregular shape of the companion galaxy, indicative of gravitational interaction with the quasar. However, the most interesting finding is that no significant host galaxy centered on the quasar position is found - we quantify this statement below. The most prominent feature is a diffuse albeit compact component, just beside the quasar (and to which we shall refer as "the blob" in the following), with a possible very faint extension around the quasar. If interpreted as an image of the host galaxy, we would have the surprising result that the quasar does not reside inside its host, but just next to it. Moreover, with a diameter of no more than 2500 parsec (pc), the blob is comparable in size to M32, the dwarf companion of the Andromeda galaxy M31, but is about 200 times brighter than M32, with an absolute magnitude of M_V = -22.

Figure 4.2 shows a portion of the spatially deconvolved two-dimensional optical spectrum. The full one-dimensional spectra of the quasar, blob, and companion galaxy are displayed on Fig. 4.3. While the spectrum of the galaxy shows a strong stellar continuum, with low excitation emission lines typical of gas in star-forming regions, the spectrum of the blob does not show any hint of a continuum. It rather consists of a series of emission lines whose intensity ratios indicate excitation by a much harder spectrum than a stellar one. The absence of a continuum component yields the second surprising result: where we would expect stellar light from a host galaxy, we only see an off-centre structure consisting essentially of gas excited by the quasar radiation. This non-detection of a significant host galaxy around HE0450-2958 may mean that either it is too compact to be separated from the quasar, or that its surface brightness is below our detection limit. These possibilities are investigated by adding to the HST images an artificial elliptical galaxy centered on the quasar position and properly convolved with the HST point spread function (PSF). If we adopt an absolute magnitude of M_V = -23, corresponding to the typical host galaxies expected for such a quasar luminosity (Floyd et al. 2004 [36]), and if we decrease its size till it cannot be detected anymore in the deconvolved image, we obtain an upper limit of 100 pc for the half-light radius $R_{1/2}$. This is much too small for a quasar host galaxy, for which $R_{1/2}$ typically ranges between 2000 and 15000 pc (Floyd et al. 2004 [36]).

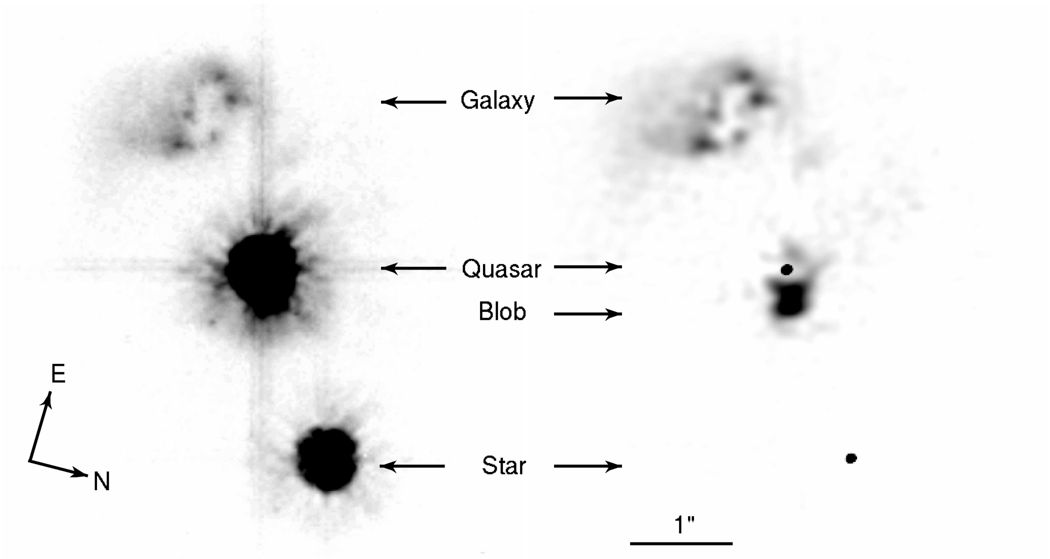

Figure 4.1: HST images of the quasar and its immediate surrounding. The original HST image of HE0450-2958 is shown on the left side, while the result of the deconvolution with the MCS algorithm is displayed on the right side. The images were obtained on October 1st, 2004 with the High Resolution Channel (HRC) of the Advanced Camera for Surveys (ACS) onboard HST. Six dithered exposures of the quasar field were taken through the F606W filter, three short ones (30 s) and three longer ones (330 s). In contrast with previous HST observations of quasar host galaxies, a significant fraction of the observing time was devoted to the PSF characterization, by observing during the same orbit both the nearest bright star and the quasar, always placing the star at the same location as the quasar on the detector. This observational strategy ensures that the PSF temporal and spatial variations are minimized. Because of the extended wings of the PSF, the blob of gas just beside the quasar can only be seen after careful processing of the images. No other related feature is found in the vicinity of the quasar-galaxy pair. From the observed fluxes, and applying the appropriate distance and spectral corrections, we obtain absolute magnitudes of M_V = -22 for the blob and M_V = -23 for the companion galaxy. After correction for dust extinction, the latter amounts to M_V = -26. All magnitudes mentioned in the text have been similarly corrected, and computed with $H_0 = 65$ km s^{-1} Mpc^{-1}.

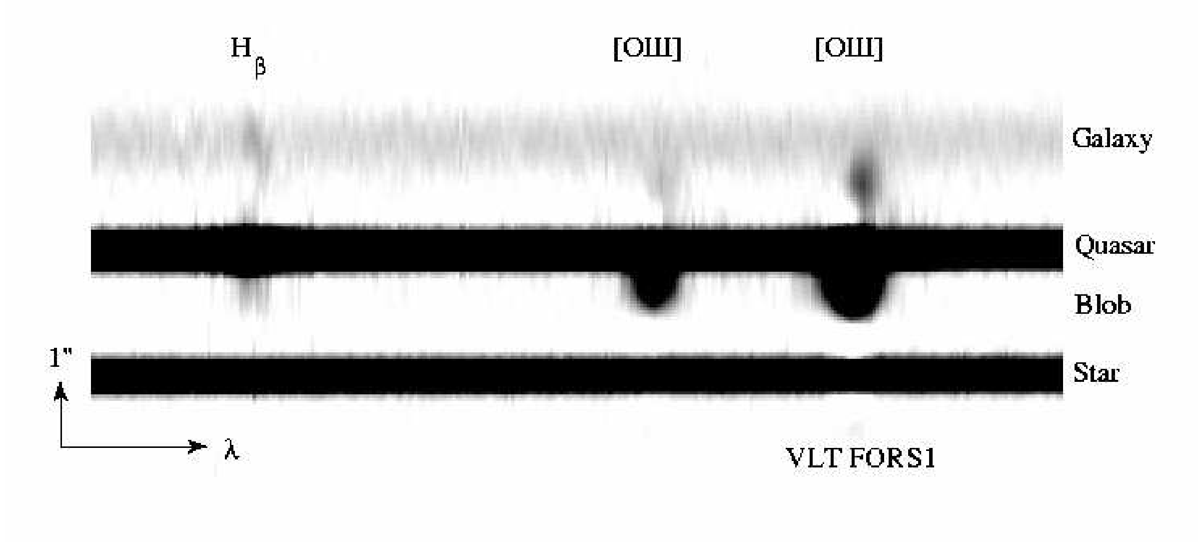

Figure 4.2: Two-dimensional VLT spectra of the quasar and neighbouring objects. These long slit spectra have been deconvolved in the spatial direction, in order to separate the different objects. The spectral direction is horizontal, while the spatial direction is vertical. The emission lines just below the quasar spectrum are, from left to right, the hydrogen Hβ (486.1 nm) and the oxygen [O III] (495.9/500.7 nm) doublet corresponding to the blob of ionized gas. Weaker emission lines are also detected in between the quasar and the companion galaxy, showing that some ionized gas is also present there. The vertical arrow gives the spatial scale (1"). Our spectroscopic observations of HE0450-2958 were carried out in a new way, taking advantage of the multi-slit mode of the VLT/FORS1 to record simultaneously the spectra of the quasar and of its host galaxy, as well as the spectra of nearby isolated stars needed for subsequent determination of the PSF. The main slit covers not only the quasar, but also the companion galaxy and a nearby object identified as a foreground star, which is used together with the isolated stars for an accurate determination of the PSF.

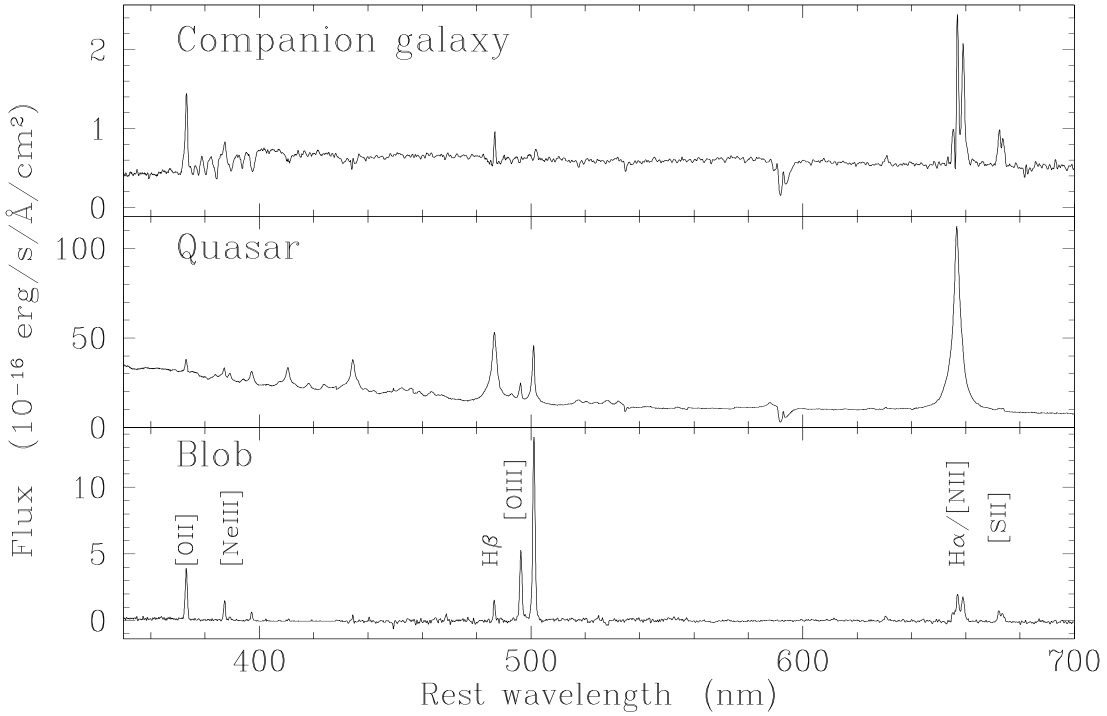

Figure 4.3: Spectra of the companion galaxy, quasar, and blob. Top: Integrated one-dimensional spectrum of the companion galaxy. Middle: Spectrum of the quasar. Bottom: spectrum of the blob. Note the absence of continuum light in the blob, which would be due to stars, and the emission line ratios (e.g. [O III]/Hβ) indicating ionization by the quasar radiation. The Balmer decrement (Hα/Hβ intensity ratio) indicates that, contrary to the quasar and blob, the companion galaxy is heavily reddened by dust. It is therefore the companion galaxy, and not the quasar, which is the strong IR emitter detected by the IRAS satellite (de Grijp et al. 1987 [27]). This also indicates that absorption of light by dust cannot explain the non-detection of a host galaxy around the quasar.

4.2 Host luminosity upper limits

To set an upper limit on the surface brightness of the putative host, we fix $R_{1/2}$ to 10 kpc, well representative of host galaxies of luminous quasars (Floyd et al. 2004 [36]), and we progressively decrease the luminosity until it falls below our detection limit. This gives an upper limit for the stellar population around the quasar, that we discuss below. The absence of any detectable extended structure is confirmed by applying standard PSF subtraction techniques. The sensitivity of our results to the presence of a host galaxy is illustrated by Fig. 4.4, which shows that, if a typical host galaxy were present around the quasar, we would indeed detect it.

The mass of the central black hole of a quasar of absolute magnitude M_V = -25.8 is predicted to be about 8.10^8 solar masses for an accretion at half the Eddington Limit with a 10% radiative efficiency. This value is in fair agreement with the estimate derived from the width of the Hβ line (Kaspi et al. 2000 [54]). Using the scaling relations recently established between the black hole mass and the host galaxy spheroid luminosity (McLure et al. 2002 [86]), we can compare the predicted magnitude of the host galaxy with our upper limit. For this purpose, we have to make assumptions about the stellar population in the host galaxy. We consider two extreme cases. On one hand, we assume a smooth spheroid of old stars (10 billion years). The predicted magnitude (Bruzual & Charlot 2003, [15]) of the host is then M_V = -23.0 and our upper limit M_V = -21.2, i.e. five times fainter than expected. On the other hand, in the case of young stars, of an age similar to the starburst population in the companion galaxy (130 million years), the predicted magnitude amounts to M_V = -23.5 and our upper limit becomes M_V = -20.5, i.e., 16 times fainter. Any reasonable estimate should lie between these two extremes. As a complementary approach, avoiding uncertainties related to the black hole mass estimates, we compare directly our upper limits to the magnitudes measured for typical quasar host galaxies. We use the HST sample of 17 quasar host galaxies from Floyd et al. (2004 [36]). After conversion of their values to our cosmology (H_0 = 65 km s^{-1} Mpc^{-1}), these quasars have absolute magnitudes in the range $-26.8 < M_V < -23.2$, with an average of M_V = -24.3, somewhat fainter than the present quasar (M_V = -25.8). A straight line fitting to the host-versus quasar- magnitude relation gives an expected host magnitude of M_V = -23.2 for a quasar of M_V = -25.8, and the scatter around the mean relation is $\sigma = 0.54$ (Fig. 4.5). Note that this value of M_V = -23.2 nicely falls between the two extreme cases considered in the previous paragraph. Our upper limit is between 6 and 12 times fainter than the expected value, depending on the assumed stellar age. In the most conservative case (i.e. a smooth spheroidal distribution of old stars), the deviation from the average relation is 3.7 σ, which is highly significant. Moreover, we should point out that such a conservative case is not really expected for galaxies involved in collisions, which generally display a distorted geometry (e.g. tidal tails) and active star formation. Taking these effects into account would make the deviation even more significant. Finally, the hydrogen emission line ratios, which indicate a strong reddening of the companion galaxy, are close to the theoretically expected values in the quasar and blob. This suggests that obscuration by dust is very limited in the vicinity of the quasar and cannot explain the non-detection of

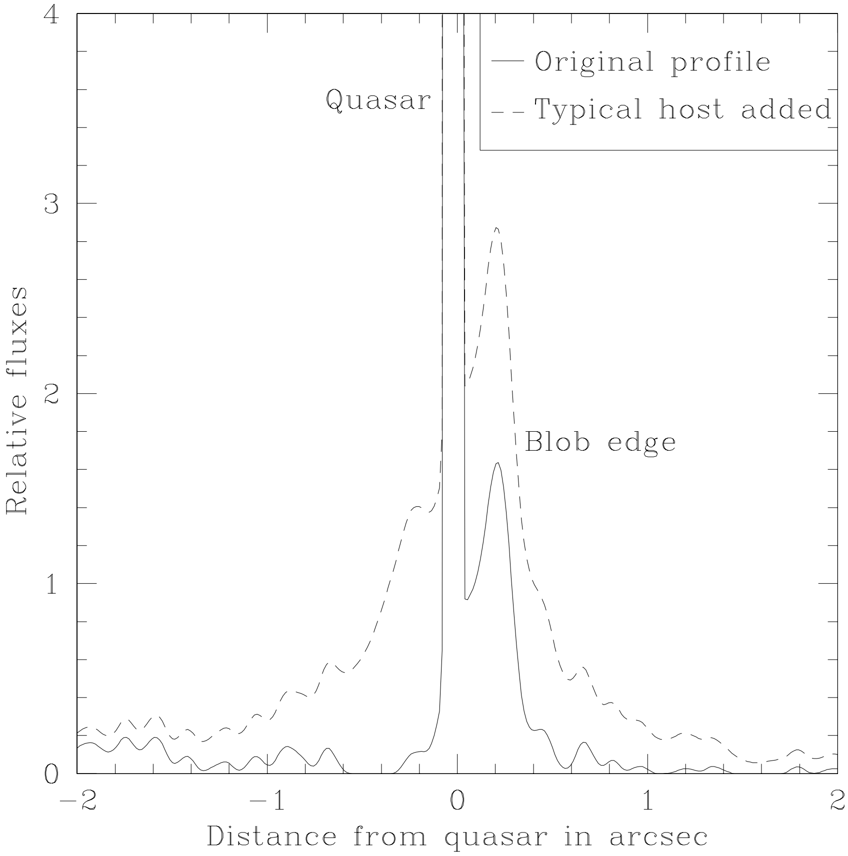

Figure 4.4: Intensity profile through the quasar position. Solid line: N-S profile of the deconvolved image. The peak just on the right of the quasar corresponds to the edge of the blob. Dashed line: corresponding profile of the deconvolved image after an elliptical host (de Vaucouleurs profile) with $R_{1/2}$ = 10 kpc and M_V = -23 has been artificially added to the original images. The comparison of the two profiles shows that any host galaxy with the expected luminosity would be easily detected.

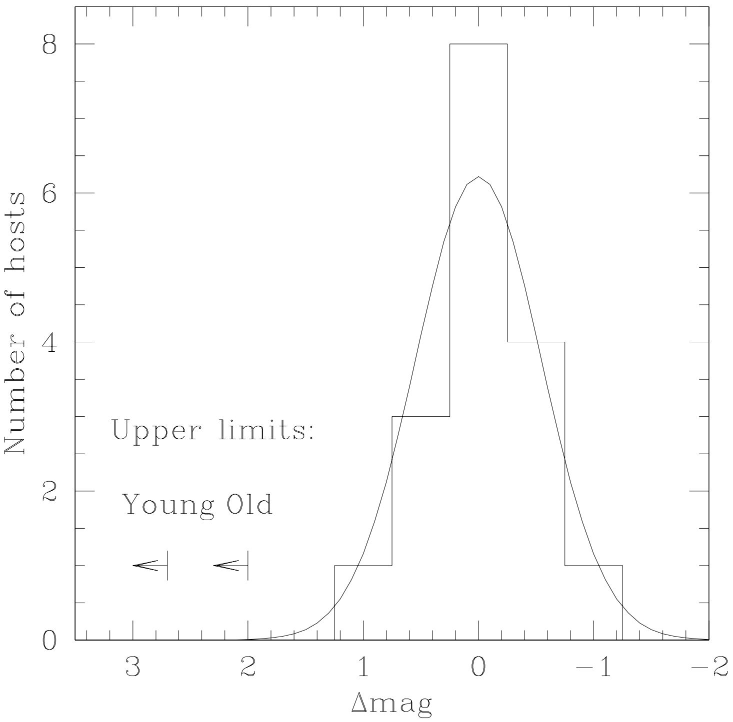

Figure 4.5: Upper limits on the host magnitudes. The histogram gives the dispersion of the host magnitudes around the mean trend in the HST luminous quasars sample (Floyd et al. 2004 [36]). The curve represents a gaussian fit to these data. Our upper limits for a smooth spheroidal distribution of either old or young stars are indicated. They both deviate from the mean by a large amount of 3.7 and 5 sigma, respectively.

the host galaxy.

4.3 Interpretation

This peculiar quasar, therefore, has a host galaxy (if any) that is significantly less luminous than expected from its nuclear luminosity and black hole mass. Moreover, it suffers a strong dynamical interaction with an ultra-luminous infrared galaxy (a rare class of galaxies, systematically involved in collisions, Canalizo & Stockton 2001 [18]). These two peculiarities are most probably related. One might suggest that the host galaxy has disappeared from our view as a result of the collision, but it is hard to imagine how the complete disruption of a galaxy could happen. An alternative suggestion would be that an isolated black hole may have captured gas and become a quasar while crossing the disk of the neighboring galaxy with a low relative speed (the radial velocity difference between the quasar and different parts of the galaxy ranges between -60 and +200 km s^{-1}). However, such a gravitational accretion of matter is very inefficient and the dynamical interaction of a large galaxy with an 8.10^8 solar masses black hole would probably not induce such strong perturbations as observed in the companion galaxy. Another possibility would be that the black hole of HE0450-2958 lies in a galaxy with not only a stellar content much lower than average, but also with an important dark halo, a "dark galaxy" (Ferrarese 2002 [34]). The interaction with such a massive object could more easily explain the peculiarities of the neighboring galaxy as well as the capture of gas, resulting in the ignition of the quasar.

Acknowledgments This work has been supported by the PPS Science Policy (Belgium), by PRODEX (ESA), and by the Swiss National Science Fundation. The observations were obtained with the ESO/VLT (Paranal, Chile) and with the NASA/ESA Hubble Space Telescope.

4.4 Compléments techniques à l'article

Vu le format requis par la revue Nature dans laquelle l'article a été publié, beaucoup de détails techniques n'ont pu y trouver place. Voici quelques compléments d'information sur les méthodes empoyées.

4.4.1 Séparation quasar/blob

Image

Comme déja évoqué dans l'introduction, la construction de la PSF pour des images du HST/ACS nécessite un raffinement important par rapport à des observations du sol, étant donné la complexité et la haute résolution de la PSF de l'instrument. Dans le cas de HE 0450-2958, outre l'adaptation de la technique de construction de PSF décrite dans la section 1.3.1, nous avons voulu tirer parti au maximum de la présence d'une étoile de champ proche du quasar (et non saturée) pour contraindre au mieux cette PSF. Divers tests de combinaison de l'étoile de PSF et de l'étoile de champ nous ont menés à la solution suivante.

La partie centrale de la PSF a été obtenue sur l'image de l'étoile proche du quasar, de laquelle nous avions préalablement soustrait la lumière du quasar lui-même à l'aide d'une précédente déconvolution pour éviter toute contamination lumineuse par le noyau actif. Les ailes de la PSF ont été construites sur base de l'étoile de PSF, saturée au centre. Nous avons ensuite relié ces deux morceaux par une pondération appropriée, ajustant les poids relatifs et rayons de recollage par essais et erreurs sur les résultas de déconvolution. La qualité de la PSF ainsi construite a pu être testée grâce à l'étoile proche du quasar, une bonne déconvolution ne devant plus laisser apparaître de structure dans le fond numérique sous cette source. De cette manière, nous sommes assurés que les résultats obtenus sous le quasar ont une signification réelle et ne sont pas dus à des artéfacts de déconvolution.

Nous avons également essayé de tirer parti de notre connaissance des spectres du quasar et de l'étoile proche pour contraindre les variations de la forme de la PSF liée au changement de couleur des sources ponctuelles. Les corrections qu'on a pu y apporter en se basant sur la différence des modèles de PSF obtenus par le logiciel TinyTim n'ont pas été concluantes, soit parce que cet effet est en réalité négligeable, soit parce que le logiciel TinyTim ne modélise pas la PSF de manière suffisamment précise.

Spectres

Les premiers résultats de déconvolution des spectres ne montrant pas de continuum sous le quasar mais uniquement des raies d'émissions intenses, avec à quelques endroits une tendance à obtenir des valeurs négatives dans le fond numérique, nous ont poussé à raffiner la PSF employée et les paramètres de déconvolution, afin de s'assurer que la non-détection de galaxie hôte est significative et non due à un artéfact de déconvolution.

Une première amélioration est venue de l'étoile de PSF elle-même. Nous avons constaté que les ailes de l'étoile devant servir à construire la PSF étaient tronquées par une mauvaise soustraction du ciel lors de la réduction des données. Le niveau du fond de ciel était estimé par la mesure du signal aux extrémités de la fente. Or, malgré la longueur de celle-ci (19 secondes d'arc), nous avons pu constater qu'au niveau de précision requis, les extrémités de la fente contenaient encore une contribution du flux de la PSF qui, bien que très faible, affectait le résultat de la déconvolution. Ceci est d'autant plus visible que, l'étoile de PSF n'étant pas parfaitement centrée sur la fente, la soustraction du ciel rendait les ailes de l'étoile asymétriques. Nous avons corrigé cet effet par une nouvelle soustraction du ciel et une symétrisation par l'ajout d'une composante linéaire au fond de ciel sous l'étoile. Un même traitement a été appliqué également aux spectres du quasar, pour lequel la difficulté de soustraction du ciel vient de la présence de nombreuses sources le long de la fente (étoile, quasar et galaxie voisine).

Grâce aux images à haute résolution du HST, nous avons pu fixer les positions relatives des sources ponctuelles (quasar et étoile), afin d'améliorer la séparation entre le quasar et le blob. Nous avons obtenu les meilleures séparations entre quasar et blob en contraignant le centre du quasar à ne varier que très légèrement et linéairement en fonction de la longueur d'onde au niveau des zones d'émission intenses du blob.

4.4.2 Limite en magnitude

Les premiers tests pour fixer une magnitude limite de détection de galaxie ont été réalisés sur les spectres. Le principe était d'ajouter aux données une galaxie artificielle, suivant un profil de Vaucouleurs de largeur et centre fixés puis de diminuer son intensité pour déterminer à partir de quel moment elle n'apparaissait plus dans le fond numérique de la déconvolution (nous avons fixé la limite de détection à 10σ au dessus du niveau du fond obtenu sans galaxie ajoutée). Ce test a été réalisé sur des tranches de longueur d'onde qui ne montrent pas de raie d'émission. Nous avons ensuite converti en magnitude les flux limites obtenus pour les différentes valeurs de centrage et de largeur, obtenant une moyenne de $M_V = -20.8$. Cette magnitude n'a cependant pas été reprise dans l'article étant donnée qu'une partie seulement de la galaxie hypothétique serait incluse dans la fente d'observation, le flux ainsi obtenu n'étant donc qu'une valeur minimale pour la galaxie.

La limite de magnitude adoptée dans l'article a donc été estimée sur l'image HST. Afin de savoir si la galaxie n'était pas détectée car trop compacte, nous avons estimé sa compacité en supposant une magnitude typique pour la galaxie hôte de ce quasar, en nous basant sur la relation masse du trou noir - masse du bulbe observée aussi bien dans les galaxies actives (McLure & Dunlop 2002 [86]) que non-actives (Marconi & Hunt 2003 [81]). Une galaxie de cette magnitude, suivant un profil de de Vaucouleurs, a été ajoutée à l'image initiale, et nous avons fait décroître sa largeur jusqu'à ce qu'elle ne soit plus détectée par notre algorithme. Et la galaxie reste visible après déconvolution jusqu'à une largeur de 100pc, ce qui est dérisoire pour une galaxie normale.

Ensuite, en fixant une largeur typique de galaxie centrée sur le quasar, dans une gamme allant de 10kpc à 20kpc, nous avons diminué la luminosité de la galaxie ajoutée jusqu'à ce qu'elle devienne non détectable après déconvolution.

4.4.3 Conversion en magnitudes absolues

Voici le détail des conversions des magnitudes apparentes en magnitudes absolues, avec le détail des hypothèses et modèles employés.

Magnitude absolue du quasar

La magnitude apparente du quasar seul, dans le filtre F606W de l'ACS est de $m_{qso}(f606w) = 15.63$. Pour convertir en magnitude absolue V, nous avons besoin, en plus de la correction de distance d_l et de l'extinction A, à la fois d'une correction pour changement de filtre de F606W à V, correction obtenue directement en comparant à l'aide du spectre les flux intégrés au travers des bandes passantes correspondantes par comparaison à Véga, et d'une correction cosmologique de largeur de bande.

$$\begin{aligned} M_{qso}(V) &= m_{qso}(f606w) - 5\log d_l + 5 - A + (V - f606w) - 2.5\log(1+z) \\ &= 15.63 - 41.00 - 0.05 - 0.0094 - 0.27 \\ &= -25.78 \end{aligned}$$

La distance luminosité est de $d_l = 1583$ Mpc, en prenant $z = 0.285$ et $h = 0.65$.

Magnitude absolue limite via les simulations

Les simulations ont donné un rapport de flux entre la galaxie artificielle limite ($glim$) détectée après déconvolution et le quasar de $F_{glim}/F_{qso} = 8 \cdot 10^{-3}$. La magnitude apparente est donnée par

$$m_{glim}(f606w) = m_{qso}(f606w) - 2.5\log(F_{glim}/F_{qso}) = 20.87$$

La conversion en magnitude absolue ne peut se faire aussi directement que pour le quasar, étant donné que nous ne disposons pas de spectre pour la galaxie (puisqu'elle n'est pas détectée) afin de déterminer la couleur entre les filtres V au repos et F606W observé. Suivant les hypothèses faites sur la galaxie hôte, cette couleur peut varier. Par exemple, pour un bulbe comprenant une population d'étoiles vieilles ($\sim$ 10 Gyr), les synthèses de population stellaire de Bruzual et Charlot (2003 [15]), après intégration de leurs modèles de flux dans les filtres employés, prédisent une couleur (V-f606w)= -0.8 mag. Si par contre on opte pour une population jeune ($\sim$ 150 Myr) comme celle trouvée dans la galaxie voisine du quasar, cette couleur devient (V-f606w)= -0.13 mag. La magnitude absolue est obtenue en combinant ces informations avec les corrections habituelles de distance et cosmologie.

$$\begin{aligned} M_{glim}(V) &= m_{glim}(f606w) - 5\log d_l + 5 + (V - f606w)_{gal} - 2.5\log(1+z) \\ &= 20.87 - 41.00 + (V - f606w)_{gal} - 0.27 \\ &= -21.2 \text{ pour une population stellaire vieille} \\ &= -20.5 \text{ pour une population stellaire jeune} \end{aligned}$$

Magnitude attendue de la galaxie

La magnitude absolue du quasar peut nous informer sur la masse attendue du trou noir μ_{tn}, en fonction de l'hypothèse faite sur le taux d'accrétion de celui-ci . Comme c'est la luminosité bolométrique du quasar qui est associée à la luminosité d'Eddington (luminosité d'un quasar en équilibre entre pression de radiation et force de gravitation créée par la masse du trou noir), nous avons employé une régression entre la magnitude d'Eddington dans la bande V, $M_{edd}(V)$, et la masse du trou noir, tirée de Floyd et al. (2004 [36]), donnant $M_{edd}(V) = -26.72$ pour un trou noir de $10^9 M_\odot$ accrétant à la limite d'Eddington ou $M_{edd}(V) = -25.97$ si le trou noir n'accrète qu'à 50% de la limite d'Eddington.

$$\mu_{tn} = 10^9 M_\odot \,.\, 10^{-0.4(M_{qso}(V)+25.97)} = 8 \cdot 10^8 M_\odot \ \ (50\% \text{ Edd.})$$

$$\mu_{tn} = 10^9 M_\odot \,.\, 10^{-0.4(M_{qso}(V)+26.72)} = 4 \cdot 10^8 M_\odot \ \ (100\% \text{ Edd.})$$

La masse du trou noir ainsi trouvée est reliée à la luminosité du bulbe de la galaxie par la relation observationnelle donnée dans McLure & Dunlop (2002 [86]) :

$$\log(\mu_{tn}/M_\odot) = -0.5 M_{bulbe}(R_C) - 2.9$$

Comme pour l'estimation de la magnitude limite de détection, la conversion de la magnitude du filtre R_C au filtre V dépend des hypothèses faites sur la galaxie. Comme ces filtres sont standards, il existe des couleurs typiques de galaxies dans Fukugita et al. (1995 [38]). Pour une galaxie avec une population stellaire vieille, $(V - R_C) = 0.61$, tandis que pour une galaxie jeune $(V - R_C) = 0.15$. Ce qui nous donne donc, pour un taux d'accrétion à 100% de la limite d'Eddington, $M_V = -22.9$ pour une galaxie jeune ou $M_V = -22.4$ pour une galaxie vieille. Pour un taux d'accrétion à 50% de la limite d'Eddington, on aura $M_V = -23.5$ pour une galaxie jeune et $M_V = -23.0$ pour une galaxie vieille.

Comme souligné depuis la parution de l'article par Merritt et al. (2006 [88]), l'estimation de la masse du trou noir via la luminosité du quasar est surestimée si le quasar accrète au dessus de la limite d'Eddington, ce qui est le cas pour les AGN à raies d'émission étroites comme semble l'être HE 0450-2958. Si on se base sur le théorème du viriel pour l'estimation de la masse centrale (Kaspi et al. 2000 [54]), on obtient $\mu_{tn} = 6.5 \cdot 10^7 M_\odot$. Ce qui nous donne alors comme magnitude attendue pour la galaxie, en suivant les mêmes conversions de couleur, $M_V = -20.8$ pour une population vieille, ou $M_V = -21.3$ pour une population jeune. Dans ce cas, donc, la magnitude limite est compatible avec la magnitude attendue, et la non détection de la galaxie pourrait être expliquée uniquement par les limites observationnelles.

Comme détaillé au chapitre 5, cette méthode d'estimation de masse centrale dans le cas des quasars à raies étroites est sujette à caution, la séparation entre les composantes large et étroite de la raie Hβ servant à l'évaluation de la masse étant ambigüe. Si, au lieu de prendre la largeur totale de Hβ comme fait ci-dessus, on sépare les deux composantes en imposant la même largeur de raie à la composante étroite de Hβ qu'à la raie étroite de [OIII], la masse centrale devient $\mu_{tn} = 1.8 \cdot 10^8 M_\odot$ et le taux d'accrétion n'est plus que légèrement inférieur à la limite d'Eddington. Les magnitudes attendues sont alors $M_V = -21.7$ pour une population vieille et $M_V = -22.15$ pour une population jeune.

Si on suit Merritt et al. (2006 [88]), il se peut donc que les magnitudes limites données dans l'article aient été un peu trop optimistes en faveur de la non-détection de la galaxie. Cependant, parmi les différents quasars présentant les caractéristiques de "Narrow Line QSOs", HE 0450-2958 est le seul pour lequel la galaxie n'est pas détectée, et reste donc dans ce cadre un cas à part, qui reflète malgré tout un ou plusieurs phénomènes hors norme à élucider.

TAB. 4.1 – Synthèse des magnitudes attendues en fonction de la population stellaire, selon la méthode d'estimation de masse du trou noir, basée (1) sur la luminosité du quasar et le taux d'accrétion ou (2) sur le théorème du viriel, et magnitudes à la limite de détection.

Méthode	Accrétion	Pop. jeune	Pop. vieille
(1)Luminosité	50% Edd.	-23.5	-23.0
	100% Edd.	-22.9	-22.4
(2)Viriel	250% Edd.	-21.3	-20.8
	90% Edd.	-22.2	-21.7
Limite détection		-20.5	-21.2

4.4.4 Le blob, partie de la NLR ?

Nous nous sommes interrogés sur la nature du nuage de gaz ionisé, appelé blob dans l'article. Il s'agit soit d'un nuage de gaz in situ qui se trouve illuminé par le quasar proche, soit de la seule partie de la galaxie hôte visible au travers d'un hypothétique nuage de poussière, soit la NLR du quasar qui serait résolue sur les images du HST et en partie sur les spectres.

Afin d'y voir plus clair, nous avons estimé le rapport quasar/blob sur l'image HST (~ 40) et ce même rapport sur les spectres intégrés (~ 65), après multiplication par la courbe de réponse du filtre employé pour l'observation avec l'ACS (F606W). La similitude des rapports confirme que le blob de l'image est essentiellement composé de gaz, mais qu'il y a certainement une partie de la source ponctuelle qui, sur les spectres, se mélange au blob. En effet, si pour la raie [OIII] 5007, la plus intense pour le blob, on ajoute au flux du blob le flux de la raie d'émission étroite du quasar, nous obtenons un rapport quasar/blob de 40.5, pratiquement identique à celui mesuré sur l'image HST. Les raies étroites du quasar pourraient donc venir du blob lui même qui ne serait autre que la NLR du quasar qu'on résoudrait. L'article de Merritt et al. [88] donne d'ailleurs une estimation empirique de la taille de la NLR se basant sur l'état d'ionisation du gaz, et cette estimation ($\sim 1.5kpc$) colle bien avec la taille observée du blob sur les images ($\sim 1.2kpc$). D'un autre côté, l'observation est également compatible avec l'hypothèse du quasar isolé, qui ne comprendrait que des raies larges, et qui ioniserait une nuage de gaz in situ recouvrant partiellement le quasar sur le plan du ciel.

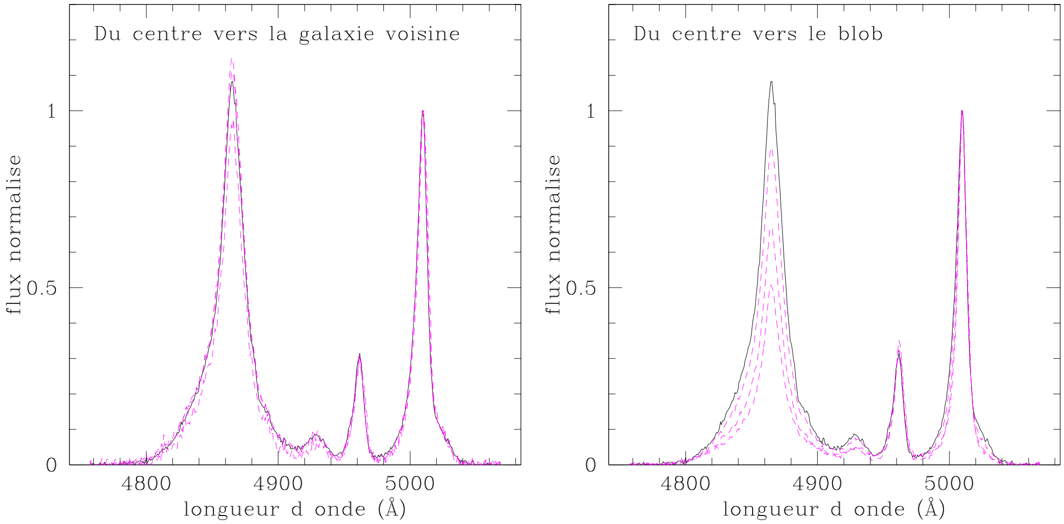

FIG. 4.6 – Profil des raies d'émission dans la zone Hβ-[OIII] des spectres VLT, après soustraction du continu et normalisation au flux du pic de [OIII], en s'éloignant spatialement du centre le long de la fente (colonne par colonne). La colonne centrale est représentée en noir, les trois colonnes suivantes superposées en violet.

Afin de déterminer si, oui ou non, le blob observé est uniquement la NLR du quasar, nous avons réalisé deux tests :

D'une part, nous avons analysé, colonne par colonne, le spectre global du quasar. Si on s'éloigne du centre vers la galaxie voisine, on constate que le rapport de flux Hβ/[OIII] reste constant, ainsi que les largeurs de raies. Si, par contre, on s'éloigne du côté du blob, on constate que le rapport Hβ/[OIII] diminue progressivement et que la raie d'[OIII] se rétrécit très légèrement (Fig. 4.6).

D'autre part, nous avons comparé le profil spatial de l'ensemble blob + quasar obtenu à partir de l'image du HST et des raies [OIII] du quasar + blob dans les spectres du VLT. Après les avoir ramenés à même résolution spatiale et orientation, nous constatons que la raie [OIII] est centrée plus proche du quasar dans les spectres que sur l'image (Fig. 4.7). Ce qui confirme que l'émission d'[OIII] du noyau existe et est non négligeable.

En conclusion, le blob observé semble être une zone d'émission qui constitue une partie seulement de la NLR du quasar (gaz *in situ* ou seule partie visible de la galaxie), mais qu'une autre partie de cette NLR ne peut être résolue et séparée du quasar, même sur les images HST.

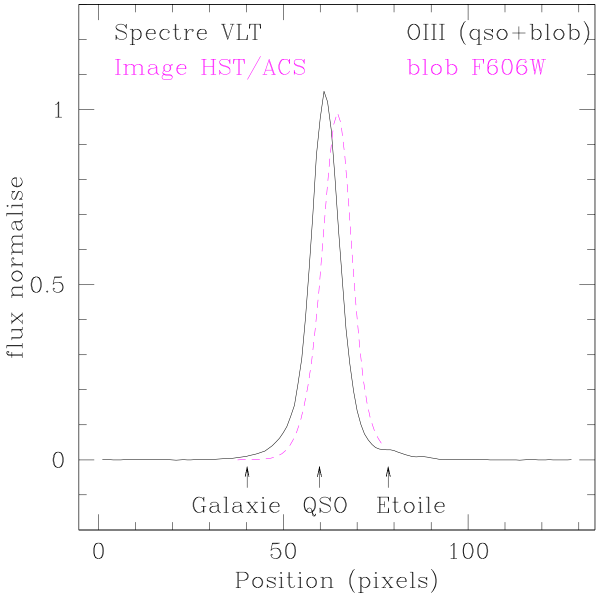

FIG. 4.7 – Comparaison des profils spatiaux : en noir profil spatial de la raie [OIII], après soustraction du continu du quasar, de la galaxie voisine et de l'étoile. En violet le profil du blob issu de l'image du HST, ramené à même résolution et position. Les positions relatives des galaxie, quasar et étoile du champ sont indiquées.

Chapitre 5

Synthèse de l'analyse de l'échantillon complet

Cet article est la synthèse du travail effectué durant la thèse. Il aborde tous les types d'analyses réalisés sur l'échantillon et en tire quelques informations sur la nature et l'évolution des galaxies qui abritent un quasar.

Ses principales conclusions concernant les galaxies hôtes :

- Les quasars lumineux se trouvent aussi bien dans des galaxies spirales qu'elliptiques, contenant pour la plupart une grande quantité de gaz ionisé (par des étoiles, ou par le quasar lui-même dans des systèmes en interaction gravitationnelle)
- Une forte proportion des galaxies hôtes sont dominées par une population stellaire typiquement jeune, où le gaz semble n'avoir été que très peu enrichi par de précédentes générations d'étoiles.
- Les galaxies elliptiques présentent des quantités importantes de gaz ionisé, probablement issues d'interactions récentes avec d'autres galaxies.

Nous avons également pu mettre en évidence quelques propriétés des quasars eux-mêmes :

- Le rougissement déduit du décrément de Balmer sur les raies larges du quasar doit être employé avec précaution comme estimateur du rougissement du continu et/ou des raies étroites du quasar dans les objets contenant beaucoup de poussière, la distribution probablement inhomogène de celle-ci ne permettant pas d'être sûr que c'est la même extinction qui s'applique à ces différentes composantes.
- Dans les systèmes réguliers, le pic de la raie Hα (suivie de Hβ) du quasar est le meilleur estimateur du redshift de celui-ci.

Enfin concernant les liens entre la galaxie et l'activité du noyau :

- L'interaction de la galaxie avec des compagnons proches est un processus très efficace pour amener gaz et poussière au centre du système et donc pour alimenter le trou noir central. Mais ce n'est pas le seul : un autre processus semble lié à la formation ou l'évolution primordiale d'au moins une partie des galaxies spirales. Il est probable que des événements locaux (non résolus par nos observations) favorisent le mouvement de matière vers le trou noir central dans les galaxies très jeunes, au riche contenu gazeux, et sans trace d'interaction.

- Le type de phénomène déclencheur de l'activité conditionne la puissance du noyau : Les trous noirs les plus massifs et les quasars les plus puissants se retrouvent dans les galaxies elliptiques à important contenu gazeux et dans les galaxies en interaction. Les trous noirs plus légers se retrouvent dans les galaxies spirales jeunes.

Cet article soulève beaucoup de questions qui ne pourront trouver réponse qu'après étude d'un échantillon plus grand et/ou combinant différents types d'observations. Citons, entre autres, les causes de l'activité dans les galaxies jeunes : si on pense que des supernovae sont capables d'alimenter le trou noir par des vents galactiques, on devrait observer dans des spectres à meilleure résolution spatiale un net enrichissement du milieu interstellaire au centre de la galaxie, puisque les observations actuelles nous montrent que, sur les spectres intégrés, ces jeunes galaxies ne sont que faiblement enrichies en métaux.

Citons encore le problème de la correction du rougissement des spectres de quasars : Il faudra investiguer si cette observation peut être reliée à des effets d'orientation du disque d'accrétion par rapport à la ligne de visée. En effet, si la BLR est entourée d'un tore de poussière comme on le représente fréquemment, on s'attend à un rougissement plus fort si la ligne de visée des observations traverse une partie plus important de ce disque de poussière. Dans le cas où la BLR serait aplatie dans la même direction, la largeur de ses raies pourrait, elle aussi, être affectée par cet effet d'orientation si on considère un mouvement de rotation du gaz dans cette zone. Une ligne de visée de plus en plus proche de la perpendiculaire au plan de ce disque nous donnerait des raies de plus en plus étroites. Nous entamons une recherche sur l'existence de telles corrélations dans des observations existantes, ainsi que leur lien potentiel avec la polarisation de la lumière du quasar. Il semble déjà que les orientations relatives entre le disque d'accrétion et le plan de la galaxie soient réparties aléatoirement, en tous cas dans les Seyferts.

Un autre aspect de l'étude à approfondir est celui des "Narrow Line QSOs". L'imagerie à meilleure résolution (via le HST) des objets de l'échantillon présentant ces caractéristiques spectrales nous permettrait d'en savoir plus sur les galaxies qui abritent ces quasars particuliers, puisque d'après la présente étude ils ne semblent pas définir sans ambiguité une classe particulière de quasars. Un premier éclaircissement viendra de l'étude de l'éventuelle influence de l'orientation de l'AGN sur la définition des NLQSOs.

On-axis spectroscopy of the host galaxies of 20 optically luminous quasars at $z \sim 0.3$

G. Letawe[1], P. Magain[1], F. Courbin[2], P. Jablonka [2,3],
K. Jahnke[4], G. Meylan[2], and L. Wisotzki[5]

1. Institut d'Astrophysique et de Géophysique, Université de Liège, Allée du 6 Août, 17, Bat. B5C, Liège 1, Belgium
2. Ecole Polytechnique Fédérale de Lausanne, Observatoire, CH-1290 Sauverny, Switzerland
3. Observatoire, Université de Genève, CH-1290 Sauverny Switzerland
4. Max-Planck-Institut für Astronomie, Königstuhl 17, 69117 Heidelberg , Germany
5. Astrophysikalisches Institut Potsdam, An der Sternwarte 16, 14482, Potsdam, Germany

To submit to the Monthly Notices of the Royal Astronomical Society, march/april 2006.

Abstract: We present the analysis of a respresentative sample of 20 bright low-redshift quasars ($M_B < -23$ and $z < 0.35$) observed spectroscopically with the VLT. The FORS1 spectra, obtained in Multi Object Spectroscopy (MOS) mode, allow to observe simultaneously the quasars and several reference stars used to spatially deconvolve the data. Applying the MCS deconvolution method, we are able to separate the individual spectra of the quasar and of the underlying host galaxy. We find that most quasar host galaxies harbour large amounts of gas, irrespective of their morphological type. Moreover, the stellar content of half of the hosts is a young Sc-like population, associated with compatible Star Formation Rates and a barely enriched interstellar medium. A significant fraction of the galaxies contain gas ionized at large distances by the quasar radiation. This large distance ionization is always associated with signs of interactions (as seen from imaging or disturbed rotation curves). The spectra of the quasars themselves provide evidence that gravitational interactions bring dust and gas in the immediate surrounding of the super massive black hole, allowing to feed it. The quasar activity might thus arise (1) in young gas-rich spiral galaxies through local events and (2) in more evolved galaxies undergoing gravitational interactions. The latter mechanism gives rise to the most powerful quasars. Furthermore, we show that the reddening deduced from the Balmer decrement in the quasar broad line spectrum cannot be applied to the continuum. This indicates that the dust is distributed inhomogeneously around the quasar. Finally, we derive mass models for the isolated spiral host galaxies and we show that the tip of the Hα line is the best estimator of the actual

redshift of the system in the quasar spectrum.

Keywords Galaxies: active, stellar content, interactions – techniques: image processing, spectroscopy – Quasars: general

Based on observations made with ANTU/UT1 at ESO Paranal Observatory, Chile (programs 65.P-0361(A), 66.B-0139(A)).

5.1 Introduction

Close to half a century has passed since the first deep spectroscopic observations of a quasi-stellar-object (QSO) (Oke 1963 [95], Greenstein & Schmidt 1964 [40]), and 30 years since the first clear spectroscopic evidence that quasars are located in the centers of much larger stellar envelopes or *host galaxies* (Boroson et al. 1984 [9]). After this pioneering spectroscopic work, most studies have concentrated on imaging, attempting to measure the shape and the luminosity of quasar host galaxies (e.g., Bahcall et al. 1997 [2], Dunlop et al. 2003 [30]). With better image processing techniques, it has become possible to derive information about the stellar content of quasar hosts using multicolour imaging (Rönnback et al. 1996 [100], Jahnke et al. 2004 [51], Sanchez et al. 2004 [101]), but very little effort has been spent on genuine deep spectroscopy, mainly because of the difficulty to accuratly decontaminate the galactic spectrum from the light of the central quasar.

The quasar-host separation problem has been circumvented, at least in part, in three ways. One is to restrict oneself to samples of obscured quasars (Kauffmann et al. 2003 [55]), with the obvious drawback that samples built in that way are biased, and that there is no easy way to accurately recover the unobscured quasar luminosity. Another technique is to carry out off-axis spectroscopy, where the spectra are obtained with the slit of the spectrograph located a few arcseconds away from the quasar (e.g., Hutchings & Crampton 1990 [47], Nolan et al. 2001 [94], Miller & Sheinis 2003 [90]). However, residual contamination by the quasar remains difficult to remove completely, the velocity information on the host is lost, and only the external parts of the host can be well studied. Finally, the 1D template-spectra of non-active galaxies can be used as a basis to perform eigenvector decomposition (Vanden Berk et al. 2005 [113]). The latter is efficient in drawing general conclusions using very large numbers of objects, but relies on a restricted number of eigenspectra which prevent the discovery of unexpected spectral features, e.g., due to the specific spatial distribution of the gas in each galaxy, to the starburst activity, or to winds and jets escaping from the central AGN.

In the present work, we take advantage of a new approach, where the quasar spectra are taken on-axis, i.e. with the slit lying directly accross the nuclear point source. Our quasar-host separation technique relies on a spatial deconvolution of the spectra, using the spectra of several PSF stars. This method has already been exploited in three previous papers (Courbin et al. 2002 [24], Letawe et al. 2004 [69], Magain et al. 2005 [76]) and allows to go beyond previous studies: 1- the spectral properties of the hosts can be determined

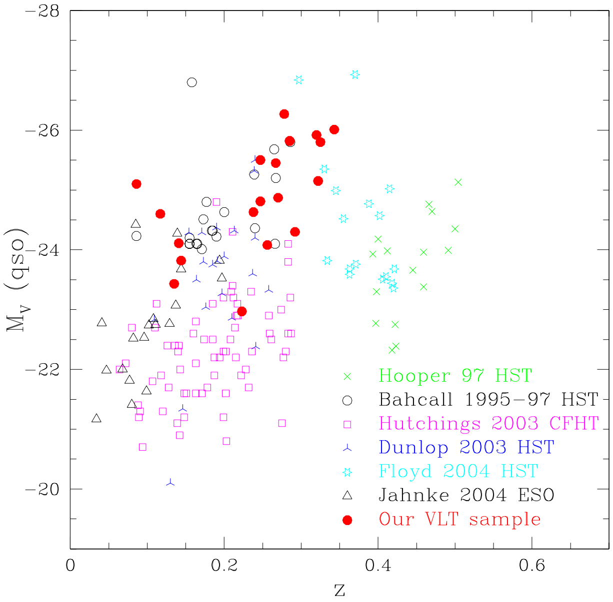

Figure 5.1: Location of our quasar sample in the absolute magnitude vs. redsdhift plane, compared with other samples observed in imaging either with the HST or from the ground (CFHT, ESO).

even in the central kpc, 2- we can separate well the stellar and gaseous contributions to the total spectrum, contrary to multicolour imaging, 3- we make no prior assumption on the host, neither spectral nor morphological, during the deconvolution process, 4- we can measure the velocity curve of the host around its central quasar.

Recent studies have argued that luminous quasars reside in massive elliptical galaxies (Dunlop et al. 2003 [30]) with globally old stellar populations, but with slightly bluer colours than their quiescent counterparts, indicative of an additional younger stellar component (Kauffmann et al. 2003 [55]; Jahnke et al. 2004 [51]; Vanden Berk et al. 2005 [113]). We show in the present paper that these general conclusions should be taken with caution, as they are influenced by the structural details of individual quasar host galaxies and by their velocity fields. In particular, we investigate how the central AGN affects the evolution of the whole galaxy by carrying out a comparative study between samples of galaxies with and without quasars. We compare their stellar populations and the ionization state of their Interstellar Medium (ISM). Whenever possible, we infer the dynamical mass of the host galaxies and we trace distorsions of their velocity field due to past or present interactions with nearby companions.

Our work is a first step towards a larger spectroscopic study of quasar hosts aimed at understanding why some galaxies are active while other are not. Many studies have characterized the morphology of the hosts, but the morphology, alone, does not reflect the actual stellar and gaseous content of the hosts. The aforementionned blue colours of quasar hosts confirm that their evolution does not follow a classical path. Where do they

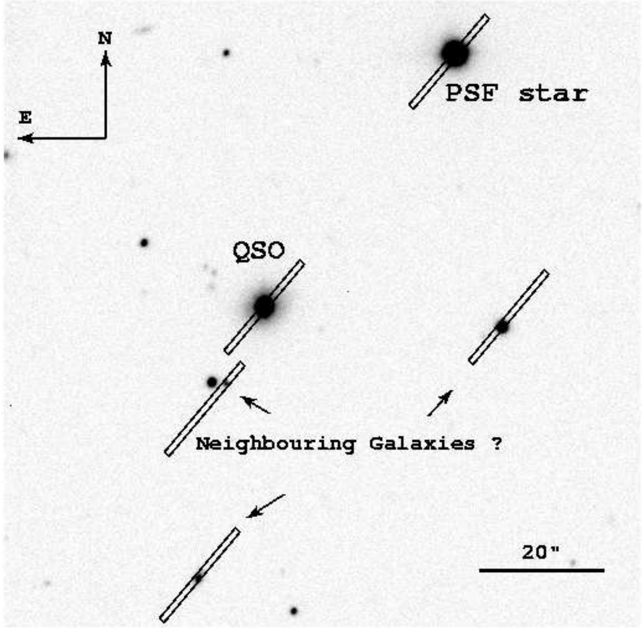

Figure 5.2: Example of a MOS mask used to carry out the FORS1 observations, for the quasar HE 1503+0208. One slitlet (19"× 1") is positioned on the quasar, and several others on PSF stars. The remaining slitlets are used to take the spectrum of possible neighbouring galaxies.

stand and how is their evolution linked to the nuclear activity ? Because of the complexity and because of the variety of physical phenomena at work in quasar host galaxies, the observational solutions of this puzzle can only come from a combined spectroscopic and imaging study.

In Section 5.2, we present our sample of 20 low-redshift optically luminous quasars. In Sections 5.3 and 5.4 we describe the observations and data processing. Imaging is treated in Section 5.5, while we give in Section 5.6 an overview of the spectral analysis further detailed in Section 5.7. Section 5.8 is devoted to the dynamics of quasar hosts and to the detection of gravitational interactions with companions, while Section 5.9 studies the links between the nuclear and host properties. Finally, Section 5.10 establishes the relation between the redshift of the quasars and that of their host galaxy. Throughout the paper, we adopt the following cosmological parameters: $H_0 = 65$ km s^{-1} Mpc^{-1}, $\Omega_m = 0.3$ and $\Omega_\Lambda = 0.7$.

5.2 The sample

Our quasar sample is selected from the flux-limited Hamburg-ESO Survey (HES) (Wisotzki et al. 2000 [119]). The HES is designed to detect optically luminous quasars and Seyferts 1 in the Southern hemisphere, with optical magnitudes $13 < B < 17.5$ and redshifts $z < 3.2$.

Table 5.1: Observational considerations for our QSO sample, sorted by increasing right ascension:(1-) Object name, (2-) integrated absolute B magnitude from the HES catalogue, (3-) observing run (A = April 2000; B = November 2000), (4-) Galactic extinction from Schlegel et al. (1998 [102]), (5-6) seeing value and exposure time for each grism (G600B, G600R, G600I).

Object name	M_B(tot) HES	Run	E(B-V)	Seeing arcsec: B, R, I	t_{exp} seconds: B, R, I
HE 0132−4313	-24.37	B	0.017	0.65-0.71-0.67	3000-1800-180
HE 0203−4221	-24.88	B	0.014	0.71-0.75-0.60	3000-1800-1800
HE 0208−5318	-24.76	B	0.026	0.61-0.50-0.50	3000-1800-1800
HE 0306−3301	-24.32	B	0.014	0.68-0.66-0.86	3000-1800-1800
HE 0354−5500	-24.70	B	0.016	0.52-0.67-0.48	3600-1800-1800
HE 0441−2826	-24.62	B	0.035	0.74-0.47-0.53	3000-1800-2400
HE 0450−2958	-25.24	B	0.015	0.54-0.67-0.57	3600-1800-1800
HE 0530−3755	-24.07	B	0.027	0.70-0.68-0.65	3000-1800-1000
HE 0914−0031	-25.01	A	0.035	2.06-2.11-2.24	1200-1200-1200
HE 0956−0720	-24.79	A	0.055	0.53-0.65-0.59	1200-1200-1200
HE 1009−0702	-24.28	A	0.033	0.69-0.64-0.70	1800-1800-1800
HE 1015−1618	-25.13	A	0.078	1.20-0.92-1.01	1200-1200-1200
HE 1029−1401	-25.07	A	0.067	1.61-1.54-1.94	1200-1200-1200
HE 1228+0131	-24.33	A	0.019	0.91-0.76-0.72	1200-1200-1200
HE 1302−1017	-26.15	A	0.043	0.60-0.60-0.50	2400-1800-1800
HE 1434−1600	-24.34	A	0.126	0.58-0.60-0.49	1200-1200-1200
HE 1442−1139	-23.81	A	0.079	0.98-1.20-1.10	1200-1200-1200
HE 1503+0228	-23.02	A	0.05	0.60-0.68-0.72	1200-1200-1200
HE 2258−5524	-23.71	B	0.013	0.88-0.70-0.76	3000-1800-1800
HE 2345−2906	-23.09	B	0.019	0.86-0.83-0.67	3000-1500-1500

Table 5.2: Main characteristics of our QSO sample, sorted by increasing right ascension: (1-) Object name, (2-) redshift determined from the Hα emission line of the quasar (see Section 5.10), (3-4) absolute V-magnitude for the quasar and host as measured from our VLT observations, (5-) host morphology as determined from other studies (see Section 5.5) and interaction signs. D stands for disk dominated, E for elliptical, U for undefined, the number coding stands for: 0 = no interaction signs, 1 = close companion outside the galaxy, 2 = tails, 3 = merger, (6-) quasar properties: objects with radio emission are indicated by R (from NVSS), but only HE1302-1017 is radio-loud. Narrow line quasars are labelled NL (see Section 5.9).

Object name	z(Hα) quasar	M_V(QSO) VLT	M_V(host) VLT	Gal	QSO
HE 0132−4313	0.237	-24.63	-22.63	U, 0	NL
HE 0203−4221	0.319	-25.92	-23.10	U, 2	
HE 0208−5318	0.344	-26.01	-23.00	U, 0	
HE 0306−3301	0.247	-24.81	-22.41	D, 2,3	
HE 0354−5500	0.267	-25.45	-23.47	D, 3	
HE 0441−2826	0.155	-	-	E, 0	R
HE 0450−2958	0.286	-25.82	-	U, 1	NL
HE 0530−3755	0.293	-24.30	-20.70	U, 1,2	
HE 0914−0031	0.322	-25.15	-22.02	D, 0	
HE 0956−0720	0.326	-25.80	-23.04	U, 0	
HE 1009−0702	0.271	-24.87	-22.94	D, 0	NL
HE 1015−1618	0.247	-25.50	-22.55	D, 0	
HE 1029−1401	0.086	-25.10	-22.53	E, 3	R
HE 1228+0131	0.118	-24.60	-21.44	E, 0	NL
HE 1302−1017	0.278	-26.27	-23.40	U, 3	R
HE 1434−1600	0.144	-23.82	-22.87	E, 1	R
HE 1442−1139	0.257	-24.08	-23.23	D, 0	
HE 1503+0228	0.135	-23.43	-22.78	D, 0	
HE 2258−5524	0.141	-24.11	-23.11	U, 3	NL
HE 2345−2906	0.223	-22.97	-22.84	D, 0	

The classification of the candidates as quasars is made spectroscopically from the broad-band features. Out of these, we selected the instrinsically luminous quasars, with absolute magnitude $M_B < -23$ and redshift $z < 0.35$. From the 32 QSOs matching these criteria, we could observe 20. No spectral or morphological selection of the object was applied prior to the observations. The only relevant factor in our choice of an object was its visibility at the time of the observing runs. Tables 5.1 and 5.2 gives the main characteristics of our sample. Figure 5.1 gives the location of all our objects in the absolute magnitude vs. redshift plane and compares them with previous studies that all use imaging rather than spectroscopy (e.g. Floyd et al. 2004 [36], Dunlop et al. 2003 [30], Bahcall et al. 1997 [2]). Our sample concentrates on the brightest part of the quasar luminosity function and is restricted to $z < 0.35$. Its characteristics compare well with those of Floyd et al. (2004 [36]) and Bahcall et al. (1997 [2]).

5.3 Observations

5.3.1 Spectroscopy

Our spectroscopic observations were taken with the ESO Very Large Telescope (VLT) and the FORS1 instrument in Multi Object Spectroscopy (MOS) mode. The data were acquired during two observing runs, in April and November 2000. All objects were observed with 3 medium resolution grisms (G600B, G600R and G600I), thus covering the full optical spectral range 3500-9000Å. The seeing varied between 0",5 and 2",2 (see Table 5.1), and the pixel scale was 0",2, using the standard resolution collimator. The slitlet (19" × 1") of the MOS mask closest to the optical axis was centered on the quasar itself (on-axis). Several slitlets were used to obtain the spectra of PSF stars with the same spectral range as the quasar, which is crucial for subsequent deconvolution of the data using the spectroscopic version of the MCS algorithm (Magain et al. 1998 [75], Courbin et al. 2000 [25], see Section 5.4). The remaining slitlets were placed on galaxies in the field, to look for possible companions, groups or clusters (see Section 5.8.2). We show in Fig. 5.2 a typical MOS mask configuration for the 5 slitlets closest to the quasar. As the slits are parallel, the orientation of the mask relative to major axis of the host galaxy (when visible prior to the deconvolution) is imposed by the necessity to observe simultaneously at least one PSF star (in fact two for the majority of the fields observed) with the same spectral coverage as for the quasar.

The reduction of the spectra is carried out with the standard IRAF packages, leading to bias-subtracted, flat-fielded, and sky-subtracted spectra. The wavelength calibration is done using Ne-Ar-He spectra obtained in the same slit configuration as the observations. It is performed on the two dimensional spectra in order to correct for slit curvature and in order to ease the sky subtraction. All spectra are rebinned to a pixel scale of 1 Å in the spectral direction and 0",2 in the spatial direction. When several exposures are available in a given grism, they are combined into one deeper spectrum using cosmic-ray rejection. Spectroscopic standard stars were observed during the two observing runs in

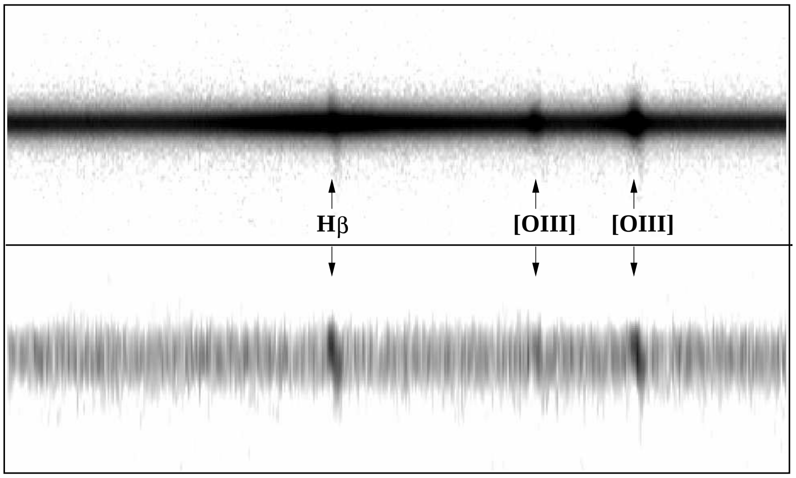

Figure 5.3: Example of spectra decomposition using the MCS algorithm, for the $z = 0.223$ quasar HE 2345-2906. The spectrum shown here spans the wavelength interval 5800-6250 Å from left to right. The top panel displays the original data with the VLT spectrum of the quasar plus host galaxy. The bottom panel is the result of the decomposition, where only the 2D-spectrum of the host is shown. The narrow emission lines of the host can be traced down to the center of the galaxy. The height of each spectrum is 19".

order to perform the flux calibration.

5.3.2 Imaging

The imaging part of the sample is limited to acquisition images obtained during the spectroscopic runs, with 30s exposure time through the R or V filters. The seeing spans a broad range, 0",5 to 1",5. The pixel scale is 0",2, as in the spectra. In one case the QSO is saturated (HE 0441-2826). The reduction of all images was performed with IRAF. It consisted in a simple bias subtraction, flat-fielding and sky subtraction. Standard stars were also observed in each run for magnitude determination.

5.4 Deconvolution of the data

The whole sample of 2D spectra and images has been deconvolved using the MCS algorithm (Magain et al. 1998 [75]) and its extension to spectra (Courbin et al. 2000 [25]). In the MCS deconvolution algorithm, the final resolution is chosen by the user, but is constrained to be compatible with the sampling of the deconvolved data. In this way, the resolution of the processed data is improved but not infinitly high, and the deconvolved data do not show any of the undesirable "deconvolution artifacts" often found using other algorithms. In addition, the MCS method is particularly well suited to the quasar host studies because of its ability to separate point sources (here the quasars) from diffuse ones (the host galaxies). Taking advantage of the availability of several stars to construct the PSF, we could as well subsample our deconvolved spectra and images, leading to a final sampling of 0",1 per pixel.

The deconvolution of spectra with MCS, as every deconvolution procedure, is highly sensitive to the accuracy of the PSF. Poor deconvolution results are always associated with problems in the PSF construction. Several weaknesses of the process account for uncertainties in the deconvolution results and difficulties in separating both components. The stars are often not bright enough in the bluer part of the G600B grism, in comparison to the quasar. This introduces extra noise at the shortest wavelengths in the deconvolved spectra. The orientation and angular separation of the slits being imposed by the geometry of the mask (see Fig. 5.2), it happens that parts of the PSF wings are lost on one side because the star could not be centered on the slit. The spectral type of the stars can influence the quality of the PSF, smoother stellar spectra being preferred to spectra with many strong absorption lines. Finally, the slight variation of the PSF profile accross the field is minimized by taking the stars closest to the quasar for PSF construction or by the use of several stars on both sides of the quasar to average the profile variation. For 85% of the objects in our sample, the simultaneous observation of several stars allows to construct reliable PSFs.

Figure 5.3 shows an example of deconvolution. The reduced spectrum is shown on the top panel of the figure, while the 2D-spectrum of the host galaxy alone is shown in the bottom panel. The MCS technique is used here essentially in order to separate nuclear and diffuse components of the data rather than for sharpening the data in the spatial direction. This results in some smoothing of the extended source or in any case, in no significant gain in resolution. Figure 5.3 nevertheless clearly demonstrates that no significant residual flux from the quasar is left in the spectrum of the host galaxy. For example, the spectrum of the host does not show any residual from the broad emission lines of the quasar.

Once the data are deconvolved, we extract 1D spectra by integrating fluxes over the spatial direction, in the quasar spectrum and in the host spectrum. The final atlas of quasar and host spectra is shown in Figs. 5.20 to 5.26.

5.5 Image analysis

A short 30-seconds *R* or *V* acquisition image was taken before a long spectroscopic exposure. Even though these images are of low signal-to-noise and were not meant to be used for scientific purpose, they are good enough to determine some basic properties of the quasars and of their hosts. We deconvolved all the available images and used them in order to determine the magnitudes of the quasar and of the host, and to unveil any obvious sign of interaction such as tails or companions. Recent HST/ACS imaging of some of our objects actually confirms that the shapes given by the deconvolution of these image are accurate enough for that purpose. Two dimensional fitting on these low signal-to-noise data remains unfortunately hazardeous.

Figure 5.5 shows the deconvolved images of the quasar hosts after removal of the quasar itself. HE 0441-2826 is missing because the quasar light reached the saturation on the

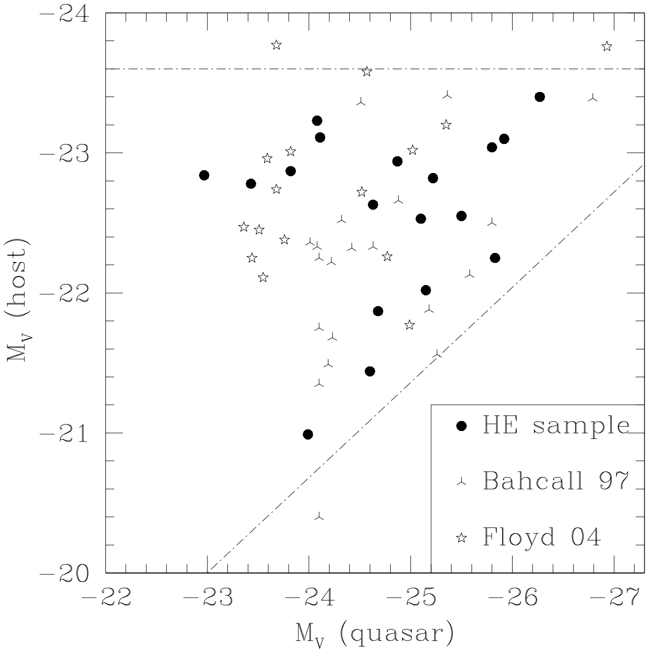

Figure 5.4: Absolute M_V magnitude of the host galaxies versus absolute M_V magnitude of the quasar. For comparison, we also plot the two samples of quasars covering the same luminosity range, from Floyd et al. (2004 [36]) and Bahcall et al. (1997 [2]), converted to our cosmology. The dotted lines show the envelope discussed in the text.

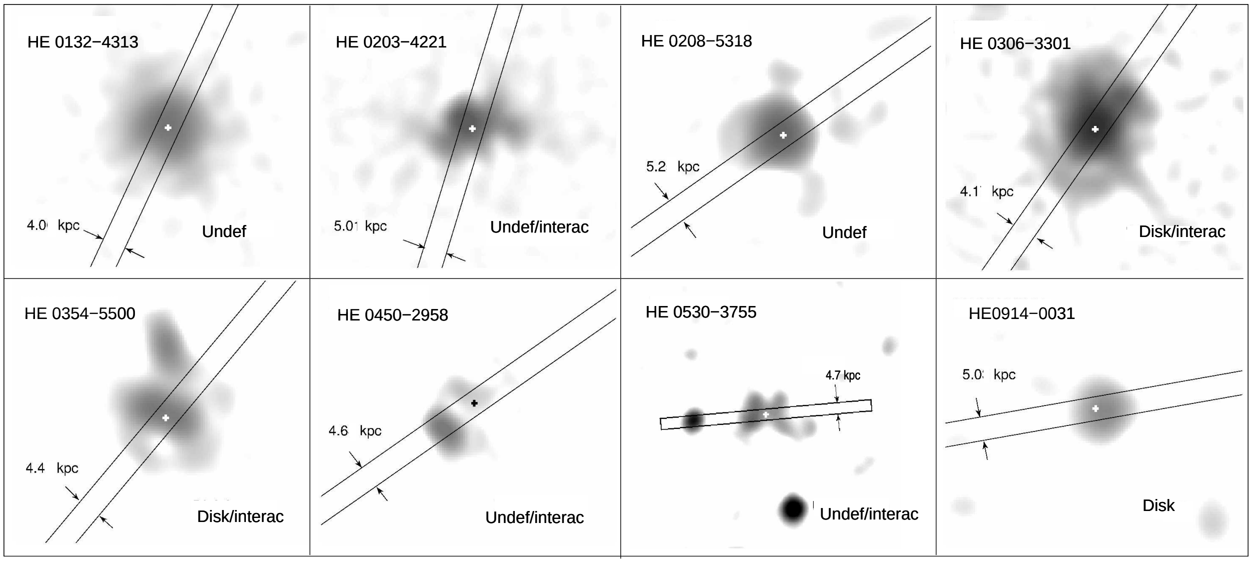

Figure 5.5: Deconvolved VLT images of the host galaxies, in R-band (HE 0132-4313, HE 0203-4221 and HE 0914-0031) or in the V-band (HE 0208-5318, HE 0306-3301, HE 0354-5500, HE 0450-2958 and HE 0530-3755). The quasar light has been removed from these images, which are displayed in logarithmic scale. Crosses indicate the location of the quasar. The 1"-wide slits used in spectroscopy are overplotted, and their physical scale on the sky is indicated. Global morphologies are derived following a 2D isophotal fitting (see Section 5.5). In each case we indicate possible signs of interactions, as can be spotted from imaging and from the radial velocity curves described in Section 5.8.1. All images are 12"-wide, except HE 0530-3755 that is 24" on a side. The intensity cuts are chosen to optimize the contrast and are not identical in all the images. North is up and East to the left.

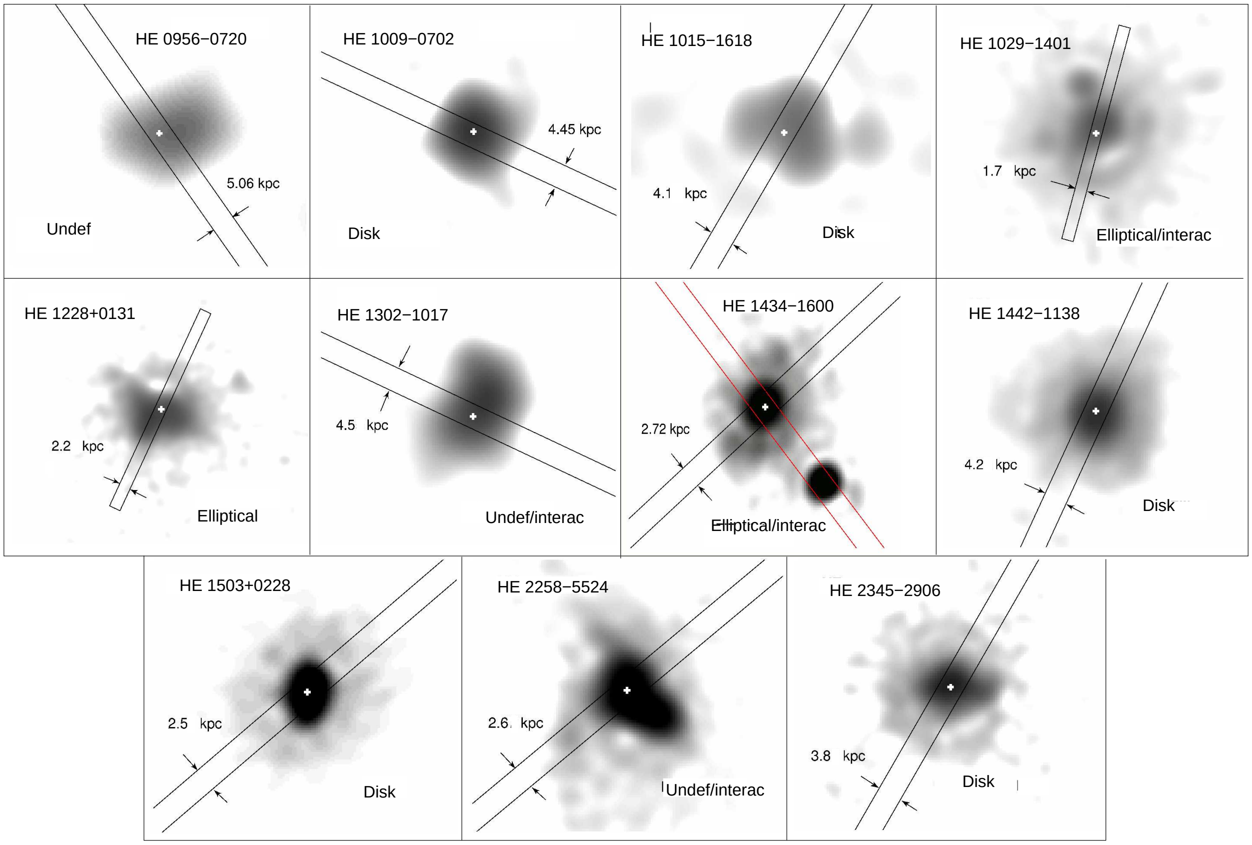

Figure 5.6: All images are in the R filter. All images are 12"-wide, except HE 1029-1401 and HE 1228+0131 that are 24"-wide. North is up and East to the left. HE 1434-1600 was re-observed with a different slit orientation in order to observe a companion galaxy at the same redshift (Letawe et al. 2004 [69]).

detector. The host images are used to measure the apparent magnitude of the host galaxies from aperture photometry. We then compute absolute magnitudes (Eq. 5.1) taking into account the K-correction between the R (or V) filter and the restframe V-band ($RV = R_{obs} - V_{\rm rf}$). This is done without any assumption on the nature of the hosts since we integrate their fluxes over the appropriate wavelength bands, directly in our VLT FORS1 spectra. The calculation can be summarized as follows:

$$\begin{aligned} M_V &= m_R - 5\log d + 5 - A - 2.5\log(1+z) - RV \\ m_R &= m_{R_0} - 2.5log(F_R) - a\tau \end{aligned} \tag{5.1}$$

where d is the distance to the object in parsecs, according to our cosmology, A the Galactic extinction (from Schlegel et al. 1998 [102]), z is the redshift, F_R is the observed R-band flux, a is the airmass, τ the atmospheric optical depth, and m_{R_0} is the zero point determined from the observation of standard stars.

The quality of the deconvolutions can be checked by inspecting the “residual maps”, as defined in Magain et al (1998 [75]). These maps are the difference between the data and the deconvolved images, reconvolved with the PSF, and in units of the photon noise per pixel. A successful deconvolution must show a flat residual map, equal to 1 on average. Based on these residual maps and on numerical simulations, we estimate that the quasar-host decomposition of our VLT acquisition images is accurate to 0.01 mag. However, given that the angular scale of the PSF is similar to that of the bulge component, part of the host flux might be left in the quasar light. This may introduce a systematic underestimate of the flux in the host, especially in cases where it has a compact bulge, which may be difficult to separate from the point source. The magnitudes given in Table 5.2 are not corrected for such systematic errors. For this reason, we avoid any interpretation relying on host magnitudes alone. However, Fig. 5.4 shows that our absolute magnitudes for hosts and nuclei are consistent with other studies in the same luminosity range (Bahcall et al. 1997 [2], Floyd et al. 2004 [36]) and are useful as a guide to compare our sample with others. While no obvious correlation is apparent between the host and quasar intrinsic luminosity, the points are all located inside an “envelope”, shown as dotted lines in Fig. 5.4. The existence of this envelope suggests that, for a given host magnitude, there is a maximum nuclear luminosity. This was already observed in earlier studies, e.g. by Floyd et al. (2004 [36]) or Jahnke et al. (2004 [51]), and is explained by the black hole mass - bulge mass relation (McLure & Dunlop 2002 [86]): for a given bulge mass (and hence bulge luminosity), the black hole mass is roughly fixed and the luminosity of the nucleus cannot exceed much the Eddington luminosity (see Section 5.9.4).

Several objects of the sample, mainly from the run of April 2000, had been previously observed by various teams. Kuhlbrodt (2003 [67]), and Jahnke et al. (2004 [51]) observed some of the objects with the ESO 3.5m New Technology Telescope in the near-IR, and decomposed the data following 2D analytical profiles for the host (exp. disk and de Vaucouleurs) and quasar. Two objects, HE 1302-1017 and HE 1029-1401, were also observed by Bahcall et al (1997 [2]) and classified as elliptical, both with small close companions.

HE 0956-0720 was classified as a disk by Percival et al. (2001 [97]). Our recent HST/ACS imaging of several objects of the sample has also allowed to detect obvious spiral arms in four hosts, namely HE 0306-3301, HE 0354-5500, HE1503+0228 and HE 2345-2906. Table 5.3 gives a summary of the morphological characterizations available, while the adopted morphology is given in Table 5.2.

5.6 Overview of the spectral analysis

Because of the extreme diversity in the gas and stellar contents of quasar host galaxies, the amount of scientific information that can be extracted from our images and spectra is variable from object to object. Most of the types of analysis proposed in the present work are performed only on subsamples presenting similar characteristics, such as the presence of emission or absorption lines, or the presence of a measurable velocity field. We summarize in Table 5.4 which type of measurements was possible for each object.

In spectroscopy, three objects have poor quasar-host separation, either because the quasar reaches the non-linear regime of the detector (1 object, HE 1228+0131), or because of poor PSF determination (2 objects, HE 0956-0720 and HE 1015-1618). However, even with such defects, we would be able to detect galactic emission lines if they were sufficiently prominent and extended. For the three object, we do not detect any underlying emission lines. These hosts are therefore very compact or gas-poor galaxies.

Among the 17 remaining objects, 16 display gas emission lines. For those, we determine the ionisation source of the gas. We classify 9 galaxies as "HII galaxies", i.e. with gas mainly ionized by stars (Section 5.7.2), and estimate the star formation rates for these hosts as well as their mean metallicities. The methods we use in order to determine these parameters rely on the gaseous properties of the HII regions only (Sections 5.7.3 and 5.7.4).

Twelve host galaxies have spatially extended emission lines, that we use to measure their velocity fields as described in Section 5.8.1. Among them, 5 are symmetrical about the central quasar and are good candidates for mass modelling through the rotation curves (Section 5.8). As a by-product, those five regular galaxies give the opportunity to compare the redshift of the object as deduced from the quasar emission lines and as obtained using the emission lines of the host (Section 5.10).

Fifteen galaxies out of the 17 that can be analyzed exhibit measurable absorption lines that we use to infer the stellar content of the hosts (Section 5.7.1). We correlate the Lick indices measured on the absorption lines with the Nucleus-to-Host ratios (N/H) determined in our VLT images, and find that the absorption lines are detected only in galaxies with $N/H \leq 15$. This converts to a limit of about $N/H \leq 45$ in the continuum of the spectra, because of the larger impact of slit losses on the host than on the quasar. We are therefore not able to measure the stellar population of the galaxies with the highest N/H, including the peculiar object HE 0450-2958 for which no continuum is detected at all (Magain et al. 2005 [76]).

Finally, we analyse in Section 5.9 the quasar spectra alone, and measure some of their main physical properties such as luminosity, mass of the central black hole and accretion

Table 5.3: Summary of the hosts morphological types and stellar populations. In each column a "E" indicates an elliptical galaxy, "D" stands for disk and "U" for undefined. (1-) Object name, (2-Lit) morphology according to Bahcall et al. (1997 [2]) and Percival et al. (2001 [97]), (3-NIR) near-IR morphology (Kuhlbrodt 2003 [67], Jahnke et al. 2004 [51]), (4-HST) HST/ACS F606W morphology from our own ongoing program, (5-Dyn) morphology as derived from the velocity curve of the host ("no D" means that a rotating disk is ruled out), (6-) stellar population from Section 5.7.1: "Y" for young spiral-like population, "O" for old elliptical-like population, and "I" for intermediate age population. HE 0450-2958 is not classified because no host is detected.

Object name	Lit.	NIR	HST	Dyn.	Stell. pop.
HE 0132−4313	-	-	-	D	I
HE 0203−4221	-	-	-	U	Y
HE 0208−5318	-	-	-	-	Y
HE 0306−3301	-	E?	D	U	Y
HE 0354−5500	-	-	D	U	Y
HE 0441−2826	-	E	-	-	Y
HE 0450−2958	-	-	-	-	-
HE 0530−3755	-	D?	-	-	-
HE 0914−0031	-	D	-	D	Y
HE 0956−0720	D	E	-	-	-
HE 1009−0702	-	D	-	D	Y
HE 1015−1618	-	D	-	-	-
HE 1029−1401	E	E	-	no D	O
HE 1228+0131	-	E	-	-	-
HE 1302−1017	E?	D?	-	U	Y
HE 1434−1600	-	E	E	no D	O
HE 1442−1139	-	D	-	-	I
HE 1503+0228	-	D	D	D	Y
HE 2258−5524	-	-	-	U	I
HE 2345−2906	-	-	D	D	Y

Table 5.4: Summary of the main spectral characteristics for the 20 host galaxies. (1-) Object name, (2-E) presence of emission lines, (3-A) detection of absorption lines, (4-7) type of analysis performed on the spectrum: gas metallicity (met), star formation rate (sfr), extraction of a radial velocity curve (rvc), and mass modelling (mass). The ionization source of the gas (AGN or young stars) could be detemined for all objects with emission lines, while Lick indices coud be measured in all objects with absorption lines.

Object name	E	A	met	sfr	rvc	mass
HE 0132−4313	x	x	-	-	x	x
HE 0203−4221	x	x	-	-	x	-
HE 0208−5318	x	x	x	x	-	-
HE 0306−3301	x	x	x	x	x	-
HE 0354−5500	x	x	-	-	x	-
HE 0441−2826	x	x	x	x	-	-
HE 0450−2958	x	-	-	-	-	-
HE 0530−3755	x	-	-	-	-	-
HE 0914−0031	x	x	x	x	x	x
HE 0956−0720	-	-	-	-	-	-
HE 1009−0702	x	x	x	x	x	x
HE 1015−1618	-	-	-	-	-	-
HE 1029−1401	x	x	-	-	x	-
HE 1228+0131	-	-	-	-	-	-
HE 1302−1017	x	x	x	x	x	-
HE 1434−1600	x	x	-	-	x	-
HE 1442−1139	-	x	-	-	-	-
HE 1503+0228	x	x	x	x	x	x
HE 2258−5524	x	x	-	-	x	-
HE 2345−2906	x	x	x	x	x	x

rate.

5.7 Stellar and gas content

We can use our spectra in order to carry out a comparative study of the gaseous and stellar contents in active and quiescent galaxies. Prior to the analysis, let us note that for several objects, the galactic Hα emission line is not perfectly separated from the quasar emission because of the combination of (1) the overcrowding of atmospheric lines in this spectral region for objects with highest redshifts, and (2) the very high nucleus-to-host flux ratio in this wavelength range (N/H up to 180). As a consequence, the determination of the amount of reddening in the host galaxy, as well as other measurements involving Hα fluxes and Equivalent Widths (EWs), are not accurate for all objects in the sample. For this reason we present all our results without any correction for dust extinction. This has little influence on most of the characteristics of our host spectra, as we carefully select the estimators of the various galactic properties analyzed here to be as independent on extinction as possible.

5.7.1 Stellar content

The main absorption features are detected in the continuum of 15 out of our 20 galaxies, allowing us to measure several of the Lick indices (Worthey et al. 1994 [120]) and to compare them with the ones measured in two samples of nearby quiescent galaxies: Kennicutt (1992ab [58] [57]; hereafter K92) for late-type galaxies and Trager et al (1998 [112]) for early-type galaxies. The R$_{\mathrm{E}}$D $^{\mathrm{uc}}_{\mathrm{m}}$E[1] package was used to carry out the measurements (Cardiel 1999 [19]). We use the published index measurements of Trager's sample, while we make our own measurements of the indices on the Kennicutt atlas of galactic spectra. As only few absorption features are detected in our spectra, estimates of the stellar velocity dispersions are not reliable. We therefore do no correct our measurments for the velocity dispersion. However, it should be pointed out that such a correction would only slightly change our results within the error bars, and would not affect the global characterization of the sample.

The most prominent absorption lines detected in our spectra are the CaII H and K lines (3969 Å and 3933 Å), the MgII triplet around 5174 Å and the G-band of CH at 4303 Å. The latter is not detected in all galaxies. Hydrogen absorption lines, when present, are always blended with emission. In Fig. 5.7 we plot the Lick indices Mg2 and G4300 as a function of the Hβ index (see Worthey et al 1994 [120] for a detailed definition of the indices). A negative index stands for Hβ in emission. CaHK is not presented because it is not available in T98. The Mg2 index windows are modified with respect to the original definition, in order to avoid contamination from the [OIII]4959 Å emission line: we change the original continuum windows [4895.125−4957.625] and [5301.125−5366.125] Å to [4895.125−4947.625] and [5301.125−5356.125] Å.

---

[1] http://www.ucm.es/info/Astrof/software/reduceme/reduceme.html

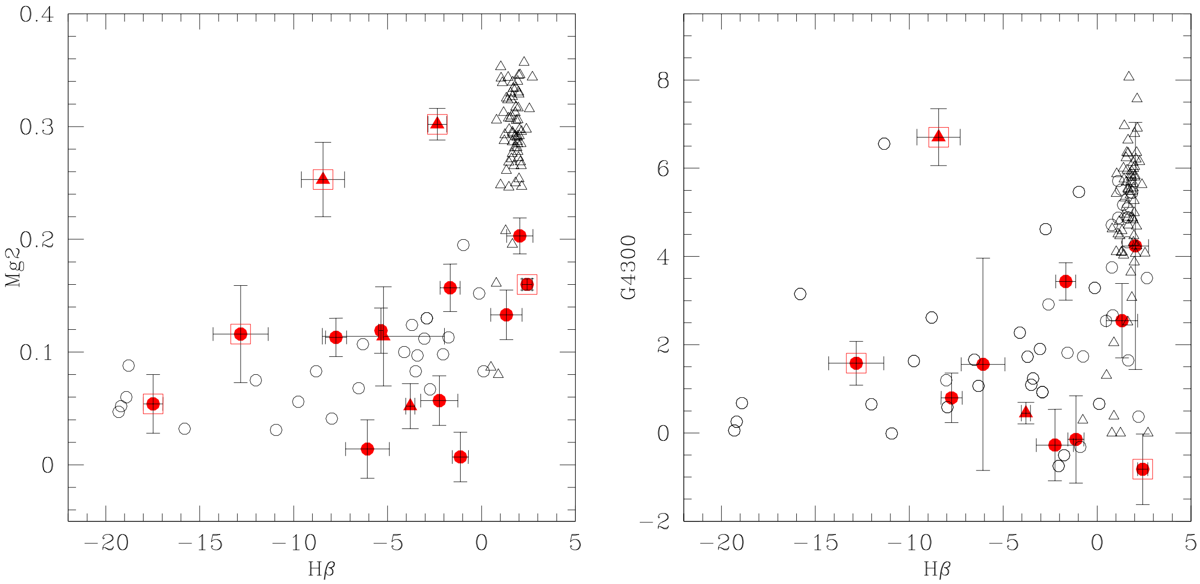

Figure 5.7: Comparison of the Lick indices measured in our quasar hosts (filled symbols) with two samples of non-active galaxies. Open squares identify the galaxies where the gas is found to be ionized by the central quasar (Section 5.7.2). The indices for the samples of Kennicutt (K92) and Trager (T98) are plotted as open symbols. For all three samples, triangles indicate ellipticals galaxies and circles indicate other types of galaxies. Our quasar hosts compare well with the late-type galaxy sample, matching the subsample of Sc or later emission line galaxies.

In Fig. 5.7, the elliptical galaxies from Trager's sample (open triangles) all show large Mg2 and G4300 indices, indicative of the high metallicities associated with old stellar population. They also show Hβ in absorption, representative of gas-poor galaxies. We restricted the Kennicutt sample (open circles) to spiral galaxies showing emission lines, as almost all galaxies of our sample show prominent emission lines. The K92 spiral galaxies are located at lower metallicities than the T98 ellipticals and display negative Hβ, accounting for globally young stellar population and important ionized gaseous content.

Our QSO hosts (filled symbols) follow well the distribution of late-type galaxies, compatible with a subsample of normal Sc population or later because of their similar Hβ emission lines. The hosts of HE 0132-4313, HE 1442-1139, and HE 2258-5524, presenting faint or barely detectable Hβ emission lines, are at the limit between the K92 and T98 samples. They likely host stellar populations characteristic of galaxies between E and Sa types. Among the galaxies identified as ellipticals from their morphology (filled triangles; Bahcall et al 1997 [2], Kuhlbrodt 2003 [67]), only two hosts, HE 1029-1401 and HE 1434-1600, stand in a range of metallicities corresponding to ellipticals, but out of the distribution of T98 comparison sample because of their important Hβ emission.

The ISM of some of our QSO hosts is found to be ionized by the central AGN itself (see Section 5.7.2). We represent these objects with an open square around the filled symbol in Fig. 5.7, as their location in the diagram is biased by a significant contribution of Hβ in emission, induced by the nuclear ionization. It is the case for the old population hosts, and probably for the two objects with extreme Hβ emission which, without this contribution, would rather be located in the bulk of the distribution.

Only two objects in our sample have stellar populations characteristic of genuine elliptical galaxies (see Table 5.3), and 3 have populations intermediate between E and Sa. The other 10 objects display stellar populations typical for young disks rather than bulge-dominated galaxies.

In the following, we classify the objects according to their host morphology. When the classification of an object is secure, we refer to it as Elliptical or Disk. Among the unclassified hosts, we indicate the galaxies with young stellar population (YP) with a distinctive symbol to distinguish them from the objects for which we have no secure information at all. In all but one object for which we have both morphological and stellar population characterization, the young stellar population of the host is associated to disk morphology.

5.7.2 Ionization source

Diagrams comparing the intensity ratios between different emission lines of the host galaxies allow to infer the source of the gas ionisation in the ISM. Such diagrams (Baldwin et al 1981 [4], Veilleux & Osterbrock 1987 [114]) are often used to discriminate between Seyferts and star-forming galaxies, when only a global quasar-plus-host spectrum of the object is available. Here we construct these diagrams for the host spectra only, after the nuclear component has been removed. We therefore determine the main source of ionization of the gas accross the galaxy, but excluding the AGN itself. As far as possible, we choose flux ratios of lines with similar wavelengths, in order to minimize the impact of dust extinction.

Our diagrams are constructed using the [OIII]/Hβ, [NII]/Hα and [SII]/Hα line ratios, the latter two being less accurate because of the difficulty to separate the quasar and host components in the high contrast Hα region. Although it is sensitive to reddening, the [OII]/[OIII] ratio is also used because it can be easily measured in the majority of our quasar hosts. Our diagrams are presented in Fig. 5.8, and the measured values are listed in Table 5.5.

Although reddening by dust cannot be corrected for exactly, its impact on the position of the points in the diagram of Fig. 5.8 can be estimated. In order to do this, we select a subsample of objects that have accurate quasar-host separation in the Hα region and we estimate their reddening from the Balmer decrement. In Fig. 5.8, the points connected by a line refer to a single object, the symbols to the right corresponding to the reddening corrected value of the line ratio. Correcting for extinction would therefore tend to shift all the points towards the right of this diagram.

We find two major sources of ionization: the hard radiation field of the active nucleus itself (power-law ionization source) and ionization by the softer photons produced by young stars in HII regions. However, if a reddening correction was to be applied, all our points in Fig. 5.8 would move further away from the HII zone. Does this mean that none of our hosts is ionized by pure stellar emission ? Most of the low ionization objects (low [OIII]/Hβ ratio) would move, when reddening is taken into account, to the region which, according to Baldwin et al. (1981 [4]), corresponds to shock-heated gas. The objects further away from the HII region locus after correction (with highest reddening) are also galaxies undergoing a minor merger, in which a small companion is being captured by the host. Those small encounters can possibly create shocks, which produce an additional source of ionization, above the young stars themselves.

Table 5.5 gives the intensity ratios integrated over the whole galaxy (without nucleus) and the corresponding classification of the ionizing source, from hot stars (H) to AGN (A). As previously discussed, some objects are, after reddening correction, at the edge of the HII locus on the diagrams, close to the locus of gas ionized by shocks (S). The availability of 2D spectra allows, for object with sufficient S/N in emission lines, to measure the intensity ratios in the external parts of the galaxy (between 2" and 4" from the nucleus). When the diagnostic for these outer regions is different from the global spectrum, we label the ionizing source as mixed (M) and give the corresponding external ratios on a second line. The object classified as intermediate (I) falls between the H and A loci, as a result of mixed but spatially unresolved ionization sources.

All but one of the elliptical galaxies harbour gas, and tend to present high ionization levels, i.e., have ISM ionized by the quasar. Even though our sample contains only 4 elliptical galaxies, there might be a connection between this tendancy and the fact that elliptical hosts exhibit bluer colours than quiescent elliptical (e.g., Jahnke et al 2004 [51]). This blue colour excess is often explained by the presence of a young stellar population, but since the ellipticals in our sample show large amounts of ionized gas and globally old stellar population, we investigate if the strong gas emission lines can account for the observed bluer colours. We therefore estimate the restframe $B-V$ colours of our elliptical hosts directly on the integrated spectra, in two ways: 1- using the 1D spectrum of the

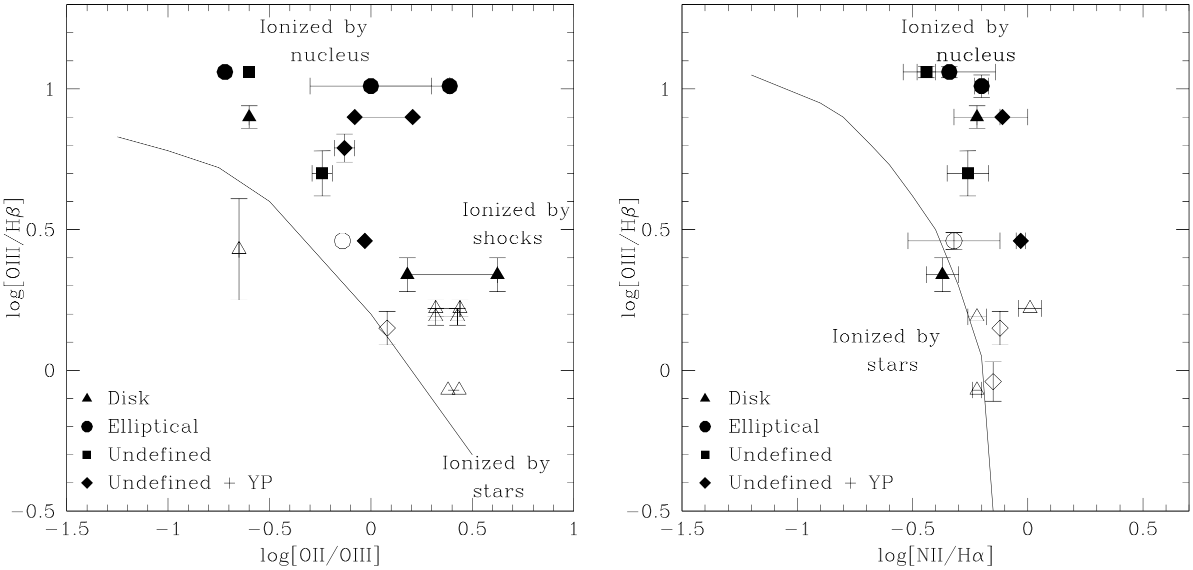

Figure 5.8: Example of diagnostic diagram as constructed following Baldwin et al. (1981 [4]), but for our sample of quasar hosts. Filled symbols are for hosts that display signs of interactions, while open symbols indicate isolated hosts. Error bars on the measurements are drawn when they exceed the symbol size. *Left:* The solid line follows the locus of typical HII regions. Most of the interacting hosts are in the upper part of the diagram, where the central AGN is responsible for the gas ionization. A correction for reddening shifts the points horizontally towards the right, i.e, further away from the HII region locus. Whenever possible, this correction has been applied (see text). A line connects in each case the original measurement and its reddenning-corrected counterpart. *Right:* Same as the left diagram but for the [NII/Hα] ratio. The solid line is the separation between ionization of the gas by stars and by the central quasar. Some of the galaxies in our sample are not shown because of unreliable spectral separation between NII and Hα (see Table 5.5).

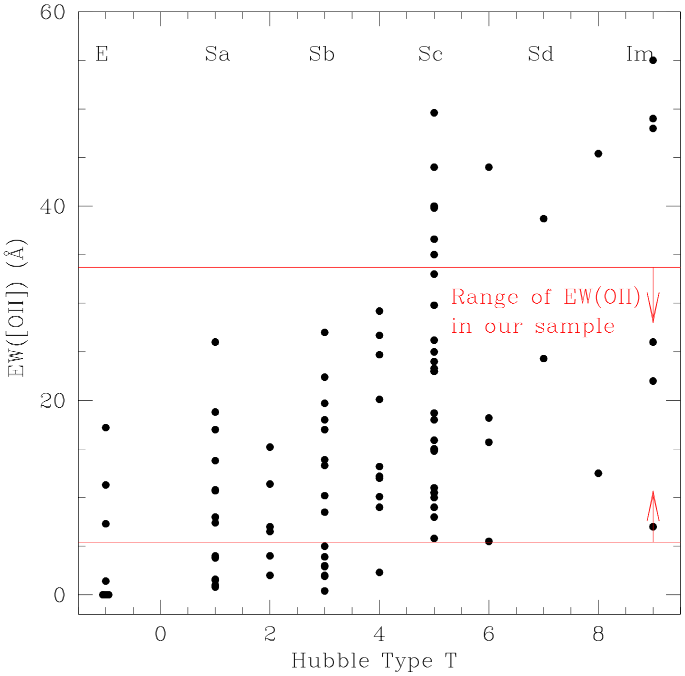

Figure 5.9: EW(OII) as a tracer of star formation rate, in the samples of galaxies from Kennicutt (1992 [58]) and from Jansen et al. (2000 [53]) restricted to the brightest part of the luminosity function. The range of EWs spanned by our HII galaxies is shown by the horizontal lines, suggesting that there are no quasar hosts with low star formation rate. The majority of quiescent elliptical galaxies presents no [OII] emission line at all while most of our elliptical hosts do.

host, and 2- using a modified version of the spectrum where the emission lines have been removed. We find that the emission lines can account for a colour variation of about 0.03 mag. As the average colour difference between active and quiescent ellipticals is as large as Δ(B-V) = 0.44 (Jahnke et al. 2004 [51]), we can conclude that the presence of ionized gas is not sufficient to explain the bluer colours in active galaxies compared to quiescent ones.

5.7.3 Star formation rate

Star formation rates can be estimated only on galaxies presenting line ratios characteristic of HII regions, thus avoiding extra emission arising from nuclear ionization. We therefore restrict this section to the objects labelled *H* in Table 5.5, excluding HE 0132-4313 in which [OII] is not detected. From the discussion of Section 5.7.1, we note that all galaxies in this subsample present a young stellar population. Five of them are spirals, one is elliptical and the last two have undefined morphologies.

Several estimators of the star formation rate (SFR) are available in the optical range,

Table 5.5: Logarithmic line ratios for the host galaxies with emission lines. The last column gives our diagnostic on the ionization source: H stands for normal HII region, S for shock heated gas, A for ionization by *active* nucleus. M (*mixed*) indicates galaxies that, as a whole, show ionizion typical for HII regions, but where ionization by the AGN is found locally (when two lines of measurements are given, the second line gives the line ratios measured between 2" and 4" away from the nucleus). I stands for *intermediate* between A and H, and consists of a spatially unresolved version of M. Oxygen line ratios indicated in parenthesis are corrected for reddening. The ratios involving the Hα line for HE 0441-2826 are only indicative, as the correction for atmospheric absorption is poor for this object (see Fig. 5.21).

Object	$\frac{\text{OII}}{\text{OIII}}$	$\frac{\text{OIII}}{\text{H}\beta}$	$\frac{\text{NII}}{\text{H}\alpha}$	$\frac{\text{SII}}{\text{H}\alpha}$	I.S.
HE 0132−4313	-	-0.04	-0.15	-	H
HE 0208−5318	0.08	0.15	-0.12	-	H
HE 0306−3301	0.18 (0.62)	0.34	-0.37	-0.63	H/S
HE 0441−2826	-0.14	0.46	(-0.32)	(-0.69)	H
HE 0914−0031	-0.65	0.43	-	-	H
HE 1009−0702	0.32 (0.44)	0.22	0.01	-0.28	H/S
HE 1302−1017	-0.03	0.46	-0.03	-0.39	H/S
HE 1503+0228	0.32 (0.43)	0.19	-0.22	-	H/S
HE 2345−2906	0.38 (0.44)	-0.07	-0.22	-0.32	H
HE 0203−4221	-0.13	0.70	-	-	M
	-0.13	0.79	-	-	
HE 0354−5500	-0.49	0.21	-0.19	-0.55	M
	-0.6	0.9	-0.22	-	
HE 2258−5524	-0.10 (0.21)	0.62	-0.20	-0.58	M
	-0.08	0.9	-0.11	-	
HE 0530−3755	-0.24	0.70	-0.26	-	I
HE 0450−2958	-0.60	1.06	-0.44	-0.28	A
HE 1029−1401	0.02 (0.39)	1.01	-0.20	-0.02	A
HE 1434−1600	-0.72	1.06	-0.34	-0.65	A

one of the most widely used being the integrated flux in the Hα emission line. However, because of the poor quasar-host separation at this wavelength for several objects, we adopt another indicator, [OII] 3727 Å, as suggested by Kennicutt (1998 [59]) and Kewley et al. (2004 [60]). In order to get rid of the effect of dust extinction, we directly compare our EW([OII]) with measurements in non-active galaxies, sorted by Hubble type. As a reference sample, we use the atlas of galaxies from K92 augmented by the sample of nearby galaxies of Jansen et al. (2000 [53]). We restrict ourselves to the brightest part of the luminosity function with $M_B < -18$, as the EW([OII]) is slightly correlated with magnitude.

Figure 5.9 shows the measurements, with a slight evolution of EW([OII]) with Hubble type, the later-type galaxies displaying larger EWs. We overplot on the reference sample the range of values spanned by our quasar hosts. Figure 5.9 shows that none of our hosts has a low star formation rate. The EW([OII]) of our sample are compatible with a population of disk-dominated regular galaxies, as the stellar population also suggest.

5.7.4 Gas metallicity

The oxygen abundance in the ISM, as an indicator of the enrichment of gas by stars in the galaxies, allows to characterize still further our sample of QSO hosts where gas is confidently ionized by stars. We first describe the methods used to evaluate the gas metallicity, then we compare our sample to non-active galaxies.

The standard measurement of the gas metallicity, log(O/H)+12, can be evaluated by the parameters R23 (ratio of collisionally excited emission-line intensities) and O32 (indicator of ionization parameter):

$$\begin{aligned} R23 &= \frac{I([\mathrm{OII}](3727)) + I([\mathrm{OIII}](4959+5007))}{I(\mathrm{H}\beta)(4861)} \\ O32 &= \frac{I([\mathrm{OIII}](4959+5007)}{I([\mathrm{OII}](3727)} \end{aligned}$$

The R23-oxygen abundance relation is globally double-valued (see e.g. McGaugh 1991 [83]). For a given value of O32, the parameter R23 is related to two metallicities, one for metal-rich gas (on the so-called *upper branch*) and one for metal-poor gas (*lower branch*). Gas with log(O/H)+12 $>$ 8.5 is considered metal-rich, while with log(O/H)+12 $<$ 8.3 it is metal-poor. In the metal-rich regime, R23 increases progressively with decreasing metallicity, since lower metal abundance implies e.g. a higher degree of collisional excitation. Below the turnaround region around log(O/H)+12 $=$ 8.4, the R23 parameter starts to decrease back with metallicity because of the greatly reduced oxygen abundances of the ISM. This R23 degeneracy is broken by the analysis of the ratios NII/OII or NII/Hα, which both grow linearly with metallicity, distinguishing between high and low metallicity regimes. We use here the calibrations for upper and lower branches from McGaugh (1991 [83]), as given in Eqs. 7 to 10 of Kobulnicky et al. (1999 [62]).

While this estimator has been widely used to infer oxygen abundances in well resolved local HII regions, Kobulnicky et al. (1999 [62]) have shown that global emission-line spectra could also indicate the chemical properties of distant star forming galaxies. A reliable

Table 5.6: Gas metallicities expressed as log(O/H) + 12, computed from McGaugh (1991 [83]) EWR23 correlation as given in Kobulnicky et al. (1999 [62]). We corrected the Hβ EWs of the last two objects for underlying stellar absorption. The maximum bulge-to-host ratio is estimated as discussed in the text.

Object name	log(O/H)+12	1σ error	bulge/host
HE 0208−5318	8.41	0.11	0.8
HE 0306−3301	8.45	0.16	0.5
HE 0441−2826	8.28	0.12	-
HE 0914−0031	8.83	0.11	0.7
HE 1009−0702	8.34	0.14	0.2
HE 1302−1017	8.48	0.08	0.8
HE 1503+0228	8.53	0.05	0.3
HE 2345−2906	8.88	0.05	0.4

estimate of the metallicity can also be reached with EWR23 and EWO32, the same parameters as R23 and O32 but computed on EWs and not on intensities (Kobulnicky et al. 2003 [63]). As the line EWs are insensitive to interstellar reddening effects, the EW version is to be preferred in our case since extinction cannot be properly corrected for the whole sample. The EWR23 method is however affected by an additional uncertainty of around 0.1 dex in comparison to other methods (Moustakas & Kennicutt 2005 [93]).

The abundances of our sample deduced from this EW calibration are listed in Table 5.6. Most of these abundances correspond to the turnaround region, with NII/OII and NII/Hα ratios pointing to the metal-rich branch. HE 0441−2826, the most metal-poor object of the sample, is at the extreme limit of validity of the upper branch.

We compare in Fig. 5.10 the oxygen abundances of QSO host galaxies presenting gas ionized by stars to other samples of integrated spectra for emission-line galaxies: a sample of blue compact galaxies, representing very metal-deficient environments (Izotov 1999 [49]), and the sample of irregulars and spirals of Jansen et al. (2000 [53]), used in the previous section for SFR characterization, with metallicities computed by Kewley et al. (2005 [61]). This sample contains all types of spirals, from S0 to Sd. The trend for earlier-type spirals (S0-Sab) is to contain gas with higher metallicity, with log(O/H)+12 around 9, while the small bump at lower metallicities (between 8 and 8.5) in this distribution corresponds roughly to irregular galaxies.

The two most metal-rich galaxies of our sample, HE 2345-2906 and HE 0914-0031, sit in the middle of the spiral distribution. As for both we find no trace of interaction, disk morphologies, and median to low SFR, we suggest that they have undergone a normal spiral galaxy evolution. In the case of HE 0914-0031, the cause of ignition of the quasar is thus still unknown. Recent HST/ACS images of HE 2345-2906, currently under treatment, reveal a prominent bar, that could be an efficient driver of gas and dust to the central region, which would trigger the QSO activity, as suggested by Crenshaw et al. (2003 [26]) for another type of AGNs, the Narrow Line Seyferts 1 (NLS1).

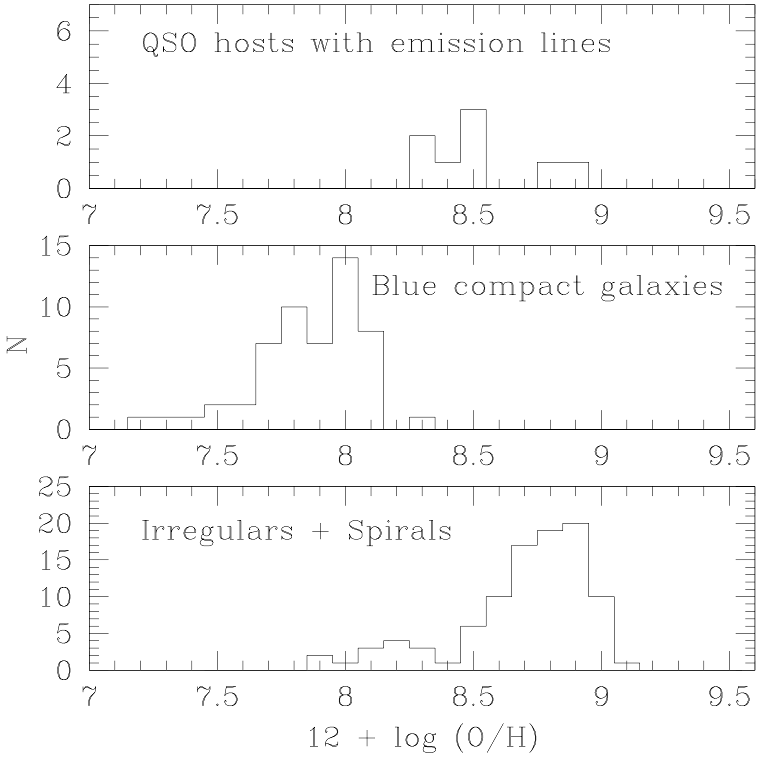

Figure 5.10: Histogram of gas metallicities estimated on global spectra in our sample (top panel), in blue compact galaxies (Isotov 1999 [49], middel panel), irregulars and spirals (Kewley et al. 2005 [61], bottom panel). While two galaxies lie perfectly in the spiral distribution, the other present intermediate metallicities, inbetween a first generation of stars and spirals.

The rest of the sample has metallicities inbetween the blue compacts and the more evolved spirals. The gas in these host galaxies is similar to the gas of irregulars, arising from a rather inefficient star formation. HE 1302-1017, with the highest SFR of the sample, an irregular radial profile and signs of small companions merging in, is thus a very young system where both nuclear activity and star formation have just been triggered by the mergers. For HE 0306-3301, the minor merger only induced nuclear activity without enhancing drastically the star formation. The four other galaxies show no trace of gravitational interaction. They must also be young systems (compatible with their young stellar population, and with the disk morphology found for most of them) but in which the origin of activity is, as in HE 0914-0031, still unexplained.

Following the $\mathrm{M_{BH}}$-$\mathrm{M_{bulge}}$ scaling relation observed in active and inactive galaxies (McLure & Dunlop 2002 [86]), the observed luminosities of the quasars and thus their central masses ($> 6 \,.\, 10^7 M_\odot$) imply a substantial bulge ($\mathrm{M}_V < -21.3$) on all those host galaxies. The young stellar and gaseous content inferred for them doesn't match a bulge population, but rather a disk-like one. We estimate the bulge/host ratios from the V magnitudes of Table 5.2 and the bulge magnitudes from the $\mathrm{M_{BH}}$ estimates of section 5.9.3 (Table 5.6). Given that these ratios are upper limits because the host magnitudes are not corrected from reddening and may be underestimated (section 5.3.2), they are fully consistent with typical late-type spiral ratios.

In the majority of the cases analyzed in this section, the quasar activity obviously appears in galaxies in which the star formation has had a low efficiency so far. This suggests that these spiral hosts are at an early stage of their evolution and, thus, that one of the mechanisms for triggering quasar activity may be linked to the formation or very early evolution of (at least some) spiral galaxies. As discussed in the next section, galactic collisions are obviously another (and more powerful) triggering mechanism.

The origin of the triggering of activity might be confined in the central part (< 1 kpc, i.e. the pixel size of our data) of the galaxy, not giving rise to any hints about it on the global characteristics as studied here.

5.7.5 Average spectra

For the sake of illustration, we computed average spectra for several subsamples of our 20 host galaxies. The averages are presented in Fig. 5.11 for galaxies classified as spirals and for galaxies with an undefined type and a young stellar population. Fig. 5.12 gives average spectra for galaxies with an ISM ionized by the central quasar on one hand and by stars on the other hand. The four spectra with the lowest signal-to-noise have been removed from the sample, as well as HE 0450-2958 for which no stellar continuum is detected at all. The averaging is performed on the spectra in the rest-frame. They are all normalized to unit flux at 5100 Å and weighted according to their signal-to-noise ratio. The two average spectra in Fig. 5.11 present similar global features, indicating that an important fraction of the galaxies with an undefined morphological type should be spirals. In Fig. 5.12, the average on galaxies with gas ionized by stars has a blue continuum while the continuum for galaxies where the gas is ionized by the nucleus is flatter. As expected in HII regions, this

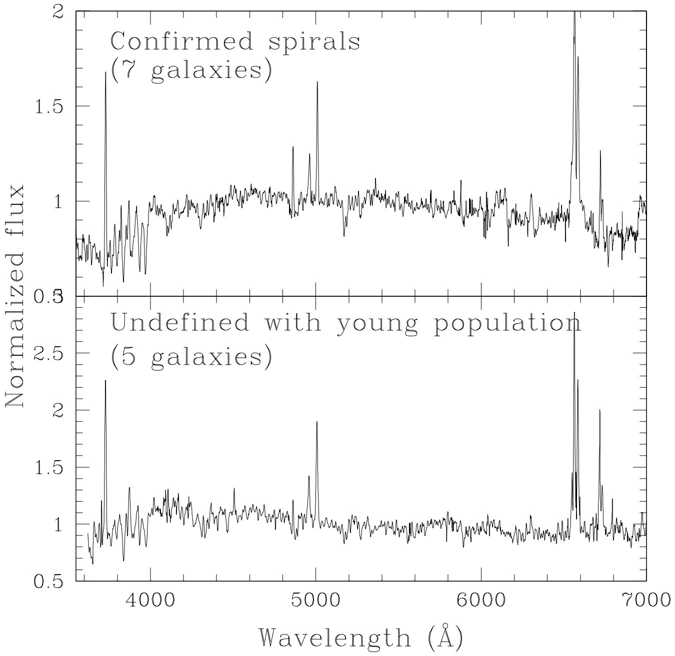

Figure 5.11: *Top:* average spectrum for spiral hosts. *Bottom:* average spectrum for hosts with an undefined morphology but young stellar population.

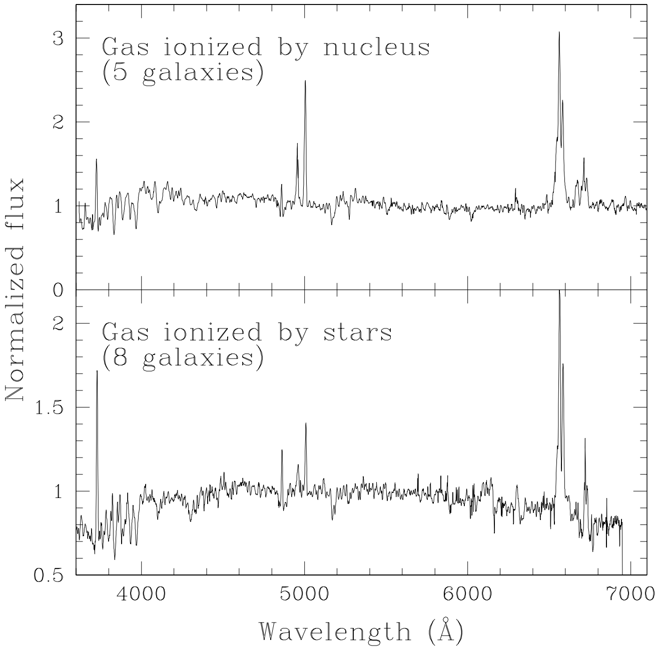

Figure 5.12: *Top:* average spectrum for quasar hosts where the gas is ionized by the quasar. *Bottom:* average spectrum for hosts where the gas is ionized by stars.

blue slope indicates young stars, while ionization by the quasar appears in a mix of galactic types with a larger range of slopes, hence producing in average a flatter continuum.

5.8 Dynamics and interaction

5.8.1 Radial velocity curves and mass modelling

We take advantage of the very different spectral widths of the emission lines in the quasar and in the host galaxy to carry out a very accurate quasar-host separation in the emission lines. This procedure, described in detail in Courbin et al. (2002 [24]), allows to extract detailed information on the velocity of the gas in the host galaxy.

This spectral decomposition method is applied to all the spectra showing sufficiently high signal-to-noise ($S/N > 5$ per pixel) in the external parts of the hosts. Figure 5.13 presents the radial velocity curves extracted in that way. When several emission lines are extracted for the same object, they are represented by different symbols on the same plot. Figure 5.13 shows that many radial velocity curves are distorted and thus cannot be fitted by simple mass models as described in Courbin et al. (2002 [24]). These galaxies are probably disturbed by ongoing or past gravitational interactions with nearby companions.

Fitting a mass model on the velocity curves requires knowledge of the inclination and Position Angle (PA) of the disk (if any is involved). They are estimated using the acquisition images taken before each spectrum, using a modified version of the MCS deconvolution algorithm that includes a 2D analytical model for the host galaxy.

The results of the mass model fits on symmetrical velocity curves (see Courbin et al. 2002 [24]) are represented by a solid line in Fig. 5.13. The corresponding mass estimates are given in Table 5.7, along with the inclination of the disk component on the line of sight and the angle of the major axis relative to the slit. The mass model includes a dark matter halo, a stellar rotating disk, and a fixed central mass (from Section 5.9.3). With our spatial resolution (0.2" per pixel, which translates into a linear scale between 0.6 and 1.0 kpc depending on redshift), adding a bulge component does not improve the fits and prior knowledge of the central mass (e.g., estimates using the $H\beta$ line of the quasar) do not constrain the model significantly. The mass modelling does not allow to weight the relative contributions of disk and bulge in the galaxies. Table 5.7 shows that these hosts are rather massive spirals, while not disproportionate relative to their inactive counterparts.

Although the velocity curves of HE 1434-1600 and HE 1029-1401 look symmetrical, they cannot be fitted with a realistic set of parameters. Close scrutiny of the images reveals, in both cases, elliptical galaxies with neighbours merging in or interacting, which excludes the assumption of a simple circular motion. The special case of HE 1434-1600 has been presented in Letawe et al. (2004 [69]). HE 1029-1401 is seen nearly face-on (Kuhlbrodt 2003 [67]), and interpreting radial velocities as rotational velocities would give unrealistic masses (up to 10^{17} $M_{\odot}$) given the inclination angle.

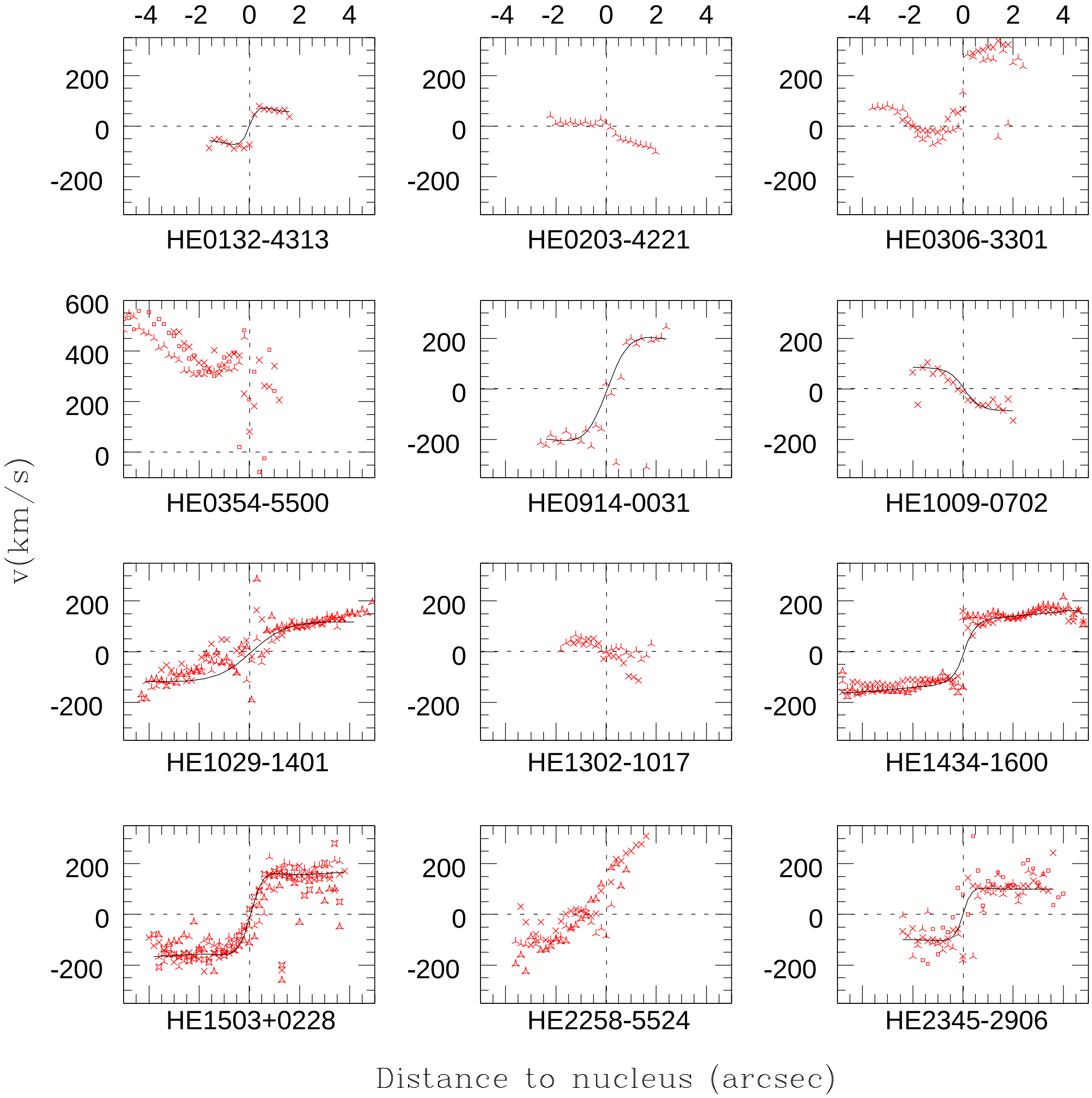

Figure 5.13: Extracted radial velocity curves for all objects with sufficient S/N in the emission lines. The Hα line is represented by 4-arms crosses. Since some grisms have overlapping spectral ranges the Hα line may appear twice. In such a case, the measurement of this line in the second grism is plotted as 4-arms stars. The [OIII] line is represented by 3-arms crosses (and stars when a second measurement is available) and the [OII] line is represented by squares. The solid lines represent mass model fits when relevant (see text).

Table 5.7: Mass estimates for spiral galaxies with symmetrical rotation curve. The adopted model consists of a rotating disk, a dark matter halo and a central mass. All masses are in solar units. i is the inclination of the disk and ϕ is the angle of the major axis of the galaxy relative to the slit. The determination of these angles is the main source of uncertainty in our mass estimates. The last two galaxies have smaller error bars because HST images are available to determine i and ϕ.

Object	ϕ (°)	i (°)	log M ($r < 10$kpc)
HE 0132−4313	78	37	$11.9^{+0.2}_{-0.7}$
HE 0914−0031	68	32	$12.6^{+0.5}_{-0.3}$
HE 1009−0702	66	29	$11.7^{+0.5}_{-0.3}$
HE 1503+0228	18	46	$11.0^{+0.1}_{-0.1}$
HE 2345−2906	70	36	$12.0^{+0.1}_{-0.1}$

5.8.2 Interactions

Signs of interaction are found for nine out of the twenty galaxies in our sample, i.e., in 2 spirals, 2 ellipticals and in 5 galaxies with undefined morphology. The hosts whose images (from this or previous studies) show irregular shapes, reminiscent of interaction are labelled "interac" in Fig. 5.5, while a classification of the signs of interactions is given in Table 5.2: close companion outside the galaxy (1), tidal tails (2) or merger, i.e. companion inside the galaxy (3). A confirmation of those perturbations is provided by the extracted radial velocity curves presented in Fig. 5.13. All the hosts with asymmetric curves also have images with irregular shapes. We find that ∼ 50% of our host galaxies display signs of interaction, which is compatible with several previous studies (Smith et al. 1986 [104], Hutchings & Neff 1992 [48], Bahcall et al. 1997 [2], Sanchez et al. 2004 [101], Jahnke et al. 2004 [51]). This is also compatible with the fraction of interacting but non-active galaxies according to Dunlop et al. (2003 [30]).

The diagnostic diagram in Fig. 5.8 to the right, shows that every galaxy with long-range ionization by the nucleus is also interacting. The mechanism at work is probably similar to the one responsible for the Extended Emission Line Regions (EELR) usually associated with radio-loud quasars (Boroson et al. 1985 [10], Stockton & McKenty 1987 [109]) or Seyferts with radio emission (Evans et al. 1999 [32]), as presented in Stockton et al. (2002 [110]). During the interaction, the dust surrounding the quasar is swept out or sufficiently perturbed, letting the ionizing nuclear beam reach the gas in the outer parts of the galaxy and ionizing it. Shocks induced by the interaction are considered as complementary sources of ionization. If the radio jet alone was sufficient to produce EELR, this phenomenon would be more common in Radio Loud Quasars. The present study widens the type of galaxies where this phenomenon appears to the hosts of radio quiet quasars (RQQ), as only 2 out of the 7 cases of ionization by the central quasar display radio emission, at a level under the limit of classification as Radio Loud. To our knowledge, almost no high level ionization in galactic gas was previously found in RQQ (only one object in Stockton & McKenty 1987 [109]) probably only because of the lack of a detailed spectral study of this kind of host galaxies.

The unused slits of MOS spectrograph were placed on galaxies in the field, looking for companions at the same redshift as the quasar. While this is far from being an exhaustive analysis of the neighbourhood of each object, we find that 13 out of the 20 quasars have no detected neighbour, 4 quasars have one neighbour, 2 quasars have two and HE 1434-1600 has 5 neighbouring galaxies with close redshifts (Letawe et al. 2004 [69]).

5.9 Nuclear properties

In this Section we derive several properties of the quasars from their spectra, and investigate their relation with their host type, properties or environment. We first correct the quasar spectra from reddening, assuming a theoretical Balmer decrement $H\alpha/H\beta = 3.1$ and using the Whitford reddening curves (Miller & Mathews 1972 [89]). The reddening correction in this optical wavelength range is not sensitive to the choice of the reddening curves.

5.9.1 Spectral characteristics

The quasar properties which have been derived from the de-reddened spectra are listed below and summarized in Tables 5.8 and 5.9:

- The luminosities of emission lines: [OII] 3727 Å and [OIII] 5007 Å, indicators of the amount of gas and ionization of the Narrow Line Region (NLR) as well as Hβ for the Broad Line Region (BLR);
- The power law index of the continuum α ($F(\lambda) \propto \lambda^{\alpha}$), indicator of the power of the source. We evaluate it from the continuum slope in the $\log F$ versus $\log \lambda$ diagram;
- The monochromatic luminosity at 5100 Å, another indicator of the power of the nucleus, used for estimating the bolometric luminosity;
- The ratio [OIII]/Hβ;
- The FWHM of Hβ, useful for black hole mass determination (see Section 5.9.3);
- The presence of Fe II lines, noticeable by emission line multiplets, such as for instance in HE 0132-4313 but not in HE 0203-4221 (see Fig. 5.20).

Some of these spectral characteristics are plotted in Fig. 5.14, which shows that the quasars involved in galactic interactions (filled symbols) have more emission from the gas in their immediate surroundings (higher luminosities in broad and narrow lines). As [OIII]

Table 5.8: Nuclear luminosities for the whole sample, in erg s^{-1}. α is the power law index of the continuum ($F(\lambda) \propto \lambda^{\alpha}$). Colons indicate the objects for which the important reddening measured on the broad lines probably does not apply to the continuum or narrow lines (see text). The atmospheric absorption overlapping Hα in HE 0441-2826 spectrum was corrected before Balmer decrement evaluation, but the deduced extinction is considered as a lower limit.

Object	A_V	log $L_{[OII]}$	log $L_{[OIII]}$	log $L_{H\beta}$	α	log λL_{5100}
HE 0132−4313	0.09	41.29	40.97	42.65	-2.4	44.95
HE 0203−4221	2.53:	43.26:	44.37	44.57	-4.4:	46.44:
HE 0208−5318	0.00	41.36	42.40	43.34	-2.7	45.07
HE 0306−3301	0.09	41.61	42.61	43.15	-2.3	45.02
HE 0354−5500	0.27	41.81	42.72	43.35	-2.5	45.01
HE 0441−2826	>1.58:	42.42:	43.33:	43.13:	-3.5:	45.66:
HE 0450−2958	0.59	43.08	43.72	44.19	-2.7	45.84
HE 0530−3755	1.71:	42.75:	43.89	43.91	-4.0:	45.48:
HE 0914−0031	0.92	41.41	42.76	43.38	-3.0	45.02
HE 0956−0720	0.47	-	42.58	43.58	-2.4	45.24
HE 1009−0702	0.91	41.48	42.63	43.36	-2.6	45.11
HE 1015−1618	0.00	41.06	42.52	43.29	-1.3	44.98
HE 1029−1401	0.81	41.55	42.60	43.32	-2.7	45.04
HE 1228+0131	0.57	-	42.56	43.15	-2.5	45.04
HE 1302−1017	1.23:	42.04:	43.37	43.81	-3.3:	45.86:
HE 1434−1600	2.53:	42.52:	43.65	43.67	-4.4:	45.29:
HE 1442−1139	0.70	41.21	41.23	42.84	-1.8	44.61
HE 1503+0228	1.02	40.71	42.09	42.85	-3.0	44.67
HE 2258−5524	0.27	41.08	41.66	42.81	-2.8	44.91
HE 2345−2906	0.76	41.41	42.28	42.81	-3.0	44.48

Table 5.9: Nuclear spectral characteristics for the whole sample and derived values of the BH mass and accretion rate. The FWHM of the broad Hβ component is expressed in km s^{-1}. Black hole masses are given in logarithm of solar masses and accretion rates in solar masses per year. Colons indicate the objects for which the important reddening measured on the broad lines probably does not apply to the continuum or narrow lines (see text).

Object	A_V	FeII	FWHM(Hβ)	$\frac{[OIII]}{H\beta}$	log M_{BH}	$\dot{M}$
HE 0132−4313	0.09	x	1056	0.02	7.24	0.93
HE 0203−4221	2.53:		7299	0.63	9.93:	27.40:
HE 0208−5318	0.00		6075	0.11	8.80	1.09
HE 0306−3301	0.09	x	2346	0.29	7.98	1.11
HE 0354−5500	0.27	x	2264	0.09	7.94	1.06
HE 0441−2826	>1.58:		5771	1.69	9.25:	1.12:
HE 0450−2958	0.59	x	1282	0.34	7.81	3.54
HE 0530−3755	1.71:		1721	0.95	8.02:	3.06:
HE 0914−0031	0.92		3072	0.24	8.20	1.05
HE 0956−0720	0.47		2636	0.1	8.22	1.71
HE 1009−0702	0.91	x	1826	0.18	7.83	1.36
HE 1015−1618	0.00	x	2212	0.17	7.89	0.98
HE 1029−1401	0.81		5887	0.19	8.85	1.37
HE 1228+0131	0.57	x	1403	0.26	7.58	1.30
HE 1302−1017	1.23:		2945	0.36	8.76:	7.40:
HE 1434−1600	2.53:		7068	0.95	9.15:	2.20:
HE 1442−1139	0.70	x	2063	0.02	7.58	0.42
HE 1503+0228	1.02		2990	0.17	7.96	0.52
HE 2258−5524	0.27	x	1352	0.07	7.40	0.78
HE 2345−2906	0.76		4138	0.29	8.10	0.32

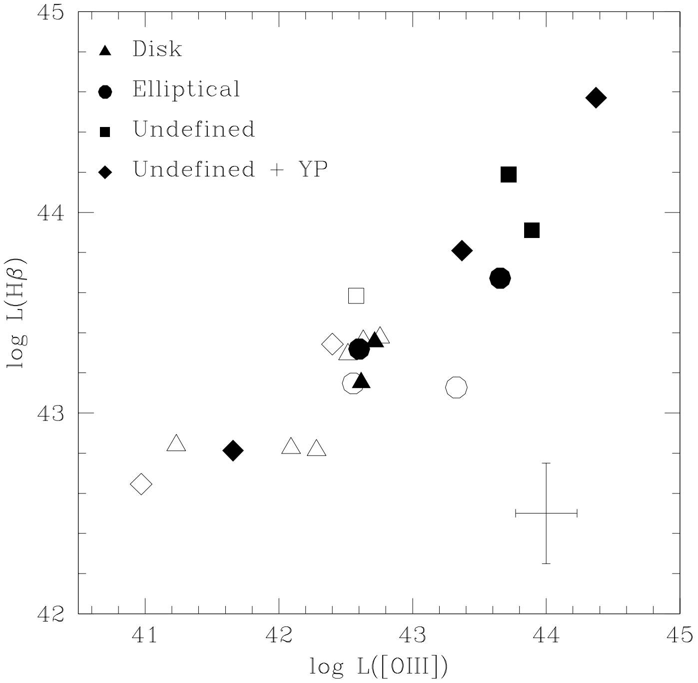

Figure 5.14: Luminosity of the nuclear Hβ versus luminosity of the nuclear [OIII] 5007 Å emission line. The characteristics of the host galaxies are as stated in the legend. Filled symbols are for quasar hosted by galaxies that display signs of interaction. Typical 1-σ error bars are shown, including errors on continuum subtraction for measurement of luminosities and uncertainties in reddening correction. Luminosities are in erg s^{-1}.

is a good tracer of AGN power (Kauffmann et al. 2003 [55]), we conclude that the quasars in interacting systems are also more powerful. This gives us direct evidence that the gravitational interactions constitute an essential process in bringing gas in the vicinity of the black hole and feeding it. Moreover, as we have seen from Fig. 5.8, highly ionized galactic gas is found in interacting systems, i.e. the ones which harbour the most powerful quasars. A high power of the quasar thus seems essential for ionizing gas at large distance from the nucleus. It should also be pointed out that no quasar with a spiral host is found among the most powerful ones. This may be linked to the fact that strong gravitational interactions are incompatible with regular spiral structure.

Narrow line quasars In examining the quasar spectral characteristics, we note that 5 quasars (HE 0132-4313, HE 0450-2958, HE 1009-0702, HE 1228+0131 and HE 2258-5524) are fulfilling the Narrow Line Seyfert 1 (NLS1) criteria, e.g. FWHM(Hβ) $< 2000\,\mathrm{km\ s^{-1}}$, strong FeII multiplets and [OIII]/H$\beta < 3$ (Bian et al. 2004 [6]), even if their luminosities are characteristic of quasars and not of Seyferts. We call them "Narrow Line QSOs" (NLQSOs), with similar properties as NLS1 but at higher luminosities (as suggested by Stepanian et al. 2003 [107]). The proportion evaluated from optically selected samples amounts to 10% only (Grupe et al. 2004 [41]), while it reaches here 25%, although our sample is also optically selected. There was no selection bias on the spectral properties of the sample, but there are only 6 objects with obvious broad components (FWHM(Hβ) $> 4000\,\mathrm{km\ s^{-1}}$), while the rest of the sample (9 objects) has intermediate broadness in hydrogen lines. A deeper investigation on HES quasar spectra reveals that 11% of the quasars in the Survey are found to have FWHM(Hβ) $< 2000\,\mathrm{km\ s^{-1}}$, as in other optically selected samples. But as the measurement of the FWHM is highly sensitive to spectral resolution and S/N (lower in HES than in this present study), only one of the 5 objects of the present sample is a NL according to the original HES spectra. The actual proportion of NLQSOs is thus probably higher than 11% in HES, and this argument might also hold for other optical surveys. While there is no criterion on emission line characteristics in HE selection, the distribution in HES is strongly peaked with a modal value of about 2700 $\mathrm{km\ s^{-1}}$ and a median of 2940 $\mathrm{km\ s^{-1}}$, not so large according to the spectral resolution used. The conventional limit of 2000 $\mathrm{km\ s^{-1}}$ for separating NLQSOs from those with broad lines does not seem to be a valid separation of distinct quasar sub-populations. For instance, we could add 4 more NL candidates in our sample if the limit was situated at 2300 $\mathrm{km\ s^{-1}}$ rather than 2000 $\mathrm{km\ s^{-1}}$ (all quasars but one presenting prominent iron lines have a Hβ FWHM close to this limit), reinforcing our suggestion that the present NLQSO classification is largely arbitrary.

We investigate nevertheless the galactic properties of those five NLQSOs: they span the whole range of magnitudes of our sample, 2 out of 5 are interacting, 3 have morphologically undefined hosts (2 with intermediate-age stellar population, 1 undefined), one spiral and one elliptical. The nucleus-to-host luminosity ratio estimated from images ranges between 3 and 18, except for the peculiar HE 0450-2958 described in Magain et al. (2005 [76]) for which the upper limit on host magnitude gives a minimum N/H of 85. Mass modelling (Section 5.8.1), applied to two of the NLQSOs reveals neither under- nor over-massive hosts compared to broad line QSOs. There is thus no clear tendency for NLQSOs to appear in a special type of host galaxy.

5.9.2 Comments on reddening and dust content around the nucleus

The reddening-corrected power law indices α listed in Table 5.8 suggest that a few quasars have a very steep continuum. These quasars are precisely the ones for which the reddening, as deduced from the Balmer decrement, is largest. This is illustrated in Fig. 5.15 (left), which shows the power law index α versus the dust absorption A_V. A clear correlation appears, confirming that the steep continua correspond to strong reddening.

We find no obvious physical interpretation for such a correlation. On the other hand, it could be understood if the distribution of dust responsible for the reddening is inhomogenous on scales smaller than the size of the BLR (e.g. patchy or in a torus around the BLR). In such a case, since the accretion disk responsible for the continuum light is expected to be much smaller than the BLR, the reddening of the continuum might be significantly different from the reddening of the BLR, as deduced from the Balmer decrement. The latter would be some kind of average, while the reddening of the continuum might be larger (in case a dense dust cloud happens to sit on the line-of-sight to the accretion disk) or smaller (in case the same line-of-sight goes through a hole in the dust distribution).

The correlation found in Fig. 5.15 (left) might then be due to a selection effect. The quasars with strong reddening of the BLR may have either (1) even stronger reddening of the continuum (dust cloud in front of the accretion disk) or (2) lower continuum reddening (hole in front of the accretion disk). In the first case, the quasar continuum becomes significantly fainter and the object is not included in our bright quasar sample. In the second case, the continuum is not much absorbed and the quasar appears bright enough to be included in our sample. This selection effect could explain why, among the quasars with strong reddening of the BLR, only those with a weaker reddening of the continuum are present in our sample. The quasar spectra of HE 0441-2826 offers a good illustration of this possible phenomenon (Fig. 5.21), with steep continuum and highly reddened broad lines.

As a consequence, the reddening deduced from the Balmer decrement is not applicable to the continuum. It is also probably not applicable to the NLR, which may be much larger than the BLR.

Derived physical values involving continuum or narrow line fluxes have thus to be taken with caution, especially for those quasars presenting a strong reddening of the BLR. Among the narrow lines used, [O II] 3727 is the most sensitive to reddening and should be avoided whenever possible.

When the BLR is significantly reddened, it is unlikely that there is no dust at all in front of the accretion disk as well as in front of the NLR. Thus, we keep the reddening-corrected values as our best choices. It should be kept in mind, however, that the reddening corrections for continuum and NLR features are probably overestimates when $A_V > 1$.

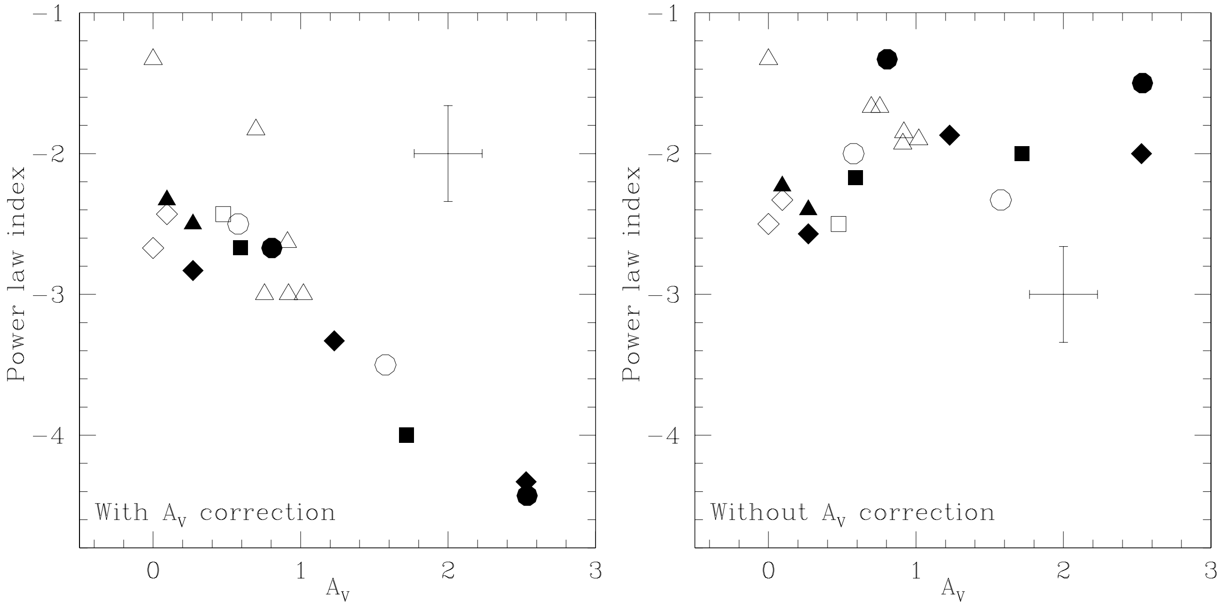

Figure 5.15: Left: Power law index corrected from reddening versus the reddening A_V estimated from the Balmer decrement. Right: same plot without correction for reddening. Symbols are as in Fig. 5.14: filled symbols for hosts with interaction, morphology of the galaxies identified by triangles for disks, circles for ellipticals, squares when undefined and diamonds when undefined with young population. Typical error bars are also indicated.

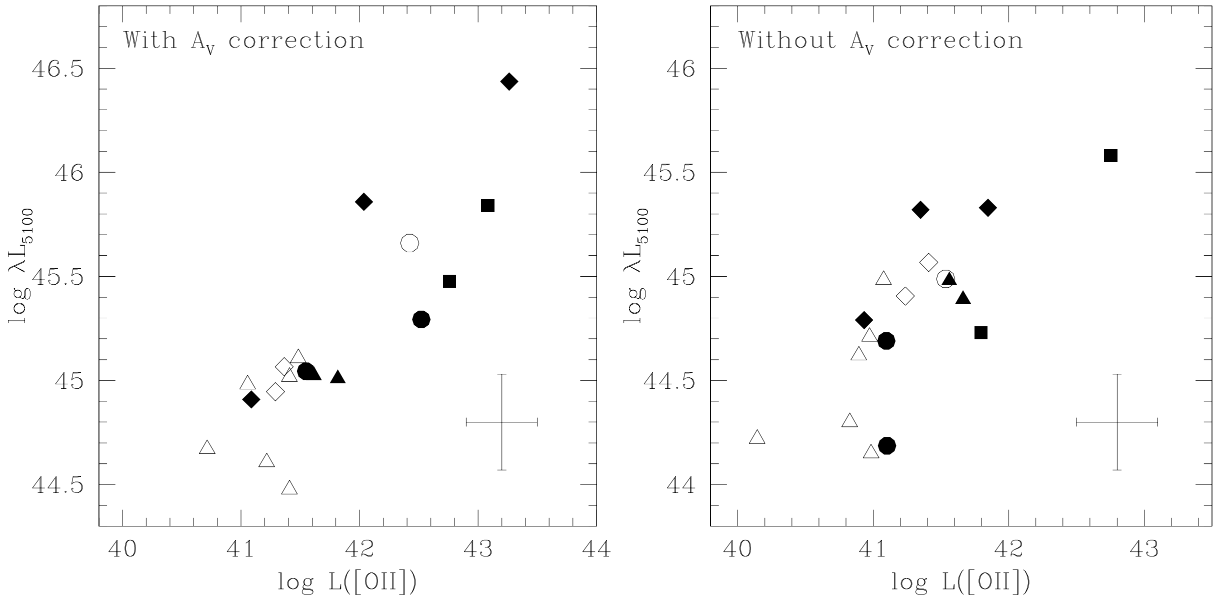

Figure 5.16: Left: Monochromatic luminosity of the quasar at 5100 Å versus luminosity of the nuclear [OII]3727 Å emission line after correction from reddening based on the Balmer decrement. Right: same plot without reddening correction. Symbols are as in Fig. 5.14: filled symbols for hosts with interaction, morphology of the galaxies identified by triangles for disks, circles for ellipticals, squares when undefined and diamonds for undefined with young population. Tyical error bars are also indicated.

For the sake of illustration of the possible misleading in correction for highly reddened quasars, Fig. 5.16 (left) presents monochromatic luminosity versus luminosity in the narrow [OII] 3727 Å. While it seems clear from this figure that interacting systems harbour more powerful quasars with more important narrow lines, we have to keep in mind that this can just reveal that interacting systems present higher dust content in their BLR, thus straightforward correction for reddening from Balmer decrement can artificially create this tendency. Fig 5.16 (right) shows the same plot without correction for reddening. We see that the separation between interacting and non interacting systems, although still present, is not so clear anymore. As already stated, the adequate correction for reddening of narrow lines and continuum probably lies in between these two extremes.

The fact that the most strongly reddened quasars are all undergoing interactions, suggests that the latter constitutes most probably an important mechanism for bringing dust into the central part of the galaxy together with feeding the black hole.

5.9.3 Central mass

There exists a widely used relation between the black hole mass (M_{BH}) and characteristics of the Broad Line Region of quasars (Kaspi et al. 2000 [54]):

$$M_{\rm BH} = R_{\rm blr} v_{\rm blr}^2 G^{-1} \tag{5.2}$$

This virial black hole mass estimate relies upon the hypothesis that dynamics in the BLR is dominated by gravitation. The reverberation mapping method has allowed to measure directly the radius of the BLR in several active nuclei, and a correlation has been found between $R_{\rm blr}$ and the AGN luminosity at 5100 Å. The velocity $v_{\rm blr}$ is estimated from the FWHM of the broad component of Hβ. In a significant fraction of our quasars, it is however problematic to estimate accurately the width of the broad part of the hydrogen line. When the narrow component cannot be clearly detected and when the broad Hβ itself tends to be rather narrow, the separation between both components depends highly on subjective assumptions that are made on flux ratio between [OIII] 5007 Å and the narrow line of Hβ, or on the adopted fixed width for the narrow component (see for instance Grupe et al. 2004 [41]). Here we choose to present mass estimates including global FWHM(Hβ) when the separation is not straightforward, assuming that in these cases the contribution of the narrow component is negligible. In parallel we evaluate the uncertainty on this values by imposing the same width for [OIII] 5007 Å and the narrow Hβ, in order to separate the latter from the broad component. This uncertainty on narrow/broad line decomposition will mainly affect the quasars with the narrowest lines, thus the lowest black hole masses, which might be underestimated.

Figure 5.17 shows histograms of black hole masses using the regression from Kaspi et al. (2000 [54]), after conversion of our luminosities to their cosmology ($H_0 = 75$ km s^{-1} Mpc^{-1}, $\Omega_m = 1$ and $\Omega_\Lambda = 0$). We find that interacting systems are hosting the most massive black holes (on average, in solar masses, $\log M_{\rm BH} = 8.4 \pm 0.8$ in interacting hosts and $\log M_{\rm BH} = 8.1 \pm 0.6$ for isolated ones). The use of the Balmer decrement to correct the monochromatic luminosity from extinction probably enhances this trend: without reddening correction, the average masses are $\log M_{\rm BH} = 8.1 \pm 0.6$ in interacting hosts and $\log M_{\rm BH} = 7.9 \pm 0.5$ for isolated ones. The difference is reduced but still present, given that the actual values probably lie in between these two extremes.

This observation of higher mass black holes in currently interacting systems is somewhat surprising. One might expect that the central mass grows during the merger process and thus reaches higher masses when the system has had time to relax. Those massive black holes might however be the result of previous mergers, being in more crowded neighbourhoods, and explaining the presence of large amounts of gas. However the uncomplete analysis of the neighbourhood made with available slits (Section 5.8.2) does not allow to give a clear answer to this question. Another possible explanation is that there exist several scenarios to feed and trigger the quasars, the most efficient being a merger, creating the most massive black holes, while lower mass black holes would follow another evolution scheme (see Section 5.7.4).

Figure 5.17 also suggests that there is a trend for spirals to host less massive black holes. This is consistent with the idea that mergers bring fuel to the nucleus. Those disk galaxies have not yet undergone major interactions, as mergers would have produced larger spheroids (Stanford & Bushouse 1991 [106]).

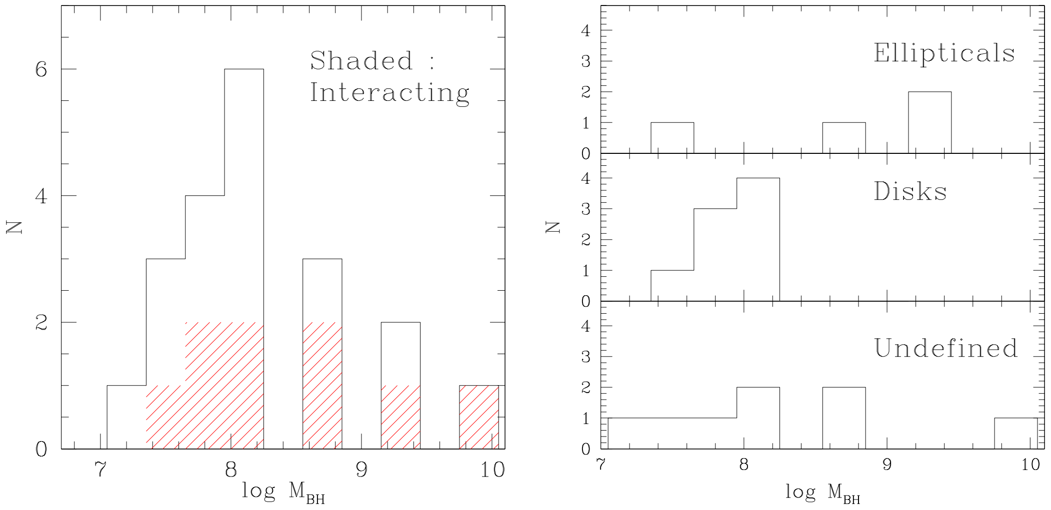

Figure 5.17: Histogram of the black hole masses found with the virialized BLR method. *Left*: global histogram where the black holes hosted in interacting system are shaded. *Right*: histograms of $M_{\rm BH}$ relative to morphological classification.

5.9.4 Accretion rates

The nuclear luminosity measured on quasar spectra can provide direct indications on accretion rates in the nucleus, as $\dot{M} = L/\eta c^2$, where L is the bolometric luminosity of the quasar and η is the efficiency of the energy transfer from mass falling to the black hole, that we assume to be constant. The observed bolometric luminosity is estimated from the optical monochromatic luminosity: $L_{obs}^{bol} \sim 10\lambda L_{5100}$ (Laor et al. 1997 [68]). In Fig. 5.18 we compare L_{obs}^{bol} to the Eddington bolometric luminosity L_E, i.e. the maximum luminosity of a source that is powered by spherical accretion. L_E was estimated from $\rm M_{BH}$ following Eq. 5.3, stating equilibrium between radiation pressure and gravitation:

$$L_E = 1.26\ 10^{38} (M_{\rm BH}/M_\odot)\ erg\, s^{-1} \tag{5.3}$$

From Figs. 5.18 and 5.19 it appears that five quasars may be accreting above the Eddington limit, four of which are indeed among the NLQSOs discussed in Section 5.9.1. Those objects are described as active nuclei in an early stage of activity. The accretion rates are high while the black holes are not very massive yet, and those rates probably fall to sub-Eddington ratios after a short period of activity. This observation is however highly sensitive to the definition of the broad Hβ component. If we had chosen to impose a separation from broad and narrow components of the hydrogen line in the estimate of BH masses, we would have found no more super Eddington luminosity or accretion rate, as shown in Fig. 5.18 by the dotted error bars and in Fig. 5.19. The dotted bars indicate the location where the objects would lie if we impose the subtraction of a narrow Hβ of the same width as [OIII] before estimating the FWHM of the broad Hβ. As can be seen from these figures, the objects most sensitive to this effect are the ones with narrow Hβ, thus

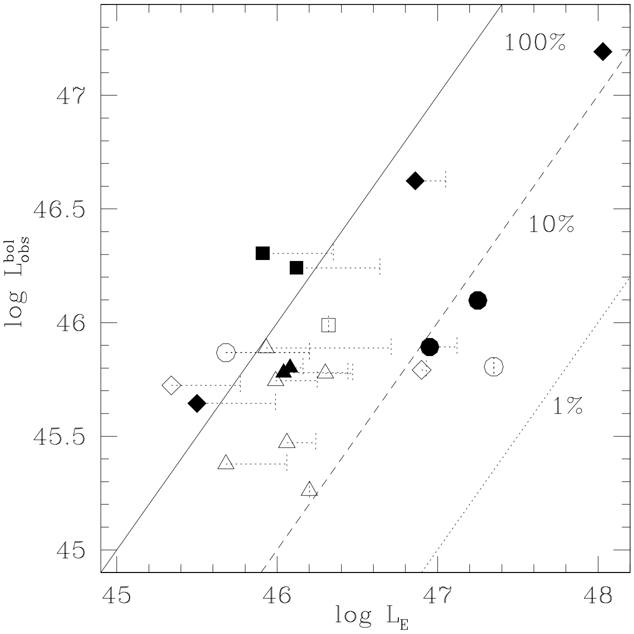

Figure 5.18: Observed nuclear luminosity versus Eddington luminosity evaluated from the BH mass. The dotted, dashed and solid lines are at 0.01, 0.1 and 1 Eddington luminosity, respectively. The asymmetric error bars account for the difficulty to separate the broad and narrow components in Hβ for M_{BH} estimation when the narrow line cannot be clearly identified in the quasar spectra (see text). Symbols are as in Fig. 5.14: filled symbols for hosts with interaction, morphology of the galaxies identified by triangles for disks, circles for ellipticals, squares when undefined and diamonds for undefined with young population.

potentially super Eddington. This points once again to the ambiguity of the classification and interpretation of the Narrow Line AGN phenomenon.

The mean accretion rates for quasars in interacting systems is 0.88 $\dot{M}_E$ while it is 0.66 $\dot{M}_E$ for non interacting ones. If we adopt a typical value for the efficiency $\eta = 0.1$, these accretion rates translate to $\dot{M} = 0.98 \pm 0.42\, M_\odot\, yr^{-1}$ for non interacting and $\dot{M} = 2.65 \pm 2.19\, M_\odot\, yr^{-1}$ for interacting hosts if we exclude the highly deviant object HE 0203-4221.

From these estimates and from Fig. 5.19 which shows the accretion rate plotted versus BH mass, it appears that on average the accretion rate is larger when there is gravitational interaction, and that for a given central mass, the Eddington ratio is higher in interacting systems. Spiral galaxies have the lower absolute accretion rates, that will lead to less massive black holes (as confirmed by Fig. 5.17). This is also coherent with the bulge-mass relation (e.g. Marconi & Hunt 2003 [81]), spirals having smaller bulges than ellipticals.

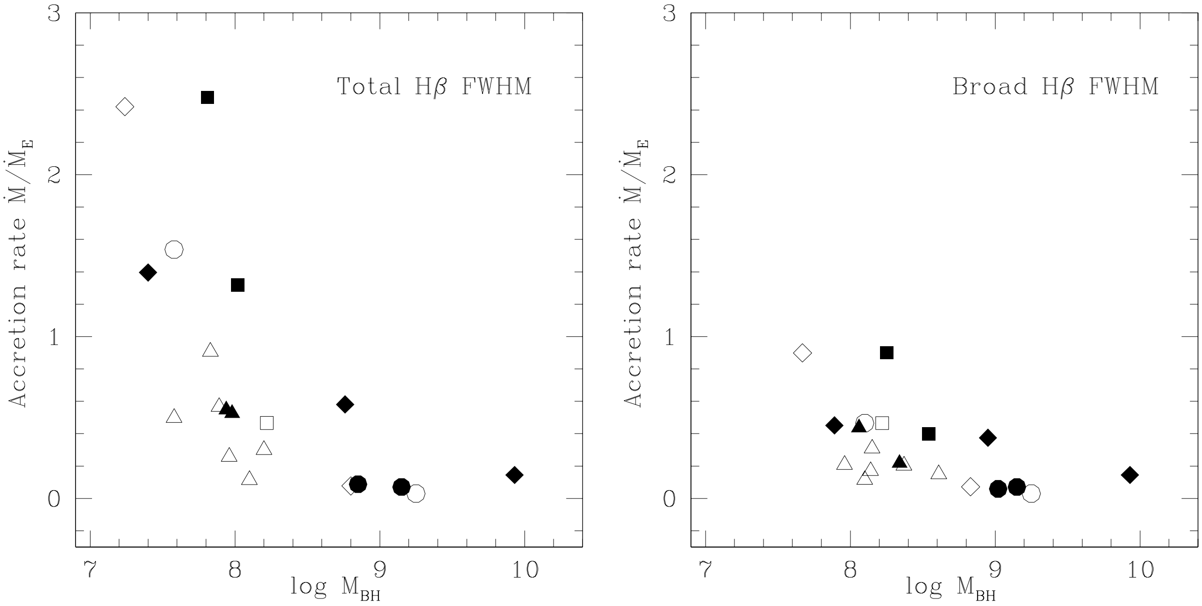

Figure 5.19: Accretion rate in unit of $\dot{M}_E$ versus black hole mass in $M_\odot$. Both values depend on the estimation of FWHM(Hβ). Symbols are as in Fig. 5.14. *Left:* estimates from the total Hβ FWHM. *Right:* estimates from the FWHM of the broad Hβ only, after subtracting a narrow component of the same width as the [OIII] line.

5.10 Redshift determination

Analysis of quasar emission lines shows, as already observed for instance by Eracleous & Halpern (2004 [31]) and Boroson (2005 [8]), that narrow lines such as [OIII] are generally bluer than broad hydrogen lines. The question is to know which lines are most suitable for measuring the actual redshift of the whole object. The availability of accurate symmetrical rotation curves in our sample provides a good opportunity to answer this question. Taking advantage of the separation we are able to make between nucleus and host emission lines, we have computed accurate redshifts for those galaxies which show the most regular rotation curves (HE 0132-4313, HE 0914-0031, HE 1009-0702, HE 1503+0228 and HE 2345-2906), averaging shifts from points of the extracted rotation curves symmetrical around the center. After that, we have searched in the quasar spectra which line was the closest estimator of the galactic redshift. For all five of them, it is the wavelength corresponding to the tip of the Hα line which best matches the galactic redshift (within 0.2 Å, or a fifth of a pixel), followed with nearly the same accuracy, by the Hβ tip. The observed shifts are summarized in Table 5.10. Assuming those 5 objects are representative of undisturbed quasar host galaxies and that the quasar is motionless in the galaxy, we conclude that the tip of the quasar Hα line (or the other main broad emission line in the optical Hβ) is the best indicator of galactic redshift. Variations of redshifts in the quasar emission lines can thus be interpreted as bluer or redder in comparison with the global object velocity and not only between each other. The redshifts measured from the position of the Hα tip for

Table 5.10: Observed shifts of the main quasar emission lines relative to the galactic lines, expressed in km s^{-1}. Each line position is estimated by a gaussian profile fitting (first line, *g*) and from the wavelength corresponding to the tip (maximum intensity, second line, *t*).

	HE 0132	HE 0914	HE 1009	HE 1503	HE 2345	Mean shift	σ
Hα(g)	+22	-104	-97	-117	-52	-70	41
Hα(t)	+7	-3	+7	+4	-30	-3	16
Hβ(g)	0	+5	-189	-133	-40	-71	84
Hβ(t)	+5	+5	+24	+4	-35	+1	21
$OIII_1$(g)	-	-27	-	-85	-109	-74	42
$OIII_1$(t)	-	-9	-	-91	-99	-66	50
$OIII_2$(g)	-	-27	-	-79	-103	-70	39
$OIII_2$(t)	-	-5	-	-79	-98	-61	49

the whole sample are presented in Table 5.2.

5.11 Comments on individual objects

- HE 0132-4313: Undefined morphology for the galaxy, but intermediate age stellar population. No sign of interaction. Quasar spectrum typical of Narrow Line Quasar (NLQSO).

- HE 0203-4221: This object shows all signs of merger-induced and enhanced activity: high ionization level found locally in the galaxy, young stellar population, large amount of reddening in the nucleus, evidence for interaction from significant distorsions in radial velocity curve and image.

- HE 0208-5318: Normal disk-like stellar population, no sign of interaction, and gas metallicity indicative of weakly enriched medium.

- HE 0306-3301: Disk in which a close tiny companion is merging, resulting in asymmetric rotation curves. Young stellar population and low metallicity.

- HE 0354-5500: Merger in a spiral galaxy, inducing high level ionization and asymmetric rotation curves.

- HE 0441-2826: Stellar content typical of disk. No information from acquisition image (saturated quasar), but radial profile pointing to elliptical morphology from previous NIR study (Kuhlbrodt 2003 [67]). No extended emission line suitable for radial velocity curve extraction. It is the only object with a clear mismatch between stellar population and morphology. The gas metallicity also points to a weak enrichement by stars. The quasar spectrum itself is peculiar, with broad Hβ blueshifted from the narrow component ($\sim 2700\,\mathrm{km\,s^{-1}}$), probably revealing an outflow. Important extinction on quasar broad lines whereas the continuum is steep even before reddening correction. Traces of shells or interaction would not be surprizing if high resolution imaging was available, as this object always sits among interacting galaxies in Figs. 5.15 to 5.19.

- HE 0450-2958: This object is a special case that has been addressed by Magain et al. (2005 [76]). Upper limits were placed on the undetected stellar contribution on the spectra of the host, and only a cloud of gas ionized by the quasar was detected. As there is no detection of host, this object is not included in global means or detailed galactic component analysis. Quasar spectrum typical of NLQSO.
- HE 0530-3755: One of the faintest hosts detected in the sample, but with a highly reddened nucleus that might suggest obscuration by dust for the host. Small amount of gas partially ionized by the quasar; images suggesting interaction with tidal tail to the West, one close companion at 6" East, that luckily partially falls on the slit and whose spectrum shows nearly identical redshift (faint galaxy, low continuum and only Hα feature detected in emission), plus another putative companion 9" South. The nucleus has an accretion rate above the Eddington limit, but without matching all the NLQSO criteria.
- HE 0914-0031: Normal spiral galaxy with high mass-to-light ratio according to the mass modelling of Section 5.8.1.
- HE 0956-0720: Bad PSF, inducing bad deconvolved spectrum. No interpretation possible with such a low S/N. Morphological classifications from previous studies are contradictory (Kuhlbrodt 2003 [67], Percival et al. 2001 [97]).
- HE 1009-0702: Normal late-type spiral galaxy according to morphology, stellar and gasous content. Quasar spectrum typical of NLQSO.
- HE 1015-1618: Poor separation from the quasar because of a bad PSF. No interpretation from spectra.
- HE 1029-1401: The lowest redshift object of the sample, luminous elliptical with minor mergers, present in several previous studies. Gas highly ionized by nucleus.
- HE 1228+0131: Poor separation of the host from the quasar, because the saturation level of the detector was almost reached. No interpretation possible. Quasar spectrum typical of NLQSO.
- HE 1302-1017 (or PKS 1302-102): This object is the only radio loud quasar in the sample. It cannot be properly classified concerning morphology. Bahcall et al. (1997 [2]) classify this object as elliptical because of its smooth and elliptical shape from HST imaging, although they find an exponential profile to fit their data slightly better. In Kuhlbrodt (2003 [67]) it is classified as disk from 2D modelling on NIR

images, but presents an irregular radial profile. It is the most luminous object of the sample. The stellar population of its galaxy is typical of Sc disk population. It has low gas metallicity and the highest SFR of the HII subsample. From Bahcall et al. (1997 [2]), it has two small companions merging in, perturbing the radial velocity curve presented in this paper and probably explaining the irregular radial profile, but without exciting highly the large amount of gas present in this host. If it is a morphologically disk-dominated galaxy, the stellar and gaseous analyses point to Sc-Sd where merger-induced star formation and activity appear, giving a counter-example of a luminous radio-loud quasar not hosted by elliptical. Otherwise if it is an elliptical galaxy, it must anyway have undergone recent mergers, which have largely enhanced star formation and brought a large amount of fresh gas, able to mask old stellar populations from our analyses.

- HE 1434-1600: Elliptical galaxy with gas ionized by the quasar at large distance from the nucleus, discussed in Letawe et al. (2004 [69]). The quasar spectrum is highly reddened.
- HE 1442-1139: Probable S0-like galaxy, with no gas detected.
- HE 1503+0228: Normal spiral host galaxy, studied as a test case in Courbin et al. (2002 [24]).
- HE 2258-5524: Major merger resulting in highly ionized gas and asymmetric rotation curve. Stellar population of a S0-Sa galaxy. Quasar spectrum typical of NLQSO.
- HE 2345-2906: Spiral host galaxy for one of the weakest quasars of the sample (at the limit of the quasar/Seyfert separation). The narrow lines of the quasar are really prominent relative to the broad components, in comparison with the rest of the sample.

5.12 Discussion

5.12.1 Quasar hosts characterization

A first striking result is that most quasar host galaxies harbour large amounts of gas (ionized by stars, by the AGN or marginally by shocks), irrespective of morphological type. We can thus safely reinforce the observations of Scoville et al. (2003 [103]), based on molecular CO detection, that high luminosity quasars are generally *not* found in normal (i.e. gas-poor) ellipticals. Previous mergers or collisions are probably the source of gas for ellipticals.

There is an obvious predominance of young global stellar population (10/15 of the hosts with analysable stellar content). As several hosts with a young stellar population have unknown morphologies, this observation could be linked to the bluer colours of elliptical quasar hosts in comparison to inactive ellipticals found in several recent multicolour imaging studies (e.g. Kauffmann et al. 2003 [55], Jahnke et al. 2004 [51], Sanchez et al. 2004 [101]). We note that the two elliptical hosts for which our stellar population analysis shows a predominantly old population (HE 1434-1600 and HE 1029-1401) are also presenting this type of bluer colours, according to Jahnke et al. (2004 [51]). They thus have a globally old stellar population, as deduced from Lick indices analyses, over which appears an additional fraction of younger stars which account for the blue colour excess, without significantly modifying the spectral absorption diagnostics of section 5.7.1. As the bluer-than-expected ellipticals display a globally old stellar population with an additional young component, and as most of the host galaxies with a globally young stellar population are disk-dominated, we can probably conclude that most of the hosts with undefined morphologies and young stellar population have a significant disk component.

From a statistical point of view, the proportion of disks found in this study (8 of the 19 radio quiet quasars, or even 7/14 if we remove the NLQSOs that are often excluded from quasar samples, thus around 45%) is compatible with the proportions found by Dunlop et al. (2003 [30]) and Floyd et al. (2004 [36]), namely around 30% among radio quiet quasars, given the limited number of objects in both samples. But as these last two studies have used several constraints on target selection, there might indeed be a selection bias in their samples towards ellipticals, while no other constraint apart from luminosity was applied to ours. Given that our proportion is a lower limit, the radio quiet quasars probably appear as often in spirals as in ellipticals.

The confirmed spirals show HII regions compatible with rather metal-poor Sc to Sd, regarding star formation and gas metallicity. Their black holes are less massive than in ellipticals (as expected from the bulge mass - black hole mass scaling relation, McLure & Dunlop 2003 [86]), and they only present few signs of interaction (2/8).

The elliptical galaxies contain ionized gas (3/4), have massive black holes and at least 50% of them present signs of interaction. The only *normal* elliptical, with no gas detected, could not be well deconvolved, so that no detailed analysis of its stellar and gas content has been possible.

It has been claimed that all quasars more luminous than $M_V = -23.5$ are hosted by massive ellipticals (Dunlop et al. 2003 [30], Floyd et al. 2004 [36]). Converting this limit to our cosmology gives $M_V < -23.25$. As seen from Table 5.2, all our quasars but one are brighter than this limit, and even if the most luminous AGNs lie in ellipticals, we find almost half of them inside disk-dominated galaxies in this magnitude range. The mean nuclear V magnitudes are $M_V = -24.5$ both for elliptical and for disk hosts, even if we remove the potential NLQSOs identified as disks from our sample (they were excluded from Dunlop's sample). This observation that the morphology of luminous quasar host galaxies are not necessarily elliptical was also put forward by Sanchez et al. (2004 [101]) in the case of higher redshift quasars ($0.5 < z < 1.1$).

5.12.2 The quasar-host connection

Influence of galactic environment on the activity of the nucleus

As shown in Section 5.9, interaction obviously brings material (gas and dust) to the central part of the galaxy and enhances the accretion rate and power of the quasar. Recent simulations of galaxy mergers (Di Matteo et al. 2005 [28], Cattaneo et al. 2005 [20]) lead to the same conclusions. The most massive black holes are hosted in systems presently interacting, while we would have expected them in systems at the end of the merging process, as discussed in Section 5.9.3. The quasar harboured by interacting systems are also more powerful. One might argue that the fact that the most powerful quasars are found in interacting systems is only due to a minimal obscuration by dust in the central parts, as it is blown out by the interaction. However, as the most strongly reddened quasars are indeed in interacting systems, this hypothesis has to be rejected. The quasars in interacting systems appear genuinely more powerful.

On the other hand, half of our quasars are found in non-interacting galaxies, with a majority of spiral hosts (6 confirmed disks, 2 ellipticals and 3 undefined). Most of them are young gas-rich systems. The predominance of a disk component ensures that these system have not undergone major mergers, as the latter tend to produce spheroids (Stanford & Bushouse 1991 [106]).

This suggests that mergers are not the only mechanism for triggering activity, as already proposed by Jahnke et al. (2004 [51]) and Dunlop et al. (2003 [30]). Alternative mechanisms may be bar-driven accretion (found to be very efficient for quasar fueling for instance in NLS1, Crenshaw et al. 2003 [26], or for HE 2345-2958 in the present study). But small scale nuclear events, related to an early stage of formation of spiral galaxies, might also trigger activity. They are undetectable with the spatial resolution of the present observations. Galactic winds arising from central supernovae are plausible drivers of fuel towards the central engine given that the weak enrichment of gas in heavy elements is measured on global spectra.

There does not seem to be a single scenario for the evolution of quasars and their hosts, but different evolution schemes lead to different characteristics of the central engine. If the system encounters major merger events, it will lead to a higher BH mass and a more powerful nucleus, but the nucleus could be active as well with less dramatic and smaller scale events in young spiral galaxies, leading to smaller and less powerful quasars.

Influence of the quasar radiation on the host galaxy

We find in 7/20 galaxies gas ionized by the quasar far from the nucleus (in ellipticals, spirals or undefined hosts). The common characteristics of those galaxies are of course the presence of gas, but also a powerful quasar, and evidences for gravitational interaction, two properties that are linked. The origin of high ionization may lie in the fact that gas and dust around the nucleus are swept by the interaction and let the powerful nuclear ionizing beam reach large distances throughout the galaxy.

The analysis of gas metallicity in quasar hosts with a HII region-like ISM shows abundances at the lower end of typical spiral metallicities. The nuclear activity in these young systems could slow down the star formation efficiency in some way, avoiding massive stars to form and slowing the enrichment of the surrounding gas. Links between star formation and quasar activity (Jahnke et al. 2004 [51]) are preferentially found for elliptical hosts where activity seems to enhance star formation. However, in that case, neither quasar activity nor star formation would be expected in an isolated host. Both are made possible by the presence of gas, probably brought by mergers with younger systems. We agree with the conclusions of Canalizo & Stockton (2001 [18]) who, from a study of UltraLuminous IR Galaxies and QSOs, conclude that it is the merging process that triggers both star formation and activity, without finding evidence for any direct influence from one of these onto the other. In contrast, it does not appear unrealistic to suggest that the quasar activity might slow down the star formation in young, isolated, gas-rich spiral galaxies.

Further spectroscopic and high resolution imaging investigations of larger samples of quasars and their hosts could allow to confirm the trends found here and allow a sharper tuning of the interpretations and hypotheses on the quasar ignition and evolution.

Acknowledgements :

G. L. is a teaching assistant supported by the University of Liège, (Belgium) . The Pôle d'Attraction Interuniversitaire, P5/36 and PRODEX 90195 (PPS Science Policy, Belgium) contracts are thanked for financial support. F. C., P. J. and G. M. acknowledge support from the Swiss National Science Fundation. K. J. was supported by the German DLR under project number 50 OR 0404 and DFG project SCHI 536/3-1.

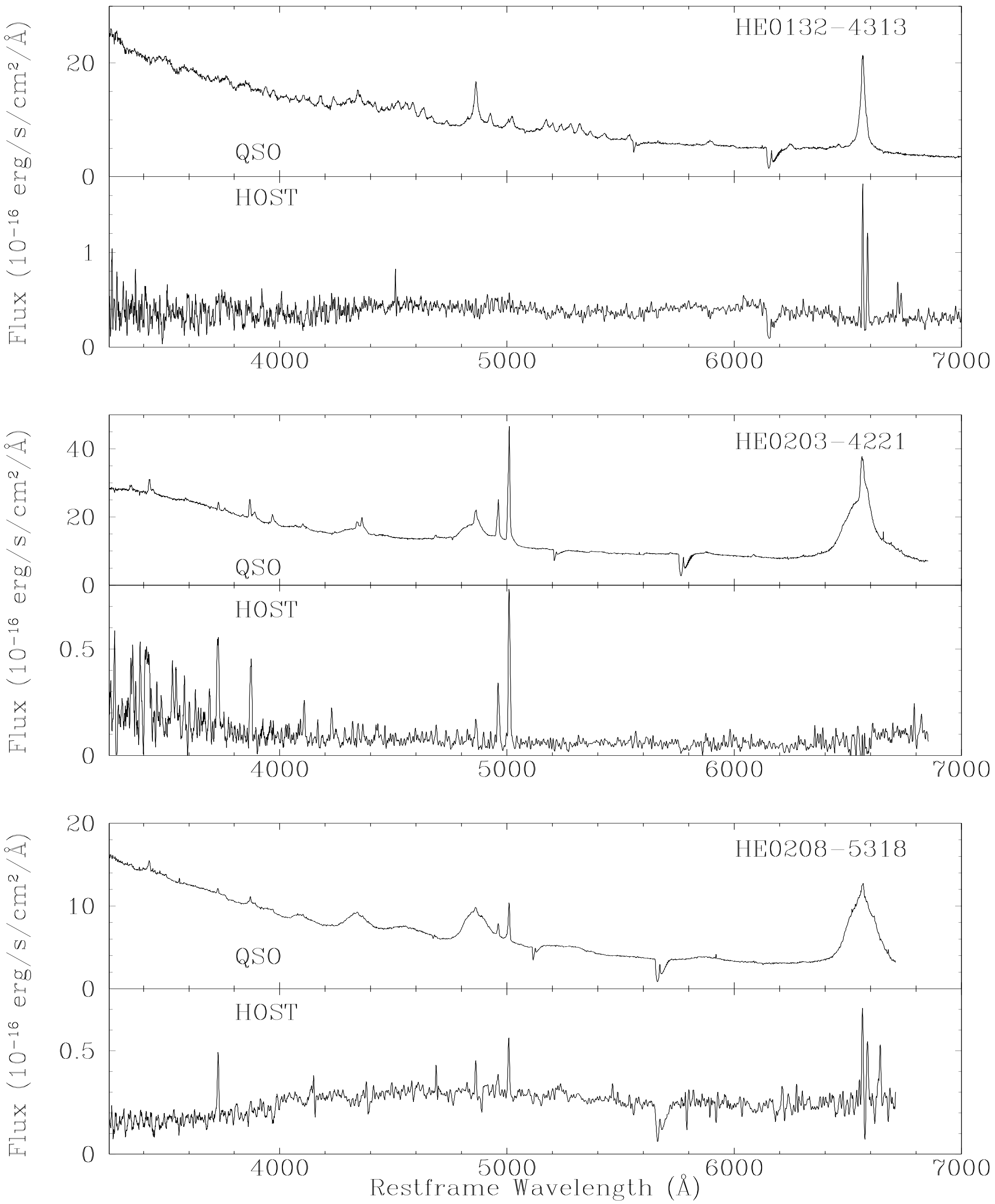

Figure 5.20: For each object, integrated spectra of the quasar-only on top and galaxy-only at the bottom, after deconvolution and separation, sorted by increasing right ascension.

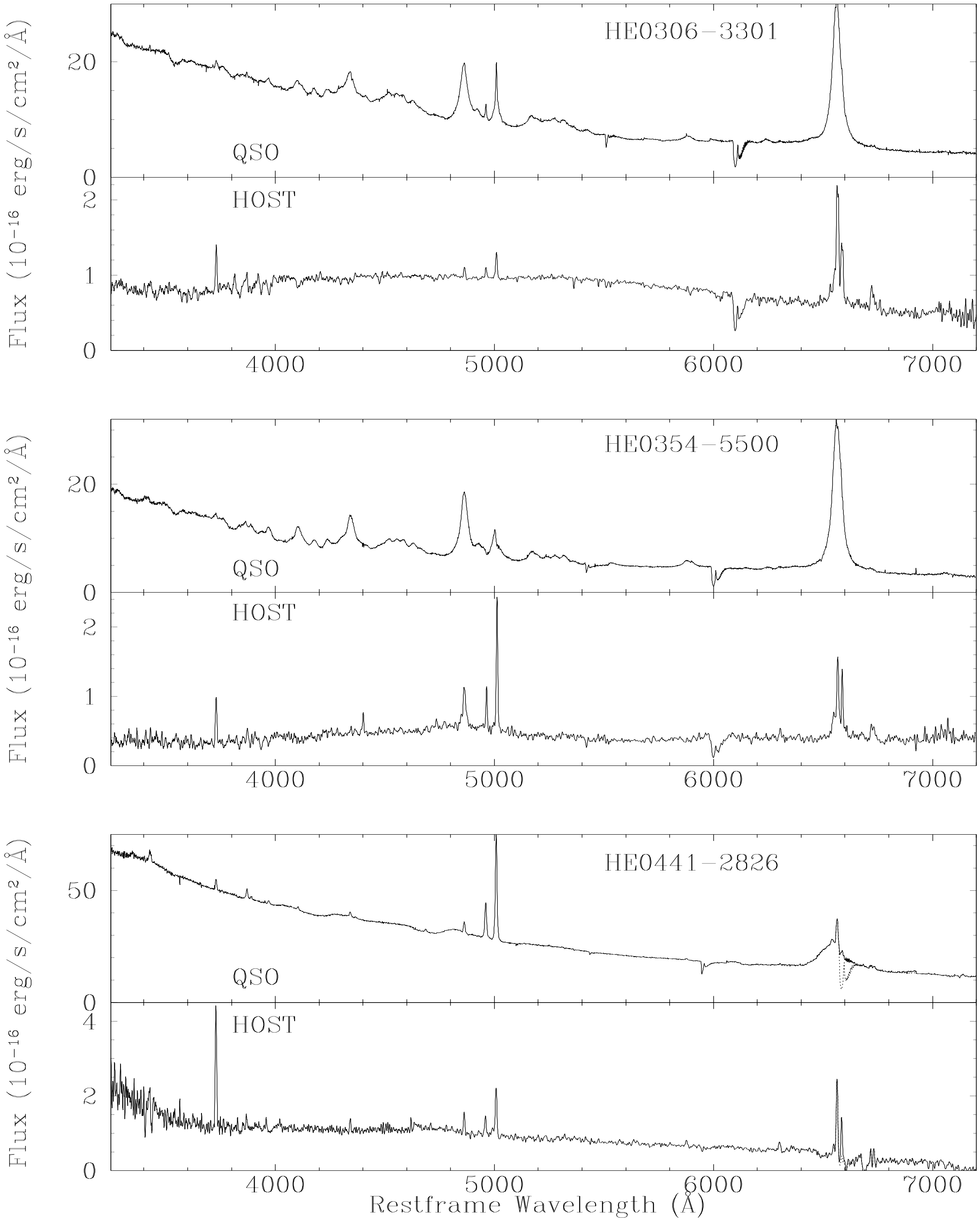

Figure 5.21: There seems to be residual nuclear light in the continuum of the galaxy of HE 0441-2826, because of a poorer PSF. The blend of Hα with atmospheric absorption (dotted line) was partially corrected.

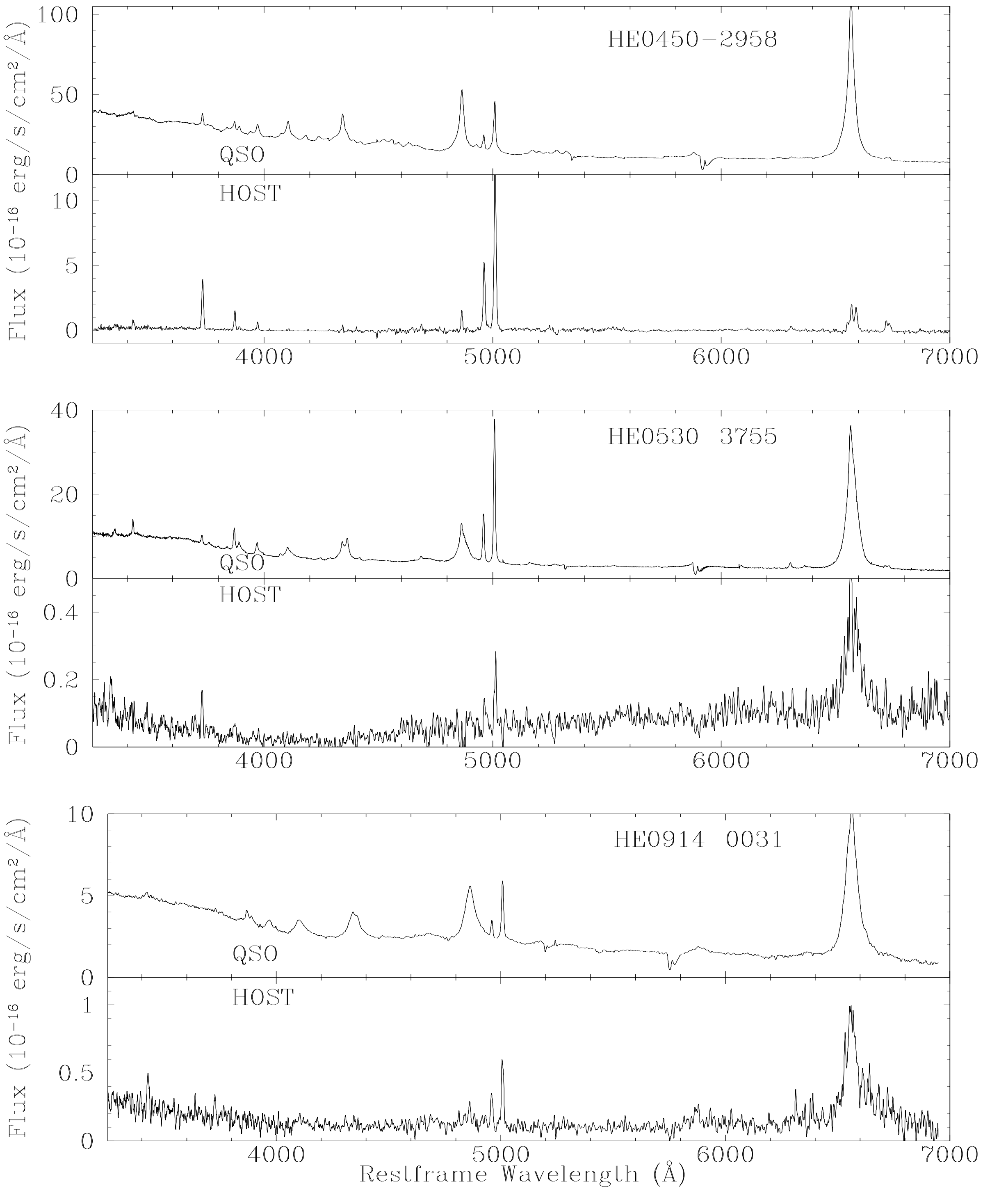

Figure 5.22: Note the absence of continuum in the host of HE 0450-2928.

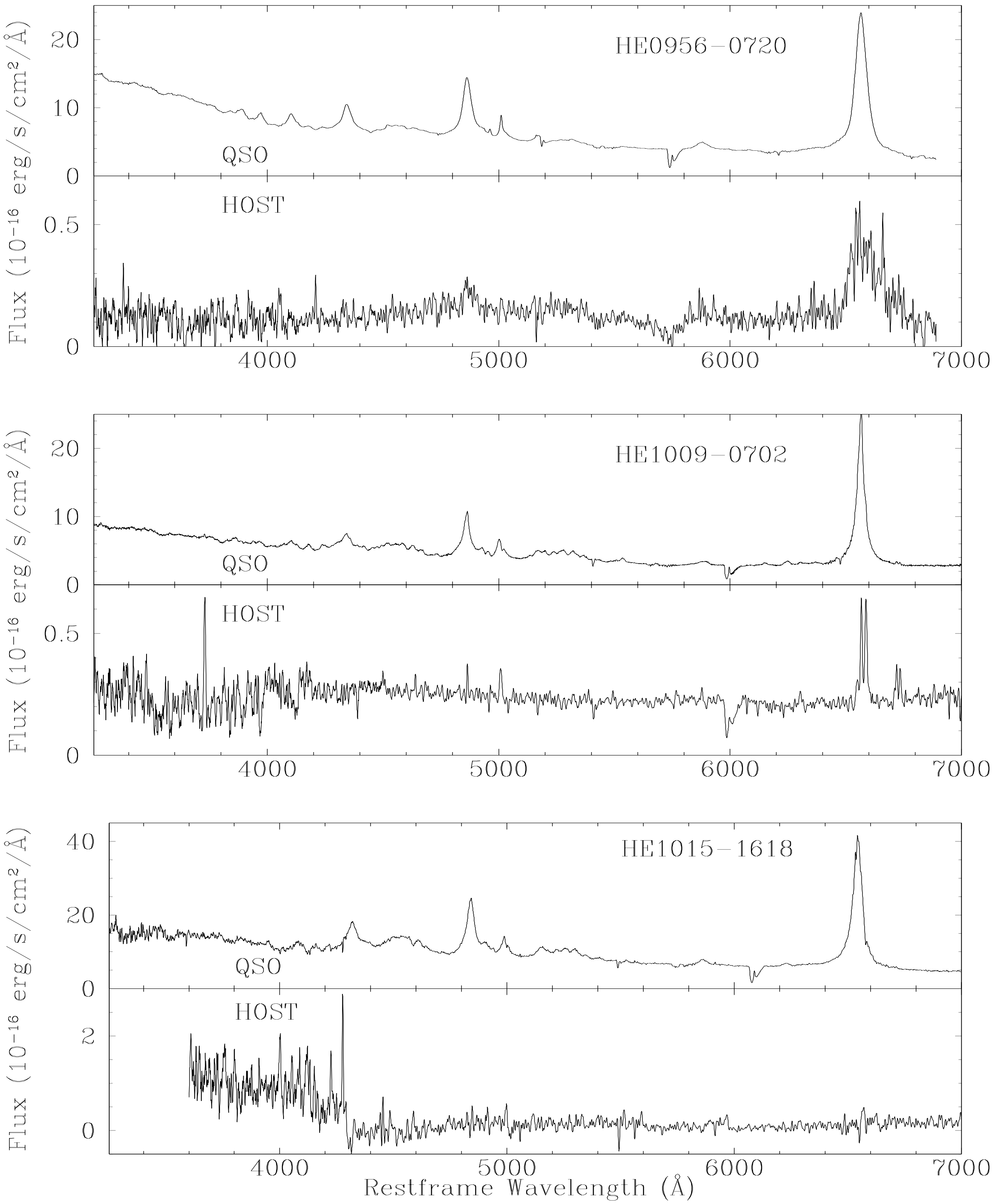

Figure 5.23: HE 0956-0720 and HE 1015-1618 could not be properly deconvolved, because of high N/H and difficult PSF construction.

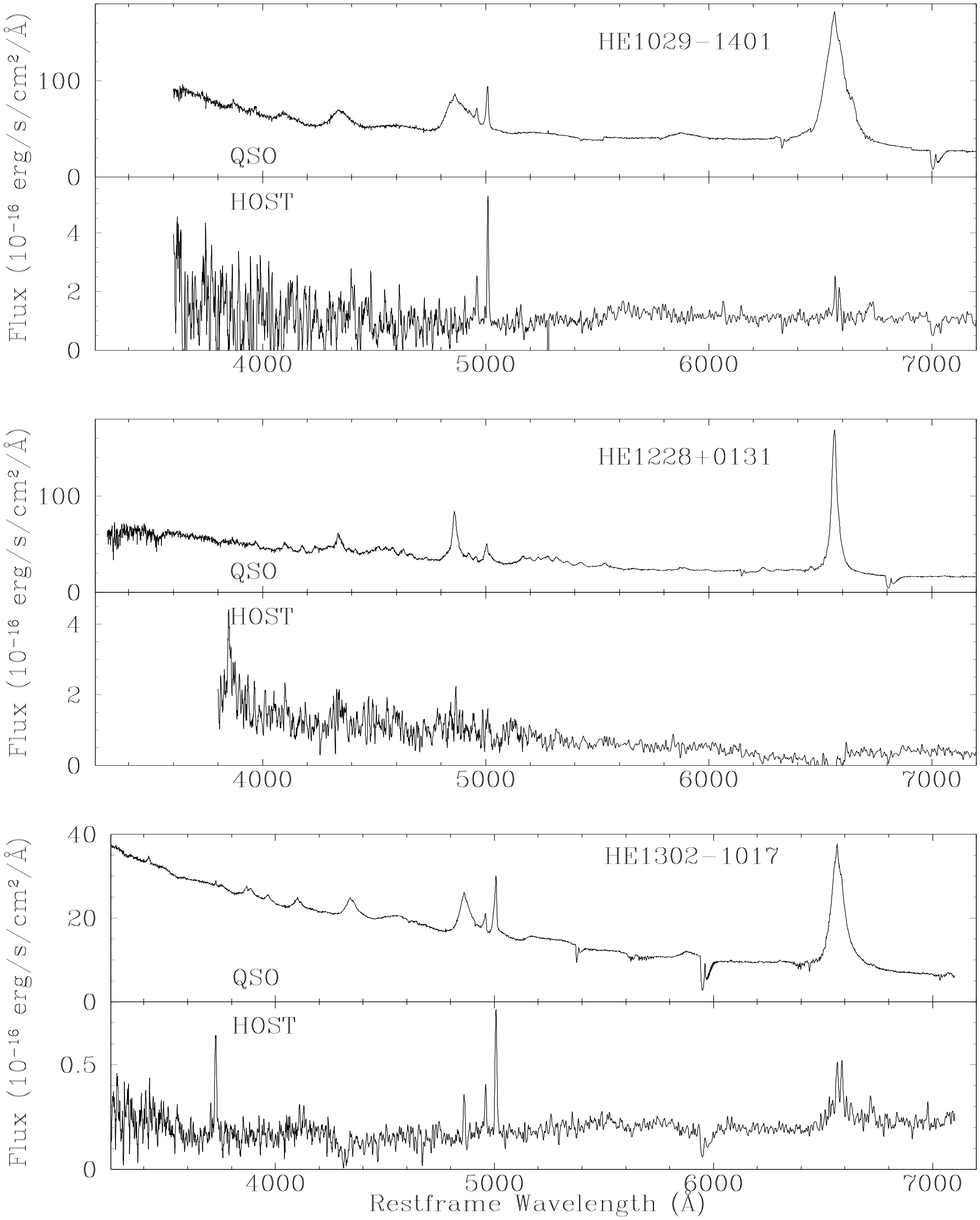

Figure 5.24: Important noise in the bluer parts of the two first objects, the PSF stars being too faint in the blue for accurate deconvolution in this wavelength range. HE 1228+0131 observations were near saturation level on the detector, leading to non adequacy of the PSF and thus poor deconvolution.

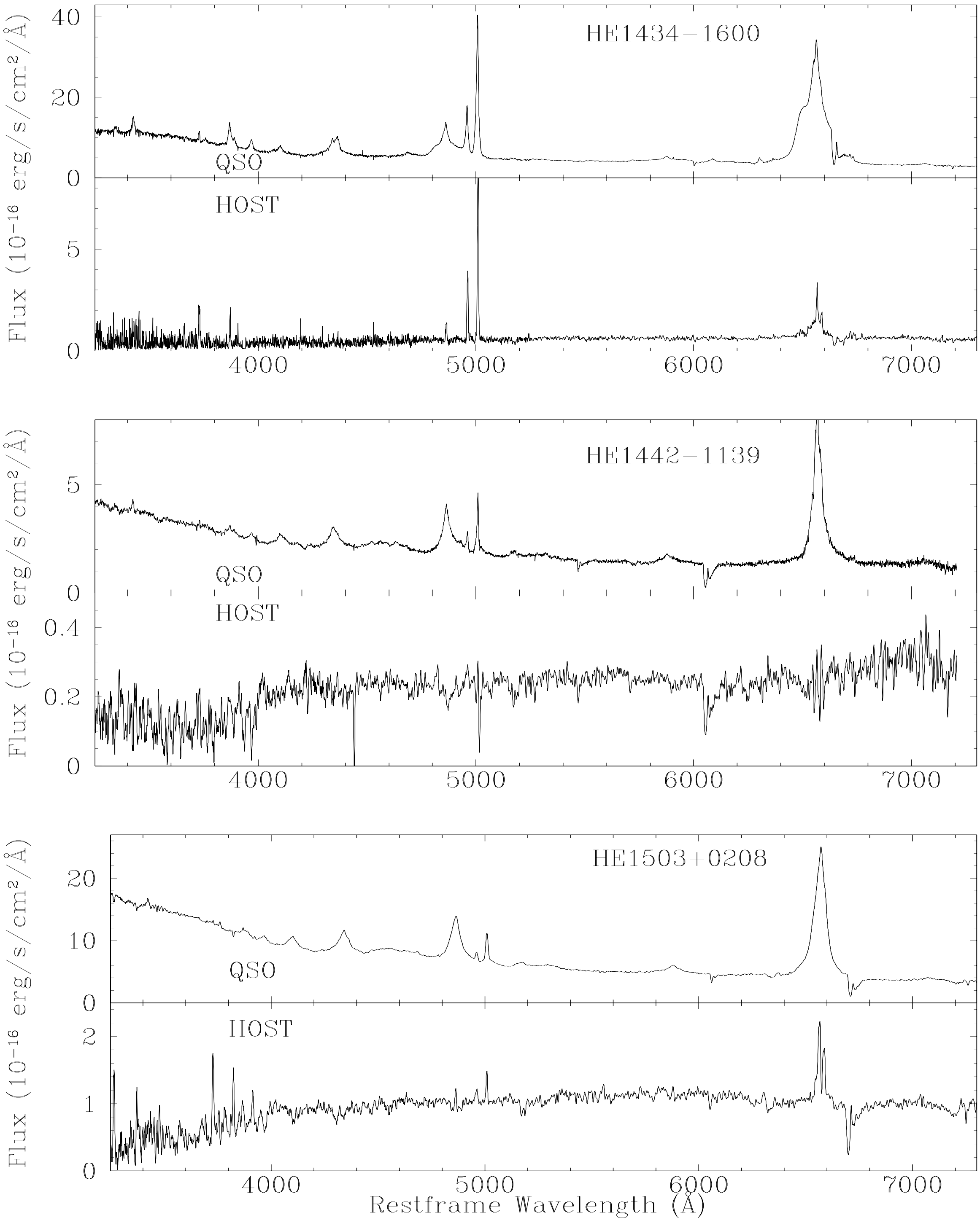

Figure 5.25: Following

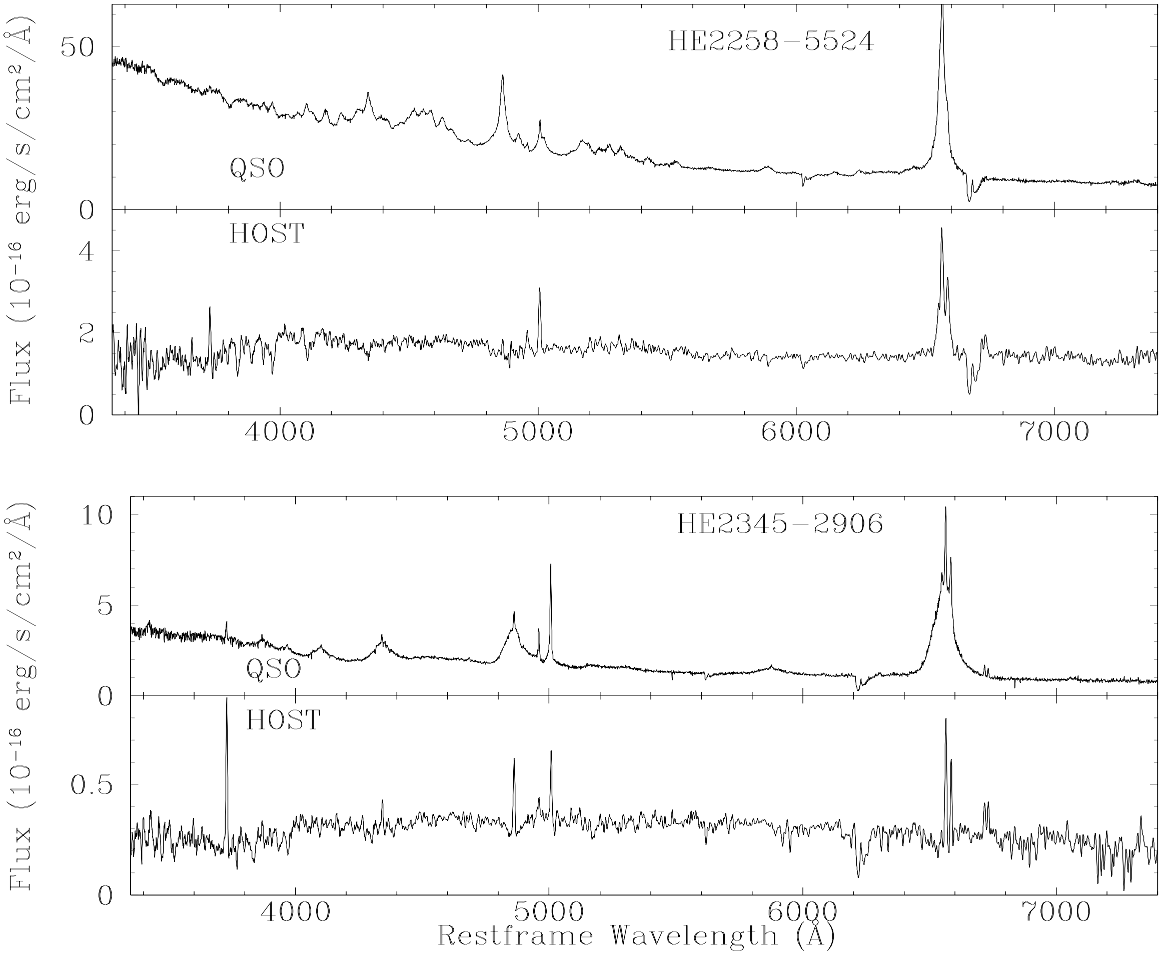

Figure 5.26: Following

Conclusions et perspectives

Les principales conclusions de ce travail sont reprises en préambule à chaque article, ainsi bien sûr que dans les articles eux-mêmes. Nous pouvons cependant rappeler les principaux résultats, tant au niveau de la technique de traitement des données employées que du point de vue de l'interprétation astrophysique des résultats obtenus.

Traitement des données

- Nous avons montré l'efficacité de la méthode de deconvolution de spectres dans le cadre de l'étude des quasars et des galaxies qui les abritent. Il est à noter que la qualité de la séparation entre noyau et galaxie est fortement dépendante de la qualité de la PSF disponible. C'est pourquoi il sera important, dans les études à venir, non seulement de bien sélectionner les étoiles qui serviront à la construction de la PSF, pour éviter par exemple une chute de flux trop importante dans les régions bleues du spectre, mais aussi d'utiliser des fentes suffisament longues pour ne pas tronquer les ailes de la PSF, afin de contraindre sa forme avec plus de précision.
- Nous avons mis en évidence la complémentarité des spectres 2D et des images à haute resolution comme celles obtenues avec le HST. Des demandes de temps d'observation supplémentaire ont d'ailleurs été soumises dans ce sens.
- Nous avons construit des algorithmes d'extraction des raies d'émission étendues ainsi que d'ajustement de courbes de vitesses radiales par modélisation de la répartition de la masse au sein de la galaxie. Cette méthode sera adaptée et appliquée dans les prochains mois aux spectres 3D (spectroscopie intégrale de champ).
- Nous avons participé à l'amélioration des techniques de déconvolution d'images et de spectres via la méthode MCS ainsi qu'à la mise au point de variantes de ces algorithmes.

Galaxies hôtes de quasars

- On trouve des quasars lumineux aussi bien dans des galaxies spirales qu'elliptiques, abritant presque toujours de grandes quantités de gaz ionisé.
- Une proportion significative des galaxies hôtes montrent les caractéristiques spectrales de galaxies spirales très jeunes.
- Les galaxies hôtes présentant du gaz fortement ionisé par le quasar sont toujours liées à la présence d'interactions gravitationnelles, et ce même sans l'influence de jets radios.

- Nous avons apporté des preuves spectrales que les interactions gravitationnelles amènent gaz et poussière au centre de la galaxie et rendent le quasar plus puissant. D'autres mécanismes, plus confinés au centre de la galaxie, sont probablement à l'œuvre dans les jeunes spirales pour alimenter le quasar.
- Plusieurs galaxies et quasars se révèlent être des systèmes particuliers. Certains ont été étudiés déjà en détail (HE 1503+0228, HE 1434-1600 ou HE 0450-2958), d'autres demanderaient des observations complémentaires pour expliquer leurs particularités (HE 0441-2826, HE 1302-1017 ou HE 0530-3755).

Perspectives

- Nous projetons d'élargir l'échantillon en spectroscopie 2D de quasars lumineux pour confirmer ou préciser les tendances qui se dégagent de ce travail (un "large program" VLT va être soumis prochainement à l'ESO).
- Des développements d'algorithmes de modélisation des champs de vitesses pour des spectres 3D sont à construire.
- Le cas particulier du système HE 0450-2958 avec sa galaxie hôte non détectée reste à éclaircir. De nombreuses données complémentaires vont être collectées dans les prochains mois, apportant, nous l'espérons, quelques éléments de réponse. Nous avons également du temps d'observation accordé au NTT pour la recherche d'autres quasars similaires à HE 0450-2958.
- La proportion plus élevée de "Narrow Line QSOs" dans notre échantillon en comparaison avec la plupart des échantillons optiques ainsi que la difficulté de caracter avec précision cette sous-classe de quasars nous poussent à explorer plus avant ce type d'objet, notamment par l'imagerie haute résolution et en évitant soigneusement de les exclure des échantillons de quasars observés.
- Nous pressentons que le problème soulevé par la correction du rougissement des quasars peut nous fournir des indications sur la structure intrinsèque des noyaux actifs. Des recherches vont êtres menées en ce sens.

Annexe

Liste des différents articles non directement liés à ce travail auxquels j'ai apporté une contribution (principalement via la déconvolution de spectres) :

- *A deconvolution based algorithm for crowded field photometry with unknown Point Spread Function*
  Magain, P. ; Courbin, F., Sohy, S., Gillon, M., Letawe, G
  soumis à Astronomy & Astrophysics (2005)

- *An optical time delay for the double gravitational lens system FBQ 0951+2635*
  Jakobsson, P. ; Hjorth, J. ; Burud, I. ; Letawe, G. ; Lidman, C. ; Courbin, F.
  Astronomy and Astrophysics, v.431, p.103-109 (2005)

- *Time delay and lens redshift for the doubly imaged BAL quasar SBS 1520+530*
  Burud, I. ; Hjorth, J. ; Courbin, F. ; Cohen, J. G. ; Magain, P. ; Jaunsen, A. O. ; Kaas, A. A. ; Faure, C. ; Letawe, G.
  Astronomy and Astrophysics, v.391, p.481-486 (2002)

- *An optical time-delay for the lensed BAL quasar HE 2149-2745*
  Burud, I. ; Courbin, F. ; Magain, P. ; Lidman, C. ; Hutsemékers, D. ; Kneib, J.-P. ; Hjorth, J. ; Brewer, J. ; Pompei, E. ; Germany, L. ; Pritchard, J. ; Jaunsen, A. O. ; Letawe, G. ; Meylan, G.
  Astronomy and Astrophysics, v.383, p.71-81 (2002)

Participation à des conférences et colloques

- QSO Hosts : Evolution and Environment, août 2005 à Leiden : *VLT on-axis spectroscopy of quasar host galaxies* (poster)
- JENAM, juin 2005, Liège, dans la session "Quasars : Host galaxies and gravitationnal lenses" : *On-axis VLT spectroscopy of quasar host galaxies at z< 0.3* (talk)

Bibliographie

[1] N. Arimoto and P. Jablonka. Evolutionary method of population synthesis for bulge-disc systems - optical-infrared colour-magnitude relation of spiral galaxies. *A&A*, 249 :374, 1991.

[2] J.N. Bahcall, S. Kirhakos, D.H. Saxe, and D.P. Schneider. Hubble space telescope images of a sample of 20 nearby luminous quasars. *ApJ*, 479 :642, 1997.

[3] J.N. Bahcall, S. Kirhakos, and D.P. Schneider. HST images of nearby luminous quasars. *ApJ*, 435 :L11, 1994.

[4] J. Baldwin, M. Phillips, and R. Terlevich. Classification parameters for the emission-line spectra of extragalactic objects. *PASP*, 93 :5, 1981.

[5] J Barnes. Evolution of compact groups and the formation of elliptical galaxies. *Nature*, 338 :123, 1989.

[6] W. Bian and Y. Zhao. Black hole masses in narrow-line seyfert 1 galaxies. *MNRAS*, 352 :823, 2004.

[7] J. Binney and S. Tremaine. *Galactic Dynamics.* Princeton : Princeton Series in Astrophysics, 1987.

[8] T. Boroson. Blueshifted [O III] emission : Indications of a dynamic narrow-line region. *AJ*, 130 :381, 2005.

[9] T. Boroson and J. Oke. Spectroscopy of the nebulosity around eight high-luminosity QSOs. *ApJ*, 281 :535, 1984.

[10] T. Boroson, S. Persson, and J. Oke. More spectroscopy of the fuzz around QSOs - additional evidence for two types of QSO. *ApJ*, 293 :120, 1985.

[11] G.D. Bothun, R.A. Mould, J.and Schommer, and M. Aaronson. The infrared color-magnitude and color-gas content relations for cluster spirals. *ApJ*, 291 :586, 1985.

[12] P.J. Boyce, M.J. Disney, J.C. Blades, et al. The host galaxies of IRAS-selected quasi-stellar objects. *ApJ*, 473 :760, 1996.

[13] P.J Boyce, M.J. Disney, and D.G Bleaken. Quasar host galaxy images from the hubble space telescope archive. *MNRAS*, 302 :L39, 1999.

[14] A.G. Bruzual. Spectral evolution of galaxies. i - early-type systems. *ApJ*, 273 :105, 1983.

[15] G. Bruzual and S. Charlot. Stellar population synthesis at the resolution of 2003. *MNRAS*, 344 :1000, 2003.

[16] I. Burud, F. Courbin, P. Magain, C. Lidman, D. Hutsemékers, J.-P. Kneib, et al. An optical time-delay for the lensed BAL quasar HE 2149-2745. *A&A*, 383 :71, 2002.

[17] G. Canalizo and Stockton A. 3C 48 : Stellar populations and the kinematics of stars and gas in the host galaxy. *ApJ*, 528 :201, 2000.

[18] G. Canalizo and A. Stockton. Quasi-stellar objects, ultraluminous infrared galaxies, and mergers. *ApJ*, 555 :719, 2001.

[19] N. Cardiel. *Star Formation in Central Cluster Galaxies.* PhD thesis, Universidad Complutense de Madrid, 1999.

[20] A. Cattaneo, F. Combes, S. Colombi, E. Bertin, and A.-L. Melchior. Spectral and morphological properties of quasar hosts in smoothed particle hydrodynamics simulations of active nucleus feeding by mergers. *MNRAS*, 359 :1237, 2005.

[21] E.T. Chatzichristou, C. Vanderriest, and Jaffe W. Spectroscopic mapping of the quasar 3C 48 at sub-arcsec resolution. *A&A*, 343 :407, 1999.

[22] J. Condon, W. Cotton, E. Greisen, Q. Yin, R. Perley, G. Taylor, and J. Broderick. The NRAO VLA sky survey. *AJ*, 115 :1693, 1998.

[23] Y. Copin and E. Cretton, N.and Emsellem. Axisymmetric dynamical models for SAURON and OASIS observations of NGC3377. *A&A*, 415 :889, 2004.

[24] F. Courbin, G. Letawe, P. Magain, L. Wisotzki, P. Jablonka, K. Jahnke, B. Kuhlbrodt, D. Alloin, G. Meylan, D. Minniti, and I. Burud. On-axis spatially resolved spectroscopy of low redshift quasar host galaxies :HE 1503+0228, at z = 0.135. *A&A*, 394 :863, 2002.

[25] F. Courbin, P. Magain, M. Kirkove, and S. Sohy. A method for spatial deconvolution of spectra. *ApJ*, 529 :1136, 2000.

[26] D.M. Crenshaw, S.B. Kraemer, and J.R. Gabel. The host galaxies of narrow-line seyfert 1 galaxies : Evidence for bar-driven fueling. *AJ*, 126 :1690, 2003.

[27] M.H.K. de Grijp, J. Lub, and G.K. Miley. Warm IRAS sources. I. a. catalogue of AGN candidates from the point source catalog. *AAS*, 70 :95, 1987.

[28] T. Di Matteo, V. Springel, and L. Hernquist. Energy input from quasars regulates the growth and activity of black holes and their host galaxies. *Nature*, 433 :604, 2005.

[29] M.J. Disney, P.J. Boyce, J.C. Blades, et al. Interacting elliptical galaxies as hosts of intermediate redshift quasars. *Nature*, 376 :150, 1995.

[30] J.S. Dunlop, R.J. McLure, M.J. Kukula, S. A. Baum, C. P. O'Dea, and D. H. Hughes. Quasars, their host galaxies and their central black holes. *MNRAS*, 340 :1095, 2003.

[31] M. Eracleous and J.P. Halpern. Accurate redshifts and classifications for 110 radio-loud active galactic nuclei. *APJSS*, 150 :181, 2004.

[32] I. Evans, A. Koratkar, M. Allen, M. Dopita, and Z. Tsvetanov. The excitation mechanism of emission-line regions in seyfert galaxies. *ApJ*, 521 :531, 1999.

[33] A.C. Fabian. The obscured growth of massive black holes. *MNRAS*, 308 :L39, 1999.

[34] L. Ferrarese. Beyond the bulge : A fundamental relation between supermassive black holes and dark matter halos. *ApJ*, 578 :90, 2002.

[35] M. Fioc and B. Rocca-Volmerange. A statistical study of nearby galaxies. i.NIR growth curves and optical-to-NIR colors as a function of type, luminosity and inclination. *A&A*, 351 :869, 1999.

[36] D.J.E. Floyd, M.J. Kukula, J.S. Dunlop, and others. The host galaxies of luminous quasars. *MNRAS*, 355 :196, 2004.

[37] R. Fosbury, C. Tadhunter, I. Danziger, and J. Bland. Very extended ionized gas in radio galaxies. III forbidden-line O III emission along the radio axis of PKS 0634-20. *MNRAS*, 208 :955, 1984.

[38] M. Fukugita, K. Shimasaku, and T. Ichikawa. Galaxy colors in various photometric band systems. *PASP*, 107 :945, 1995.

[39] P. Goudfrooij and E. Emsellem. Ionized gas in early-type galaxies : its effect on Mgb and other stellar line-strength indices. *A&A*, 306 :45, 1996.

[40] J.L. Greenstein and M. Schmidt. The quasi-stellar radio sources 3c 48 and 3c 273. *ApJ*, 140 :1, 1964.

[41] D. Grupe, B.J. Wills, K.M. Leighly, and H. Meusinger. A complete sample of soft x-ray-selected AGNs. i. the data. *AJ*, 127 :156, 2004.

[42] M. G. Haehnelt, M. B. Davies, and M. J. Rees. Possible evidence for the ejection of a supermassive black hole from an ongoing merger of galaxies. *MNRAS*, 366 :22, 2006.

[43] P. Heinämäki, J. Einasto, M. Einasto, et al. The mass function of the las campanas loose groups of galaxies. *A&A*, 397 :63, 2003.

[44] L. Hoffman and A. Loeb. Three-body kick to a bright quasar out of its galaxy during a merger. ApJL, in press, astro-ph/0511242, 2006.

[45] D.H. Hughes, M.J. Kukula, J.S. Dunlop, and T. Boroson. Optical off-nuclear spectra of quasar hosts and radio galaxies. *MNRAS*, 316 :204, 2000.

[46] J.B. Hutchings. Quasars - hosts of possibilities. *Nature*, 376 :118, 1995.

[47] J.B. Hutchings and D. Crampton. Images and off-nuclear spectroscopy of QSOs. *AJ*, 99 :37, 1990.

[48] J.B. Hutchings and S.G. Neff. Optical imaging of QSOs with 0.5 arcsec resolution. *AJ*, 104 :1, 1992.

[49] Y. Izotov and T. Thuan. Heavy element abundances in blue compact galaxies. *ApJ*, 511 :639, 1999.

[50] K. Jahnke. *Stellar populations of* QSO *host galaxies.* PhD thesis, Universität Hamburg, 2002.

[51] K. Jahnke, B. Kuhlbrodt, and K. Wisotzki. Quasar host galaxy star formation activity from multicolour data. *MNRAS*, 352 :399, 2004.

[52] K. Jahnke and K. Wisotzki. The B-band luminosities of quasar host galaxies. *MNRAS*, 346 :304, 2003.

[53] R.A. Jansen, D. Fabricant, M. Franx, and N. Caldwell. Spectrophotometry of nearby field galaxies : The data. *ApJSS*, 126 :331, 2000.

[54] S. Kaspi, P.S. Smith, H. Netzer, et al. Reverberation measurements for 17 quasars and the size-mass-luminosity relations in active galactic nuclei. *ApJ*, 533 :631, 2000.

[55] G. Kauffmann, T.M. Heckman, C. Tremonti, J. Brinchmann, S. Charlot, S.D. White, S.E. Ridgway, et al. The host galaxies of active galactic nuclei. *MNRAS*, 346 :1055, 2003.

[56] K. Kellermann, R. Sramek, D. Schmidt, D. Shaffer, and R. Green. VLA observations of objects in the palomar bright quasar survey. *AJ*, 98 :1195, 1989.

[57] R. Kennicutt. The integrated spectra of nearby galaxies - general properties and emission-line spectra. *ApJ*, 388 :310, 1992.

[58] R. Kennicutt. A spectrophotometric atlas of galaxies. *ApJS*, 79 :255, 1992.

[59] R.C. Kennicutt. Star formation in galaxies along the hubble sequence. *ARAA*, 36 :189, 1998.

[60] L.J. Kewley, M.J. Geller, and R.A. Jansen. [O II] as a star formation rate indicator. *AJ*, 127 :2002, 2004.

[61] L.J. Kewley, R.A. Jansen, and M.J. Geller. Aperture effects on star formation rate, metallicity, and reddening. *PASP*, 117 :227, 2005.

[62] H.A. Kobulnicky, R.C. Kennicutt, and J.N. Pizagno. On measuring nebular chemical abundances in distant galaxies using global emission-line spectra. *ApJ*, 514 :544, 1999.

[63] H.A. Kobulnicky and A.C. Phillips. Measuring global galaxy metallicities using emission-line equivalent widths. *ApJ*, 599 :1031, 2003.

[64] T. Köhler, D. Groote, D. Reimers, and L. Wisotzki. The local luminosity function of QSOs and seyfert 1 nuclei. *A&A*, 325 :502, 1997.

[65] W. Kollatschny. Spin orientation of supermassive black holes in active galaxies. *A&A*, 412 :L61, 2003.

[66] H.J. Krolik. *Active Galactic Nuclei.* Princeton : Princeton Series in Astrophysics, 1999.

[67] B. Kuhlbrodt. *Analysis of Quasar Images, the luminosity function of agn host galaxies.* PhD thesis, Universität Hamburg, 2003.

[68] A. Laor, F. Fiore, M. Elvis, B.J. Wilkes, and J.C. McDowell. The soft x-ray properties of a complete sample of optically selected quasars. II. final results. *ApJ*, 477 :93, 1997.

[69] G. Letawe et al. On-axis spectroscopy of the z = 0.144 radio-loud quasar HE 1434-1600 : an elliptical host with a highly ionized ISM. *A&A*, 424 :455, 2004.

[70] S. Lipari and R. Terlevich. Evolutive unification in composite active galactic nuclei. submitted to MNRAS, astro-ph/0602090, 2006.

[71] S. Lipari, R. Terlevich, W. Zheng, et al. Infrared mergers and infrared quasi-stellar objects with galactic winds-III. mrk231, an exploding young quasi-stellar object with composite outflow/broad absorption line (and multiple expanding superbubbles). *MNRAS*, 360 :416, 2005.

[72] F.J. Low, R.M. Cutri, J.P. Huchra, and S.G. Kleinman. Infrared color-selected quasars and seyfert 1 galaxies. *ApJ*, 327 :L41, 1988.

[73] F.D Macchetto. Supermassive black holes in spiral galaxies. In I. Shlosman Eds. S. Collin, F. Combes, editor, *Active Galactic Nuclei : from Central Engine to Host Galaxy*, volume 290, page 567. ASP Conference Series, 2003.

[74] F.D. Macchetto, A. Marconi, D.J. Axon, et al. The supermassive black hole of M87 and the kinematics of its associated gaseous disk. *ApJ*, 489 :579, 1997.

[75] P. Magain, F. Courbin, and S. Sohy. Deconvolution with correct sampling. *ApJ*, 494 :472, 1998.

[76] P. Magain, G. Letawe, F. Courbin, P. Jablonka, et al. Discovery of a bright quasar without a massive host galaxy. *Nature*, 437 :381, 2005.

[77] J. Magorrian, S. Tremaine, D. Richstone, et al. The demography of massive dark objects in galaxy centers. *AJ*, 115 :2285, 1998.

[78] V. Mainieri, D. Rigopoulou, I. Lehmann, S. Scott, et al. Submillimeter detection of a high redshift type-2 QSO. *MNRAS*, 356 :1571, 2005.

[79] A. Marconi, D. J. Axon, A. Capetti, et al. Is there really a black hole at the center of NGC 4041 ? constraints from gas kinematics. *ApJ*, 586 :868, 2003.

[80] A. Marconi, A. Capetti, D.J. Axon, et al. Peering through the dust : Evidence for a supermassive black hole at the nucleus of centaurus a from VLT infrared spectroscopy. *ApJ*, 549 :915, 2001.

[81] A. Marconi and L.K. Hunt. The relation between black hole mass, bulge mass, and near-infrared luminosity. *ApJ*, 589 :L21, 2003.

[82] I. Marquez, P. Petitjean, B. Theodore, et al. Adaptive optics imaging of low and intermediate redshift quasars. *A&A*, 371 :97, 2001.

[83] S. McGaugh. Hii region abundances : model oxygen line ratio. *ApJ*, 380 :140, 1991.

[84] K.K. McLeod and G. H. Rieke. Luminous quasars in luminous early-type host galaxies. *ApJ*, 454 :L77, 1995.

[85] K.K. McLeod, G. H. Rieke, and L. J. Storrie-Lombardi. Quasars and ultraluminous infrared galaxies : At the limit ? *ApJ*, 511 :L67, 1999.

[86] R. J. McLure and J. S. Dunlop. On the black hole-bulge mass relation in active and inactive galaxies. *MNRAS*, 331 :795, 2002.

[87] R. J. McLure, M. J. Kukula, J. S. Dunlop, S. A. Baum, C. P. O'Dea, and D. H. Hughes. A comparative HST imaging study of the host galaxies of radio-quiet quasars, radio-loud quasars and radio galaxies - I. *MNRAS*, 308 :377, 1999.

[88] D. Merritt, T. Storchi Bergmann, A. Robinson, D. Batcheldor, D. Axon, and R. Cid Fernandes. The nature of the he0450-2958 system. MNRAS, in press, astro-ph/0511315, 2006.

[89] J.S. Miller and W.G. Mathews. The recombination spectrum of the planetary nebula NGC 7027. *ApJ*, 172 :593, 1972.

[90] J.S. Miller and A.I. Sheinis. Keck spectroscopy of four quasi-stellar object host galaxies. *ApJ*, 588 :L9, 2003.

[91] R. Morganti, T. Oosterloo, J. Holt, et al. IC 5063 : AGN driven outflow of warm and cold gas. *The ESO Messenger*, 113 :67, 2003.

[92] R. Morganti, T. Oosterloo, and Z. Tsvetanov. A radio study of the seyfert galaxy IC 5063 : Evidence for fast gas outflow. *AJ*, 115 :915, 1998.

[93] J. Moustakas and R. Kennicutt. Integrated nebular abundances of disk galaxies. Submitted to ApJ, astro-ph/0511731, 2005.

[94] L.A. Nolan, J.S. Dunlop, M.J. Kukula, D.H. Hughes, T. Boroson, and R. Jimenez. The ages of quasar host galaxies. *MNRAS*, 323 :308, 2001.

[95] J.B. Oke. Absolute energy distribution in the optical spectrum of 3C 273. *Nature*, 197 :1040, 1963.

[96] M. Page, J. Stevens, Ivison R., and Carrera F. The evolutionary sequence of active galactic nuclei and galaxy formation revealed. *ApJ*, 611 :85, 2004.

[97] W. Percival, L. Miller, R. McLure, and J. Dunlop. the host galaxies of luminous radio-quiet quasars. *MNRAS*, 322 :843, 2001.

[98] B. Peterson. *An introduction to Active galactic Nuclei.* Cambridge University Press, 1997.

[99] D. Richstone, E. A. Ajhar, R. Bender, et al. Supermassive black holes and the evolution of galaxies. *Nature*, 395 :A14, 1998.

[100] J. Rönnback, E. van Groningen, I. Wanders, and E. Örndahl. The host galaxies of intermediate redshift radio-loud and radio-quiet quasars. *MNRAS*, 283 :282, 1996.

[101] S.F. Sanchez, K. Jahnke, L. Wisotzki, D.H. McIntosh, E.F. Bell, et al. Colors of active galactic nucleus host galaxies at 0.5<z<1.1 from the gems survey. *ApJ*, 614 :586, 2004.

[102] D.J. Schlegel, D.P. Finkbeiner, and M. Davis. Maps of dust infrared emission for use in estimation of reddening and cosmic microwave background radiation foregrounds. *ApJ*, 500 :525, 1998.

[103] N. Scoville, T. Frayer, E. Schinnerer, and N. Christopher. The host galaxies of optically bright quasi stellar objects : Molecular gas in z<0.1 palomar green quasi stellar objects. *ApJ*, 585 :L105, 2003.

[104] E.P. Smith, T.M. Heckman, G.D. Bothun, W. Romanishin, and B. Balick. On the nature of QSO host galaxies. *ApJ*, 306 :64, 1986.

[105] L. Sodré and G. Stasińska. The emission line sequence of normal spiral galaxies. *A&A*, 345 :391, 1999.

[106] S.A. Stanford and H.A. Bushouse. A near-infrared imaging survey of interacting galaxies - the disk-disk merger candidates subset. *ApJ*, 371 :92, 1991.

[107] J.A. Stepanian, E. Benitez, Y. Krongold, I. Cruz-Gonzalez, J.A. de Diego, et al. A multiwavelength study of narrow-line seyfert 1 galaxies from the second byurakan survey. *ApJ*, 588 :746, 2003.

[108] A. Stockton, G. Canalizo, and L. Close. PG 1700+518 revisited : Adaptive-optics imaging and a revised starburst age for the companion. *ApJ*, 500 :L121, 1998.

[109] A. Stockton and J. MacKenty. Extended emission-line regions around QSOs. *ApJ*, 316 :584, 1987.

[110] A. Stockton, J. MacKenty, E. Hu, and T. Klim. The extended emission-line region of 4C 37.43. *ApJ*, 572 :735, 2002.

[111] C. Tadhunter and Z. Tsvetanov. Anisotropic ionizing radiation in NGC 5252. *Nature*, 341 :422, 1989.

[112] S.C. Trager, G. Worthey, S.M. Faber, et al. Old stellar populations. VI. absorption-line spectra of galaxy nuclei and globular clusters. *ApJS*, 116 :1, 1998.

[113] D.E. Vanden Berk, J. Shen, C. Yip, D.P. Schneider, A.J. Connolly, R.E. Burton, et al. Spectral decomposition of broad-line AGNs and host galaxies. *AJ*, 131 :84, 2006.

[114] S. Veilleux and D. Osterbrock. Spectral classification of emission-line galaxies. *ApJS*, 63 :295, 1987.

[115] J. Vernet, R. Fosbury, M. Villar-Martin, et al. Radio galaxies at z 2.5 : Results from keck spectropolarimetry. *A&A*, 366 :7, 2001.

[116] D.W. Weedman. *Quasar Astronomy.* Cambridge astrophysical Series, 1986.

[117] R. Wilman, R. Johnstone, and C. Crawford. Extended line emission around seven radio-loud quasars at redshift z= 2. *MNRAS*, 317 :9, 2000.

[118] A. Wilson and Z Tsvetanov. Ionization cones and radio ejecta in active galaxies. *AJ*, 107 :1127, 1994.

[119] L. Wisotzki, N. Christlieb, N. Bade, et al. The Hamburg/ESO survey for bright QSOs. III. a large flux-limited sample of QSOs. *A&A*, 358 :77, 2000.

[120] G. Worthey, S.M. Faber, and D. Gonzalez, J.J.and Burstein. Old stellar populations. 5 : Absorption feature indices for the complete LICK/IDS sample of stars. *ApJSS*, 94 :687, 1994.

[121] G. Wright, P. James, R. Joseph, and I. McLean. Elliptical-like light profiles in infrared images of merging spiral galaxies. *Nature*, 344 :417, 1990.